![Chalmers University of Technology logo](CHALMERS UNIVERSITY OF TECHNOLOGY)

Control of a subsea PMSM with a very long feeding cable using a top-side converter – design and performance evaluation

Master of Science Thesis

Junfei Tang

Division of Electric Power Engineering

Department of Energy and Environment

Chalmers University of Technology

Gothenburg, Sweden, 2016

THESIS FOR THE DEGREE OF MASTER OF SCIENCE

Control of a subsea PMSM with a very long feeding cable using a top-side converter – design
and performance evaluation

Junfei Tang

Performed at: Chalmers University of Technology
Gothenburg, Sweden

Examiner: Lundberg Stefan
Division of Electric Power Engineering
Department of Energy and Environment
Chalmers University of Technology
Gothenburg, Sweden

Supervisor: Francesco Marra
Senior researcher – Subsea facilities
Statoil RDI
Trondheim, Norway

Control of a subsea PMSM with a very long feeding cable using a top-side converter – design and performance evaluation

Master of Science Thesis

Junfei Tang

Abstract

In oil and gas extraction applications, Permanent Magnet Synchronous Motors (PMSMs) are becoming a more preferred choice to drive Electric Submersible Pumps in order to achieve a higher efficiency than Induction Motors (IMs). In the drive system, a subsea PMSM is fed from a top-side Variable Speed Drive (VSD) through a transmission system including a step-up transformer and a long feeding cable. In this work, both the series impedance and the shunt admittance of the transmission system are taken into consideration. Sensorless control of such a subsea PMSM is implemented and evaluated in this thesis work.

The sensorless control is realized by the combination of the Static Compensated Voltage Model (SCVM) method and the High Frequency Injection (HFI) method. An equivalent IM model current controller is developed to deal with the transformer shunt branch and a static estimator is implemented to estimate the PMSM voltage and current. The developed controller can successfully start and accelerate the PMSM up to 6000 rev/min within 5 s and the efficiency during steady state operation achieves 91.65% excluding the iron-core loss of the PMSM. The steady state angle estimation error with perfect parameters is -0.8506° with peak dynamic angle estimation errors at +0.7063° and -4.7335° respectively. A ±10% parameter error is acceptable for a successful PMSM start-up except for a -10% PMSM magnet flux linkage error which generates a too large angle estimation error during the start-up and leads to a start-up failure.

In conclusion, the field-oriented sensorless control of a PMSM through a transmission system is possible. A five-level inverter needs to be applied to reduce the harmonic contents to realize a successful start-up of the PMSM. It is also suggested that the accuracy of the PMSM magnet flux linkage and the stator inductance are of essential importance.

Index terms: PMSM, Subsea, Electric Drive System, Long Feeding Cable, Sensorless Control.

Acknowledgement

First of all, I would like to express my gratitude for the workplace provided to me by the Division of Electric Power Engineering at Chalmers University of Technology.

I need to thank my examiner Stefan Lundberg for his super patience and efficient guidance to develop and modify the electric drive system.

I would like to thank my supervisor Francesco Marra for giving me the opportunity to carry out such a challenging work and the timely instructions every week to overcome so many problems.

Thank Tarik Abdulahovic for his support with software issues.

In addition, I should thank Professor Bo Egardt from the Division of Automatic Control for his help of building the state space model for the transmission system.

Finally, thank my family for their endless encouragement and support.

<div align="right">

Junfei Tang

Gothenburg, 2016

</div>

Contents

List of Figures

List of Tables

1   Introduction

1.1   Problem Background

In oil and gas applications, Electric Submersible Pumps (ESPs) are often utilized to increase the flow in production wells with insufficient natural pressure to achieve profitable flow levels. ESPs are basically composed of a pump and a motor, and are usually supplied by a topside Variable Speed Drive (VSD) through a feeding cable that can have a length of several kilometers [1]. The structure of the ESP system can be presented as shown in Figure 1-1. In order to manage the feeding scenario of such a long transmission distance, a step-up transformer can be used at the sending end of the cable to increase the feeding voltage to a level that can be transmitted. These ESPs range up to a few MW in size, and were originally driven by Induction Motors (IMs) which offer a high reliability but a relatively low efficiency. However, thanks to the development of the motor technology, now Permanent Magnet Synchronous Motors (PMSMs) may become a more preferred choice in this subsea application, due to their high power density, higher efficiency and higher power factor [2] [3]. A position-sensorless control of the PMSM is required in order to reduce the cost of the sensor together with the communication system which sends the acquired position information back to the controller, and also to improve the system reliability. Since if the sensor breaks down, the ESP should be pulled out from the sea before the replacement can be done.
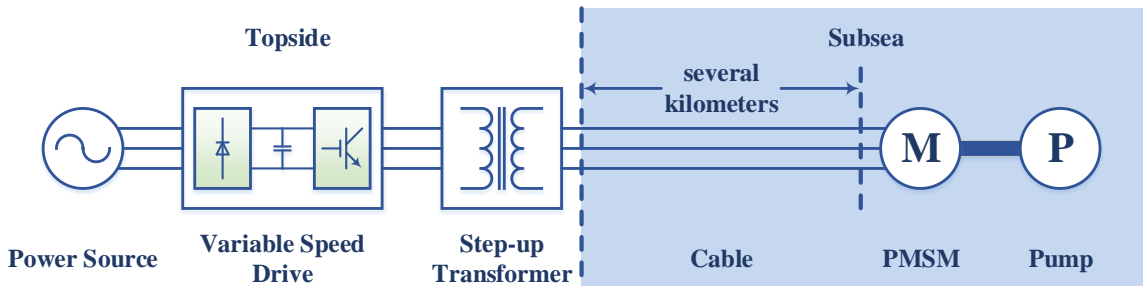
Figure 1-1 System structure of the subsea electric drive system for the ESP application

In a previous work [4], a similar system structure as shown in Figure 1-1 was used together with a non-salient PMSM and an ideal converter, and only the series impedance of the cable and transformers were taken into consideration. The previous work mainly focused on different control schemes, while the shunt branches together with the converter non-idealities were not considered. From the industrial application, there is an interest to investigate if these shunt branches have an influence on the ESP system and the controllers. There is also an interest to investigate if a sensorless control structure can be used for the ESP system. In the Future Work of [4], it has also been mentioned that the continued work should consider a salient PMSM, a more realistic VSD, the magnetization of the transformers and the energization of the cable.

1.2   Aim

The purpose of the work is to study the performance of an underwater PMSM drive system including a realistic power electronic inverter, a step-up transformer, a long feeding cable and a salient PMSM. The effects of the shunt branches on the system and on the sensorless estimator should be investigated. The ESP system should be able to start from standstill and to accelerate up to 6000 rev/min within 10 s.

1.3   Scope

The start-up of the ESP PMSM is the major scope of this thesis work instead of the steady state operation and therefore, the field-weakening algorithm, the Maximum Torque per Ampere (MTPA) algorithm and the topside grid disturbances are not considered. Due to the short duration of the start-up, the dc-link voltage can be regarded as constant in the work, which means that the topside grid voltage before the VSD is assumed to be perfectly sinusoidal.

In addition, as has been concluded in the previous work [4], field-oriented control (vector control) can provide the drive system with better performance than V/f control (scalar control). In this thesis work only field-oriented control will be applied with a rotor position estimation algorithm. The selected sensorless control strategy must either be insensitive to the initial rotor position or be able to detect the initial rotor position. However, the identification of the initial rotor position is not included in the work which means that the initial rotor position is assumed to be known.

The effects of the transmission system should be studied and the controller needs to be restructured to deal with the negative effects from the transmission system accordingly. In the end, parameter errors are introduced and their corresponding effects are studied.

A desirable method to evaluate this system should be based on both simulation and laboratory tests. However, due to the complexity and the time limitation, laboratory tests are left to the future work. Therefore, the design, implementation and evaluation of the system is only carried out in simulation and practical tests are not included in the project plan.

1.4   Methods

The general system consists of a 500 kW PMSM, supplied by an inverter through a step-up transformer and a 15 km cable. A realistic load torque is applied to the PMSM according to the application. A magnetization branch is included in the structure of the step-up transformer and the energization branches are included in the cable model. The converter is based on a two-level topology in the beginning, which later is changed to a multi-level topology to improve the performance if necessary. The built-in blocks from the *SimPowerSystems* toolbox in MATLAB/Simulink are used for building the model of the system and the controllers are implemented with the standard Simulink blocks.

The power electronic converter is supposed to be modelled with realistic parameters. The modeling of the transformer can be based on two coupling windings and the PMSM is modeled by dq frame equations. Considering the length of the cable, and in order to guarantee acceptable modelling accuracy, the feeding cable can be represented by several π models of series impedance and shunt admittance. The controller design is based on the Inner Model Control (IMC) method [5] [6].

The modeling sequence is divided into nine parts as can be seen in Table 1-1. The implementation goes from Model 1 towards Model 9 following a simple to advanced model approach. In Model 1, the most basic configuration, an ideal converter is directly connected to the PMSM without the transmission system and the PMSM further delivers power to the pump. For this model a continuous time vector controller with a position- and speed-sensor is used. The thesis work starts with this most simple and ideal case in order to make sure that the current control and the speed control are able to work properly. Then, the position-sensorless control is applied in Model 2 in order to investigate the performance of the sensorless control algorithms. Up to here, an ideal converter is applied with continuous control which is not the case in reality. Therefore, in Model 3, controller discretization is carried out and the ideal converter is replaced with a realistic switching converter.

Model 1 to 3 are further developed to Model 4 to 6 respectively, where the series impedance of the transmission system is added. The effects from the series impedance to the current controller and the sensorless control algorithms should firstly be investigated and then, proper tuning strategies are supposed to be found and verified. Then, Model 4 to 6 are further developed to Model 7 to 9 respectively, where the shunt admittance of the transmission system is further added. Similarly, the disturbance from the shunt admittance to the current controller and the sensorless control algorithms should firstly be investigated. Then, proper compensation strategies for the shunt currents, including the restructuring of the current controller and of the sensorless estimator are performed and implemented.

Table 1-1 Modeling sequence

Model Structure	Vector Control with Sensor	Position-Sensorless Control	Realistic Converter & Discrete-Time Control
Converter + PMSM + Pump	Model 1	Model 2	Model 3
+ Series Impedance	Model 4	Model 5	Model 6
+ Cable Shunt Branch + Transformer Excitation Branch	Model 7	Model 8	Model 9

1.5   Previous Work

In the previous work [4] conducted in 2013, four control strategies have been studied:

- Open-loop scalar control

The PMSM equations are greatly simplified that the resistive voltage drop is neglected and the V/f ratio is supposed to be kept as a constant so that a certain level of flux linkage can be held. The slops of V/f are defined in both the low speed region and the high speed region. This scheme is simple but a high magnetizing current is required.

- Closed-loop scalar control

Taking the resistive voltage drop into consideration, a current feedback is input into the controller to decide the voltage reference and a stabilizer is used to avoid the PMSM from losing synchronism when confronting power or speed oscillations. Much lower current is required than the open-loop scalar control.

- Vector control with position sensor

Field-oriented control is applied and a smooth start-up performance has been shown in the simulation results without any overshoots and the current rise time agrees with the bandwidth of the current controller. In addition, the response of the current controller to load disturbances is almost ideal.

- Vector control without position sensor

The control scheme is switched from V/f control to sensorless vector control after the short start-up period. The position estimator gives accurate position information after taking over the control from V/f scheme. This case is similar to Model 6 in this continued thesis work except for the difference that Model 6 starts the PMSM from standing still by directly applying sensorless vector control.

As has been concluded, the vector control algorithm has shown a faster and more accurate performance than the scalar control algorithms. And in order to control the PMSM in subsea applications, sensorless control is a necessity. Therefore, this thesis work is mainly continued from the last case in the previous work.

2   Component Description

The descriptions of each component in the system are presented in this chapter except for the power electronic converter which is described with its SVPWM algorithm.

2.1   Permanent Magnetic Synchronous Motor

The αβ and dq coordinate systems are a basic knowledge to understand the structure of the Permanent Magnetic Synchronous Motors (PMSMs) and therefore is presented in the beginning of the section. Then the structures of both non-salient and salient PMSMs are introduced, which is followed by the equations and modelling of the salient PMSM used in this thesis work.

2.1.1   αβ and dq Coordinate Systems

The field-oriented control, the converter modulation technique and the illustration of the PMSM rotor structure are based on the concept of space vectors. Apart from time-domain functions, space vectors are a graphic expression of dynamic three-phase variables. Assuming no zero-sequence component, the sums of three-phase voltages and currents are zero

$$x_A(t) + x_B(t) + x_C(t) = 0 \tag{2-1}$$

where $x_A(t)$, $x_B(t)$ and $x_C(t)$ are the three-phase voltages or currents. In this case, the three-phase quantities are not independent which means that if two of them are known, then the third one can be calculated by utilizing (2-1). By applying the addition rule of vectors, the three-phase quantities can be presented as a space vector

$$\begin{aligned}
\underline{x}^s(t) &= x_\alpha(t) + jx_\beta(t) \\
&= \frac{2}{3}K\left[x_A(t) + x_B(t)e^{j\frac{2\pi}{3}} + x_C(t)e^{j\frac{4\pi}{3}}\right] \\
&= \frac{2}{3}K\left[x_A(t)\underline{a} + x_B(t)\underline{b} + x_C(t)\underline{c}\right]
\end{aligned} \tag{2-2}$$

where $\underline{x}^s(t)$ is the voltage or current space vector in the stationary frame, $x_\alpha(t)$ and $x_B(t)$ are the components of the space vector in the horizontal- and vertical-axis respectively, $\underline{a}$, $\underline{b}$ and $\underline{c}$ are unit vectors for the phases and K is the scaling factor applied during the transformation. As is indicated in Table 2-1, the scaling factor can be selected depending on different applications. Power-invariant transformation is convenient for the instantaneous power calculation which for example is applied in [7]. RMS-invariant transformation can be applied in which the rms values can be detected directly. In this thesis work, amplitude-invariant transformation will be applied for its convenience in detecting the amplitudes of the phase quantities.

Table 2-1 The scaling factor K in abc-αβ transformation

Amplitude-Invariant	$K = 1$	$\|\underline{x}\| = \hat{x}_a = \hat{x}_b = \hat{x}_c$
Power-Invariant	$K = \dfrac{\sqrt{3}}{\sqrt{2}}$	$p = u_a i_a + u_b i_b + u_c i_c = u_\alpha i_\alpha + u_\beta i_\beta$
RMS-Invariant	$K = \dfrac{\sqrt{2}}{2}$	$\|\underline{x}\| = X_{a\cdot rms} = X_{b\cdot rms} = X_{c\cdot rms}$

Furthermore, the rotating dq coordinate system is defined in order to transform the AC quantities in the stationary system into the DC quantities in the rotation system. The d-axis indicates the direct-axis and the q-axis indicates the quadrature-axis. Figure 2-1 shows the relationship between the abc, the αβ and the dq coordinate systems. As can be seen from the figure, in αβ coordinate system, the α-axis is aligned with the a-axis of the three-phase system.

In dq coordinate system, the d-axis is defined to be aligned with the rotor flux linkage $\underline{\psi}_r$. The relationship between the quantities in the αβ and dq coordinate systems can be expressed as

$$\underline{x} = \underline{x}^s e^{-j\theta_r}$$
$$\begin{bmatrix} x_d(t) \\ x_q(t) \end{bmatrix} = \begin{bmatrix} \cos(\theta_r) & \sin(\theta_r) \\ -\sin(\theta_r) & \cos(\theta_r) \end{bmatrix} \begin{bmatrix} x_\alpha(t) \\ x_\beta(t) \end{bmatrix} \tag{2-3}$$

Where $\underline{x}$ is the space vector in the dq frame, $x_d(t)$ and $x_q(t)$ are the components in the d- and q-axis respectively.
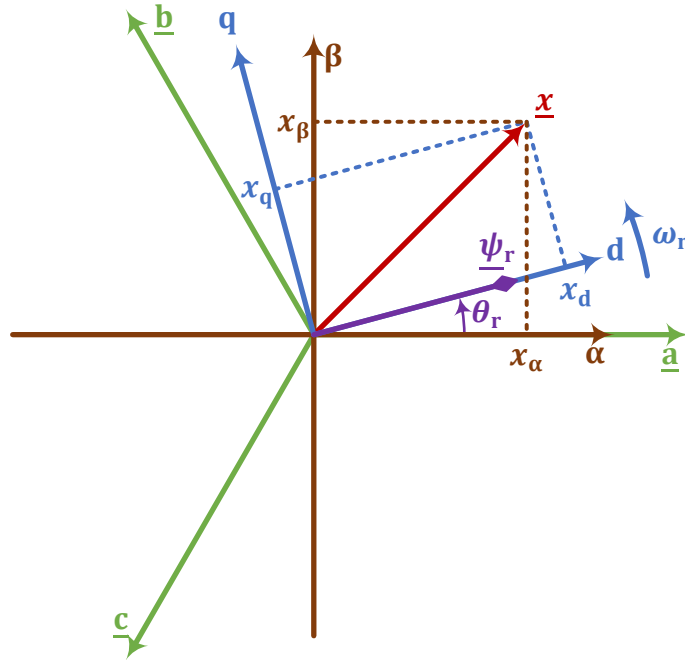
Figure 2-1 The relationship among the abc, αβ and dq coordinate systems

2.1.2 SPMSM and IPMSM

PMSMs can be classified into two groups by the rotor structure: Surface-mounted Permanent Magnet Synchronous Motors (SPMSMs) and Insert-mounted Permanent Magnet Synchronous Motors (IPMSMs) [8] [9]. The Insert-mounted Permanent Magnet (IPM) rotors can be further divided into Inset PM rotors and Interior PM rotors [2] as shown in Figure 2-2.

(a)   (b)   (c)
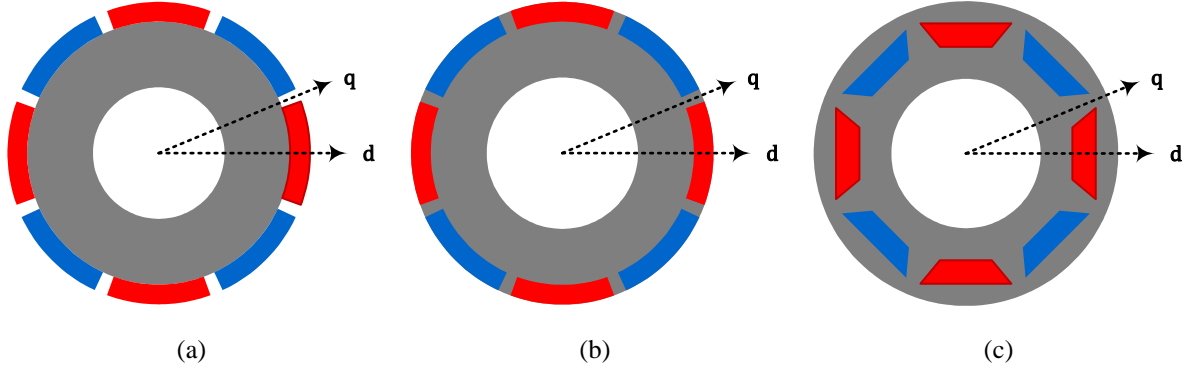
Figure 2-2 Classification of PMSM rotors

(a) Surface-mounted PM rotor   (b) Inset PM rotor   (c) Interior PM rotor

(non-salient)   (moderate salient)   (high salient)

Since the relative permeability of the magnets $\mu_{r \cdot mag}$ is almost the same as the one of air $\mu_{r \cdot air}$

$$\mu_{r \cdot mag} \approx \mu_{r \cdot air} = 1 \tag{2-4}$$

while the relative permeability of the core $\mu_{r \cdot core}$ is much larger than the one of air $\mu_{r \cdot air}$

$$\mu_{r \cdot core} \gg \mu_{r \cdot air} \tag{2-5}$$

the difference of reluctance along d- and q-axis depends on the difference of thickness of the core along the axis.

Figure 2-2 (a) shows the structure of Surface-mounted Permanent Magnet (SPM) rotors. The magnets are attached to the outer surface of the rotor. The thickness of the core along the d-axis is the same as the one along the q-axis and therefore, there is no reluctance difference between d- and q-axis, which means no saliency: the stator inductances are exactly the same whenever it is aligned with the d-axis or q-axis of the rotor [8]. Hence it can be expressed that

$$L_{sd} = L_{sq} = L_s \tag{2-6}$$

where L_{sd} is the stator inductance along the d-axis, L_{sq} is the stator inductance along the q-axis and L_s is the general notation of the stator inductance when there is no salience. In this case, the electromagnetic torque T_e is entirely produced by the interaction between stator currents i_s and rotor magnet flux linkage ψ_{pm} [8].

Figure 2-2 (b) shows the structure of Inset Permanent Magnet rotors. The magnets are inset the outer surface of the rotor. A saliency appears due to the teeth that locate in between the adjacent magnet pairs. As the core is thinner in the direction of d-axis than of q-axis, the d-axis inductance is lower than the q-axis inductance

7

$$L_{sd} < L_{sq} \tag{2-7}$$

In this case, apart from the interaction between stator current and rotor magnet flux linkage, a reluctance torque is produced which is similar to the mechanism employed by reluctance motors [8].

Figure 2-2 (c) shows the structure of Interior Permanent Magnet rotors. The magnets are placed in the interior of the rotor. The magnetic structure shows a greater saliency than the previous Inset Permanent Magnet rotors. An even higher saliency can be introduced by placing multi-layers than single-layer [10].

In conclusion, SPMSMs are non-salient and (2-6) satisfies; while IPMSMs are salient and (2-7) satisfies. The IPMSMs have several advantages compared to SPMSMs [2] [9]: IPMSMs give a higher power factor which allows higher efficiency, and its saliency makes an approach of the speed and position detection possible by injecting suitable high frequency signals.

2.1.3   Electrical Model of the IPMSM

Due to the fact that it is a salient PMSM that is used in this work, the machine modeling is performed in the dq coordinate system. In addition, the field-oriented control is applied in the dq frame since it is simpler to control DC quantities than to control AC quantities. Therefore, the dq coordinate model is used both for the machine modeling and for the controller design.

For a salient PMSM, the flux linkage is produced by the stator current and the rotor permanent magnet [11]

$$\begin{bmatrix} \psi_{sd} \\ \psi_{sq} \end{bmatrix} = \begin{bmatrix} L_{sd} & M_{sdq} \\ M_{sqd} & L_{sq} \end{bmatrix} \begin{bmatrix} i_{sd} \\ i_{sq} \end{bmatrix} + \begin{bmatrix} \psi_{pm} \\ 0 \end{bmatrix} \tag{2-8}$$

where i_{sd} is the d-axis stator current, i_{sq} is the q-axis stator current, $M_{sdq} = M_{sqd}$ are the cross-coupling stator inductance, ψ_{sd} and ψ_{sq} are the stator flux linkage along the d- and q-axis respectively and ψ_{pm} is the rotor permanent magnet flux linkage seen from the stator side. In the case of sinusoidal spatial distribution of the stator windings, the cross-coupling stator inductance are regarded as zero, which means that $M_{dq} = M_{qd} = 0$ can be applied [11]. Due to this fact and by using complex notation, the stator flux linkage can be formulated as

$$\underline{\psi}_s = L_{sd}i_{sd} + jL_{sq}i_{sq} + \psi_{pm} \tag{2-9}$$

where $\underline{\psi}_s$ is the flux linkage vector on the stator side in the dq coordinate system. Then the stator voltage equation can be directly written in the dq coordinate system as the sum of the voltage across the stator resistance and the EMF of the stator flux linkage [8]

$$\underline{u}_s = R_s\underline{i}_s + \frac{d\underline{\psi}_s}{dt} + j\omega_r\psi_{pm} \tag{2-10}$$

8

where $\underline{u}_s$ is the stator voltage in the dq coordinate system and ω_r is the rotor speed. As can be seen from (2-10), the EMF of the stator flux linkage in dq frame has two components, one from the change of the stator flux linkage and the other from the rotation of the rotor. Equation (2-10) can be decomposed into the real part (d-axis) and the imaginary part (q-axis)

$$u_{sd} = R_s i_{sd} + \frac{d\psi_{sd}}{dt} - \omega_r \psi_{sq} = R_s i_{sd} + L_{sd}\frac{di_{sd}}{dt} - \omega_r L_{sq} i_{sq} \tag{2-11}$$

$$u_{sq} = R_s i_{sq} + \frac{d\psi_{sq}}{dt} + \omega_r \psi_{sd} = R_s i_{sq} + L_{sq}\frac{di_{sq}}{dt} + \omega_r L_{sd} i_{sd} + \omega_r \psi_{pm} \tag{2-12}$$

As can be seen, $\omega_r L_{sq} i_{sq}$ and $\omega_r L_{sd} i_{sd}$ are the cross-coupling terms which couple the d-axis quantity to the q-axis and q-axis quantity to the d-axis and $\omega_r \psi_m$ is the back-EMF term. From (2-11) and (2-12), the PMSM equivalent circuits in dq coordinate system can be drawn as shown in Figure 2-3. These two circuits are useful for both salient ($L_d \neq L_q$) and non-salient ($L_d = L_q$) PMSMs.

(a)   (b)
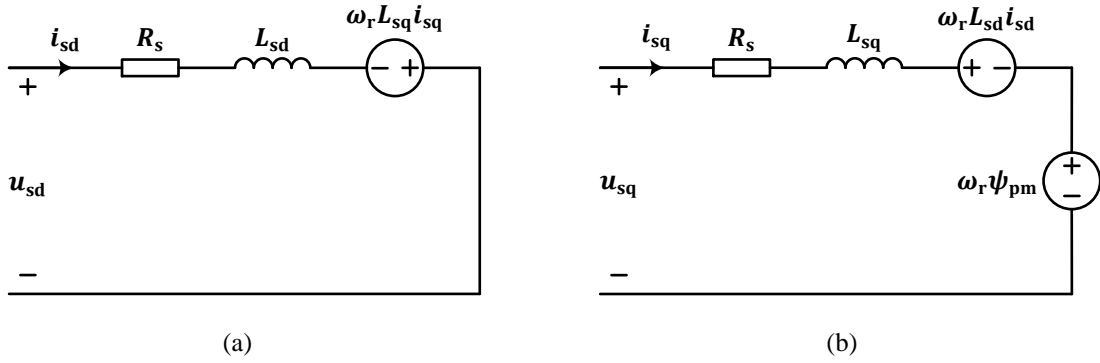
Figure 2-3 The PMSM equivalent circuits in dq coordinate system

(a) d-axis circuit   (b) q-axis circuit

2.1.4 Mechanical Model of the IPMSM

The electromagnetic torque of a salient PMSM is produced by the stator flux linkage and the stator current [12]

$$T_e = \frac{3n_p}{2}\text{Im}\left\{\underline{\psi}_s{}^*\underline{i}_s\right\} = \frac{3n_p}{2}\left[(L_{sd} - L_{sq})i_{sd}i_{sq} + \psi_{pm}i_{sq}\right] \tag{2-13}$$

where T_e is the electromagnetic torque of a salient PMSM and n_p is the number of pole-pairs. As can be seen from (2-13), the total electromagnetic torque T_e can be divided into two parts: the torque produced by the rotor permanent magnet T_{pm}

$$T_{pm} = \frac{3n_p}{2}\psi_{pm}i_{sq} \tag{2-14}$$

and the torque produced by the difference between the reluctance of the d- and q-axis $T_\Re$

$$T_\Re = \frac{3n_p}{2}\left(L_{sd} - L_{sq}\right)i_{sd}i_{sq} \tag{2-15}$$

9

The total load torque can be given as the combination of the viscous damping torque from the PMSM itself and an extra torque due to the pump

$$T_L = B\Omega_r + T_{pump} \tag{2-16}$$

where T_L is the total load torque, B is the viscous factor of the PMSM which is assumed to be a constant, Ω_r is the mechanical speed and T_{pump} is the pump load torque which is a function of the pump speed and will be shown in Section 2.3.

The mechanical systems of the IPMSM and the pump can be described as one mass system

$$J\frac{d\Omega_r}{dt} = \frac{J}{n_p}\frac{d\omega_r}{dt} = T_e - T_L \tag{2-17}$$

where J is the total inertia of the PMSM and the pump. The electrical speed ω_r can be described as the derivative of the electrical rotor angle ϕ_r as

$$\omega_r = \frac{d\phi_r}{dt} \tag{2-18}$$

The electrical rotor angle ϕ_r is defined as the angle between the d-axis and the α-axis. Under perfect orientation, the electrical rotor angle ϕ_r is equal to the transformation angle θ_r used for αβ-dq transformation

$$\phi_r = \theta_r \tag{2-19}$$

2.1.5   PMSM Parameters

Since no real PMSM is available in this thesis work, the PMSM parameters must be properly decided from the PMSM specifications which are provided by the industry and are listed in Table 2-2.

Table 2-2 The PMSM specifications

P_n	500 [kW]	U_n	4.2 [kV]	I_n	77 [A]
$\cos\varphi$	0.9	n_p	2	Ω_n	6000 [rev/min]

From the steady state performance, the relationship among the PMSM stator resistance R_s, q-axis stator inductance L_{sq} and permanent flux linkage ψ_{pm} can be decided by the active power P, stator voltage U_s^{rms}, number of pole-pairs n_p, rated speed Ω_r and power factor $\cos\varphi$. The overall relationship can be described as

$$\left.\begin{array}{c} \dfrac{T_e}{n_p\psi_{pm}} \quad \Rightarrow \quad i \\[2mm] \left.\begin{array}{c} R_s i_s \\ \omega_r L_s i_s \\ \omega_r\psi_{pm} \end{array}\right\} \quad \Rightarrow \quad u \\[2mm] \cos\varphi \end{array}\right\} \quad \Rightarrow \quad P \tag{2-20}$$

where the stator current is related with the PMSM electromagnetic torque, the stator voltage is composed by the resistive voltage drop, the cross-coupling terms and the back-EMF, while the active power is decided by the stator current, the stator voltage together with the power factor.

In steady state, under perfect flux orientation and non-field-weakening performance, it can be assumed that

$$i_{sd} = 0 \qquad \frac{di_{sd}}{dt} = 0 \qquad \frac{di_{sq}}{dt} = 0 \qquad\qquad (2\text{-}21)$$

Then, the electrical and mechanical equations in (2-11), (2-12) and (2-13) can be simplified as

$$u_{sd} = -\omega_r L_{sq} i_{sq} \qquad\qquad (2\text{-}22)$$
$$u_{sq} = R_s i_{sq} + \omega_r \psi_{pm} \qquad\qquad (2\text{-}23)$$
$$T_e = \frac{3n_p}{2} \psi_{pm} i_{sq} \qquad\qquad (2\text{-}24)$$

respectively. The total stator voltage u_s and the steady state electromagnetic power P_e can be calculated as

$$u_s = \sqrt{u_{sd}^2 + u_{sq}^2} \qquad P_e = T_e \cdot \Omega_r \qquad\qquad (2\text{-}25)$$

Furthermore, if the three-phase line rms voltage and current are considered, then

$$u_s = \frac{\sqrt{2}}{\sqrt{3}} U_s^{rms} \qquad i_{sq} = \sqrt{2} I_s^{rms} \qquad\qquad (2\text{-}26)$$

Therefore, the minimum flux linkage and the maximum inductance can be decided

$$\psi_{pm} = \frac{\sqrt{2}}{\sqrt{3}} \frac{U_s^{rms} \cos\varphi}{\omega_r} \qquad\qquad (2\text{-}27)$$

$$L_{sq} = \frac{\sqrt{U_s^{rms\,2}(U_s^{rms}\cos\varphi)^2 - \left(R_s P_e + U_s^{rms\,2}\cos^2\varphi\right)^2}}{\omega_r P_e} \qquad\qquad (2\text{-}28)$$

As can be seen, a higher ψ_{pm} corresponds to a higher power factor $\cos\varphi$. The electrical parameters of the PMSM in this thesis work are selected as listed in Table 2-3 with both real values and per unit values which satisfies the relationship shown above. The values are compatible with the motors in [13] which is also used in a subsea application.

Table 2-3 The PMSM parameters in real values and per unit values

	Real Value	Base Value	Per Unit Value
R_s	0.1 [Ω]	35.28 [Ω]	0.0028 [p.u.]
L_sd	4 [mH]	28.07 [mH]	0.1425 [p.u.]
L_sq	8 [mH]	28.07 [mH]	0.2850 [p.u.]
ψ_pm	2.456 [Wb]	2.729 [Wb]	0.9000 [p.u.]
J_PMSM	1.125 [kg·m^2]	-	-
B_PMSM	0.1 [N·m·s/rad]	-	-

It should be pointed out that, the selection of such a high viscous damping factor B_PMSM is because of the filled dielectric oil and the high pressure in the subsea application. Such dielectric oil is filled at a high pressure in order to introduce a counter-pressure from inside the PMSM to balance the subsea water pressure from outside the PMSM. Article [14] indicates that a high liquid pressure will cause a high viscous damping loss which is the case in the thesis work. The viscous loss in percentage here is 7.31% which is within the same range as 3.125% in [15]. Therefore, the parameters can be considered to be within the expected range.

2.2   Power Transmission System

The transmission system from the topside converter to the PMSM includes the transformer and the subsea cable. The whole transmission system shall be capable to deliver enough power to the motor and guarantee the rms line-to-line motor voltage with some tolerance. A 10% margin at full load condition is taken into consideration to determine the current rating of the cable, so that the cable current rating will not be exceeded.

2.2.1   Step-up Transformer

Table 2-4 shows the rating and the parameters of the step-up transformer used in this thesis work. As can be noticed from the table, the transformer is rated at 1.2 MVA, and the reason for selecting such a high rated apparent power is to make sure that the series impedance is low enough in order to limit the voltage drop across the transformer.

The parameters of the transformer are selected based on the 1.25 MVA power distribution transformers in a datasheet from MØRE TRAFO AS [16] and a guidance from Helmerverken [17]. The series impedance is relatively higher and the shunt impedance is relatively lower than those transformers in the datasheets, so that a worse operation condition is taken into consideration. Therefore, the selection keeps the investigation on the safe side, since if such a worse case can work, a normal case can operate without problem.

Table 2-4 The initial parameters of the step-up transformer

Apparent Power	S_n	1.2	[MVA]
Input Voltage	U_1	630	[V]
Output Voltage	U_2	4800	[V]
Boosting Factor	α	7.619	
Type	YNd11		
Series Resistance	R_T	0.036	[p.u.]
Series Reactance	X_T	0.085	[p.u.]
Shunt Resistance	R_{Tc}	900	[p.u.]
Shunt Reactance	X_{Tm}	65	[p.u.]

A detailed model with the magnetizing branch and the iron core taken into consideration is applied in this case as shown in Figure 2-4. R_{T1} and L_{T1} are the primary side resistance and inductance, R_{T2} and L_{T2} are the secondary side resistance and inductance and R_{Tc} and L_{Tm} are the iron core resistance and magnetization inductance respectively.
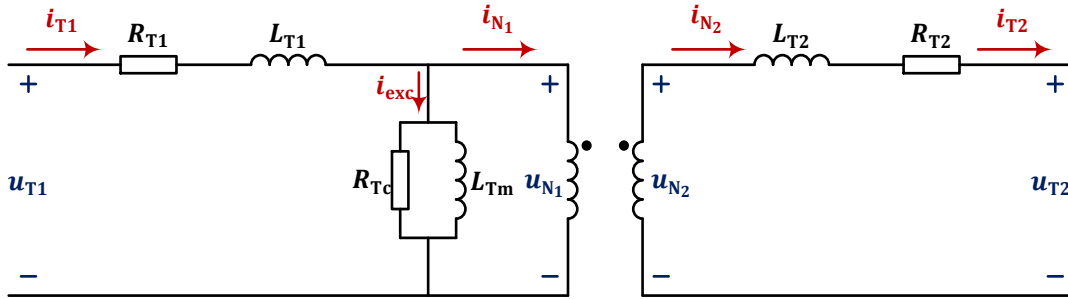
Figure 2-4 Detailed model of the transformer

It should be pointed out that, due to the Δ connection on the primary side of the transformer, any zero-sequence component from the secondary side of the transformer is blocked. Therefore, from the controller's side of view, zero-sequence current does not exist. Accordingly, although the secondary side of the transformer may contain zero-sequence, the current controller will only control the non-zero-sequence components.

2.2.2 Cable

For the 15 km cable, several parameters are used for simulation which can be obtained from the cable datasheet: rated voltage V_{lim}, rated current I_{lim}, per unit length resistance r_0, per unit length inductance l_0 and per unit length capacitance c_0. The total resistance, inductance and capacitance can be calculated by multiplying the per unit length parameters by the length of the cable ℓ. Special attention should be paid for the per unit length resistance r_0: the datasheet only provides the DC resistance $r_{0 \cdot DC}$ at 20 °C, but in the thesis work, the AC resistance r_{0AC} at 65 °C is of interest which is a conservative assumption from the industry. Therefore, a transformation from $r_{0 \cdot DC \cdot 20°C}$ to $r_{0 \cdot AC \cdot 65°C}$ is needed. From [18], the DC resistance at 20 °C is given for each type of cable. The conversion of DC resistance to AC resistance is illustrated in Appendix B.

13

Several aspects have to be taken into consideration when selecting a proper cable. In this thesis work, only the rated current of the cable, the voltage rating and the voltage drop are considered. The cable selection is expected to take a 10% current rating margin into account. The rated current can be calculated as

$$I_{\text{rated}} = \frac{P}{\sqrt{3}V_{\text{line}}\cos\varphi} \times 1.1 \tag{2-29}$$

Considering an active power of 500 kW and a minimum cable voltage rating at 4.2 kV which equals the system operation voltage, (2-29) gives a rated current of 84 A.

For the subsea application, it is preferable to limit the voltage drop across the cable to 10 ~ 15% of the sending end voltage of the cable U_{s}. In order to investigate the voltage drop across the cable and the transformer, load flow calculations in PowerFactory DIgSILENT are performed. Figure 2-5 shows the simulation model in PowerFactory DIgSILENT used for this investigation.
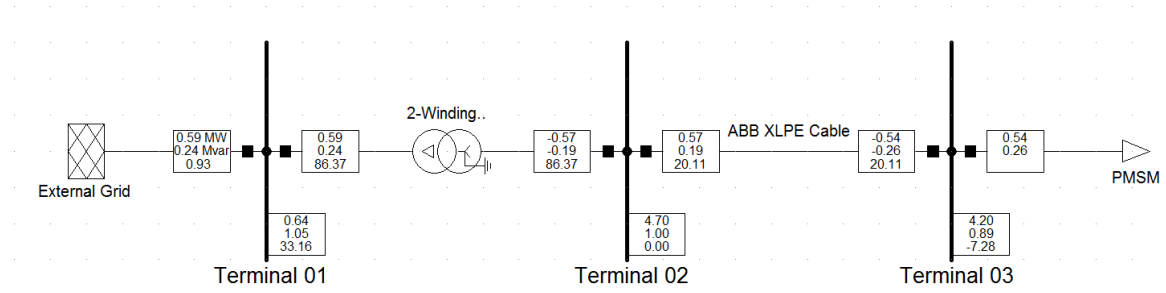
Figure 2-5 PowerFactory DIgSILENT load flow calculation of the transmission line

The calculations are performed at the rated power. As can be found out that in order to limit the voltage drop across the transformer and the cable to 10%, a three-core XLPE cable with a cross-section of 240 mm^2 from the 10 (12) kV cable class is needed. A voltage of at least 4.65 kV is required at the sending end to guarantee the voltage of 4.20 kV at the receiving end. As can be noticed, it is the voltage drop that is the dimensioning case in this application. The cable parameters for the selected cable is shown in Table 2-5.

Table 2-5 ABB 240 mm^2 three-core XLPE 10 kV ($U_{\text{m}} = 12$ kV) cable

Diameter	d	18.0 [mm]	Rated Current	$I_{\text{rated·rms}}$	410 [A]
DC Resistance	$r_{0\cdot\text{DC}\cdot20\,°C}$	0.0754 [Ω/km]	AC Resistance	$r_{0\cdot200\text{Hz}\cdot65\,°C}$	0.1192 [Ω/km]
Inductance	l_0	0.28 [mH/km]	Reactance	$x_{0\cdot200\text{Hz}}$	0.3519 [Ω/km]
Capacitance	c_0	0.44 [µF/km]	Susceptance	$b_{0\cdot200\text{Hz}}$	553 [µS/km]

Three different models can be used to represent the cable [19]: the short, medium and long line models. The *Short Line Model* is suitable for transmission lines shorter than 80 km. The transmission line is modeled as a resistance R_{CB} series connected with an inductance L_{C} as shown in Figure 2-6. The *Medium Line Model* is suitable for transmission lines between 80 km and 250 km. The model takes the shunt admittance into consideration where a shunt capacitance C_{CB} is included, forming a π-section to represent the cable as shown in Figure 2-7.
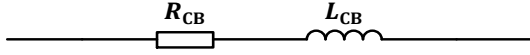
Figure 2-6 Short Line Model of the cable   Figure 2-7 Medium Line Model of the cable
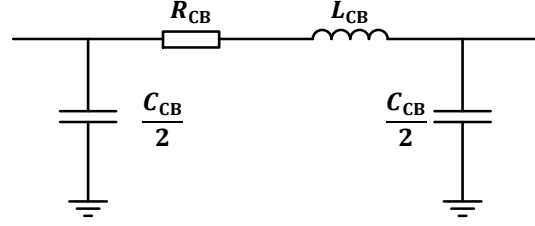
The *Long Line Model* is suitable for the transmission lines longer than 250 km. An exact model with one π-section for the cable can be built by applying hyperbolic correction of the cable parameters. However, such model is only accurate at the frequency where the hyperbolic correction is carried out. If the distributed resistance, inductance and capacitance are r, l and c respectively, then the distributed impedance z and the distributed admittance y are

$$z = r + j\omega l \qquad y = j\omega c \qquad (2\text{-}30)$$

where ω is the angular speed where the hyperbolic correction is performed. The surge impedance Z_c and propagation constant γ are defined as [19]

$$Z_c = \sqrt{\frac{z}{y}} \qquad \gamma = \sqrt{z \cdot y} \qquad (2\text{-}31)$$

The corrected impedance and admittance can be calculated by applying Laplace transform [19] and finally can be expressed as

$$Z = R + j\omega L = Z_c \cdot \sinh(\gamma \cdot l_\pi) = \sqrt{\frac{z}{y}} \cdot \sinh\left(\sqrt{z \cdot y} \cdot l_\pi\right) \qquad (2\text{-}32)$$

$$Y = \frac{2}{Z_c} \cdot \tanh\left(\gamma \cdot \frac{l_\pi}{2}\right) = 2\sqrt{\frac{y}{z}} \cdot \tanh\left(\sqrt{z \cdot y} \cdot \frac{l_\pi}{2}\right) \qquad (2\text{-}33)$$

where l_π is the length of the cable π-section. The corrected resistance R, inductance L and capacitance C for the π-section shown in Figure 2-7 are

$$R = \text{real}(Z) \qquad L = \frac{\text{imag}(Z)}{\omega} \qquad C = \frac{\text{imag}(Y)}{\omega} \qquad (2\text{-}34)$$

One target of this thesis work is to study the effect from the cable shunt capacitance and therefore, though the cable length of 15 km is within 80 km, the *Short Line Model* is not going to be used. In addition, the start-up transients of the PMSM and the switching harmonics make it impossible to apply the *Long Line Model* (distributed parameter model) here since more than one frequency appears during the operation. Hence the cable is modelled by several π-sections with lumped parameters connected in series to improve the accuracy over a wider frequency range. The minimum number of π-sections needed to accurately model the cable up to a certain frequency can be calculated as [20]

$$N = \frac{8f^{\max}\ell_C}{v} \qquad (2\text{-}35)$$

where N is the necessary number of π-sections, $f^{\max}$ is the maximum frequency that can be studied in Hz and is chosen as 55 times the fundamental frequency in steady state operation which is 11 kHz in this thesis work so that up to 55th harmonic can be analyzed, ℓ_C is the total length of the cable in km and v is the propagation velocity in km/s which is calculated as

$$v = \frac{1}{\sqrt{l_C c_C}} \qquad (2\text{-}36)$$

The propagation velocity for the selected cable is 90094 km/s and the least number of π-sections N is calculated as 14.65. Hence an approximate case with 15 π-sections, each section for 1 km, is decided to be applied in the thesis work. In order to be accurate in terms of the steady state performance, Simulink carries out hyperbolic correction of the cable parameters automatically. In this thesis work, since the steady state performance is at 6000 rev/min, the corresponding hyperbolic correction at 400π rad/s is made.

2.2.3   Resonance Frequency of the Transmission System and the PMSM

The components in the system are modelled with inductance and capacitance which sometimes may give resonances. Such resonances should be avoided to be triggered by the components generated by the converter. The transfer function of the transmission system and the PMSM can be derived from the state space model in MATLAB which is attached in Appendix D. The inverter voltages, u_d and u_q are considered as the inputs, while the inverter currents i_d and i_q are considered as the outputs of the transfer function. The Bode diagram of the transfer functions from d-axis voltage to d-axis current and from q-axis voltage to q-axis current are plotted in Figure 2-8.
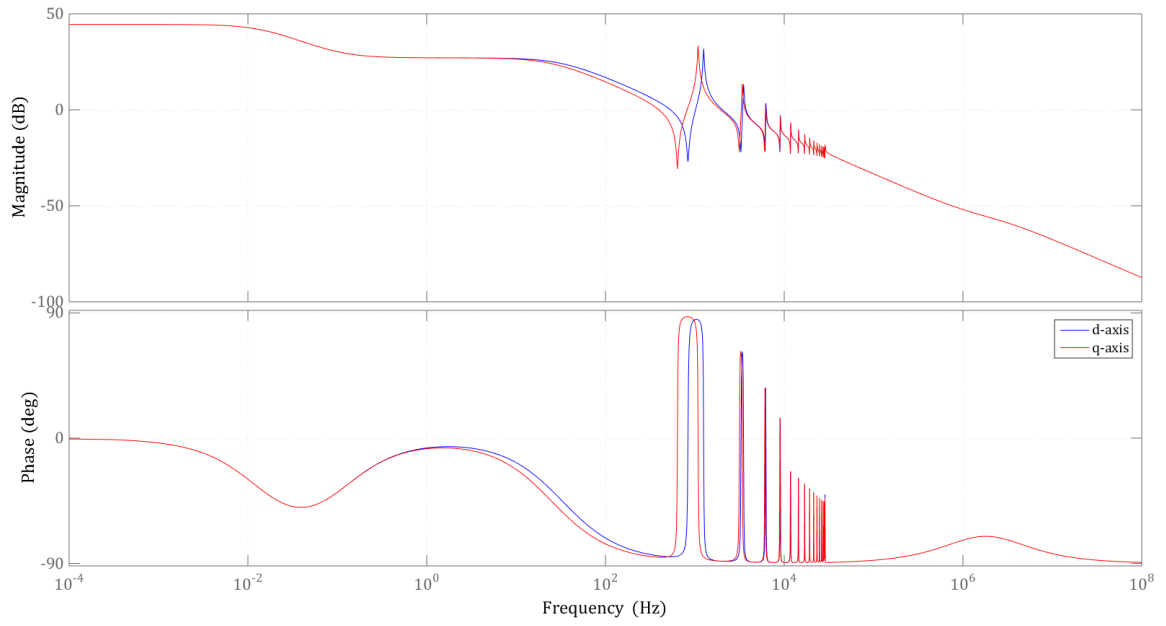
Figure 2-8 Bode diagram of the transmission system transfer function derived in high frequency region

It should be pointed out that although the curves are shown in the d- and q-axis in the figure, actually they are in the αβ frame since here the dq frame stands still with the αβ frame. The Bode diagram is presented in d- and q-axis since it is a salient PMSM that is applied in the work. The corresponding resonance frequencies of the transmission system shown in Figure 2-8 are listed in Table 2-6.

Table 2-6 Resonance frequencies of the system

	$f_{\text{res·1}}$	$f_{\text{res·2}}$	$f_{\text{res·3}}$	$f_{\text{res·4}}$	$f_{\text{res·5}}$	$\cdots$	$f_{\text{res·last}}$
d-axis	838 Hz	1254 Hz	3281 Hz	3511 Hz	6118 Hz	...	28592 Hz
q-axis	639 Hz	1088 Hz	3149 Hz	3393 Hz	6042 Hz	...	28572 Hz

The resonance frequencies are higher than the PMSM fundamental frequency which is at 200 Hz. The resonance frequencies should be taken into consideration when designing the controller and selecting the switching frequency of the converter so that components at these resonance frequencies will not be generated from the converter to the circuit.

2.3   Pump

A centrifugal pump rated 500 kW at 6000 rev/min is used in this application which is directly connected to the PMSM. As was described in Section 2.1.4, the PMSM and the pump are modelled as a one inertia system, where the inertia of the pump is given to be 0.35 kg·m² and added to the PMSM inertia. The pump torque is the composition of the pump load torque and the pump rotational friction torque

$$T_{\text{pump}} = T_{\text{pump·load}} + T_{\text{pump·friction}} \tag{2-37}$$

The pump load torque is proportional to the square of the mechanical speed Ω_{r}

17

$$T_{\text{pump·load}} = k\Omega_r{}^2 \tag{2-38}$$

where k is a constant of the load.

A classic expression of the pump rotational friction torque is composed by three parts: the Stribeck friction T_{Stribeck}, the Coulomb friction T_{Coulomb} and the viscous friction T_{viscous} [21] [22]

$$T_{\text{pump·friction}} = T_{\text{Stribeck}} + T_{\text{Coulomb}} + T_{\text{viscous}} \tag{2-39}$$

The Stribeck friction T_{Stribeck} takes place in the low-speed region and has a negative slope characteristic, while the Coulomb friction T_{Coulomb} is a constant value and the viscous friction T_{viscous} is proportional to the speed. In the vicinity of zero speed, the sum of T_{Stribeck} and T_{Coulomb} is referred to as the breakaway torque T_{break}. The rotation friction can then be modelled as

$$T_{\text{pump·friction}} = \left[T_{\text{Coulomb}} + (T_{\text{break}} - T_{\text{Coulomb}})e^{-c_v|\Omega_r|}\right]\text{sign}(\Omega_r) + B\Omega_r \tag{2-40}$$

where c_v is a coefficient of the load, B is the viscous coefficient and $\text{sign}(\Omega_r)$ is the sign function of Ω_r

$$\text{sign}(\Omega_r) = \begin{cases} 1 & \text{if} \quad \Omega_r > 0 \\ 0 & \text{if} \quad \Omega_r = 0 \\ -1 & \text{if} \quad \Omega_r < 0 \end{cases} \tag{2-41}$$

The Stribeck friction, Coulomb friction, viscous friction and the total friction are exemplified in Figure 2-9 where the friction torques are shown as part of the total friction. As can be noticed in the figure, the total friction curve has a minimum value and it is dominated by the seal friction at low velocities while by the viscous friction at high velocities. The Coulomb friction simply adds a shift to the total friction curve at all speeds.
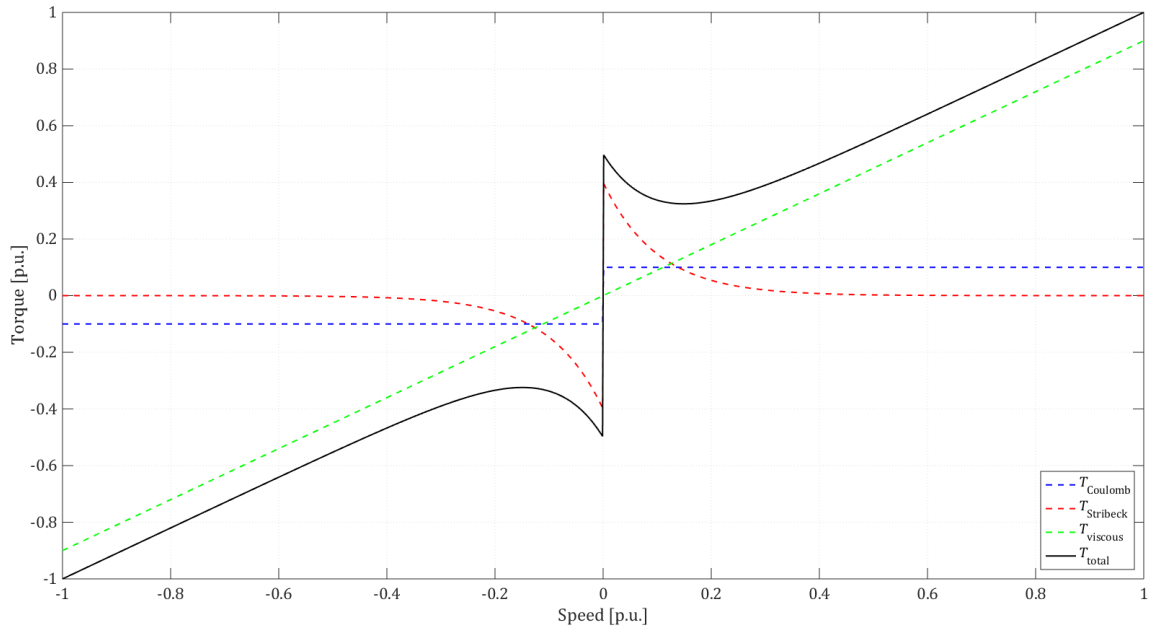
Figure 2-9 The Stribeck friction, Coulomb friction, viscous friction and the total friction curve
plotted in per unit of the rotor friction at 1 per unit speed

It can be assumed that the Stribeck and Coulomb frictions are negligible for the PMSM in comparison with the pump. Therefore, only the viscous friction of the PMSM is taken into consideration which has been mentioned in the previous section. The used electric submersible pump is rated 500 kW at 6000 rev/min which gives a rated torque of 796 N·m in the thesis work. The pump has a non-linear torque-speed characteristic curve which is provided by the industry and is shown in Figure 2-10.
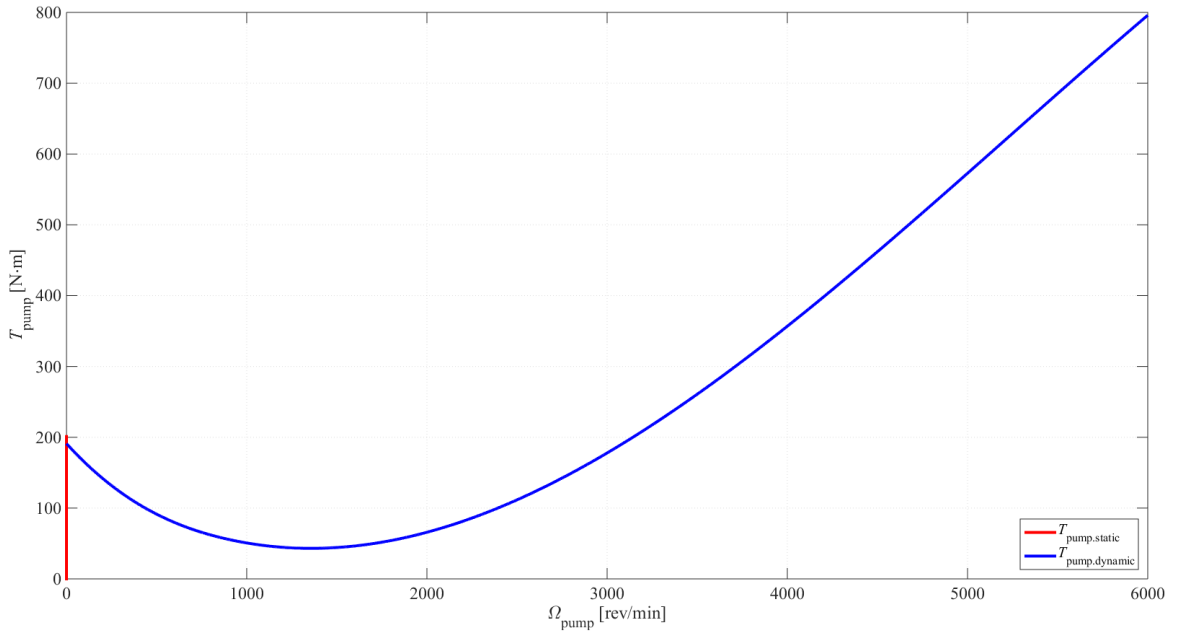
Figure 2-10 The torque-speed characteristic curve of the pump given by the industry

In Figure 2-10, the red curve shows the static torque of the pump while the blue curve shows the dynamic torque of the pump. The maximum value of the static torque is a little higher than the dynamic torque at zero speed. The logical judgement of the pump torque configuration is listed in Table 2-7. In the table, Ω_r is the PMSM mechanical speed, T_e is the PMSM electromagnetic torque and T_{th} is the static friction torque threshold of the pump. When the PMSM stands still, if T_e is lower than T_{th}, the static friction torque cancels T_e which keeps the PMSM standing still. When T_e grows to be larger than T_{th}, the static friction torque is not able to cancel T_e anymore, so the PMSM starts to rotate. Then, the static friction torque disappears since the PMSM is not in static condition anymore. Instead, the dynamic friction torque, which corresponds to the dynamic torque-speed curve of the pump, is applied to the PMSM during the rotation. The corresponding modelling of the pump torque in Simulink is shown in Figure 2-11.

Table 2-7 Pump torque configuration: the pump curve is applied

after the electromagnetic torque T_e overcomes the threshold T_{th}, e.g. the maximum of the static friction torque

Case		T_{pump}
$\Omega_r = 0$	$T_e \leq T_{th}$	T_e
	$T_e > T_{th}$	Pump Curve
$\Omega_r \neq 0$		Pump Curve
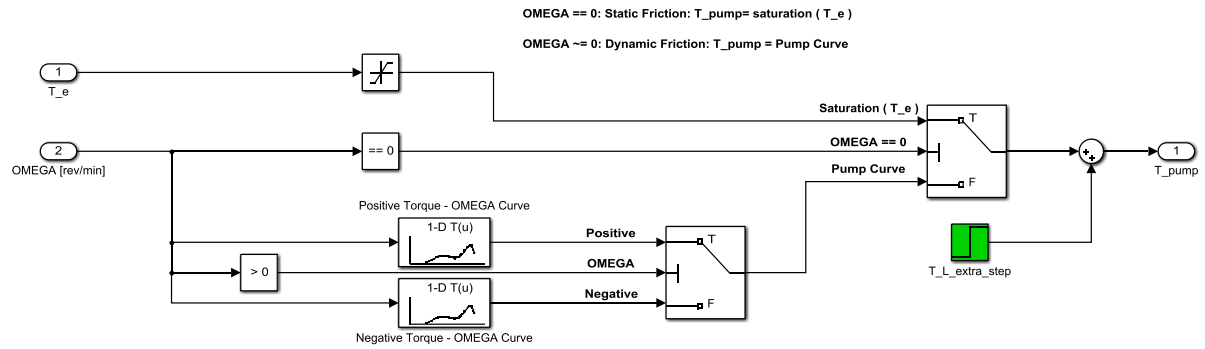
Figure 2-11 The modelling of the pump torque

This implementation is necessary, otherwise if the static and dynamic friction torques are defined as one single friction torque, then at zero speed and before enough torque is produced by the PMSM, the friction torque is larger than the electromagnetic torque and will force the PMSM to rotate backwards, which is not the case in reality.

3   PMSM Current and Speed Controller Design

As has been illustrated in the previous work [4], in an electric submersible pump application, a constant torque is preferred and therefore, a current control loop would be enough. However, if a constant speed performance is required, the PMSM is usually under speed control. The PMSM speed can be manipulated by controlling the electromagnetic torque. Therefore, two control loops are expected to be built: the inner current control loop to take care of the torque production and the outer speed control loop to make the speed follow the reference. In other words, the idea of the PMSM controller design is to control the angular speed of the rotor flux linkage vector by applying a suitable stator voltage vector which gives a suitable current vector and thus a suitable electromagnetic torque.
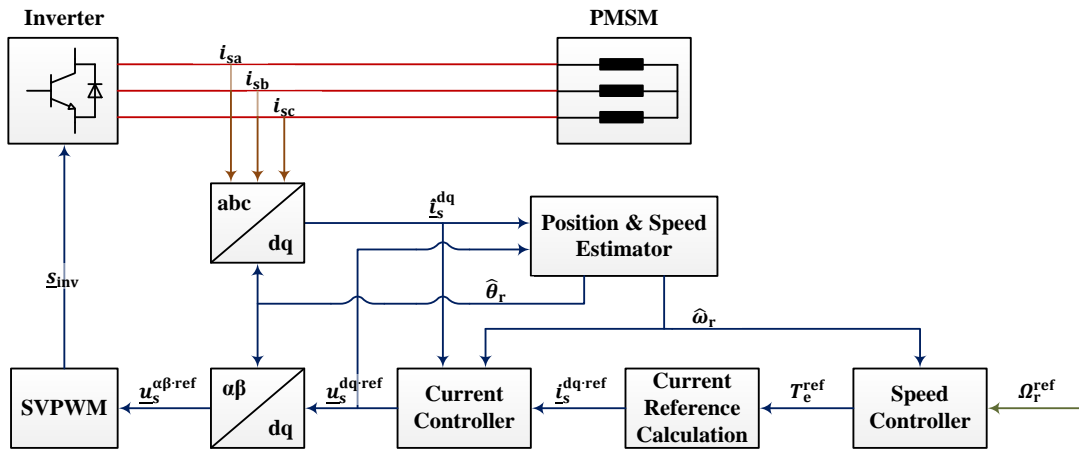
Figure 3-1 General configuration of PMSM drive systems

Red line: power transmission; Brown line: measurement & estimation; Blue line: signals.

Figure 3-1 shows the corresponding general configuration of the PMSM drive systems. The speed controller gets the estimated speed from the speed estimator, compares it with the speed reference and generates a torque reference. The current reference calculation block converts the torque reference to current reference, limits the current reference and passes the current reference to the current controller. The current controller then compares the measured current with the current reference and generates the voltage reference which guides the SVPWM modulator to generate the switching signals of the three-phase inverter. The three-phase currents are measured and transformed from abc frame to dq frame so that the current controller can work with dq quantities, while the voltage references are transformed from dq frame to αβ frame so that the SVPWM modulator can work with αβ quantities. The position & speed estimator calculates the angle for the transformations and speed for speed and current controller by investigating the measured current and the voltage reference.

The PI controller design for current and speed control loops is based on the *Internal Model Control* (IMC) Method [23]. The idea is to cancel the coupling terms and disturbances, and then add a PI controller to convert the closed-loop system into a first-order system with a specific bandwidth. Since the method is explained in [4], only a brief derivation will be given in this

report. The current controller of the PMSM is implemented in the dq coordinate system with the flux linkage from the magnets located on the d-axis. When designing the current controller, it is assumed that the transformation angle from the position & speed estimation block is ideal, i.e. the magnet flux linkage is on the d-axis. In Chapter 4, the estimation of the position and the speed will be explained, and in Chapter 5, the illustration of three-phase inverters and the space vector pulse width modulation algorithm will be given.

3.1   Bandwidths of Controllers

The PMSM controller is structured as a cascade system: the outer speed loop and the inner current loop. The current controller bandwidth α_c should be selected properly: it should be low enough for the power electronic converter to follow and high enough to guarantee a fast current response. In addition, a large gap should be inserted between the current controller bandwidth and the speed controller bandwidth. Due to the requirement that the PMSM needs to be started up in 5 s, the bandwidth of the speed controller can be set as a quite low value. In this project, the speed controller is decided to be 100 times slower than the current controller. Moreover, a proper selection of the bandwidths of the controllers should also take the bandwidth of the speed & position estimator into consideration which will be discussed in Chapter 4. The bandwidth of the controller corresponds to a rise time t_{rise}. For a first-order system, the bandwidth α and the rise time t_{rise} satisfies [23]

$$\alpha = \frac{\ln 9}{t_{\text{rise}}} \tag{3-1}$$

3.2   Current Controller

3.2.1   Current Reference Calculation

The full expression of PMSM electromagnetic torque is shown in (2-13) and under two conditions can it be simplified:

- In terms of non-salient PMSMs, the difference between L_{sd} and L_{sq} are negligible, which means $L_{\text{sd}} - L_{\text{sq}} = 0$;

- In terms of no flux linkage control from the stator side, for instance, no field-weakening, no MTPA, etc. which means $i_{\text{sd}} = 0$.

Under these two cases, the term $(L_{\text{sd}} - L_{\text{sq}})i_{\text{sd}}i_{\text{sq}}$ equals zero, and the torque expression can be simplified as

$$T_e = \frac{3n_p}{2}\psi_{\text{pm}}i_{\text{sq}} \tag{3-2}$$

Equation (3-2) is the case used in this thesis work, since neither of field-weakening or MTPA is considered, which means that $i_{\text{sd}}^{\text{ref}} = 0$. Therefore, (3-2) is applied in the controller design

while (2-13) is applied in the modelling of the PMSM component. As can be detected, torque T_e is only proportional to i_{sq} and is independent from i_{sd}. However, when the high frequency injection sensorless control method is applied, $i_{sd} \neq 0$ and $\left(L_{sd} - L_{sq}\right)i_{sd}i_{sq}$ is not fixed to zero any more, therefore, the effect of i_{sd} must be taken into consideration. This generates an oscillating electromagnetic torque even under perfect flux orientation and consequently causes a small oscillation in the speed.

From the torque equation (3-2), the d-axis current reference i_{sq}^{ref} can be decided from the electromagnetic torque reference T_e^{ref} and since field-weakening is not used, i_{sd}^{ref} is set to zero

$$\underline{i}_s^{ref} = i_{sd}^{ref} + j i_{sq}^{ref} = 0 + j \frac{2}{3} \frac{T_e^{ref}}{n_p \psi_{pm}} \tag{3-3}$$

3.2.2   IMC Design

IMC is applied to design a current PI controller with a bandwidth of α_c. By applying Laplace transformation to (2-11) and (2-12), the electrical process can be expressed in the s-domain as

$$i_{sd} = \frac{u_{sd} + \omega_r L_{sq} i_{sq}}{s L_{sd} + R_s} \tag{3-4}$$

$$i_{sq} = \frac{u_{sq} - \omega_r L_{sd} i_{sd} - \omega_r \psi_m}{s L_{sq} + R_s} \tag{3-5}$$

These two transfer functions of the PMSM are shown in the "PMSM Physical System" block in Figure 3-2. As can also be seen from the figure, the back-EMF and cross-coupling terms can be cancelled with feedforward terms.
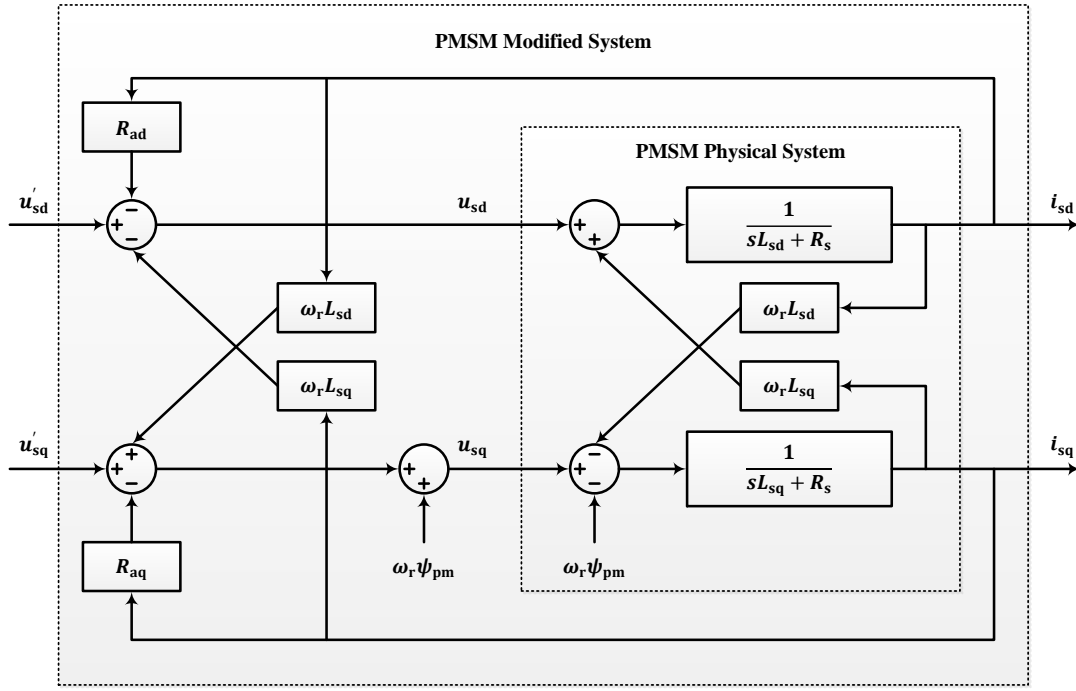
Figure 3-2 PMSM modified system

If perfect cancellation is assumed and by adding an active damping term R_a to either of the axes [6], the system can be expressed as

$$i_{sd} = \frac{u_{sd}}{sL_{sd} + R_s + R_{ad}} \tag{3-6}$$

$$i_{sq} = \frac{u_{sq}}{sL_{sq} + R_s + R_{aq}} \tag{3-7}$$

The modified process is used to design the closed current control loop. The closed-loop system is shown in Figure 3-3.
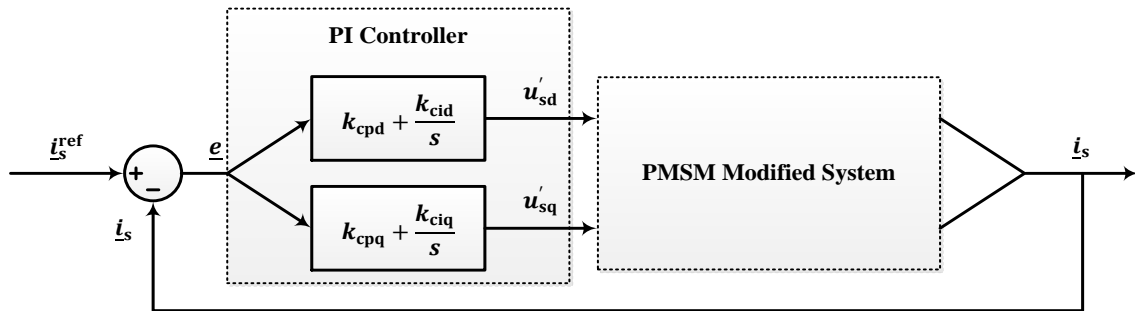
Figure 3-3 The closed-loop current controller

The closed-loop transfer function is shaped into a first-order system, and this gives that the PI controller parameters should be calculated as

$$k_{cpd} = \alpha_c L_{sd} \qquad k_{cid} = \alpha_c(R_s + R_{ad}) = \alpha_c{}^2 L_{sd} \tag{3-8}$$

$$k_{cpq} = \alpha_c L_{sq} \qquad k_{ciq} = \alpha_c(R_s + R_{aq}) = \alpha_c{}^2 L_{sq} \tag{3-9}$$

where the modified transfer function of the process is tuned to have the same bandwidth as the closed-loop system α_c [6] which means the active damping resistance should be selected as

$$R_{ad} = \alpha_c L_{sd} - R_s \qquad R_{aq} = \alpha_c L_{sq} - R_s \qquad (3\text{-}10)$$

In time domain, the voltage reference is calculated as

$$u_{sd}^{ref} = \left(i_{sd}^{ref} - i_{sd}\right)\left(k_{cpd} + \frac{k_{cid}}{s}\right) - R_{ad}i_{sd} - \omega_r L_{sq}i_{sq} \qquad (3\text{-}11)$$

$$u_{sq}^{ref} = \left(i_{sq}^{ref} - i_{sq}\right)\left(k_{cpq} + \frac{k_{ciq}}{s}\right) - R_{aq}i_{sq} + \omega_r L_{sd}i_{sd} + \omega_r \psi_m \qquad (3\text{-}12)$$

A voltage limiter and an anti-windup mechanism should further be added since the inverter output voltage has a maximum voltage output and the current controller should be informed of when such a threshold is hit [6]. A voltage limiter is therefore added after the current PI controller which limit is set as the maximum inverter output voltage. When the voltage limit is hit, a surplus voltage error $\left(\underline{u}_{s,lim}^{ref} - \underline{u}_s^{ref}\right)$ appears, which cannot be taken care of by the controller. This surplus voltage error $\left(\underline{u}_{s,lim}^{ref} - \underline{u}_s^{ref}\right)$ must be back-calculated to cancel the current error feeding the integrator so that the integrator can stop integrating. Thus the new current error $\underline{e}'$ based on the original current error $\underline{e}$ is defined to feed the integrator as

$$\underline{e}' = \underline{e} + \frac{\underline{u}_{s,lim}^{ref} - \underline{u}_s^{ref}}{k_{cp}} \qquad (3\text{-}13)$$

where $\underline{e} = \underline{i}_s^{ref} - \underline{i}_s$ is the original current error.

3.3 Speed Controller

The IMC is applied again to design a speed PI controller with a bandwidth of α_ω. In s-domain, the mechanical process can be expressed as

$$\Omega_r = \frac{T_e - T_L}{sJ + B} \qquad (3\text{-}14)$$

Active damping is applied to change the bandwidth of (3-14) to be a preferred one by selecting a proper viscous damping factor B_a

$$\Omega_r = \frac{T_e - T_L}{sJ + B + B_a} \qquad (3\text{-}15)$$

where B_a can be calculated as

$$B_a = \alpha_\omega J - B \qquad (3\text{-}16)$$

The speed PI controller parameters can be calculated by shaping the entire closed-loop mechanical system into a first-order system with a bandwidth of α_ω

$$k_{\omega p} = \alpha_\omega J \qquad k_{\omega i} = \alpha_\omega (B + B_a) = \alpha_\omega^2 J \tag{3-17}$$

After the speed controller, the torque reference is transformed into current reference as illustrated in (3-3). Similar to the current controller, a current limiter is added after the speed controller and the torque-current transformation in order to limit the output current reference

$$i_{sq}^{ref} < I_s^{rated} \tag{3-18}$$

Furthermore, an anti-windup algorithm is also implemented after the speed controller to hold on the speed controller integrator during the current saturation, i.e. the torque saturation. A transformation from the limited current reference to the limited torque reference should be carried our as presented in (3-3) before the anti-windup algorithm. Then, the anti-windup algorithm for the speed controller can be implemented by back calculation again

$$e' = e + \frac{T_{e,lim}^{ref} - T_e^{ref}}{k_{\omega p}} \tag{3-19}$$

where $e = \Omega_r^{ref} - \Omega_r$ is the original speed error and e' is the modified speed error.

3.4   Controller Discretization

In a realistic control system, it is practical to apply a Digital Signal Processor (DSP) instead of an analogue controller. Therefore, it is necessary to convert the controller from a continuous-time (CT) model to a discrete-time (DT) model, which can be described as

$$\begin{array}{ccc} \text{Continuous} - \text{Time Model} & \Rightarrow & \text{Discrete} - \text{Time Model} \\ \dot{x}(t) = f[x(t), u(t)] & \Rightarrow & x(k+1) = f[x(k), u(k)] \\ y(t) = g[x(t), u(t)] & & y(k) = g[x(k), u(k)] \end{array} \tag{3-20}$$

where $x(t)$ represents the states, $u(t)$ represents the inputs, $y(t)$ represents the outputs, t represents the time in continuous-time model and k represents the step in discrete-time model, f represents the function to calculate the state derivatives and g represent the function to calculation the outputs.

Zero Order Hold (ZOH) discretization is performed in this section. ZOH only updates its memory at the sampling instant while keeps the memory to be the same value during the sampling interval [24]. Therefore, if a continuous-time transfer function $H(s)$ and its corresponding discrete-time transfer function $H(z)$ start to respond to a step input simultaneously, their step responses are supposed to be equal

$$x_{step}(t) = \mathcal{L}^{-1}\left\{\frac{1}{s}H(s)\right\} = \mathcal{Z}^{-1}\left\{\frac{z}{z-1}H(z)\right\} \tag{3-21}$$

From this, the discrete-time transfer function $H(z)$ with the same step response as the continuous-time transfer function $H(s)$ can be expressed as

$$H(z) = \frac{z-1}{z} \mathcal{Z}\left\{\mathcal{L}^{-1}\left\{\frac{H(s)}{s}\right\}\right\}$$

(3-22)

To exemplify this, the discrete-time transfer functions for an integrator and a first-order Low Pass Filter (LPF) can be calculated as

$$H(s) = \frac{1}{s} \quad \Leftrightarrow \quad H(z) = \frac{T_s}{z-1}$$

(3-23)

$$H(s) = \frac{\alpha}{s+\alpha} \quad \Leftrightarrow \quad H(z) = \frac{1 - e^{-\alpha T_s}}{z - e^{-\alpha T_s}}$$

(3-24)

where T_s is the sampling period. For more complicated transfer functions, the MATLAB command "c2d" can do such discretization without manual calculation and it is used in this work [24].

4   Position-Sensorless Control Algorithm

The absolute rotor position must be located in order to decide the direction of the rotor flux linkage and to apply the field-oriented control discussed in Chapter 3. In order to detect the rotor position, either a position-sensor is to be installed, or position-sensorless techniques are to be applied. However, for subsea applications, position-sensors are not preferred since [25] [26]

- The long travelling distance from the position-sensors installed in the PMSM to the controller will greatly deteriorate the signal. Then the controller may get more noise than useful information.

- The position-sensors are mostly sensitive to temperature which makes them not reliable enough.

- If the position-sensor fails at deep water, the maintenance or replacement of it may be a huge inconvenience.

- The size and complexity of the structure of the PMSM will be increased.

- The cost of maintenance of position sensors will be significant.

Therefore, position-sensorless control is preferred in subsea applications, in which a position estimator is used to implement the same function as a position-sensor. The task of the estimator is to calculate the rotor position and speed from the stator voltage and current of the PMSM. In this chapter, different estimation methods are introduced in the beginning and two algorithms are selected, introduced in details and implemented in the following part.

The control strategy in this application must have initial rotor position insensitivity or initial rotor position detection ability. The position-sensorless control can only work if the estimator can adjust the estimated angle to any initial rotor position or the initial rotor position can be detected by the estimator. The evaluation or implementation of such function is not included in this thesis work as has been mentioned in the Scope, but various solutions have been published for the selected algorithms to solve the problem with the unknown initial position [27] [28] [29].

In addition, the position-sensorless control should be able to be tolerant with parameter insensitivity. During the operation, the transformer, the cable and the PMSM will present variable resistances due to temperature increase and variable inductances due to flux saturation, and therefore, robustness is required for the estimator.

4.1   Introduction of Different Position Estimation Methods

The rotor-position can be obtained by the measured electrical quantities of the PMSM: stator voltages and stator currents. The bases of position-sensorless algorithms can be generally classified into two groups: fundamental frequency excitation signal algorithms and high

frequency signal injection algorithms [10]. The classification of the algorithms is presented in Figure 4-1 and the algorithms are presented in details in the following sections.
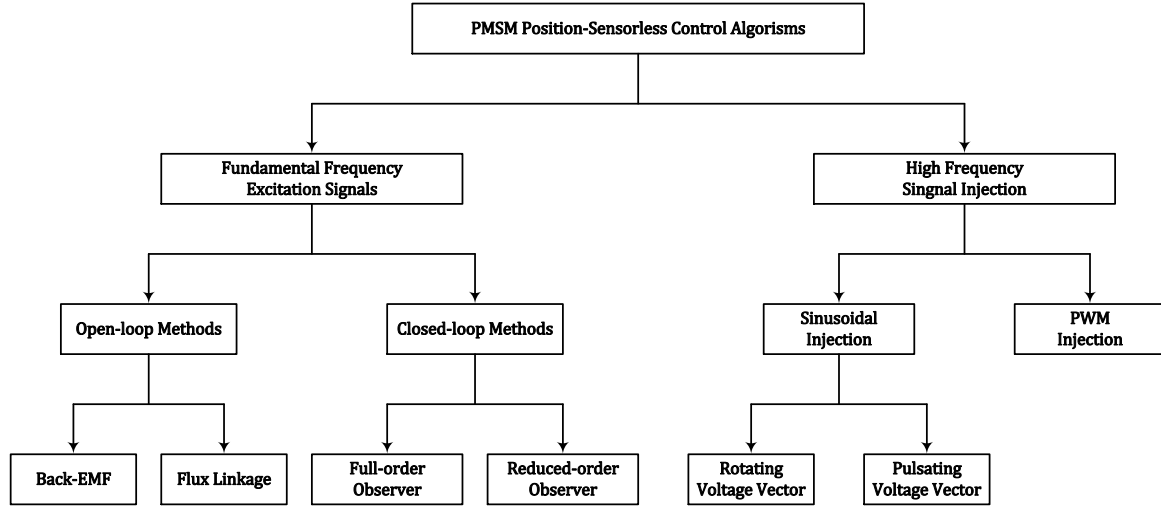
Figure 4-1 Position-sensorless control algorithm [10]

4.1.1 Fundamental Frequency Excitation Signal Methods

As is shown in Figure 4-1, the fundamental frequency excitation signal methods can be divided into open-loop methods by applying direct calculations and closed-loop methods by building inner correction mechanisms [10]. The open-loop methods are developed from the PMSM model, which calculate the rotor position directly without applying any inner correction mechanism. These methods work quite well during low start torque and non-zero speed operation requirements. For PMSMs, the *open-loop methods* can be further divided into *back-EMF methods* and *stator flux linkage methods*.

The *back-EMF methods* utilize the fact that a relative movement between the rotor magnet and the stator windings will induce a motional back-EMF on the stator windings [30]. Therefore, the speed and position can be extracted by analyzing the back-EMF. However, the back-EMF methods cannot operate in low-speed region constantly since the amplitude of the back-EMF is not significant enough for the estimator to decide the rotor angle. In addition, imperfect PMSM parameters will introduce errors to the estimation and a large enough error may lead to a failure of the control. Although several disadvantages are reported, a back-EMF-based method named *Static Compensated Voltage Model* (SCVM) has been developed which is reported to be able to operate with any initial rotor position during the start-up [30].

In the *stator flux linkage methods*, the stator flux linkage can be calculated by applying the stator electrical equations in αβ frame [4] [8] [31]

$$\underline{\psi}_s^s = \int \left(\underline{u}_s^s - R_s \underline{i}_s^s \right) \mathrm{d}t \qquad (4\text{-}1)$$

Based on this predicted stator flux linkage, a prediction of the stator current can be made with a predetermined rotor angle. Thereafter, the stator current error can be calculated by comparing the predicted and real stator currents and the correction of the rotor angle can further be made.

The stator flux linkage and stator current are introduced to correct the rotor angle estimation. Nevertheless, an integrator drift problem is reported since the stator flux linkage is obtained through integrating $\left(\underline{u}_s^s - R_s \underline{i}_s^s\right)$. Therefore, a compensation technique must be applied. Again, the accuracy of this method is also impacted by the parameter errors.

In terms of the closed-loop methods, observers are used as the one presented in Figure 4-2 [10]. A state estimator, which is a "copy" of the real system, is modeled and run in parallel with the real system at the same time. The error between the estimated and measured quantities will be calculated and used to correct the states of the "copy". The *closed-loop method* includes *full-order methods* and *reduced-order methods*.
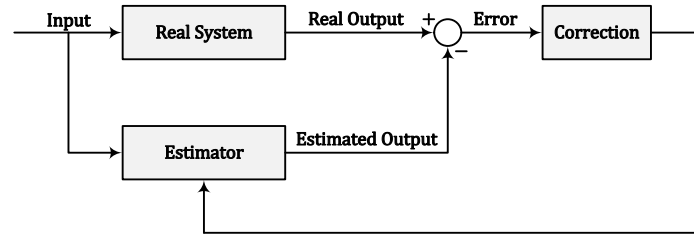
Figure 4-2 General Layout of a Position Observer

The reduced-order observers only contain electrical quantities, while the full-order observers contain both electrical and mechanical parts of the PMSM [10]. Reduced-order observers can be mainly divided into current observers and flux linkage observers. In full-order observers, electrical quantities are input into the stator model and go through the mechanical model. Then the rotor angle is calculated which can be used by the controller. Thereafter, the estimated current can be calculated by an inverse magnetic model. The estimated current will further be compared with the measured current and then the error will be used for the correction inside the observer. Such closed-loop methods are robust but complicated to implement and also need to detect or align the initial rotor angle [10].

4.1.2   High Frequency Signal Injection Methods

In the high frequency signal injection methods, a certain high frequency signal is superimposed on the fundamental stator voltage and is used for saliency detection [32]. Since the saliency, $L_{sd} \neq L_{sq}$, is introduced by the rotor structure, the detected saliency can point out the rotor position. Such algorithm can be applied both at standing still and high speeds [33]. However, one inherent problem with the method is that the saliency can be shown in both the positive and negative directions of the q-axis compared with the d-axis. This gives that there is a possibility to estimate the rotor angle with a 180° electrical degree error.

In the high frequency signal injection methods, three approaches are mainly applied: rotating sinusoidal injection in αβ frame, pulsating sinusoidal injection in dq frame and PWM injection. For the method that utilizes a rotating sinusoidal injection in the αβ frame, the superimposed high frequency rotating voltage vector is [32]

$$\underline{u}_{HF}^s = U_{HF}e^{j\omega_h t} = U_{HF}[\cos(\omega_{HF}t) + j\sin(\omega_{HF}t)] \qquad (4\text{-}2)$$

where $\underline{u}_{HF}^s$ is the injected high frequency voltage signal, U_{HF} and ω_{HF} are the amplitude and the angular speed of the injected HF signal respectively. In high frequency region, the voltage across the stator inductance will be the dominant term, which means that the other terms in the stator equation of the PMSM can be neglected, thus the current can be solved and decomposed into positive and negative components [32]

$$\underline{i}_{HF}^s = \underline{i}_{HF\cdot p}^s + \underline{i}_{HF\cdot n}^s = \frac{L_\Sigma}{L_{sd}L_{sq}}\frac{\underline{u}_{HF}^s}{j\omega_{HF}} - \frac{L_\Sigma}{L_{sd}L_{sq}}e^{j2\theta_r}\frac{\underline{u}_{HF}^{s\,*}}{j\omega_{HF}} \qquad (4\text{-}3)$$

where $\underline{i}_{HF}^s$ is the HF current with $\underline{i}_{HF\cdot p}^s$ as its positive sequence component and $\underline{i}_{HF\cdot n}^s$ as its negative sequence component and L_Σ is the average inductance which is usually defined together with the difference inductance L_Δ

$$L_\Sigma = \frac{L_{sd} + L_{sq}}{2} \qquad L_\Delta = \frac{L_{sq} - L_{sd}}{2} \qquad (4\text{-}4)$$

Then the angle information can be extracted by applying a demodulation process to the negative sequence part [32]. The high frequency current in this algorithm will give a torque ripple and therefore an extra loss. Such a method is reported for a limited popularity and is more suitable for induction motor applications [10].

In contrast, the high frequency injection in the dq frame is more suitable for PMSMs [10]. Similar to the high frequency signal injection in the αβ frame, an HF voltage signal can be injected in the dq frame and a corresponding HF current signal can be received [32]. After a low pass filter and a demodulation process, the rotor angle information can be extracted.

In the PWM injection method, a square wave voltage is injected in the αβ frame with the same frequency as the switching frequency [34] [35]. The resulting current derivative of each phase is used to identify the differential phase inductance along the applied voltage vector. Then, based on the angular dependent inductances, the corresponding angle can be obtained. One advantage of this method is that no additional measurement sequence or hardware is needed for initial angle detection [10].

4.1.3   Position-sensorless Control Scheme Selection

The observer design will be highly sophisticated due to the non-linear PMSM equations. Although the observer method can provide an excellent robustness, the high computational requirement makes it rarely used in practical application [10]. Therefore, such an observer design may not be a proper choice for subsea applications where the transmission system should be included which will make the observer design even more complicated. Both the back-EMF methods and the flux linkage methods are suitable for the PMSM application if the PMSM is directly connected to the inverter. However, if a transmission system is added in the between, then the stator current correction loop in the flux linkage method may not be easy to implement. Therefore, the Static Compensated Voltage Model (SCVM) which belongs to the back-EMF methods is selected as one method in this thesis work.

Although an extra loss and torque ripple appear, signal injection method gives accurate position information at all speeds. In terms of the PWM injection technique, the high frequency component should be injected at the switching frequency while the switching frequency components are not welcome in the transmission system in order to avoid resonance. In addition, it is reported that dq frame pulsating injection is better than αβ frame rotating injection for PMSM applications [32]. Therefore, pulsating injection in dq frame is selected which will be denoted as HFI in the following sections of this thesis report.

One technique to align the rotor to a certain position by applying a DC current is not suitable due to the transformer in the system. The SCVM method is guaranteed to be insensitive to any initial rotor position [30] and the algorithm of initial rotor position detection is also available for HFI [36]. However, since this is not the focus of the thesis work, it will always be assumed the initial angle is known in the simulation.

4.2   Static Compensated Voltage Model (SCVM)

The Static Compensated Voltage Model is introduced in [30]. The starting equation for the SCVM is the PMSM stator voltage equation in αβ coordinate system

$$\underline{u}_s^s = R_s \underline{i}_s^s + \frac{d\underline{\psi}_s^s}{dt} = R_s \underline{i}_s^s + L_s \frac{d\underline{i}_s^s}{dt} + \frac{d\underline{\psi}_{pm}^s}{dt} \tag{4-5}$$

Therefore, the permanent magnet flux linkage vector in αβ frame can be estimated as

$$\hat{\underline{\psi}}_{pm}^s = j\hat{\omega}_r \hat{\psi}_{pm} e^{j\hat{\theta}_r} = \int \hat{\underline{E}}_f^s dt = \int \left(\underline{u}_s^s - \hat{R}_s \underline{i}_s^s \right) dt - \hat{L}_s \underline{i}_s^s \tag{4-6}$$

where $\hat{\underline{E}}_f^s$ is the estimated back-EMF. In s-domain, the back-EMF can be expressed as

$$\hat{\underline{\psi}}_{pm}^s = \frac{\underline{u}_s^s - \hat{R}_s \underline{i}_s^s - s\hat{L}_s \underline{i}_s^s}{s} = \frac{\hat{\underline{E}}_f^s}{s} \tag{4-7}$$

This system is a pure integrator, which usually works fine only if perfect parameters are guaranteed, otherwise, oscillations will occur. In order to stabilize this estimator, an additional leakage factor α_v is introduced to damp the oscillation and convert the integrator to a low pass filter

$$\hat{\underline{\psi}}_{pm}^s = \frac{\hat{\underline{E}}_f^s}{s + \alpha_v} \tag{4-8}$$

However, the damping factor α_v introduces an error to the estimated flux linkage $\hat{\underline{\psi}}_{pm}^s$ compared with the real flux linkage $\underline{\psi}_{pm}^s$. By assuming perfect parameters, the estimated back-EMF $\hat{\underline{E}}_f^s$ would be equal to the real back-EMF $\underline{E}_f^s$

$$\underline{\hat{E}}_f^s = \{\text{assuming perfect parameters}\} = \underline{E}_f^s = s\underline{\psi}_{\text{pm}}^s \qquad (4\text{-}9)$$

and by (4-7), the estimated flux linkage $\underline{\hat{\psi}}_{\text{pm}}^s$ can be related to the real flux linkage $\underline{\psi}_{\text{pm}}^s$ both in dynamic performance and static performance

$$\begin{array}{ccc}
\text{dynamic} & & \text{static} \\[4pt]
\underline{\hat{\psi}}_{\text{pm}}^s = \dfrac{s}{s+\alpha_v}\underline{\psi}_{\text{pm}}^s & \xleftrightarrow{\ s\leftrightarrow j\omega_r\ } & \underline{\hat{\psi}}_{\text{pm}}^s = \dfrac{j\omega_r}{j\omega_r+\alpha_v}\underline{\psi}_{\text{pm}}^s
\end{array} \qquad (4\text{-}10)$$

A small error in dynamics is acceptable, but it should be eliminated in steady-state. As can be found in (4-10), the estimation error is large at low speeds ($|\omega_r| \ll \alpha_v$). At low speeds, the estimation can be approximated as

$$\underline{\hat{\psi}}_{\text{pm}}^s \approx \frac{j\omega_r}{\alpha_v}\underline{\psi}_{\text{pm}}^s \neq \underline{\psi}_{\text{pm}}^s \qquad (4\text{-}11)$$

In order to get around this problem, α_v can be selected as speed-dependent with a coefficient λ, so that the damping factor can be adjusted according to the speed

$$\alpha_v = \lambda|\omega_r| \qquad (4\text{-}12)$$

With this speed dependent damping factor, the dynamic and static estimator equations become

$$\underline{\hat{\psi}}_{\text{pm}}^s = \frac{\underline{\hat{E}}_f^s}{s+\lambda|\omega_r|} = \frac{\underline{u}_s^s - \hat{R}_s\underline{i}_s^s - s\hat{L}_s\underline{i}_s^s}{s+\lambda|\omega_r|} \qquad (4\text{-}13)$$

$$\underline{\hat{\psi}}_{\text{pm}}^s = \frac{j\omega_r}{j\omega_r+\lambda|\omega_r|}\underline{\psi}_{\text{pm}}^s = \frac{1}{1-j\lambda\dfrac{|\omega_r|}{\omega_r}}\underline{\psi}_{\text{pm}}^s = \frac{1}{1-j\lambda\,\text{sign}(\omega_r)}\underline{\psi}_{\text{pm}}^s \qquad (4\text{-}14)$$

where $\text{sign}(\omega_r)$ is the sign function of ω_r

$$\text{sign}(\omega_r) = \begin{cases} 1 & \text{if} \quad \omega_r > 0 \\ 0 & \text{if} \quad \omega_r = 0 \\ -1 & \text{if} \quad \omega_r < 0 \end{cases} \qquad (4\text{-}15)$$

As can be noticed from (4-14), the estimation error due to the damping factor is now independent of the speed except for the direction of the rotation.

In steady-state, the estimation error introduced by the damping factor should be eliminated. This can be done by multiplying the estimation with the inverse of the steady-state error in (4-14). The estimation can then be expressed as

$$\underline{\hat{\psi}}_{\text{pm}}^s = \frac{\underline{\hat{E}}_f^s}{j\omega_r+\lambda|\hat{\omega}_r|}\frac{j\omega_r+\lambda|\hat{\omega}_r|}{j\omega_r} = \frac{1-j\lambda\,\text{sign}(\hat{\omega}_r)}{s+\lambda|\hat{\omega}_r|}\underline{\hat{E}}_f^s \qquad (4\text{-}16)$$

In this way, the static error introduced by the damping factor can be canceled by the static compensation term $[1-j\lambda\,\text{sign}(\hat{\omega}_r)]$.

The estimator is moved to dq frame by applying αβ-dq transform to (4-16)

$$\frac{d\hat{\psi}_{pm}}{dt} + j\hat{\omega}_r\hat{\psi}_{pm} = [1 - j\lambda\,\text{sign}(\hat{\omega}_r)]\underline{\hat{E}}_f - \lambda|\hat{\omega}_r|\hat{\psi}_{pm} \qquad (4\text{-}17)$$

The derivative term of the permanent magnet flux linkage is put to zero since magnetic saturation in the stator core is neglected which means the amplitude of the magnet flux linkage seen from the stator side is constant. The estimated back-EMF in dq frame $\underline{\hat{E}}_f$ can be decomposed to $\hat{e}_d$ and $\hat{e}_q$ as

$$\underline{\hat{E}}_f = \begin{bmatrix} \hat{e}_d \\ \hat{e}_q \end{bmatrix} = \begin{bmatrix} \hat{u}_{sd} \\ \hat{u}_{sq} \end{bmatrix} - \begin{bmatrix} \hat{R}_s & -\hat{\omega}_r\hat{L}_{sq} \\ \hat{\omega}_r\hat{L}_{sd} & \hat{R}_s \end{bmatrix} \begin{bmatrix} \hat{\imath}_{sd} \\ \hat{\imath}_{sq} \end{bmatrix} - \begin{bmatrix} \hat{L}_{sd} & 0 \\ 0 & \hat{L}_{sq} \end{bmatrix} \frac{d}{dt} \begin{bmatrix} \hat{\imath}_{sd} \\ \hat{\imath}_{sq} \end{bmatrix} \qquad (4\text{-}18)$$

The derivative of the stator current $\frac{d(\hat{\imath}_{sd} + j\hat{\imath}_{sq})}{dt}$ is neglected due to their fast response compared with the estimator [30]. By this, the estimated back-EMF is calculated as

$$\begin{bmatrix} \hat{e}_d \\ \hat{e}_q \end{bmatrix} = \begin{bmatrix} \hat{u}_{sd} \\ \hat{u}_{sq} \end{bmatrix} - \begin{bmatrix} \hat{R}_s & -\hat{\omega}_r\hat{L}_{sq} \\ \hat{\omega}_r\hat{L}_{sd} & \hat{R}_s \end{bmatrix} \begin{bmatrix} \hat{\imath}_{sd} \\ \hat{\imath}_{sq} \end{bmatrix} \qquad (4\text{-}19)$$

Then the imaginary part of (4-17) can be expressed by $\hat{e}_d$ and $\hat{e}_q$ from (4-19)

$$\hat{\omega}_r\psi_{pm} = \hat{e}_q - \lambda\,\text{sign}(\hat{\omega}_r)\,\hat{e}_d \qquad (4\text{-}20)$$

and therefore, the rotor speed and position can be estimated

$$\hat{\omega}_r = \frac{\hat{e}_q - \lambda\,\text{sign}(\hat{\omega}_r)\,\hat{e}_d}{\psi_{pm}} \qquad \hat{\theta}_r = \int \hat{\omega}_r dt \qquad (4\text{-}21)$$

From this, it can be noticed that the estimator belongs to the open-loop structure as shown in Figure 4-1. A suitable selection of λ should be based on the stability analysis of the system. According to [37], λ decides the bandwidth of the SCVM estimator α_{SCVM}. The SCVM estimator should be much faster than the speed controller, otherwise, the estimated speed may fail to follow the reference, but it should also be much slower than the current controller, otherwise, oscillations will happen since the derivative of the stator current $\frac{d(\hat{\imath}_{sd} + j\hat{\imath}_{sq})}{dt}$ is neglected during the derivation. In this work, a proper selection of λ is made in each specific case through trial and error.

4.3 Pulsating Signal Injection on D-Axis (HFI)

The algorithm of the pulsating signal injection on d-axis method is introduced in [34]. The structure of the algorithm implementation is shown in Figure 4-3, where the upper path is the signal through the current controller and the injection of the HF voltage signal, while the lower

part is the extraction, demodulation and analysis of the HF current signal to obtain the rotor angle information. The illustration is given in the following sections.
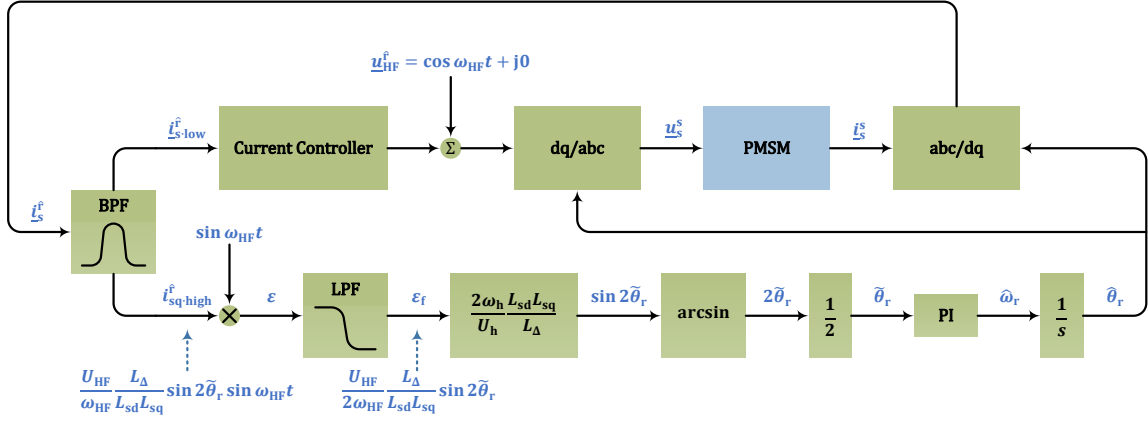
Figure 4-3 The pulsating signal injection method

4.3.1 The Principle of the High Frequency Signal Injection Method

In this section, the principle of the HF signal injection method is shown. The start equation is the stator electrical equation in matrix form

$$\begin{bmatrix} u_{sd} \\ u_{sq} \end{bmatrix} = R_s \begin{bmatrix} i_{sd} \\ i_{sq} \end{bmatrix} + \begin{bmatrix} L_{sd} & 0 \\ 0 & L_{sq} \end{bmatrix} \frac{d}{dt} \begin{bmatrix} i_{sd} \\ i_{sq} \end{bmatrix} + \omega_r \begin{bmatrix} 0 & -L_{sq} \\ L_{sd} & 0 \end{bmatrix} \begin{bmatrix} i_{sd} \\ i_{sq} \end{bmatrix} + \omega_r \psi_{pm} \begin{bmatrix} 0 \\ 1 \end{bmatrix} \quad (4\text{-}22)$$

For the high frequency superimposed voltage, the voltage across the inductance becomes the dominant component in this equation and the HF current can thereby be approximated as

$$\begin{bmatrix} i_{sd\cdot HF} \\ i_{sq\cdot HF} \end{bmatrix} = \begin{bmatrix} L_{sd} & 0 \\ 0 & L_{sq} \end{bmatrix}^{-1} \int \begin{bmatrix} u_{sd\cdot HF} \\ u_{sq\cdot HF} \end{bmatrix} dt \quad (4\text{-}23)$$

Therefore, under perfect orientation, if a d-axis HF voltage is injected, a d-axis HF current can be obtained while the q-axis HF current is zero

$$\begin{bmatrix} u_{sd\cdot HF}^r \\ u_{sq\cdot HF}^r \end{bmatrix} = U_h \begin{bmatrix} \cos \omega_{HF}t \\ 0 \end{bmatrix} \quad \Rightarrow \quad \begin{bmatrix} i_{sd\cdot HF}^r \\ i_{sq\cdot HF}^r \end{bmatrix} = \frac{U_h}{\omega_h L_{sd}} \begin{bmatrix} \sin \omega_{HF}t \\ 0 \end{bmatrix} \quad (4\text{-}24)$$

where the superscript r indicates the real rotor frame, i.e. the real dq frame. However, under non-perfect orientation, the HF voltage is injected in the predicted d-axis

$$\begin{bmatrix} u_{sd\cdot HF}^{\hat{r}} \\ u_{sq\cdot HF}^{\hat{r}} \end{bmatrix} = U_h \begin{bmatrix} \cos \omega_{HF}t \\ 0 \end{bmatrix} \quad (4\text{-}25)$$

where the superscript $\hat{r}$ indicates the estimated rotor-frame, i.e. the estimated dq frame. Thus the voltage vector in the real dq frame r can be expressed as

$$\begin{bmatrix} u^{\mathrm{r}}_{\mathrm{sd\cdot HF}} \\ u^{\mathrm{r}}_{\mathrm{sq\cdot HF}} \end{bmatrix} = \begin{bmatrix} \cos\tilde{\theta}_{\mathrm{r}} & \sin\tilde{\theta}_{\mathrm{r}} \\ -\sin\tilde{\theta}_{\mathrm{r}} & \cos\tilde{\theta}_{\mathrm{r}} \end{bmatrix} \begin{bmatrix} u^{\hat{\mathrm{r}}}_{\mathrm{sd\cdot HF}} \\ u^{\hat{\mathrm{r}}}_{\mathrm{sq\cdot HF}} \end{bmatrix} = U_{\mathrm{h}} \begin{bmatrix} \cos\tilde{\theta}_{\mathrm{r}}\cos\omega_{\mathrm{HF}}t \\ -\sin\tilde{\theta}_{\mathrm{r}}\cos\omega_{\mathrm{HF}}t \end{bmatrix} \qquad (4\text{-}26)$$

where $\tilde{\theta}_{\mathrm{r}}$ is the angle error between the real d-axis and the estimated d-axis. The angle error is defined as

$$\tilde{\theta}_{\mathrm{r}} = \theta_{\mathrm{r}} - \hat{\theta}_{\mathrm{r}} \qquad (4\text{-}27)$$

where θ_{r} is the real rotor angle and $\hat{\theta}_{\mathrm{r}}$ is the estimated rotor angle, which means that the real d-axis leads the estimated d-axis by $\tilde{\theta}_{\mathrm{r}}$. Therefore, the voltage vector in the real dq frame r lags that in the estimated dq frame $\hat{\mathrm{r}}$ by $\tilde{\theta}_{\mathrm{r}}$. In the reverse way, the high frequency current in the estimated dq frame $\hat{\mathrm{r}}$ will be

$$\begin{bmatrix} i^{\hat{\mathrm{r}}}_{\mathrm{sd\cdot HF}} \\ i^{\hat{\mathrm{r}}}_{\mathrm{sq\cdot HF}} \end{bmatrix} = \begin{bmatrix} \cos\tilde{\theta}_{\mathrm{r}} & -\sin\tilde{\theta}_{\mathrm{r}} \\ \sin\tilde{\theta}_{\mathrm{r}} & \cos\tilde{\theta}_{\mathrm{r}} \end{bmatrix} \begin{bmatrix} i^{\mathrm{r}}_{\mathrm{sd\cdot HF}} \\ i^{\mathrm{r}}_{\mathrm{sq\cdot HF}} \end{bmatrix} = \frac{U_{\mathrm{HF}}\sin\omega_{\mathrm{HF}}t}{\omega_{\mathrm{HF}}} \begin{bmatrix} \left(\dfrac{\cos^{2}\tilde{\theta}_{\mathrm{r}}}{L_{\mathrm{sd}}} + \dfrac{\sin^{2}\tilde{\theta}_{\mathrm{r}}}{L_{\mathrm{sq}}} \right) \\ \dfrac{L_{\Delta}}{L_{\mathrm{sd}}L_{\mathrm{sq}}}\sin 2\tilde{\theta}_{\mathrm{r}} \end{bmatrix} \qquad (4\text{-}28)$$

As can be seen from Figure 4-3, the HF current will be seen in the estimated dq frame in the controller. From (4-28), the q-axis HF current contains the useful error angle information

$$i^{\hat{\mathrm{r}}}_{\mathrm{sq\cdot HF}} = \frac{U_{\mathrm{HF}}}{\omega_{\mathrm{HF}}} \frac{L_{\Delta}}{L_{\mathrm{sd}}L_{\mathrm{sq}}}\sin 2\tilde{\theta}_{\mathrm{r}}\sin\omega_{\mathrm{HF}}t \qquad (4\text{-}29)$$

The error angle $\tilde{\theta}_{\mathrm{r}}$ can be extracted by multiplying the q-axis HF current with $\sin\omega_{\mathrm{h}}t$

$$i^{\hat{\mathrm{r}}}_{\mathrm{sq\cdot HF}}\sin\omega_{\mathrm{HF}}t = \frac{U_{\mathrm{HF}}}{2\omega_{\mathrm{HF}}} \frac{L_{\Delta}}{L_{\mathrm{sd}}L_{\mathrm{sq}}}\sin 2\tilde{\theta}_{\mathrm{r}} - \frac{U_{\mathrm{HF}}}{2\omega_{\mathrm{HF}}} \frac{L_{\Delta}}{L_{\mathrm{sd}}L_{\mathrm{sq}}}\sin 2\tilde{\theta}_{\mathrm{r}}\cos 2\omega_{\mathrm{HF}}t \qquad (4\text{-}30)$$

The first term can be easily extracted from a LPF

$$\mathrm{LPF}\{i^{\hat{\mathrm{r}}}_{\mathrm{sq\cdot HF}}\sin\omega_{\mathrm{HF}}t\} = \frac{1}{2}\frac{U_{\mathrm{HF}}}{\omega_{\mathrm{HF}}} \frac{L_{\Delta}}{L_{\mathrm{sd}}L_{\mathrm{sq}}}\sin 2\tilde{\theta}_{\mathrm{r}} \qquad (4\text{-}31)$$

and $\tilde{\theta}_{\mathrm{r}}$ can be further calculated as

$$\begin{aligned} \tilde{\theta}_{\mathrm{r}} &= \frac{1}{2}\arcsin\left[\frac{2\omega_{\mathrm{HF}}}{U_{\mathrm{HF}}} \frac{L_{\mathrm{sd}}L_{\mathrm{sq}}}{L_{\Delta}}\mathrm{LPF}\{i^{\hat{\mathrm{r}}}_{\mathrm{sq\cdot HF}}\sin\omega_{\mathrm{HF}}t\} \right] \\ &\approx \frac{\omega_{\mathrm{HF}}}{U_{\mathrm{HF}}} \frac{L_{\mathrm{sd}}L_{\mathrm{sq}}}{L_{\Delta}}\mathrm{LPF}\{i^{\hat{\mathrm{r}}}_{\mathrm{sq\cdot HF}}\sin\omega_{\mathrm{HF}}t\} \end{aligned} \qquad (4\text{-}32)$$

The extracted error angle can then be used as an input to a PI controller which adjusts the estimated speed to put the angle estimation error to zero. It should be pointed out that, all the operation points that satisfies

$$\tilde{\theta}_{\mathrm{r}} = \theta_{\mathrm{r}} - \tilde{\theta}_{\mathrm{r}} = \pm n\pi \quad n = 1, 2, 3 \cdots \qquad (4\text{-}33)$$

can be considered as stable in the HF injection method since $\sin 2\tilde{\theta}_r$ gives zero under these conditions which fools the estimator. This phenomenon is consistent with the possible 180° estimation error indicated in Section 4.1.2.

A proper selection of the injected voltage amplitude should be made. A too low amplitude will give a current response that will be submerged by the noise and a too high amplitude will give a too high loss. In [38], the injection voltage amplitude is about 10% of the PMSM rated voltage, and this 10% level voltage injection is applied in this thesis work.

In addition, a proper frequency must be assigned to the injected voltage. The injected frequency f_{HF} should not be too high because this would lead to some problems like

- The frequency modulation index to modulate the HF voltage signal $m_{f \cdot HF}$ will not be high enough, i.e. the PWM algorithm will fail to deliver the HF voltage reference since the HF voltage component changes too much in one switching period T_{sw}.

- The amplitude of $i_{sq \cdot HF}^{\hat{r}}$ will be too little since it is inversely proportional to the injected frequency f_{HF} as can be seen from (4-29).

However, it cannot be selected too low either in order to guarantee a proper separation from the PMSM fundamental frequency f_1. In addition, f_{HF} should be selected high enough so that the terms other than the inductive voltage drops can be neglected in (4-22). Therefore, the frequency requirement for the injected HF signal is

$$f_1 \ll f_{HF} \ll f_{sw} \tag{4-34}$$

4.3.2   Separation of the Current Components

As can be noticed from Figure 4-3, both the fundamental frequency and the injected high frequency components exist in the PMSM stator current. Therefore, it is necessary to separate the high frequency current component which is used for the rotor angle estimation and the fundamental frequency current component which is used for the current control.

A second-order Band Pass Filter (BPF) can be utilized to extract the high frequency current component. The transfer function of a BPF can be expressed as

$$H_{BPF}(s) = H_0 \frac{\beta_{BPF} \cdot s}{s^2 + \beta_{BPF} \cdot s + \omega_0^2} \tag{4-35}$$

where H_0 is the band pass gain, ω_0 is the center frequency and β_{BPF} is the bandwidth. The cut-off frequencies can be further calculated based on steady state operation as

$$\frac{|H_{BPF}(j\omega)|}{H_0} = \frac{|j\omega \cdot \beta_{BPF}|}{|-\omega^2 + j\omega \cdot \beta_{BPF} + \omega_0^2|} = \frac{\sqrt{2}}{2} \tag{4-36}$$

which yields

$$\omega_{\text{cut·low}} = \frac{-\beta_{\text{BPF}} + \sqrt{\beta_{\text{BPF}}^2 + 4\omega_0^2}}{2} \qquad \omega_{\text{cut·high}} = \frac{\beta_{\text{BPF}} + \sqrt{\beta_{\text{BPF}}^2 + 4\omega_0^2}}{2} \qquad (4\text{-}37)$$

It can be verified that

$$\omega_0 = \sqrt{\omega_{\text{cut·low}} \cdot \omega_{\text{cut·high}}} \qquad \beta_{\text{BPF}} = \omega_{\text{cut·high}} - \omega_{\text{cut·low}} \qquad (4\text{-}38)$$

To select the BPF parameters, the signal that should be extracted needs to be studied. According to (4-29), the signal that the BPF needs to extract is an amplitude modulated (AM) component $i_{\text{sqh}}^{\hat{r}} = \frac{U_{\text{HF}}}{\omega_{\text{HF}}} \frac{L_\Delta}{L_{\text{sd}} L_{\text{sq}}} \sin 2\tilde{\theta}_r \sin \omega_h t$. For an AM signal

$$
\begin{aligned}
y(t) &= m(t) \cdot c(t) = M \cos(\omega_m t + \varphi) \cdot A \sin(\omega_c t) \\
&= \frac{AM}{2} \{ \sin[(\omega_c + \omega_m)t + \varphi] + \sin[(\omega_c - \omega_m)t - \varphi] \}
\end{aligned} \qquad (4\text{-}39)
$$

where $m(t)$ is the modulation signal that has a variable frequency of ω_m and a variable phase angle of φ and $c(t)$ is the carrier signal at a constant frequency of ω_c. Therefore, the frequency spectrum of the AM signal has a central frequency at ω_c, which in this work is ω_{HF} and two sidebands at approximately $(\omega_c \pm \omega_m)$ as plotted in Figure 4-4. No clear way has been found to calculate a proper ω_m due to the non-linearity of the sine function. In this work, a proper bandwidth of the BPF β will be selected by trial-and-error.
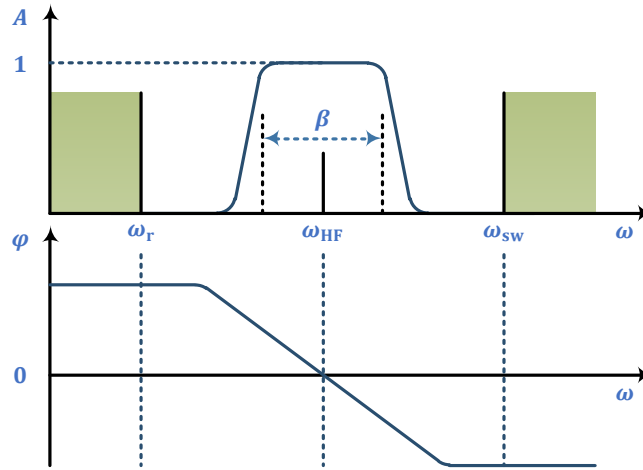
Figure 4-4 The frequency spectrum and the expected Bode diagram of the BPF

From what have been discussed above, both the amplitude to frequency and the phase to frequency Bode diagrams of the BPF should be paid attention to:

- The central frequency of the BPF should be

$$\omega_0 = \omega_{HF} \tag{4-40}$$

- The amplitude at the central frequency of the BPF should be unit since the accurate information of the amplitude is required

$$H_0 = 1 \tag{4-41}$$

- The phase shift at the central frequency of the BPF should be zero

$$\varphi_0 = 0 \tag{4-42}$$

- The bandwidth of the BPF β_{BPF} should be selected high enough so that the sidebands of the spectrum can be included since they contain the information of the error angle.

4.3.3 PLL-type Estimator

The q-axis high frequency current component is caused directly by the angle error as shown in (4-29). The angle error can be detected by the *Demodulation Process* which can be regarded as a *Phase Detector*. If the scaling factor $\dfrac{U_{HF}}{\omega_{HF}}\dfrac{L_\Delta}{L_{sd}L_{sq}}$ in (4-29) is included in the *Phase Detector*, then the whole structure in Figure 4-3 can be equalized and simplified as in Figure 4-5.
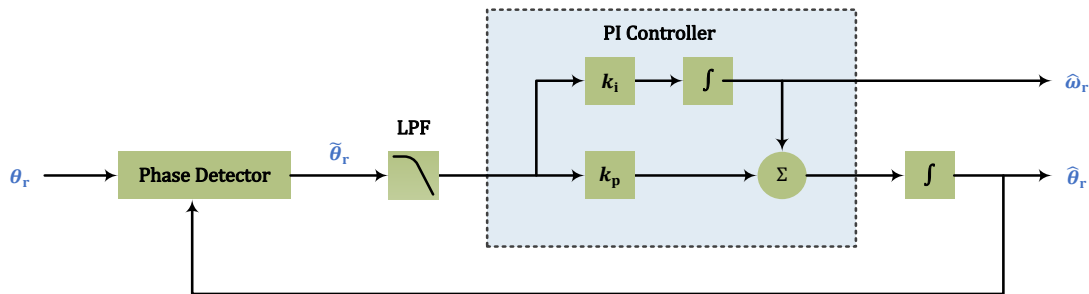
Figure 4-5 PLL-type estimator

As can be noticed in Figure 4-5, the estimation of the rotor angle is through both the proportional path and the integral path, while the estimation of the rotor speed is only through the integral path. Such a design is based on a consideration to avoid direct effect from the angle error to the speed estimation, so that the feedback of the speed to the speed controller will be relatively smooth [39].

The task of the LPF is to remove the high frequency components while the PI controller is expected to eliminate the low frequency angle estimation error. A separation design of the LPF and the PI controller requires a much higher bandwidth of the LPF than the PI controller. However, in the thesis work, the LPF cannot be fast enough in comparison with the PI controller since a relatively fast response of the PI controller is already demanded. Therefore, an integrated

40

design of the LPF and the PI controller is preferred. In this case, both the open-loop and closed-loop transfer functions of the estimator can be derived

$$G_{\text{open}}(s) = H_{\text{LPF}}H_{\text{PI}} = \frac{\alpha_{\text{LPF}}}{s + \alpha_{\text{LPF}}}\left(k_{\text{p}} + \frac{k_{\text{i}}}{s}\right)\frac{1}{s} = \frac{\alpha_{\text{LPF}}k_{\text{p}}s + \alpha_{\text{LPF}}k_{\text{i}}}{s^3 + \alpha_{\text{LPF}}s^2} \qquad (4\text{-}43)$$

$$G_{\text{close}}(s) = \frac{N(s)}{D(s)} = \frac{G_{\text{open}}(s)}{1 + G_{\text{open}}(s)} = \frac{\alpha_{\text{LPF}}k_{\text{p}}s + \alpha_{\text{LPF}}k_{\text{i}}}{s^3 + \alpha_{\text{LPF}}s^2 + \alpha_{\text{LPF}}k_{\text{p}}s + \alpha_{\text{LPF}}k_{\text{i}}} \qquad (4\text{-}44)$$

where it is assumed that the transfer function of the *phase detector* in Figure 4-5 is 1. The *phase detector* in this case means everything from the injected HF voltage to after the demodulator in Figure 4-3. An assumed transfer function of 1 means that this system is much faster than the PLL and therefore the system can be considered to be always in steady-state compared with the PLL. In order to stabilize the response, negative triple roots are preferred which means three negative real poles overlapping each other [38]. Therefore, the denominator should be

$$D(s) = (s + p)^3 = s^3 + 3ps^2 + 3p^2s + p^3 \qquad (4\text{-}45)$$

where p is the pole of the closed-loop transfer function. By comparing (4-45) with the denominator of (4-44), the gains should be selected as

$$\alpha_{\text{LPF}} = 3p \qquad k_{\text{p}} = \frac{3p^2}{\alpha_{\text{LPF}}} = p \qquad k_{\text{i}} = \frac{p^3}{\alpha_{\text{LPF}}} = \frac{p^2}{3} \qquad (4\text{-}46)$$

and this gives a closed-loop system as

$$G_{\text{close}}(s) = \frac{3p^2s + p^3}{s^3 + 3ps^2 + 3p^2s + p^3} = \frac{p^2(3s + p)}{(s + p)^3} \qquad (4\text{-}47)$$

In this thesis work, the estimator should follow the change of the angle error. The pole is selected by trial and error in each specific case.

4.4   Position-Sensorless Control Combination

Both of the SCVM and the HFI algorithms have their limitations. The SCVM cannot support sustained operation at low speeds while the HF signal injection method gives limited dynamic performance [38]. Therefore, it is suggested that the SCVM can be applied throughout the whole speed range, while the HF injection method can be applied in the low speed range to enhance the estimation. The combination of the HF signal injection method and the voltage model method is indicated in [38].

A participation factor k_{HF} is defined to represent the percentage that the HFI participates in the estimation

$$k_{\text{HF}} = \begin{cases} \dfrac{\omega_{\text{r}}^{\text{th}} - |\widehat{\omega}_{\text{r}}|}{\omega_{\text{r}}^{\text{th}}} & |\widehat{\omega}_{\text{r}}| \le \omega_{\text{r}}^{\text{th}} \\ 0 & |\widehat{\omega}_{\text{r}}| > \omega_{\text{r}}^{\text{th}} \end{cases} \qquad (4\text{-}48)$$

where $|\widehat{\omega}_r|$ is the absolute value of the speed estimation and ω_r^{th} is the threshold of the HFI participation. The percentages of participation of the SCVM and the HFI are shown in Figure 4-6.
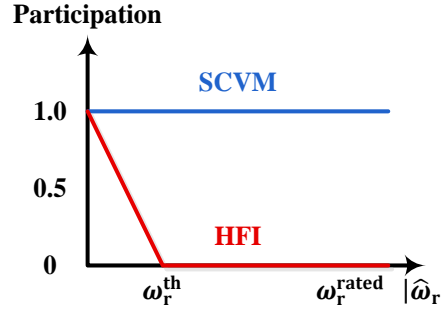
Figure 4-6 Participation of the SCVM and the HFI in the combined sensorless estimator

As can be noticed in Figure 4-6, the HFI gives a decreasing contribution to the angle and speed estimation as the speed estimation goes up. As will be shown later, the total switch-over, which is decided by ω_r^{th}, is preferred to occur after the current limit is hit, and therefore a smooth stator current and rotor acceleration can be achieved. The calculation of k_{HF} can be implemented in Simulink as shown in Figure 4-7.
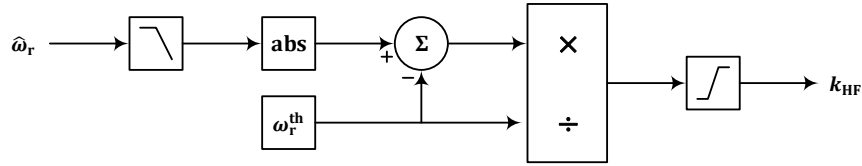
Figure 4-7 Calculation of participation factor k_{HF} for the participation of HFI

The signal $\widehat{\omega}_r$ first passes through a low pass filter in order to prevent possible speed oscillations from affecting the factor k_{HF} and further affecting the operating of the estimator. The bandwidth of the low pass filter can be selected to be a low frequency which is decided as 1 Hz in this thesis work. The combination of the SCVM and the HFI estimator is shown in Figure 4-8.
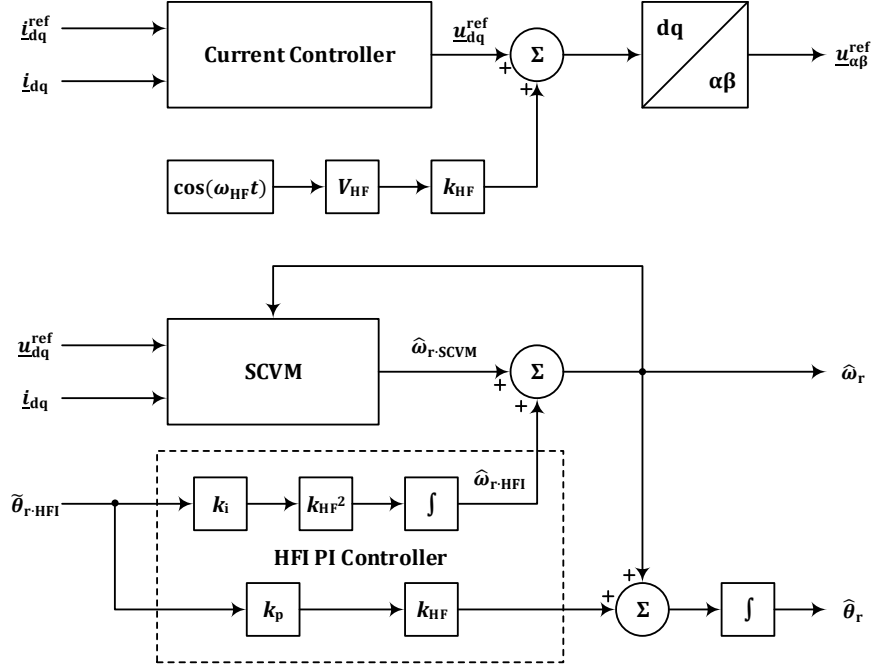
Figure 4-8 Combined speed & position estimator

As can be noticed in Figure 4-8, the total speed estimation is composed by adding the SCVM and HFI speed estimations together. Similar to the structure of the PLL-type estimator shown in Figure 4-5, the speed estimation and the response from the HFI proportional part are summed up and integrated to generate the angle estimation. In addition, as the speed goes up, the HFI is scheduled to be turned off gradually. The turning off of the HFI is performed by decreasing the HFI PI controller bandwidth gradually to zero, which is further realized by moving the pole of the PLL in the HFI towards the origin by applying a decreasing k_{HF}. In other words, the previously fixed pole p in (4-45) is going to be changed to a moving pole p_{HF} as

$$p_{\mathrm{HF}} = k_{\mathrm{HF}} \cdot p \tag{4-49}$$

Then, the PI parameters k_{p} and k_{i} should be replaced by $k_{\mathrm{HF \cdot p}}$ and $k_{\mathrm{HF \cdot i}}$ correspondingly

$$\begin{cases} k_{\mathrm{p}} = p \\ k_{\mathrm{i}} = \dfrac{p^2}{3} \end{cases} \Rightarrow \begin{cases} k_{\mathrm{HF \cdot p}} = p_{\mathrm{HF}} = k_{\mathrm{HF}} \cdot p = k_{\mathrm{HF}} \cdot k_{\mathrm{p}} \\ k_{\mathrm{HF \cdot i}} = \dfrac{p_{\mathrm{HF}}^2}{3} = k_{\mathrm{HF}}^2 \cdot \dfrac{p^2}{3} = k_{\mathrm{HF}}^2 \cdot k_{\mathrm{i}} \end{cases} \tag{4-50}$$

This is the reason why the proportional part is multiplied by k_{HF} while the integral part is multiplied by k_{HF}^2 in Figure 4-8. In addition, similar to the HFI estimator, the level of the HF voltage injection after the current controller is also multiplied by k_{HF} so that the high frequency losses are faded away synchronously with the HFI estimator.

5   Power Electronic Converter

5.1   Power Electronic Converter for Subsea Motors

Harmonics generated by PWM strategy may easily cause high frequency oscillations and voltage ringing when the switching harmonics encounter the resonance frequency of the transmission system [40]. Besides, voltage reflection will occur in the cable since the PWM waveform is a set of step inputs. Therefore, a voltage as high as two times the input voltage may occur [40]. Furthermore, high dv/dt stress on the insulation may appear which also leads to high cable charging current [41]. In addition, the switching frequency can be selected high enough so that the harmonics can be removed by adding a small output filter of the converter if a problem would occur. In order to reduce the voltage harmonic content more, the SVPWM algorithm is selected instead of the SinePWM algorithm [42] [43].

In term of the devices, sinewave filters and multilevel inverters are often applied to mitigate the negative effects from PWM. Sinewave filters add series inductance to the transmission system and therefore shift the resonance frequencies of the transmission system to a lower frequency region [44]. Several choices are available for sine wave filters: L filter, LC filter and LCL filter, among which, the L filter is a common one as it is simple and free of resonance itself. Multilevel inverters can be applied to shift the switching harmonic frequencies to a higher frequency region which can be filtered out more easily. In this thesis work, a cascaded H-bridge multilevel inverter is implemented for its modular architecture (the cells). The advantage is that if one cell breaks down, the inverter can continue working by by-passing the broken cell [45]. Such H-bridge multilevel inverter in subsea applications is considered and analyzed in [46]. The main drawback of a cascaded H-bridge multilevel inverter is that it requires an independent dc voltage source for each cell. This further requires a transformer with multi windings on the secondary side which increases the complexity of the converter configuration.

A three-phase two-level inverter topology is shown in Figure 5-1 and a three-phase H-bridge five-level inverter topology is shown in Figure 5-2. In the models of the electric drive simulations, it is always assumed that the dc-link voltages are constant. Therefore, the power supply and the diode rectifier are not included and the dc-links are represented as dc voltage sources in Figure 5-1 and Figure 5-2.
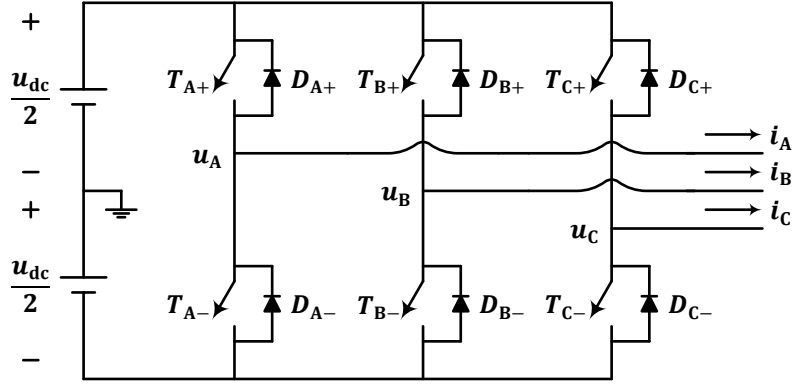
Figure 5-1 Three-phase two-level inverter
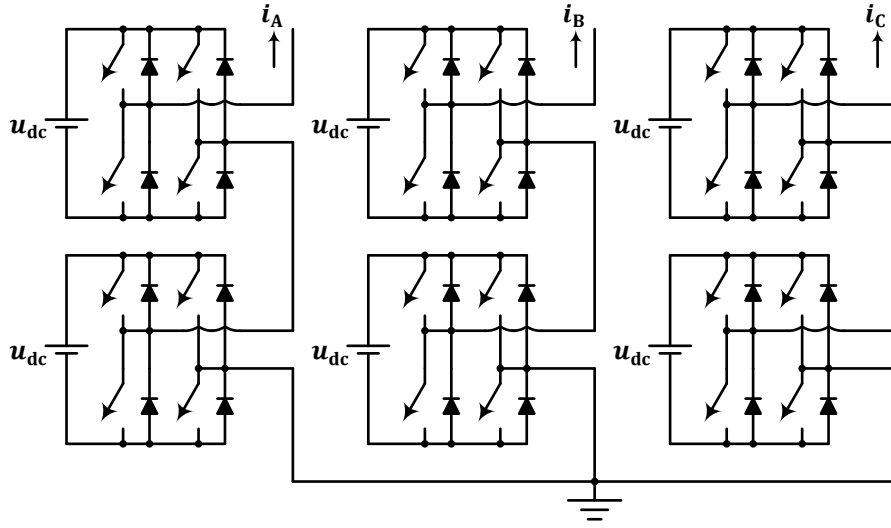
Figure 5-2 Three-phase cascade H-bridge five-level inverter [47]

The terms "two-level" and "five-level" indicate the number of levels in each phase voltage. The two-level inverter shown in Figure 5-1 is commonly used where each phase is composed by a half-bridge which can either gives $+\frac{u_{dc}}{2}$ or $-\frac{u_{dc}}{2}$. However, in the five-level inverter shown in Figure 5-2, each phase is composed by two series-connected H-bridge modules. Since each module gives three voltage levels: $+u_{dc}$, zero and $-u_{dc}$, the two series-connected modules will give five voltage levels in each phase voltage: $+2u_{dc}$, $+u_{dc}$, zero, $-u_{dc}$ and $-2u_{dc}$.

5.2   Space Vector Pulse Width Modulation (SVPWM)

Space Vector Pulse Width Modulation (SVPWM) was firstly introduced in the control of induction machines and brushless DC machines [48]. It gives three main advantages compared with SinePWM in the modulation and therefore is selected as the modulation algorithm in the thesis work [49]:

45

- Slightly lower harmonics compared to sinusoidal PWM technique

- Good cooperation with field-oriented motor control

- Higher voltage output in comparison with normal sinusoidal PWM

In this section, the two-level SVPWM is introduced first followed by the five-level SVPWM.

5.2.1   Two-Level SVPWM

As has been mentioned in Section 5.1, in a two-level inverter, each phase has two voltage levels, either the upper switch is on, which is denoted as single-phase voltage state 1, or the lower switch is on, which is denoted as single-phase voltage state 0. Then, by placing the three single-phase voltage states in a sequence as Phase A, Phase B and Phase C, a three-phase voltage state can be formed. Totally $2^3 = 8$ three-phase voltage states can be achieved which are listed in Column 2 to 5 in Table 5-1.

Table 5-1 Voltage vectors in two-level voltage source converters

Space Vectors	States	S_A	S_B	S_C
$\underline{V_0}$	[0 0 0]	S_{A-}	S_{B-}	S_{C-}
$\underline{V_1}$	[1 0 0]	S_{A+}	S_{B-}	S_{C-}
$\underline{V_2}$	[1 1 0]	S_{A+}	S_{B+}	S_{C-}
$\underline{V_3}$	[0 1 0]	S_{A-}	S_{B+}	S_{C-}
$\underline{V_4}$	[0 1 1]	S_{A-}	S_{B+}	S_{C+}
$\underline{V_5}$	[0 0 1]	S_{A-}	S_{B-}	S_{C+}
$\underline{V_6}$	[1 0 1]	S_{A+}	S_{B-}	S_{C+}
$\underline{V_7}$	[1 1 1]	S_{A+}	S_{B+}	S_{C+}

In Table 5-1, the three-phase voltage states in Column 2 can also be regarded as voltage vectors which are denoted in Column 1. These eight voltage vectors can be named as "basic vectors". The value "1" in the states indicates the upper switch is on in the corresponding leg which means the phase output voltage is $\frac{1}{2}u_{dc}$, while the value "0" indicates vice versa and means the phase output voltage is $-\frac{1}{2}u_{dc}$. By applying the abc-αβ transformation which is introduced in Section 2.1.1, the eight basic vectors form a hexagon in the αβ frame, as shown in Figure 5-3 (a).

(a)   (b)
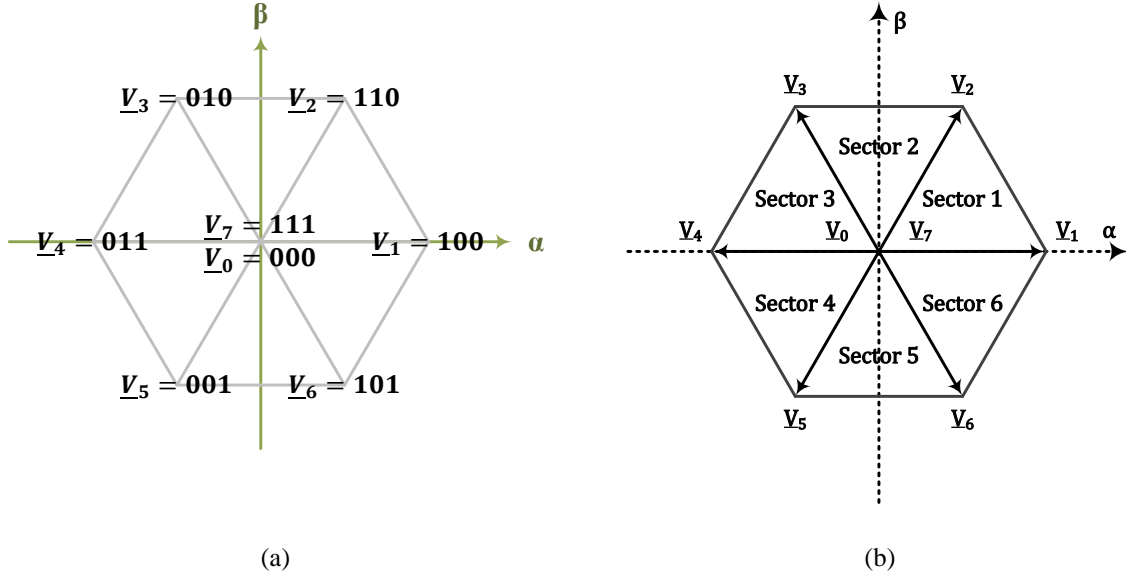
Figure 5-3 Three-phase two-level SVPWM hexagon

(a) eight basic voltage vectors   (b) six sectors

Among the eight basic voltage vectors, the amplitudes of $\underline{V}_0$ and $\underline{V}_7$ are zero, while the amplitudes of the six vectors from $\underline{V}_1$ to $\underline{V}_6$ are be equal to $\frac{2}{3}u_{dc}$, since amplitude-invariant is used in this thesis work

$$\left|\underline{V}_1\right| = \left|\underline{V}_2\right| = \left|\underline{V}_3\right| = \left|\underline{V}_4\right| = \left|\underline{V}_5\right| = \left|\underline{V}_6\right| = \frac{2}{3}u_{dc} \tag{5-1}$$

The hexagon in Figure 5-3 (a) indicates the output voltage limit of a three-phase two-level voltage source converter. Further, the eight basic voltage vectors divide the hexagon into six sectors as shown in Figure 5-3 (b). Any voltage reference vector in αβ frame can be composed by the two adjacent basic vectors together with the basic vector 0 and 7. The composition can be realized by applying the eight basic vectors in a sequence, each vector with a proper duty cycle, so that the average output voltage vector in one switching cycle can be equal to the voltage reference vector. For example, a voltage reference vector in Sector 1 can be composed by $\underline{V}_1$, $\underline{V}_2$, $\underline{V}_0$ and $\underline{V}_7$ by applying proper weights, i.e. duty cycles, to each one of them

$$u_\alpha^{ref} + ju_\beta^{ref} = \underline{u}^{ref} = \underline{u}_1^{ref} + \underline{u}_2^{ref} = \underline{V}_1 d_1 + \underline{V}_2 d_2 + \underline{V}_0 d_0 + \underline{V}_7 d_7 \tag{5-2}$$

where d_1, d_2, d_0 and d_7 are the duty cycles of $\underline{V}_1$, $\underline{V}_2$, $\underline{V}_0$ and $\underline{V}_7$ respectively. The mechanism in (5-2) is illustrated in Figure 5-4 (a). The reference vector $\underline{u}^{ref}$ is composed by $\underline{u}_\alpha^{ref}$ and $\underline{u}_\beta^{ref}$ and is further decomposed into $\underline{u}_1^{ref}$ and $\underline{u}_2^{ref}$. $\underline{u}_1^{ref}$ can be realized by applying $\underline{V}_1$ for a duty cycle d_1 and $\underline{u}_2^{ref}$ can be realized by applying $\underline{V}_2$ for a duty cycle d_2. The remaining time during the switching period $(1 - d_1 - d_2)$ is evenly filled by the zero vectors $\underline{V}_0$ with d_0 and $\underline{V}_7$ with d_7. Furthermore, by continuously sending the SVPWM

47

modulator the instantaneous voltage vector reference, such averaged output voltage vectors can be composed continuously as requested. Then a continuous rotation of the vector will appear in the αβ frame as shown in Figure 5-4 (b).

(a)   (b)
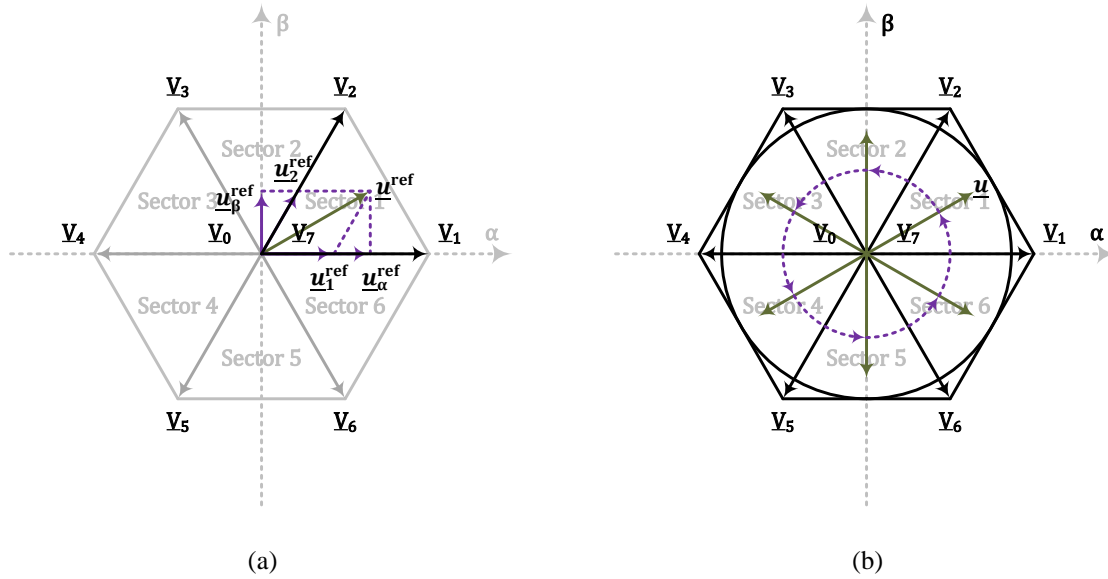
Figure 5-4 Two-level voltage source converter voltage vectors

(a) eight voltage vectors and six sectors   (b) rotation of the voltage vectors

As can be noticed in Figure 5-4 (b), in order to achieve a continuous rotation of the output voltage vector with a fix amplitude, the amplitude of the output vector should be limited within the inscribed circle of the hexagon. Therefore, the output voltage limit can be calculated as the radius of the inscribed circle

$$\left| \underline{u}_{\text{SVPWM·lim}} \right| = \frac{2}{3} u_{\text{dc}} \cos 30° = \frac{u_{\text{dc}}}{\sqrt{3}} \tag{5-3}$$

The general ideal of the SVPWM has been given and now the algorithm of forming the switching sequence with proper duty cycles or operating time intervals in every switching cycle will be illustrated. A proper switching sequence should be selected to reduce the number of switching commutations so that the harmonic contents can be reduced and the possible implementation in practical cases can be guaranteed.

- The sequence should be symmetric in a switching period T_{sw}, which means that the sequence should first be selected in $\frac{T_{sw}}{2}$ and then be mirrored. This approach to center the pulses within one switching cycle is reported to achieve a reduction of harmonic contents [50].

- Only one leg switching state is changed per switching action in the sequence in order to reduce the total number of switching actions.

In terms of a voltage vector reference in Sector 1, the switching sequence can be selected as Figure 5-5 shows.
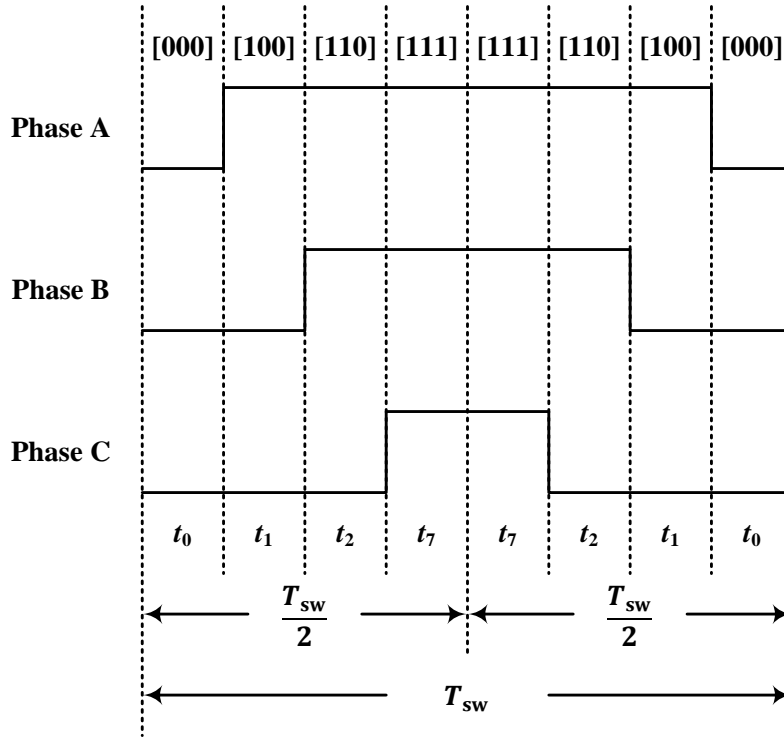
Figure 5-5 Switching pattern of Space Vector Pulse Modulation

The active switching time t_1 and t_2 can be decided as [50]

$$t_1 = \frac{\left|\underline{u}_1^{\text{ref}}\right|}{\left|\underline{V}_1\right|} \frac{T_{sw}}{2} = \frac{u_\alpha^{\text{ref}} - u_\beta^{\text{ref}} \cot 60°}{\frac{2}{3} u_{dc}} \frac{T_{sw}}{2} = \frac{3u_\alpha^{\text{ref}} - \sqrt{3}u_\beta^{\text{ref}}}{4u_{dc}} T_{sw} \qquad (5\text{-}4)$$

$$t_2 = \frac{\left|\underline{u}_2^{\text{ref}}\right|}{\left|\underline{V}_2\right|} \frac{T_{sw}}{2} = \frac{u_\beta^{\text{ref}} \sec 60°}{\frac{2}{3} u_{dc}} \frac{T_{sw}}{2} = \frac{\sqrt{3}u_\beta^{\text{ref}}}{2u_{dc}} T_{sw} \qquad (5\text{-}5)$$

and the zero-voltage switching time t_0 and t_7 can be filled into the remaining time in the switching period

$$t_0 = t_7 = \frac{1}{2}\left(\frac{T_{sw}}{2} - t_1 - t_2\right) = \left(\frac{1}{4} - \frac{3u_\alpha^{ref} + \sqrt{3}u_\beta^{ref}}{8u_{dc}}\right)T_{sw} \tag{5-6}$$

For the other sectors, the time intervals can be calculated with the same equations after rotating the voltage reference vector to Sector 1 as

$$\underline{u}_{Sector\,1}^{ref} = \underline{u}^{ref} \cdot e^{-j\theta_{Sector}} \tag{5-7}$$

where $\underline{u}^{ref}$ is the original voltage vector reference, $\underline{u}_{Sector\,1}^{ref}$ is the voltage vector reference rotated to Sector 1. The angle θ_{Sector} is the rotation angle which is determined by the location of $\underline{u}^{ref}$

$$\theta_{Sector} = \begin{cases} 0 & \underline{u}^{ref} \text{ in Sector 1} \\ \dfrac{1}{3}\pi & \underline{u}^{ref} \text{ in Sector 2} \\ \dfrac{2}{3}\pi & \underline{u}^{ref} \text{ in Sector 3} \\ \pi & \underline{u}^{ref} \text{ in Sector 4} \\ -\dfrac{2}{3}\pi & \underline{u}^{ref} \text{ in Sector 5} \\ -\dfrac{1}{3}\pi & \underline{u}^{ref} \text{ in Sector 6} \end{cases} \tag{5-8}$$

If the voltage limit of the SVPWM, $\frac{u_{dc}}{\sqrt{3}}$, is selected as the base voltage, then (5-4), (5-5) and (5-6) can be expressed in per unit

$$t_1 = \frac{\sqrt{3}u_\alpha^{ref\cdot p.u.} - u_\beta^{ref\cdot p.u.}}{4}T_{sw} \tag{5-9}$$

$$t_2 = \frac{u_\beta^{ref\cdot p.u.}}{2}T_{sw} \tag{5-10}$$

$$t_0 = t_7 = \frac{1}{2}\left(\frac{T_{sw}}{2} - t_1 - t_2\right) = \left(\frac{1}{4} - \frac{\sqrt{3}u_\alpha^{ref\cdot p.u.} + u_\beta^{ref\cdot p.u.}}{8}\right)T_{sw} \tag{5-11}$$

In order to keep one switching action per commutation, a specific space vector sequence should be selected. The selection of the sequences in six sectors is illustrated in Figure 5-6. The purple arrows show the switching actions moving from one state to another and the number on each arrow shows the order of such switching action. In odd number sectors, i.e. Sector 1, 3 and 5, the switching actions go from [0 0 0] to [1 1 1] by following the anti-clockwise direction in the first half switching cycle, i.e. switching action 1, 2 and 3, while the switching actions go from [1 1 1] back to [0 0 0] by following the clockwise direction in the second half switching cycle,

i.e. switching action 4, 5 and 6. The opposite direction is followed in even number sectors, i.e. Sector 2, 4 and 6. In this case, the number of switching actions can be reduced to minimum in one switching period. The sequence and the corresponding time intervals in one switching cycle can also be shown in a table as listed in Table 5-2. In the table, it is clearly shown which time interval should be assigned to which voltage vector in different sectors.
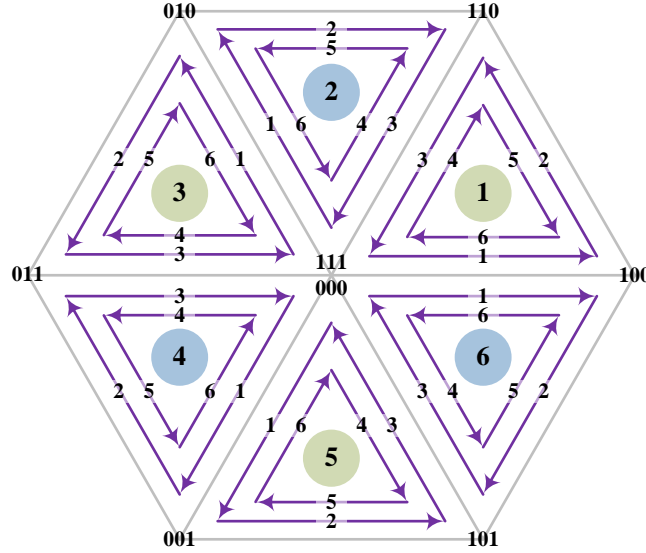
Figure 5-6 Sequence of the two-level states in six sectors

Table 5-2 Space vector sequences and corresponding time intervals

	Space Vector Sequences							
Sector 1	$\underline{V_0}$	$\underline{V_1}$	$\underline{V_2}$	$\underline{V_7}$	$\underline{V_7}$	$\underline{V_2}$	$\underline{V_1}$	$\underline{V_0}$
	t_0	t_1	t_2	t_7	t_7	t_2	t_1	t_0
Sector 2	$\underline{V_0}$	$\underline{V_3}$	$\underline{V_2}$	$\underline{V_7}$	$\underline{V_7}$	$\underline{V_2}$	$\underline{V_3}$	$\underline{V_0}$
	t_0	t_2	t_1	t_7	t_7	t_1	t_2	t_0
Sector 3	$\underline{V_0}$	$\underline{V_3}$	$\underline{V_4}$	$\underline{V_7}$	$\underline{V_7}$	$\underline{V_4}$	$\underline{V_3}$	$\underline{V_0}$
	t_0	t_1	t_2	t_7	t_7	t_2	t_1	t_0
Sector 4	$\underline{V_0}$	$\underline{V_5}$	$\underline{V_4}$	$\underline{V_7}$	$\underline{V_7}$	$\underline{V_4}$	$\underline{V_5}$	$\underline{V_0}$
	t_0	t_2	t_1	t_7	t_7	t_1	t_2	t_0
Sector 5	$\underline{V_0}$	$\underline{V_5}$	$\underline{V_6}$	$\underline{V_7}$	$\underline{V_7}$	$\underline{V_6}$	$\underline{V_5}$	$\underline{V_0}$
	t_0	t_1	t_2	t_7	t_7	t_2	t_1	t_0
Sector 6	$\underline{V_0}$	$\underline{V_1}$	$\underline{V_6}$	$\underline{V_7}$	$\underline{V_7}$	$\underline{V_6}$	$\underline{V_1}$	$\underline{V_0}$
	t_0	t_2	t_1	t_7	t_7	t_1	t_2	t_0

5.2.2 Five-Level SVPWM

The five-level SVPWM introduces more switching states compared to the two-level SVPWM, but the other aspects are remaining the same. The switching states are illustrated in Figure 5-7

[51] [52] [53]. As can be noticed from the figure, the hexagon is developed from one layer to four layers for the five-level SVPWM. The states on the edges of the hexagon are unique while more and more state redundancy is available when going from the edges to the center.
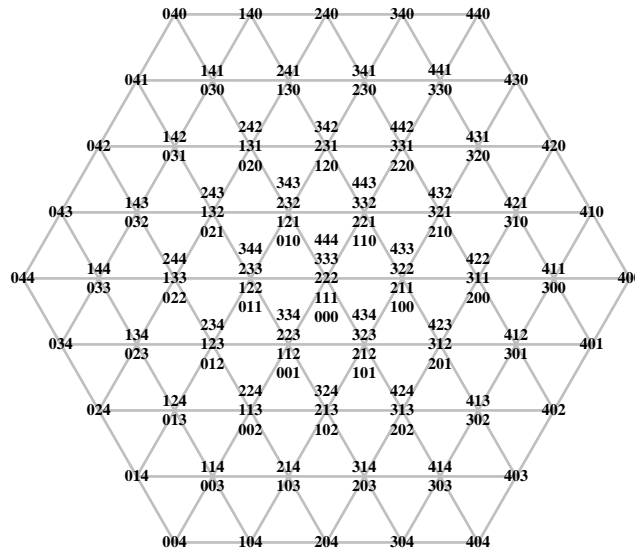
Figure 5-7 Five-level SVPWM voltage vectors

(a)   (b)
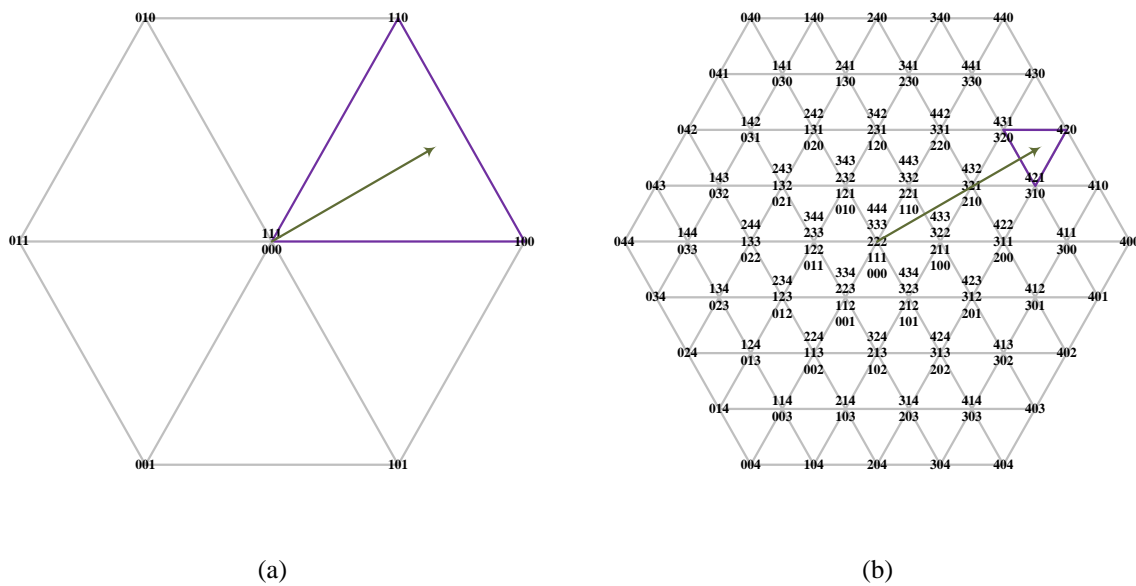
Figure 5-8 Vector composition in SVPWM

(a) Vector composition in two-level SVPWM   (b) Vector composition in five-level SVPWM

A comparison between the two-level and the five-level SVPWM are shown in Figure 5-8. As can be noticed, by dividing the two-level SVPWM hexagon in Figure 5-8 (a) into more triangles in Figure 5-8 (b), a more elaborate SVPWM composition is introduced by multilevel SVPWM. Instead of decomposing the voltage vector reference in a sector, i.e. the big purple triangle in

Figure 5-8 (a), the decomposition is done in a subsector, i.e. the much smaller purple triangle in Figure 5-8 (b). Therefore, the jumps between the states in one switching cycle become much smaller when the two-level SVPWM is replaced by the five-level SVPWM.

The algorithm to perform the multilevel SVPWM is similar to the two-level SVPWM. However, two differences should be mentioned if the multilevel SVPWM is conducted compared with the aforementioned two-level SVPWM.

- After rotating the vector into Sector 1, a further detection should be made to locate which subsector, i.e. "small triangle", the voltage vector belongs to. Such subsector detection can be realized by comparing the distances between the voltage reference and the centers of each subsector. The shortest distance indicates the subsector that the voltage reference belongs to. Then a base point should be selected for decomposition. Such base point can be selected in such a way as illustrated in Figure 5-9 (a) where the vertices of triangles are named and the triangles are assigned with their corresponding base points. In each triangle pointing upwards, the base point is the left below point of the triangle, while in each triangle pointing downwards, the base point is the right above point of the triangle. Then, based on the selected base point, a decomposition can be achieved in each subsector similar to the two-level SVPWM as shown in Figure 5-9 (b) and (c).

- Based on the decomposition in the subsector, the required switching states can be decided. Then the corresponding switching intervals can be calculated similarly to the two-level case. In addition, the corresponding voltage space vectors can be assigned and placed in a switching sequence as shown in Figure 5-6.
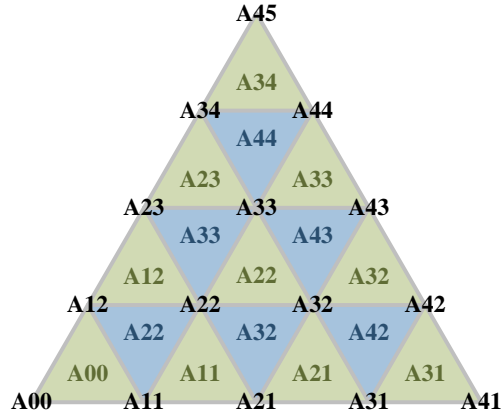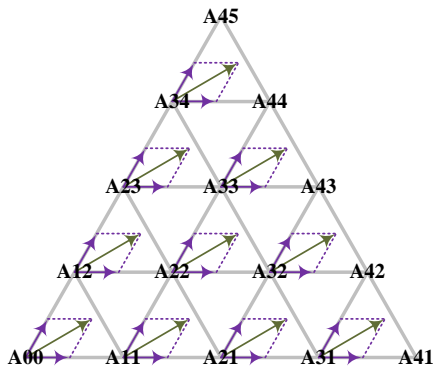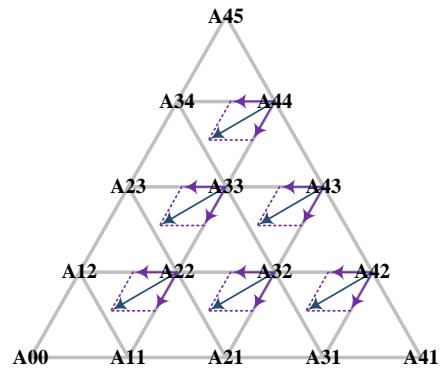
Figure 5-9 Subsector decomposition

(a) Selection of base points

(b) Decomposition in upward pointing triangles (c) Decomposition in downward pointing triangles

Both the two-level and the multilevel SVPWM algorithms can be generalized and shown as a flow chat in Figure 5-10. After the SVPWM algorithm is activated, the voltage reference is firstly converted into per unit system by dividing the voltage reference by the maximum voltage output capability in continuous operation of the inverter. Then the angle of the voltage reference vector is detected and the reference vector is rotated into Sector 1. After that, the decomposition is made and if the multilevel SVPWM is applied, further subsector detection is performed. In the end, switching intervals are determined and the corresponding voltage vectors are assigned so that the switching pattern is decided.
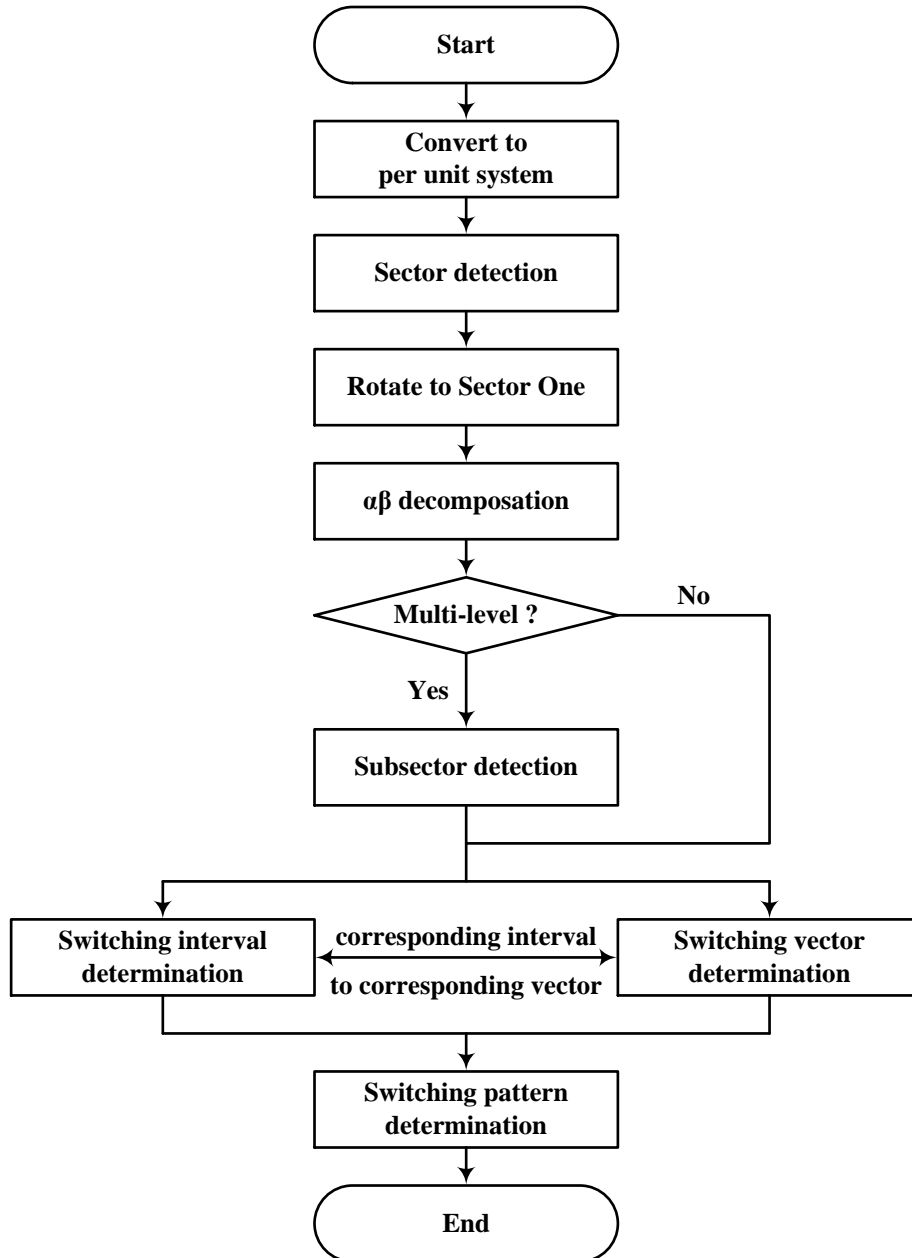
Figure 5-10 General flow chat of SVPWM

5.3   Implementation Aspects

Implementation aspects concerning the current sampling and the controller discretization are considered and discussed in this section.

5.3.1   Current Sampling Technique

Since the current controller is designed to only deal with the fundamental components, it is essential to make sure that the current value input to the controller is the fundamental component regardless of harmonics. The inverter current can be expressed as

$$i_{\text{inv}} = i_{\text{inv}(1)} + \sum i_{\text{inv}(\text{sw})} \tag{5-12}$$

where i_{inv} is the inverter current, $i_{\text{inv}(1)}$ is the fundamental components and $i_{\text{inv}(\text{sw})}$ is the switching harmonic components. Therefore, if the harmonics can be removed, then the fundamental $i_{\text{inv}(1)}$ will be left. A sampling techniques *instantaneous sampling* can be applied [54] which illustrates that if proper sampling points are selected, the sampled values are located right at the average value of each period, and therefore, the current ripples can be eliminated.

The explanation of the *instantaneous sampling* technique in [54] is given as follows. For a Y-connected drive system with neutral point floating, under three-phase load balance, the load phase voltages have the following relationship

$$\begin{cases} u_{An} = u_{AN} - u_{nN} \\ u_{Bn} = u_{BN} - u_{nN} \\ u_{Cn} = u_{CN} - u_{nN} \end{cases} \qquad u_{An} + u_{Bn} + u_{Cn} = 0 \tag{5-13}$$

where u_{An}, u_{Bn} and u_{Cn} are the load phase voltages, u_{AN}, u_{BN} and u_{CN} are the inverter output phase-to-negative voltages and u_{nN} is the neutral-to-negative voltage. Therefore, the neutral-to-negative voltage can be calculated as

$$u_{nN} = \frac{u_{AN} + u_{BN} + u_{CN}}{3} \tag{5-14}$$

If the switching frequency f_{sw} is high enough, then the back-EMF in one switching cycle T_{sw} can be considered as constant and equal to the average load phase voltage. In addition, if the PWM voltage waveform is symmetric in one switching cycle, the voltage and current waveform in one switching cycle can be drawn as shown in Figure 5-11, considering the switching pattern in Figure 5-5 for example.
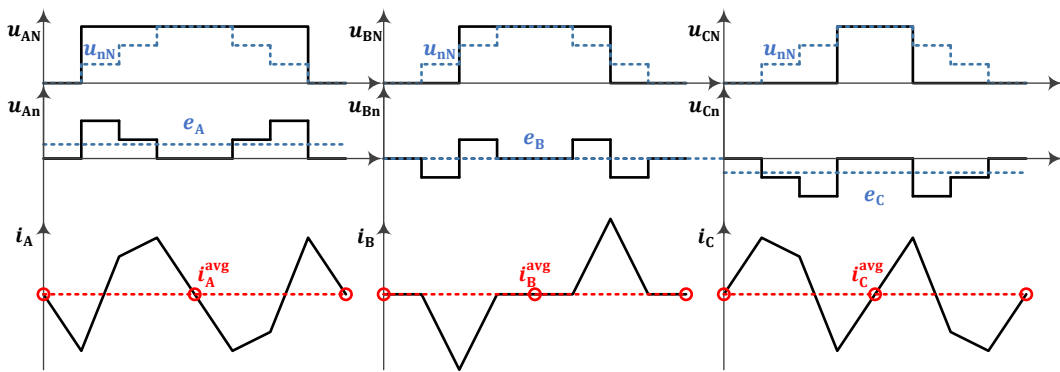
Figure 5-11 Proper sampling point selection

In Figure 5-11, u_{nN} is the unique neutral point voltage among the three phases which is the average of u_{AN}, u_{BN} and u_{CN}. The load phase voltages u_{An}, u_{Bn} and u_{Cn} are the subtraction of u_{AN}, u_{BN} and u_{CN} by u_{nN}. The back-EMFs e_{A}, e_{B} and e_{C} are the

averages of u_{An}, u_{Bn} and u_{Cn} respectively. The differences between u_{An}, u_{Bn} and u_{Cn} and e_{A}, e_{B} and e_{C} are applied on the three-phase load inductors and therefore decide the slopes of the currents i_{A}, i_{B} and i_{C}. The currents i_{A}, i_{B} and i_{C} are shown in the bottom subplots with their averages in one switching cycle. A similar figure is also illustrated in [54]. As can be found out, if the sampling points are located at the ends or the mid points of each switching cycle T_{sw}, then only the fundamental current component will be sampled while the current ripples will be "filtered out" [54]. Both "single sampling" and "double sampling" can be applied. "Single sampling" means that one sample is taken in one switching period, which indicates the sampling frequency equals the switching frequency

$$T_{\mathrm{ctrl}} = T_{\mathrm{sw}} \tag{5-15}$$

where T_{ctrl} indicates the sampling period defined in the controller, while "double sampling" means the sampling is performed at both the midpoint and the end of one switching period which indicates the sampling frequency is twice of the switching frequency

$$T_{\mathrm{ctrl}} = 2T_{\mathrm{sw}} \tag{5-16}$$

5.3.2 Voltage Reference Vector Transformation Angle Compensation

During the switching period T_{sw}, the dq frame rotates from d_1 in the start of the period to d_2 in the end of the period for an angle $\Delta\theta_{\mathrm{r}}$ as shown in Figure 5-12, while the SVPWM switching signals must be generated in one fixed angle during the same period which is the $\hat{\theta}_{\mathrm{r}}$ in Figure 3-1. If the SVPWM switching signals are generated at d_1, then the output will lag the reference since the output is kept at the same direction while the reference rotates forward, and vice versa if the SVPWM switching signals are generated at d_2.
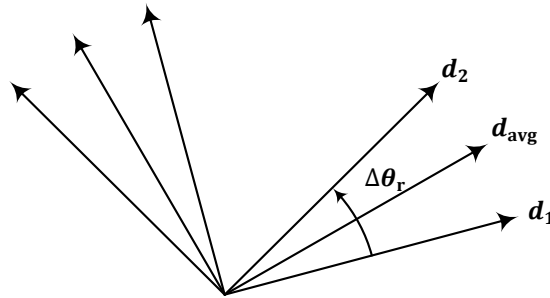
Figure 5-12 Transformation Angle Delay caused by Switching

Therefore, an angle compensation can be performed by calculating the average transformation angle

$$\theta_{\mathrm{r}}^{\mathrm{avg}} = \theta_{\mathrm{r}} + \frac{\Delta\theta_{\mathrm{r}}}{2} = \theta_{\mathrm{r}} + \frac{T_{\mathrm{sw}}\omega_{\mathrm{r}}}{2} \tag{5-17}$$

This averaged transformation angle after such a compensation is going to be utilized in the controller for transforming the voltage reference vector from dq frame to αβ frame. In a real digital controller, since an addition time delay of one switching period is needed to perform all

the calculation in the controller, the compensation angle should be $\frac{3\Delta\theta_r}{2}$ which is $\frac{3T_{sw}\omega_r}{2}$ [55]. However, in the thesis work, since MATLAB holds on the simulation during performing the calculation in the controller, a compensation of $\frac{\Delta\theta_r}{2}$ is needed.

5.3.3 Switching Harmonics and Switching Frequency Selection

This section describes the switching harmonic distribution and the switching frequency selection for a two-level inverter. In order to illustrate the selection of the switching frequency, a frequency modulation index m_f is defined as [56]

$$m_f = \frac{f_{sw}}{f_{(1)}} \tag{5-18}$$

For a single leg of the inverter, any switching harmonic frequency f_h can be expressed as [57]

$$f_h = hf_1 \qquad h = jm_f \pm k \tag{5-19}$$

where f_1 is the fundamental frequency, h is the harmonic order and h can be further expressed as a jth center of m_f and a kth sideband. An odd j corresponds to an even k and an even j corresponds to an odd k. The index m_f is suggested to be an odd integer to result in half-wave symmetry $f(t) = -f\left(t + \frac{T_{(1)}}{2}\right)$ so that the even harmonics are cancelled.

In terms of a three-phase inverter, from the analytical solution of harmonic contents addressed in [57], there is no need to select the m_f as a multiple of three, since the centers of the switching harmonics will be automatically cancelled regardless of the selection of m_f. From [56], it is suggested that for a small m_f ($m_f \leq 21$), *synchronous PWM* should be applied, which means m_f must be an integer throughout the motor start-up in order to avoid subharmonics. In this case, the switching frequencies should be adapted simultaneously as the speed goes up in order to keep m_f as a constant. In contrast, for a large m_f ($m_f > 21$), *synchronous PWM* is not necessary due to the reduction of subharmonics as m_f increases.

In this thesis work, m_f is selected as 21 which is at the boundary of the two cases, so that on one hand, the switching frequency is not too high in the subsea application which would be dangerous to encounter the transmission system resonance, while on the other hand, *non-synchronous PWM* can still be applied to some extent in order to avoid the complex implementation and analysis of *synchronous PWM*. Taking $m_f = 21$ into consideration, a switching frequency $f_{sw} = 4200 \text{ Hz}$ is selected.

6   Transmission System Modelling and Compensation

In the previous chapters, an electric drive system has been described where the inverter is directly connected to the PMSM as shown in Figure 6-1 (a). In this chapter, the step-up transformer and the 15 km long cable will be added between the inverter and the PMSM which is shown in Figure 6-1 (b). The reason why the transformer output current needs to be measured will be explained in Section 6.1.

(a)

(b)
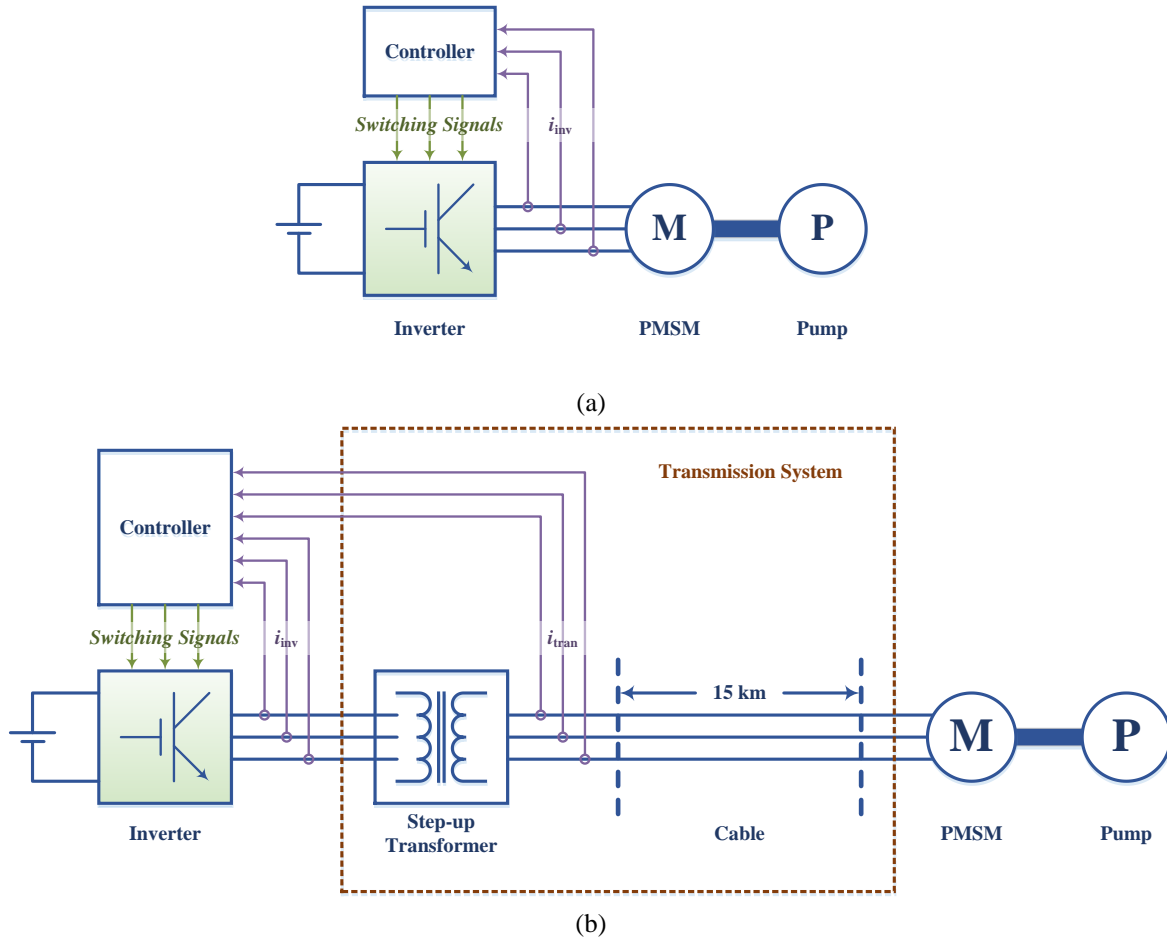
Figure 6-1 The addition of the transmission system in the electric drive system

(a) Electric drive system described in Chapter 3 ~ 5 without the transmission system

(b) Electric drive system to be described in Chapter 6 with the transmission system

In order to achieve a desirable control of the PMSM at the receiving end of the transmission system, the voltage reference given by the current controller should be compensated so that a proper voltage vector is able to reach the terminals of the PMSM. In terms of such compensation, an estimator needs to be implemented in order to get the states of the PMSM electric quantities, based on which, the level of compensation can be decided. In the beginning, a state space model with perfect parameters is designed to provide the controller with dynamic estimations as described in Appendix D. However, when parameter errors are introduced, the implementation of dynamic estimations with state feedbacks is tricky and therefore, only the

steady state quantities are estimated later on, which means a static estimator can be built instead of a dynamic estimator. The performances of both the dynamic estimator and the static estimator are illustrated in Chapter 7. Throughout the modification of the controller, only the current control loop needs to be modified while the speed control loop should be kept untouched, since the restructure of the system only changes the voltage distribution while the mechanical parameters are still the same.
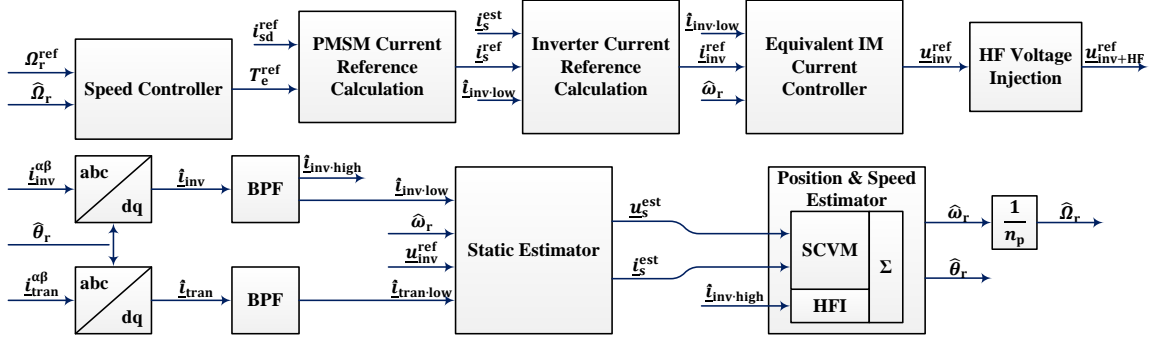
Figure 6-2 Controller configuration for transmission system compensation

Therefore, the controller structure should be changed to be as illustrated in Figure 6-2. In the bottom path of the figure, both the inverter output current $i_{inv}^{\alpha\beta}$ and the transformer output current $i_{tran}^{\alpha\beta}$ are measured and transformed from $\alpha\beta$ frame to dq frame with the help of the estimated rotor angle $\hat{\theta}_r$. Then the two dq frame current signals $\hat{\imath}_{inv}$ and $\hat{\imath}_{tran}$ go through the BPFs to separate the HF components and the fundamental components. The fundamental components $\hat{\imath}_{inv\cdot low}$ and $\hat{\imath}_{tran\cdot low}$ are fed into the static estimator together with the speed estimation and the inverter output voltage reference. The static estimator gives steady state estimation of the PMSM quantities $\underline{u}_s^{est}$ and $\underline{i}_s^{est}$. The HF component $\hat{\imath}_{inv\cdot high}$ goes into the HFI algorithm, while the estimated PMSM quantities $\underline{u}_s^{est}$ and $\underline{i}_s^{est}$ go to the SCVM algorithm, and the two algorithms cooperator together to provide the controller with the speed and angle estimations.

In the top path of Figure 6-2, an inverter current reference calculation is added into the current control loop and the previous PMSM current controller is replaced by an equivalent IM model current controller. The inverter current reference calculation gives the inverter current reference based on the PMSM stator current reference and the shunt current estimation which is calculated from the inverter current and the PMSM stator current estimation. The equivalent IM model current controller tries to follow the inverter current reference which is built by considering the entire circuit including the transformer, the cable and the PMSM to be an equivalent induction motor.

In conclusion, the following modifications are made and the details of the configuration will be explained in this chapter:

- Apart from the inverter current, the transformer output current is measured.

- A static estimator is designed to provide the controller with instantaneous PMSM states.

- An inverter current reference calculation algorithm is designed to generate the inverter current reference based on the PMSM stator current reference.

- The current controller is modified so that it takes the structure of the transmission system into consideration.

6.1 Transformation System Modelling and Static Estimator

As has been described in Chapter 2, the transformer is described as a T-model while the cable is modelled by π-sections. The cable in the circuit is represented by 15 π-sections while the controller views the cable as 1 π-section. The series impedance of the transmission system contributes to a larger voltage drop before the PMSM back-EMF. The shunt admittance contributes to the current leakage from the power transmission path which means that the inverter and the PMSM currents are not really the same.

The added step-up transformer can be divided into two parts, the primary part connected to the inverter and the secondary part connected to the cable. The controller views the entire system from the primary side of the transformer, and therefore, the component parameters on the secondary side should be converted to the primary side by applying
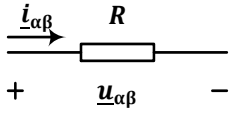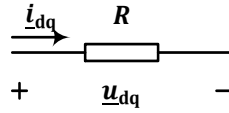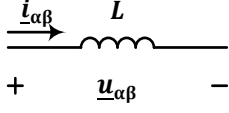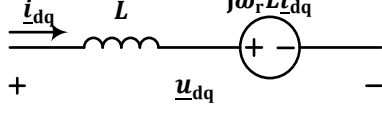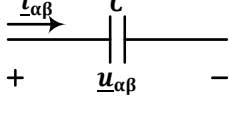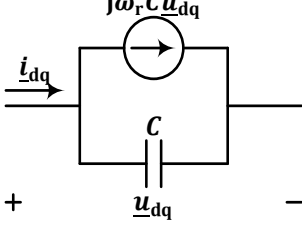
$$\frac{R'}{R} = \frac{N_1{}^2}{N_2{}^2} \qquad \frac{L'}{L} = \frac{N_1{}^2}{N_2{}^2} \qquad \frac{C'}{C} = \frac{N_2{}^2}{N_1{}^2} \qquad (6\text{-}1)$$

where R, L and C are the resistance, inductance and capacitance on the secondary side respectively, R', L' and C' are the corresponding parameters converted to the primary side, and N_1 and N_2 are the numbers of turns on the primary and secondary sides respectively. Since R, L and C are linear components, they satisfy the superposition law, which means the conversion of the entire transmission system from the secondary side to the primary side equals the conversion of each component independently and then composed together as the same circuit from the primary's side of view.

The transmission system is modelled in the αβ frame, and the controller views the entire system in the dq frame. Therefore, in order to describe the transmission system inside the controller, it is necessary to carry out the αβ-dq transformation for the R, L and C components in the transmission system. The transformation is summarized in Table 6-1 where a cross-coupling

voltage source $j\omega L\underline{i}$ appears in series to each inductor L and a cross-coupling current source $j\omega C\underline{u}$ appears in parallel to each capacitor C in the dq frame.

Table 6-1 The R, L and C components described in αβ and dq frames

	αβ Frame	dq Frame
R	$\underline{i}_{\alpha\beta} \rightarrow$ R, $+$ $\underline{u}_{\alpha\beta}$ $-$	$\underline{i}_{dq} \rightarrow$ R, $+$ $\underline{u}_{dq}$ $-$
	$\underline{u}_{\alpha\beta} = R\underline{i}_{\alpha\beta}$	$\underline{u}_{dq} = R\underline{i}_{dq}$
L	$\underline{i}_{\alpha\beta} \rightarrow$ L, $+$ $\underline{u}_{\alpha\beta}$ $-$	$\underline{i}_{dq} \rightarrow$ L $j\omega_r L\underline{i}_{dq}$, $+$ $\underline{u}_{dq}$ $-$
	$\underline{u}_{\alpha\beta} = L\dfrac{d\underline{u}_{\alpha\beta}}{dt}$	$\underline{u}_{dq} = L\dfrac{d\underline{i}_{dq}}{dt} + j\omega_r L\underline{i}_{dq}$
C	$\underline{i}_{\alpha\beta} \rightarrow$ C, $+$ $\underline{u}_{\alpha\beta}$ $-$	$\underline{i}_{dq} \rightarrow$ $j\omega_r C\underline{u}_{dq}$, C, $+$ $\underline{u}_{dq}$ $-$
	$\underline{i}_{\alpha\beta} = C\dfrac{d\underline{u}_{\alpha\beta}}{dt}$	$\underline{i}_{dq} = C\dfrac{d\underline{u}_{dq}}{dt} + j\omega_r C\underline{u}_{dq}$

Based on the summary illustrated in Table 6-1, the entire transmission system in the dq frame with 15 π-sections is shown in Figure 6-3. In steady state, since the dq frame current and voltage derivatives are zero, the terms $L\dfrac{d\underline{i}_{dq}}{dt}$ and $C\dfrac{d\underline{u}_{dq}}{dt}$ will disappear in the equations as

$$\underline{u}_{dq} = L\frac{d\underline{i}_{dq}}{dt} + j\omega_r L\underline{i}_{dq} \xrightarrow{\textit{Steady State}} \underline{u}_{dq} = j\omega_r L\underline{i}_{dq} \tag{6-2}$$

$$\underline{i}_{dq} = C\frac{d\underline{u}_{dq}}{dt} + j\omega_r C\underline{u}_{dq} \xrightarrow{\textit{Steady State}} \underline{i}_{dq} = j\omega_r C\underline{u}_{dq} \tag{6-3}$$

Therefore, in steady state, the inductor can be represented by the voltage source $j\omega L\underline{i}$ while the capacitor can be represented by the current source $j\omega C\underline{u}$. In this way, the static states (steady state quantities) of the PMSM can be calculated from the sending end towards the receiving end of the transmission system by following the circuit in Figure 6-4.
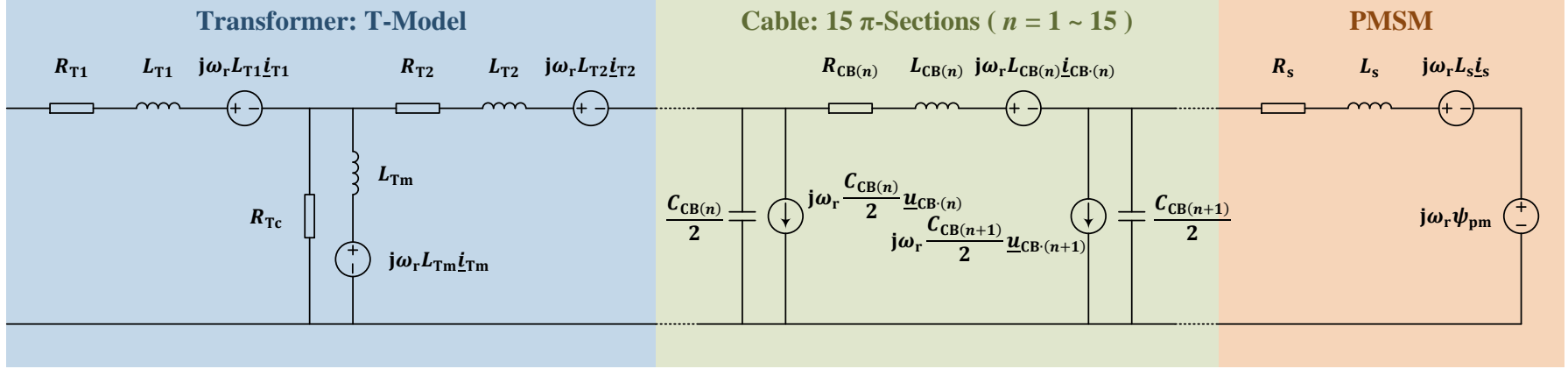
Figure 6-3 Modelling of the transmission system and the PMSM in the real circuit (15 π-sections for the cable modelling)
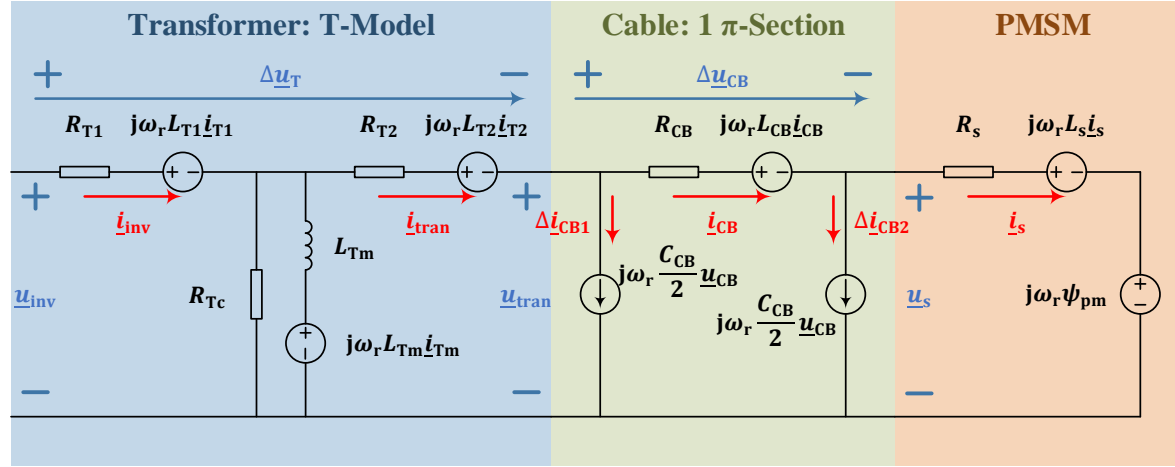
Figure 6-4 Modelling of the transmission system and the PMSM in the static estimator in the controller (1 π-section for the cable modelling)

Detailed illustration of Figure 6-4 can be given as follows. Since the inverter output current $\underline{i}_{inv}$ and the transformer output current $\underline{i}_{tran}$ can be obtained by current measurement, the voltage drop across the transformer $\Delta\underline{u}_T$ can be calculated as the sum of the voltage drops on both sides of the transformer

$$\Delta\underline{u}_T = (R_{T1} + j\omega_r L_{T1}) \cdot \underline{i}_{inv} + (R_{T2} + j\omega_r L_{T2}) \cdot \underline{i}_{tran} \tag{6-4}$$

Since an immediate response of SVPWM can be assumed, the inverter output voltage $\underline{u}_{inv}$ can be assumed to be equal to the inverter output voltage reference $\underline{u}_{inv}^{ref}$. Then the transformer output voltage $\underline{u}_{tran}$ can be calculated as

$$\underline{u}_{tran} = \underline{u}_{inv} - \Delta\underline{u}_T = \underline{u}_{inv}^{ref} - \Delta\underline{u}_T \tag{6-5}$$

Based on $\underline{u}_{tran}$, the shunt current at the sending end of the cable $\Delta\underline{i}_{CB1}$ can be obtained as

$$\Delta\underline{i}_{CB1} = j\omega_r \frac{C_{CB}}{2} \cdot \underline{u}_{tran} \tag{6-6}$$

and the current going through the cable $\underline{i}_{CB}$ can be calculated as

$$\underline{i}_{CB} = \underline{i}_{tran} - \Delta\underline{i}_{CB1} \tag{6-7}$$

Further, by taking the voltage drop across the cable

$$\Delta\underline{u}_{CB} = (R_{CB} + j\omega_r L_{CB}) \cdot \underline{i}_{CB} \tag{6-8}$$

into consideration, the voltage at the terminals of the PMSM $\underline{u}_s$, i.e. the voltage at the receiving end of the cable, can be obtained as

$$\underline{u}_s = \underline{u}_{CB1} - \Delta\underline{u}_{CB} \tag{6-9}$$

The leakage current at the PMSM terminals $\Delta\underline{i}_{CB2}$ can be calculated as

$$\Delta\underline{i}_{CB2} = j\omega_r \frac{C_{CB}}{2} \cdot \underline{u}_s \tag{6-10}$$

giving the PMSM stator current $\underline{i}_s$ as

$$\underline{i}_s = \underline{i}_{CB} - \Delta\underline{i}_{CB2} \tag{6-11}$$

Up to here, from (6-4) to (6-11), the static estimation of the PMSM stator voltage $\underline{u}_s$ and current $\underline{i}_s$ is done.

However, the application of such static estimation can hardly be applied to the transformer inductive shunt branch L_{Tm}, since in the simulation, it makes the control system unstable. The explanation may be that the transients of the inductive shunt branch current cannot be neglected. This result indicates that other solutions should be searched for in order to solve this problem. One solution can be that a reliable state space model should be built with a proper feedback, so that all the states of the circuit can be observed instantaneously. An alternative is to skip the

estimation of the inductive shunt branch by adding an additional current measurement point after the transformer so that the transformer output current can be directly measured instead of being estimated inside the controller. In this thesis work, since a complexity appears during the discretization of the state space model which is out of the scope of the thesis, an additional current measurement point at the secondary side of the transformer is added as shown in Figure 6-1 (b).

6.2 Current Control Loop Modifications

In Section 6.1, the estimation of the PMSM stator voltage and current has been implemented. The next issue is to make the current control loop operate properly with the help from the static estimator in order to deliver a suitable voltage vector to the PMSM stator so that the PMSM stator current can follow the reference. Two basic ideas are available to make the current control loop modifications:

- The current controller can be the same as the previous PMSM current controller which decides the PMSM stator voltage reference $\underline{u}_s^{\text{ref}}$ to make the PMSM stator current follow the reference. The PMSM current can be estimated by the static estimator and the PMSM stator voltage reference $\underline{u}_s^{\text{ref}}$ needs to be compensated by predicting a voltage drop across the transmission system to become $\underline{u}_{\text{inv}}^{\text{ref}}$.

- The previous PMSM current controller can be modified to be an inverter current controller so that the inverter output current $\underline{i}_{\text{inv}}$ can be controlled directly by applying a suitable inverter output voltage $\underline{u}_{\text{inv}}^{\text{ref}}$. In this case, the PMSM stator current reference $\underline{i}_s^{\text{ref}}$ needs to be compensated to an inverter current reference $\underline{i}_{\text{inv}}^{\text{ref}}$ by taking the shunt currents into consideration.

In this thesis work, the second option is preferred because the inverter can be heated up much more quickly than the PMSM due to the much lower mass of the inverter. Hence it is safer to make the inverter output voltage and current under direct control so that any possible damage can be prevented. Therefore, an inverter current reference calculation block will be created and modifications to the current controller will be made in order to control the inverter current directly as will be shown in the following sections.

6.2.1 Inverter Current Reference Calculation

The task of the inverter current reference calculation block is to calculate the inverter current reference $\underline{i}_{\text{inv}}^{\text{ref}}$ by adding the estimated total shunt current $\underline{i}_{\text{shunt}}^{\text{est}}$ to the PMSM stator current

reference $\underline{i}_{s}^{\mathrm{ref}}$. The total shunt current $\underline{i}_{\mathrm{shunt}}^{\mathrm{est}}$ is further estimated by the subtraction of the measured inverter current by the estimated PMSM stator current. Since the shunt current estimation may be fluctuating which may further affect the current controller, an LPF is necessary to filter out the high frequency components in the shunt current estimation. The inverter current reference is calculated as

$$\underline{i}_{\mathrm{inv}}^{\mathrm{ref}} = \underline{i}_{s}^{\mathrm{ref}} + \mathrm{LPF}\{\underline{i}_{\mathrm{shunt}}^{\mathrm{est}}\} = \underline{i}_{s}^{\mathrm{ref}} + \mathrm{LPF}\{\underline{i}_{\mathrm{inv}} - \underline{i}_{s}^{\mathrm{est}}\} \tag{6-12}$$

where $\underline{i}_{s}^{\mathrm{est}}$ is calculated by (6-11).

6.2.2   Current Controller Modifications

The previously applied IMC method for the PMSM current controller is still utilized in designing this modified version of the current controller. However, the complicated structure of the system is not suitable to directly perform the same procedure of IMC. Therefore, the resistive shunt branch of the transformer and the capacitive shunt branches of the cable are neglected in order to achieve a simpler structure of the circuit which is shown in Figure 6-5. Such neglected terms will appear as unexpected disturbances to the control loop which hopefully would be taken care of by the robustness of the IMC method.
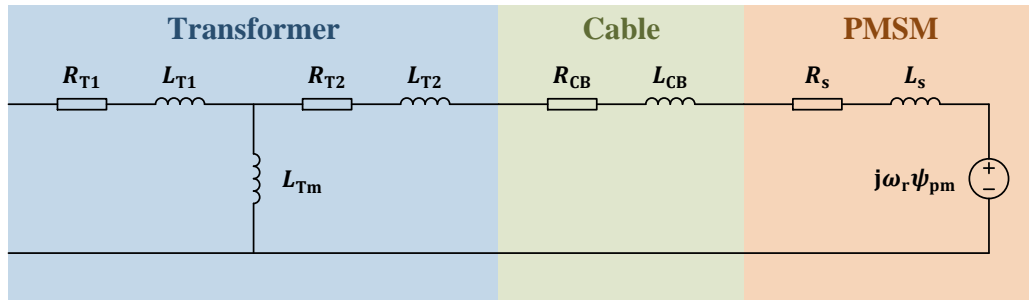
Figure 6-5 Equivalent T model of the transmission system and the PMSM

In Figure 6-5, the secondary side impedance of the transformer, the cable impedance and the PMSM stator impedance can be summed together and an equivalent T model of the circuit can be realized as shown in Figure 6-6 (a). The equivalent parameters in Figure 6-6 (a) can be calculated from the parameters in Figure 6-5 as

$$R_1 = R_{\mathrm{T1}} \qquad R_2 = R_{T2} + R_{\mathrm{CB}} + R_{\mathrm{s}} \tag{6-13}$$

$$L_1 = L_{\mathrm{T1}} \qquad L_{\mathrm{m}} = L_{\mathrm{Tm}} \qquad L_2 = L_{T2} + L_{\mathrm{CB}} + L_{\mathrm{s}} \tag{6-14}$$

where L_{s} is an equivalent PMSM stator inductance and will be explained as follows.

For a salient PMSM, $L_{\mathrm{sd}} \neq L_{\mathrm{sq}}$, which separates the equivalent circuit into a d-axis circuit and a q-axis circuit. However, since L_{sd} and L_{sq} are in series with L_{CB} and L_{T2}, in terms of the

entire secondary d-axis inductance L_{2d} and the entire secondary q-axis inductance L_{2q}, the difference will be minor

$$L_{T2} + L_{CB} + L_{sd} = L_{2d} \quad \approx \quad L_{2q} = L_{T2} + L_{CB} + L_{sq} \tag{6-15}$$

Hence the salience can be neglected when the entire circuit is considered for the current controller design and an equivalent stator inductance L_s can be defined by taking the average of L_{sd} and L_{sq},

$$L_s = \frac{L_{sd} + L_{sq}}{2} \tag{6-16}$$

It should be pointed out that, such an equivalent stator inductance L_s is only utilized in the design of the modified current controller, while in other parts of the controller, L_{sd} and L_{sq} are still used instead of L_s.

This equivalent T model in Figure 6-6 (a) is similar to a T model of an induction motor. Therefore, similar transformation can be applied to convert the T model in Figure 6-6 (a) to an inverse-Γ model in Figure 6-6 (b) [58].

(a)   (b)
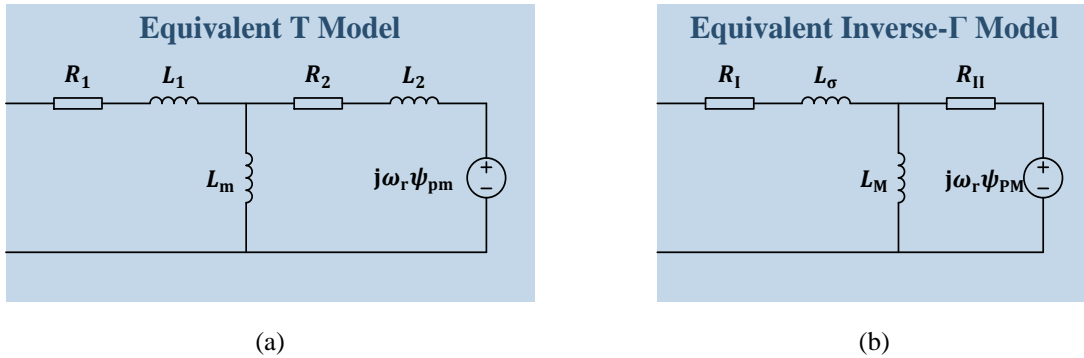
Figure 6-6 Equivalent models of the transmission system and the PMSM

(a) Equivalent T model   (b) Equivalent inverse-Γ model

The derivation of the transformation from the T model to the inverse-Γ model is available in Appendix E, and the calculation formulas of the converted parameters are summarized below. The conversion starts with a definition of a scaling factor

$$b = \frac{L_m}{L_2} \tag{6-17}$$

Then, the inverse-Γ model parameters in Figure 6-6 (b) are defined by the T model parameters in Figure 6-6 (a) along with the help of the scaling factor b as

$$R_I = R_1 \quad L_M = bL_m \quad L_\sigma = L_1 - L_M \quad R_{II} = b^2 R_2 \quad \underline{\psi}_{PM} = b\underline{\psi}_{pm} \tag{6-18}$$

Up to here, all the parameters in the inverse-Γ model shown in Figure 6-6 (b) have been defined. Thereafter, the IMC method can be applied to design a current controller for such an equivalent IM described by the inverse-Γ model. Similar design process is performed as the previous PMSM current controller design in Section 3.2.2. The active damping term and the PI regulator gains for the equivalent IM current controller can be selected as

$$R_a = \alpha_c L_\sigma - R_I - R_{II} \tag{6-19}$$

$$k_{cp} = \alpha_c \cdot L_\sigma \qquad k_{ci} = \alpha_c{}^2 \cdot L_\sigma \tag{6-20}$$

6.3 Position Estimator Modifications

6.3.1 SCVM

After adding the transmission system into the circuit, the SCVM still targets the original PMSM instead of the equivalent IM defined in Section 6.2.2. Therefore, the SCVM algorithm is kept the same as the previous SCVM implementation in Section 4.2. The PMSM stator current and voltage is calculated by the static estimator. The speed and angle estimations are calculated as

$$\begin{bmatrix} \hat{e}_d \\ \hat{e}_q \end{bmatrix} = \begin{bmatrix} \hat{u}_{sd} \\ \hat{u}_{sq} \end{bmatrix} - \begin{bmatrix} \hat{R}_s & -\hat{\omega}_r \hat{L}_{sq} \\ \hat{\omega}_r \hat{L}_{sd} & \hat{R}_s \end{bmatrix} \begin{bmatrix} \hat{\imath}_{sd} \\ \hat{\imath}_{sq} \end{bmatrix} \tag{6-21}$$

$$\hat{\omega}_r = \frac{\hat{e}_q - \lambda \, \mathrm{sign}(\hat{\omega}_r) \, \hat{e}_d}{\psi_{pm}} \qquad \hat{\theta}_r = \int \hat{\omega}_r \mathrm{d}t \tag{6-22}$$

As can be noticed in (6-21), the steady state equations for the PMSM are used to calculate the back-EMF of the PMSM from the stator voltage and current. By using the static estimator, this is expanded to calculate the steady state back-EMF from the inverter voltage and the current instead. From the estimated steady state back-EMF, the speed and angle of the PMSM are estimated with the same SCVM equations.

6.3.2 HFI

The Bold diagrams and the resonance frequencies of the series-connected circuit including the transmission system and the PMSM are illustrated in Figure 2-8 and Table 2-6 respectively. In order to apply the HFI method successfully, a suitable selection of the HFI operation frequency region should be done. Four criteria should be fulfilled for such a selection of frequency interval in the αβ frame by referring the Bode diagram in Figure 2-8:

- The interval must skip the resonance frequencies.

- The phase response within the interval must be close to -90°.

- The magnitude response during the interval must not be too small. Otherwise, a really high HF voltage needs to be injected to get a suitable HF current which will exceed the output capability of the inverter.

- The interval must be longer than 200 Hz so that it can cover the fundamental frequency during the entire PMSM start-up.

By taking the above four criteria into consideration, an injection frequency of 400 Hz is a possible choice, which means during the start-up, the HF signal will appear within 400 ~ 600 Hz in the αβ frame.

The remaining problem is to decide the scaling factor after the demodulation process in HFI. In the original HFI method, the scaling factor $\frac{U_{\mathrm{HF}}}{\omega_{\mathrm{HF}}} \frac{L_\Delta}{L_{\mathrm{sd}} L_{\mathrm{sq}}}$ shown in Figure 4-3 is based on the derivation in (4-29). Now since the structure of the system has been changed, the derivation needs to be performed again.

Following the original idea of the HFI method, in the high frequency region, the minor effects from the series resistance, the back-EMF term and the cross-coupling terms in the dq frame are not considered. In addition, the shunt branch inductance and resistance of the transformer are assumed to be high enough so that they can be neglected in order to simplify the circuit even more. By taking the above two points into consideration, the simplified circuit is drawn as shown in Figure 6-7.
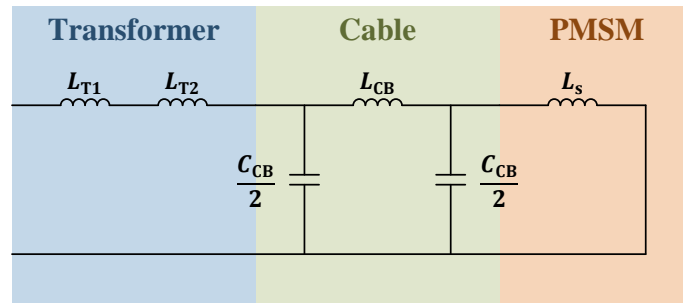
Figure 6-7 Simplified circuit for deriving the HFI equation with the transmission system

The complete transfer function in the high frequency region corresponding to the circuit shown in Figure 6-7 becomes

$$G(s) = \frac{C_{\mathrm{CB}}^2 L_{\mathrm{CB}} L_{\mathrm{s}} s^4 + 2C_{\mathrm{CB}}(L_{\mathrm{CB}} + 2L_{\mathrm{s}})s^2 + 4}{C_{\mathrm{CB}}^2 L_{\mathrm{CB}} L_{\mathrm{T}} L_{\mathrm{s}} s^5 + 2C_{\mathrm{CB}}(L_{\mathrm{CB}} L_{\mathrm{T}} + L_{\mathrm{CB}} L_{\mathrm{s}} + 2L_{\mathrm{T}} L_{\mathrm{s}})s^3 + 4(L_{\mathrm{CB}} + L_{\mathrm{T}} + L_{\mathrm{s}})s} \quad (6\text{-}23)$$

Thereafter, since the injection frequency 400 Hz is a relatively low frequency, all the high order terms in (6-23) can be assumed to be zero which yields

$$G(s) \approx \frac{4}{4(L_{CB} + L_T + L_s)s} = \frac{1}{s(L_T + L_{CB} + L_s)} = \frac{1}{sL_{eq}} \tag{6-24}$$

where $L_{eq} = L_T + L_{CB} + L_s$ is the equivalent inductance which is defined in d- and q-axis separately

$$L_{eq \cdot d} = L_T + L_{CB} + L_{sd} \qquad L_{eq \cdot q} = L_T + L_{CB} + L_{sq} \tag{6-25}$$

The old scaling factor $\frac{U_{HF}}{\omega_{HF}} \frac{L_\Delta}{L_{sd}L_{sq}}$ is then replaced by the equivalent new scaling factor

$\frac{U_{HF}}{\omega_{HF}} \frac{L_\Delta}{L_{eq \cdot d}L_{eq \cdot q}}$ which is defined by the equivalent inductance $L_{eq \cdot d}$ and $L_{eq \cdot q}$. Therefore,

similar to (4-29), the new equation to express the HF q-axis current is

$$i_{eq \cdot qh}^{\hat{r}} = \frac{U_{HF}}{\omega_{HF}} \frac{L_\Delta}{L_{eq \cdot d}L_{eq \cdot q}} \sin 2\tilde{\theta}_r \sin \omega_{HF} t \tag{6-26}$$

where the inductance difference L_Δ is still kept the same, since the difference between the d- and q-axis inductances is unchanged. The same configuration is applied for the demodulation process and the PLL-type estimator as the original HFI estimation algorithm.

As can be found out that, throughout the entire derivation, the key point to apply HFI in the new system is the way to calculate the equivalent inductance $L_{eq \cdot d}$ and $L_{eq \cdot q}$. In order to roughly verify whether the approximation is accurate or not, a comparison between the Bode diagram based on the real system transfer function in (6-23) and the Bode diagram based on the approximated transfer function in (6-24) is shown in Figure 6-8.

In Figure 6-8, the responses from real system transfer function are denoted as d-axis and q-axis while the responses from approximated transfer function are denoted as d-axis-ctrl and q-axis-ctrl. Figure 6-8 (a) can provide a general feeling of how the approximation works. The approximated responses are straightly decaying lines throughout the spectrum and need to almost intersect the real system responses in the corresponding operation frequency region. Figure 6-8 (b) is the zoomed-in plot of Figure 6-8 (a) which covers the range of the operation region. As can be seen in Figure 6-8 (b), both the magnitude and phase responses of the approximated transfer function are quite close to the ones of the real system transfer function. In addition, the magnitude responses are around zero and the phase responses are close to -90°. Therefore, it can be concluded that all of the four criteria are fulfilled and the approximated system transfer function is relatively accurate compared with the real system transfer function.
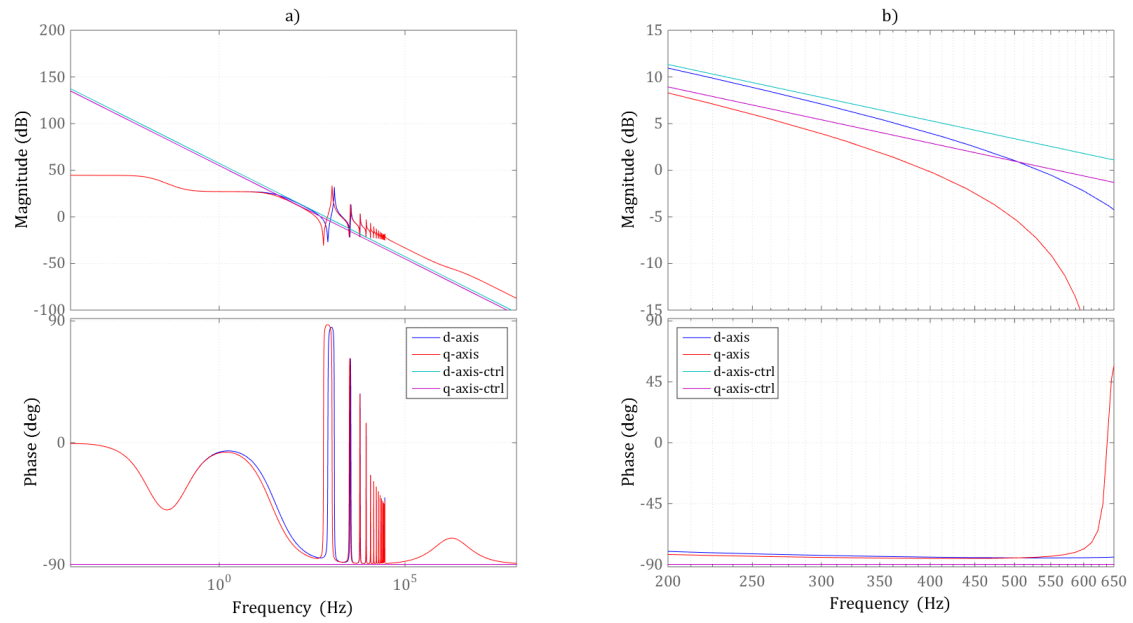
Figure 6-8 Comparison between the real system transfer function (the d-axis and q-axis curves) and the simplified system transfer function (the d-axis-ctrl and q-axis-ctrl curves) in Bode diagram

(a) Comparison from low frequency region   (b) Zoomed-in of the comparison

until high frequency region   from 200 Hz and 650 Hz

71

7 Simulation Results

The simulation results and the corresponding discussions are presented in this chapter. Figure 7-1 shows the implementation of the simulation models in Simulink, where the controller and the pump function are built by Simulink fundamental blocks, while the electric circuit including the inverter, the transformer, the cable and the PMSM are built by *SimPowerSystems* blocks.
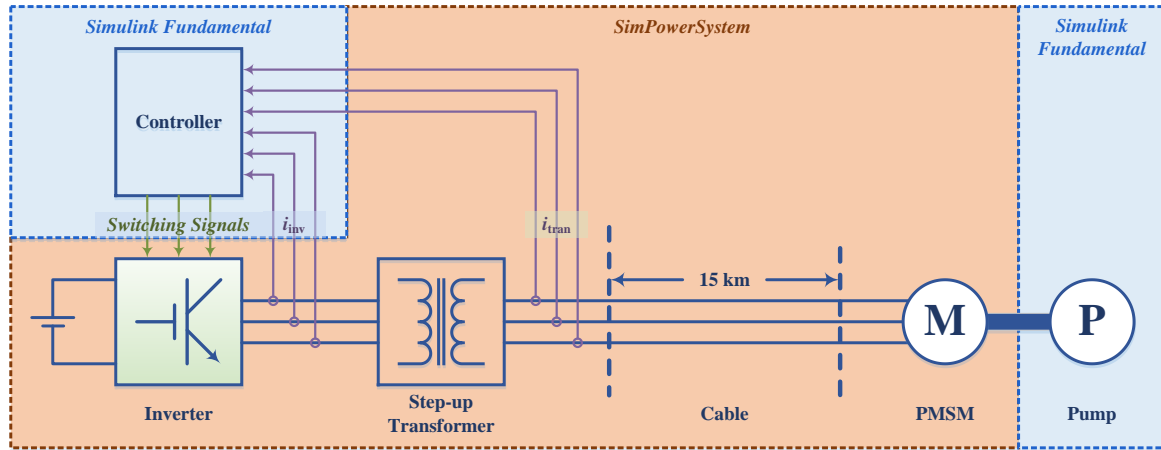
Figure 7-1 Simulation model implementation

In Simulink, the global solver sets the configuration for all standard blocks provided by Simulink, while the powergui solver only sets the configuration for *SimPowerSystems* blocks. The overall configuration is listed in Table 7-1 and the explanation is attached in Appendix F.

Table 7-1 Simulink configuration

Global Solver	Solver type	Variable-step
	Solver	Continuous solver: ode45
	Zero-crossing detection	Non-adaptive
Powergui Solver	Solver type	Continuous
	Ideal Switch	No snubber circuit

This simulation result chapter is formed in a sequence which follows the modelling sequence as shown in Table 1-1. In the beginning, the PMSM is directly connected to the inverter without the transmission system which corresponds to Model 1 to 3:

- PMSM current and speed controllers (Model 1)

- Sensorless control (Model 2)

- SVPWM (independent model)

- Realistic converter with digital control (Model 3)

In Model 1, the PMSM current and speed controllers are tested with an ideal inverter in order to verify the performance of the original IMC design. Then in Model 2, the sensorless control algorithms, including SCVM and HFI together with their combination, are implemented also with the ideal inverter. The SVPWM test after Model 2 is a necessary preparation for the

implementation of the realistic inverter in Model 3. The SVPWM is tested in an independent circuit which has no relationship with other models. Such a SVPWM test makes a comparison of the harmonic distribution between the two-level and five-level SVPWM and can provide a possible improvement for the performance of the inverter which may be essential for the models afterwards. Then in Model 3, the controller is discretized and the realistic inverter is applied which is modulated by the SVPWM technique.

Model 4 to 6 have the same structures as Model 1 to 3 respectively and the only difference is that Model 4 to 6 consider the series impedance of the transmission system which can be integrated into the series-connected stator impedance of the PMSM. The start-up of the PMSM in Model 4 to 6 requires a higher voltage level from the inverter while other details are almost the same. Therefore, Model 4 to 6 are not interesting enough for presentation. Model 7 to 9 are decided to be shown on the next step in which the control structures are similar to Model 1 to 3 but include the entire transmission system, i.e. both the series impedance and the shunt admittance. The models are used to investigate:

- Equivalent IM current and speed controllers with transmission system (Model 7)

- Sensorless control with transmission system (Model 8)

- Realistic converter with digital control with transmission system (Model 9)

In the end, the robustness of the final model, i.e. Model 9, will be tested by introducing parameter errors. Thereafter, conclusions can be made to summarize the study.

7.1 PMSM Current and Speed Controllers (Model 1)

In this section, the PMSM current and speed controllers are tested in order to verify the performance of the original IMC design. Therefore, in the simulation here, the PMSM is directly connected to the inverter, which means the transmission system is not included. Based on the information in Section 3.1, the bandwidths of the current and speed control loops are finally selected and listed in Table 7-2. The corresponding rise times are also calculated based on (3-1).

Table 7-2 Bandwidths in the controller

Parameters	Symbols	Bandwidths		Rise time
		[Hz]	[rad/s]	[ms]
Current Controller	α_c	100	200π	3.5
Speed Controller	α_ω	1	2π	350

As has been illustrated in Section 3.2, the current controller is composed by the PI regulator, the feedforward terms, the active damping terms and the anti-windup algorithm as shown in Figure 3-2 and Figure 3-3. Speed control is applied in the simulation so that both the speed and current control loops show their performance.

The speed, torque and dq frame quantities of the test are shown in Figure 7-2, where a speed step reference of 6000 rev/min is given at 0.1 s to test the speed control loop and the q-axis

current control loop, while a d-axis current step reference of -10 A is given at 4 s to test the d-axis current control loop.
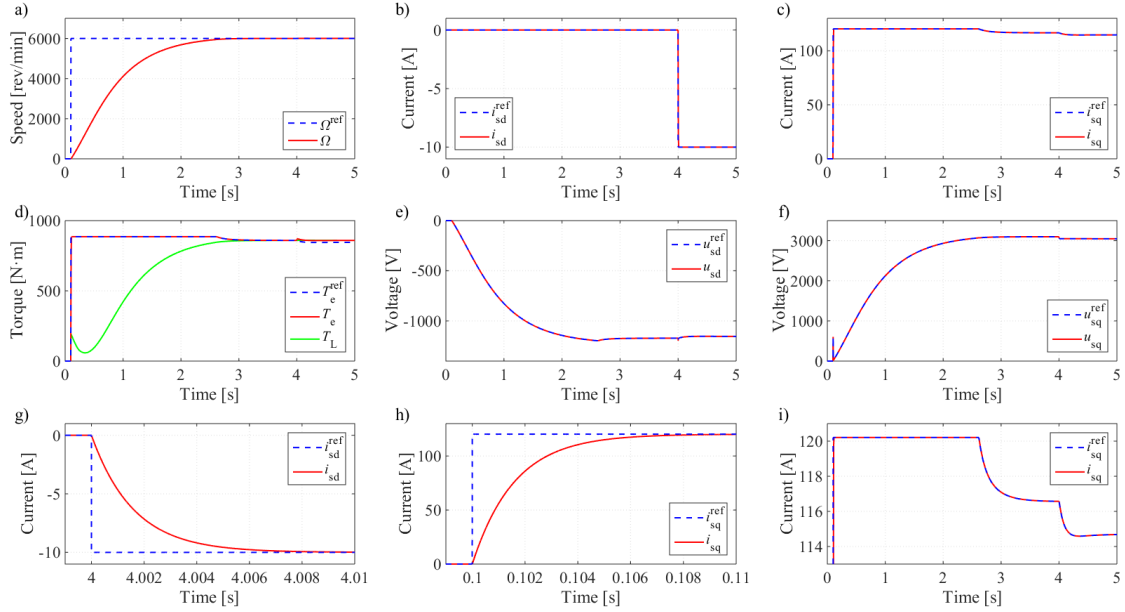
Figure 7-2 Speed control performance (Model 1): speed, torque and dq quantities

a) rotor speed	b) d-axis current	c) q-axis current
d) torque	e) d-axis voltage	f) q-axis voltage
g) d-axis current rise	h) q-axis current rise	i) q-axis current zoomed-in

In the beginning, the PMSM stands still until the speed step reference of 6000 rev/min is applied at 0.1 s as can be seen in Figure 7-2 (a). The q-axis current and the electromagnetic torque response almost immediately and hit the limits as can be seen from (c) and (d). As the PMSM begins to accelerate, the pump torque changes as the pump torque-speed characteristic in Figure 2-10. The q-axis voltage shown in (f) goes up to support the q-axis current and to compensate for the back-EMF and the voltage across the q-axis stator resistance. The d-axis current in (b) is kept at zero before the d-axis current step as expected since no field current is needed. However, the d-axis voltage in (e) deviates from zero as it needs to compensate for the cross-coupling term. When the speed is about to catch the reference, the speed error is not significant enough so that the q-axis current reference leaves the saturation at around 3 s as clearly shown in the zoomed-in plot in (i). Finally, the PMSM speed catches the reference within 4 s.

At 4 s when the PMSM has entered steady state, a d-axis current step reference of -10 A is given. As can be detected in (i), the q-axis current decreases since a negative d-axis current can contribute to an increase of electromagnetic torque as shown in (2-13), which means less q-axis current is needed. In addition, as shown in (d), the electromagnetic torque starts to deviate from the reference since the configuration of the current reference calculation is based on zero d-axis current in (3-12). In other words, the electromagnetic torque reference only indicates the q-axis current reference by assuming zero d-axis current.

Table 7-3 The rise times of current and speed in simulation

	$t_{10\%}$	$t_{90\%}$	$t_{\text{rise}}^{\text{sim}} = t_{90\%} - t_{10\%}$	$t_{\text{rise}}^{\text{thr}} = \dfrac{\ln 9}{\alpha}$
i_{sd}	0.1002 [s]	0.1037 [s]	3.5 [ms]	3.5 [ms]
i_{sq}	4.0002 [s]	4.0037 [s]	3.5 [ms]	
Ω_{r}	0.2254 [s]	1.6771 [s]	14517 [ms]	350 [ms]

The zoomed-in plot of the d- and q-axis current rises are shown in (d) and (e) respectively. The rise times of the current and the speed are measured and listed in Table 7-3. In the table, $t_{10\%}$ and $t_{90\%}$ are the time instants when the corresponding quantities rise up to 10% and 90% of the steady state value, $t_{\text{rise}}^{\text{sim}}$ is the rise time measured from simulation and $t_{\text{rise}}^{\text{thr}}$ is the rise time calculated by the bandwidth in theory. The current rise times satisfy the bandwidths which indicates the PI regulator and feedforward terms work perfectly. However, the speed rise time cannot satisfy the bandwidth, which means there is a deviation from the design. This phenomenon is due to two reasons:

- The current hits the limit which means not enough current is injected into the PMSM as expected from the speed controller. In other words, the speed control loop is cut off during the saturation of the current.

- Only the PMSM viscous constant is considered as the load torque during the speed controller design while the pump torque is regarded as a disturbance which is out of the initial expectation of the speed controller IMC design.

Among the above two points, Point One contributes to the deviation in the current saturation interval, while Point Two contributes to the deviation in the current non-saturation interval. Point Two can be overcome by adding a feedforward term based on a detailed function of the load, but since most of the start-up time belongs to the current saturation interval, Point One is the major reason and there is no need to implement such improvement for Point Two.

Figure 7-3 shows the three-phase currents and voltages, along with the motor power consumption and power factor. Both currents and voltages have a perfect sinusoidal form with a frequency of 200 Hz in steady state as shown in (b) and (e). As expected, the motor consumes an active power of about 540 kW in steady state, only a little higher than the mechanical power, which seems to indicate a high efficiency of the drive system. However, it should be pointed out that the iron-core loss is not included in the PMSM model in this work as can be noticed in Figure 2-3. The power factor decreases in (f) as the q-axis current goes up since the stator inductance consumes more reactive power with an increasing current. It can be concluded that both the current and speed controller can give expected performance and can accelerate the PMSM to 6000 rev/min with expected motor power consumption and time limit.
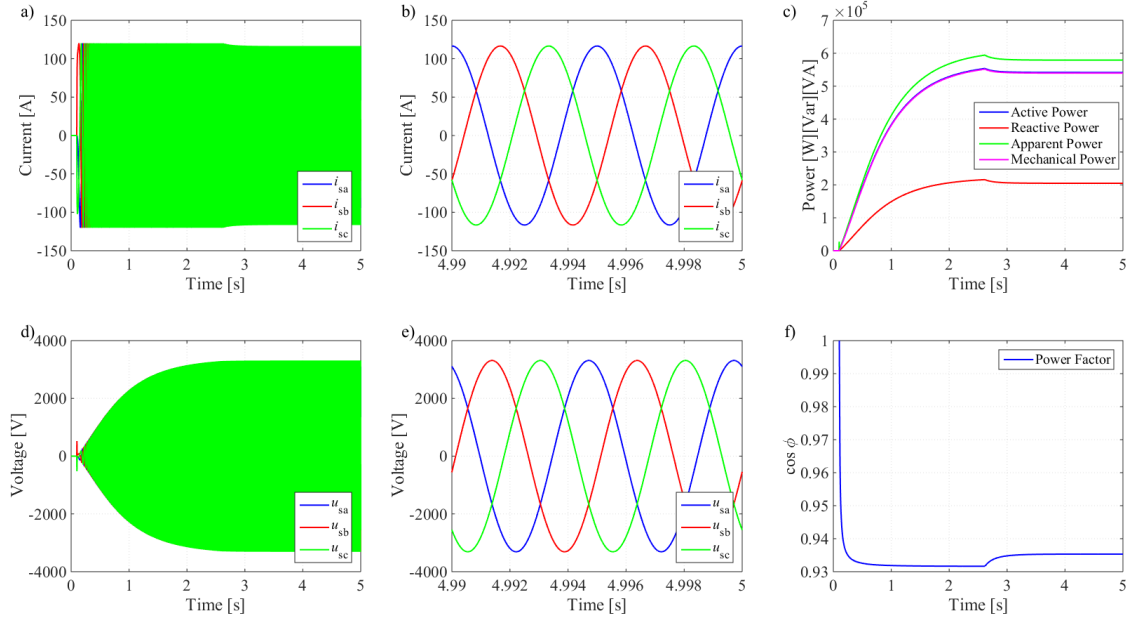
Figure 7-3 Speed control performance (Model 1): abc quantities and motor power consumption

a) abc currents	b) abc currents	c) motor power consumption
d) abc voltages	e) abc voltages	f) power factor

The electromagnetic power p_mec, active power p, reactive power q, apparent power s and power factor $\cos\varphi$ in Figure 7-3 are calculated as

$$p_\mathrm{mec} = T_\mathrm{e}\Omega_\mathrm{r} \tag{7-1}$$

$$p = u_\mathrm{a}i_\mathrm{a} + u_\mathrm{b}i_\mathrm{b} + u_\mathrm{c}i_\mathrm{c} \tag{7-2}$$

$$q = u_\mathrm{cb}i_\mathrm{a} + u_\mathrm{ac}i_\mathrm{b} + u_\mathrm{ba}i_\mathrm{c} \tag{7-3}$$

$$s = \sqrt{p^2 + q^2} \tag{7-4}$$

$$\cos\varphi = \frac{p}{s} \tag{7-5}$$

It should be pointed out that the electromagnetic power p_mec is the power output from the electric system to the mechanical system instead of the shaft power which is the electromagnetic power subtracting the friction power loss of the PMSM.

7.2 Sensorless Control (Model 2)

The angle and speed feedbacks are replaced by sensorless estimator in this case while the PMSM is still connected to the inverter directly without the transmission system in the between.

7.2.1 HFI Method

The structure of the HFI estimator has been presented in Chapter 4.3, but as has been indicated at the end of the chapter, the decision of the suitable estimator parameters needs to be done by

a trial-and-error process. Therefore, a tuning strategy is presented in the beginning of the section followed by the simulation results.

Tuning Strategy

Step 1: Tune the BPF before the current controller

As shown in Figure 4-3, a BPF is used to separate the HF signal and the fundamental frequency signal. A suitable bandwidth of such BPF should be selected to make sure that the HFI does not disturb the current controller too much.

- Disconnect the estimator and feed the controller with the actual speed and angle. Apply current control.

- Adjust the BPF to make sure that the d- and q-axis currents follow the references as first-order systems with the correct rise times.

- Adjust the BPF to limit the d- and q-axis voltage reference oscillations within at most 10% of the injected HF voltage. Otherwise, the injected HF voltage signal will be phase shifted and a phase shift will appear in the resulted HF current signal. Then the estimated angle will be disturbed.

Step 2: Tune the LPF and the PI regulator in the estimator

As shown in Figure 4-3, an LPF is used in the demodulation process and a PI regulator is applied to eliminate the angle estimation error to zero. As has been illustrated in Section 4.3.3, the LPF and the PI regulator can be integrated as one closed-loop transfer function in (4-47). Here, the triple pole p of such an integrated transfer function should be selected.

- Connect the estimator and lock the PMSM speed to a constant value. The lock of the PMSM speed can be done by set the PMSM speed derivative to be zero in the PMSM s-function which is attached in Appendix A. Also set the integrator of the PI regulator in the HFI estimator to be the speed reference. Apply current control to test whether the HFI estimator can follow a constant speed and reject the disturbance to some level:

  ➢ Apply a current step.

  ➢ Inject an angle step disturbance of about 10 degrees.

- Adjust the triple pole p of the integrated transfer function and make sure that the estimator can follow the real speed and angle.

Step 3: Speed control

The speed control loop can be added after the aforementioned current control tests, where the current controller and the estimator can be considered to be cooperating properly already. From (2-13), the torque and speed oscillations can be detected since the electromagnetic torque is related to both d- and q-axis currents.

77

From the principle of HFI, at least one of the d- and q-axis currents will oscillate. The oscillating current will generate an oscillating torque and consequently an oscillating speed as well. This may cause *consecutive zero-crossings* of the speed in the beginning of the PMSM start-up. The solution is to apply a higher current loop bandwidth and a higher current reference ramp slope to make the electromagnetic torque go up and overwhelm the pump torque swiftly.

Table 7-4 The selected HFI parameters in this work

Parameter		Symbol	Expression	Value
Injected frequency		f_{HF}		1000 Hz
Injected amplitude		U_{HF}	$U_{ph\cdot rms} \times 10\%$	242.49 V
BPF bandwidth		β_{BPF}		500 Hz
Closed-loop transfer function pole		p		60 Hz
LPF bandwidth		α_{LPF}	$3p$	180 Hz
PI regulator	Proportional gain	k_p	p	60
	Integral gain	k_i	$\dfrac{p^2}{3}$	1200

In the end, the parameters in Table 7-4 are selected for the HFI implementation. In the table, $U_{ph\cdot rms}$ denotes the PMSM rated rms phase voltage. The expression of α_{LPF}, k_p and k_i can be found in (4-46). Once the pole of the closed-loop transfer function has been decided, the parameters of the LPF and the PI regulator can be decided.

Simulation Results

The successful start-up is shown in Figure 7-4, where the PMSM achieves 6000 rev/min, again in 4 s. As can be seen in (b) and (c), the HF voltage is injected at d-axis and then both d- and q-axis HF currents appear. The torque shown in (d) is therefore oscillating due to the oscillating current. Since the q-axis current oscillation is due to the angle estimation error, the key of a successful HFI is to maximize the d-axis current oscillation and minimize the q-axis current oscillation.

The performance of the estimator is illustrated in (g) and (h). In (h), θ^{err} is the real angle estimation error while θ_{ES}^{err} is the angle estimation error detected by the PI regulator inside the PLL-type HFI estimator. The estimation errors of both angle and speed decay to zero when the PMSM enters steady state. The maximum of the speed estimation error is about 42 rev/min which is adjustable if the LPF and the PI regulator parameters are modified. As can also be detected, at about 3 s, the current leaves the saturation region and the estimation error suddenly drops simultaneously. This may be because of the following reasons.

- The BPF before the HFI estimator to extract the HF components is not ideal and therefore the fundamental component still remains to some extent in the HFI estimator and affect the estimation result.

- When the amplitude of the fundamental component drops, the HF current component becomes relatively more significant, i.e. the signal to noise ratio increases from the estimator's point of view. Therefore, since a clearer error signal is detected by the estimator, a more accurate estimation is made.

A constant current oscillation generates a constant loss caused by the harmonics. In (i), the three-phase currents can be found to be distorted by the HF current component. Therefore, the HF signal injection method is not a good choice to be applied in steady state.
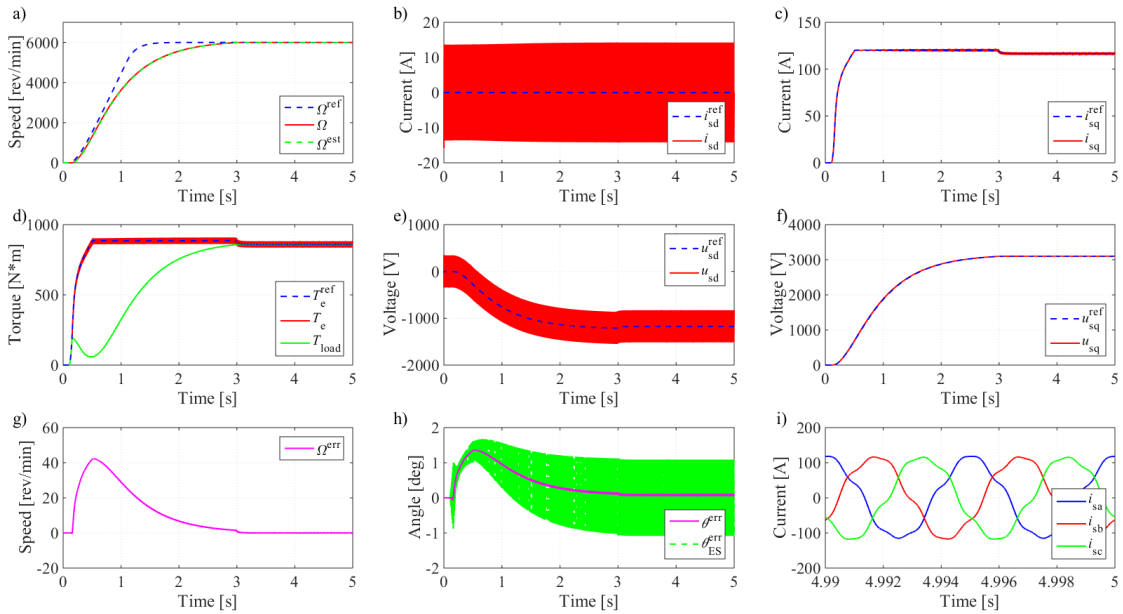
Figure 7-4 HFI performance (Model 2): speed, torque, estimation, dq and abc quantities

a) rotor speed	b) d-axis current	c) q-axis current
d) torque	e) d-axis voltage	f) q-axis voltage
g) speed estimation error	h) angle estimation error	i) abc currents

Figure 7-5 shows the performance of the BPF. As can be noticed, the HF signals and the fundamental signals are well separated by comparing the BPF input in (a) and (d) with the BPF output HF components in (b) and (e) and fundamental components in (c) and (f). Although the curves of the fundamental components shown in (c) and (f) seem smooth, the zoomed-in plots shown in (g) and (h) indicates that there is still a small amount of HF components remaining which are sent to the current controller. The HF component at 2000 Hz appears in both d- and q-axis currents. Although the HF component at 1000 Hz can only be apparently seen in the q-axis current, it is also contained in the d-axis current.
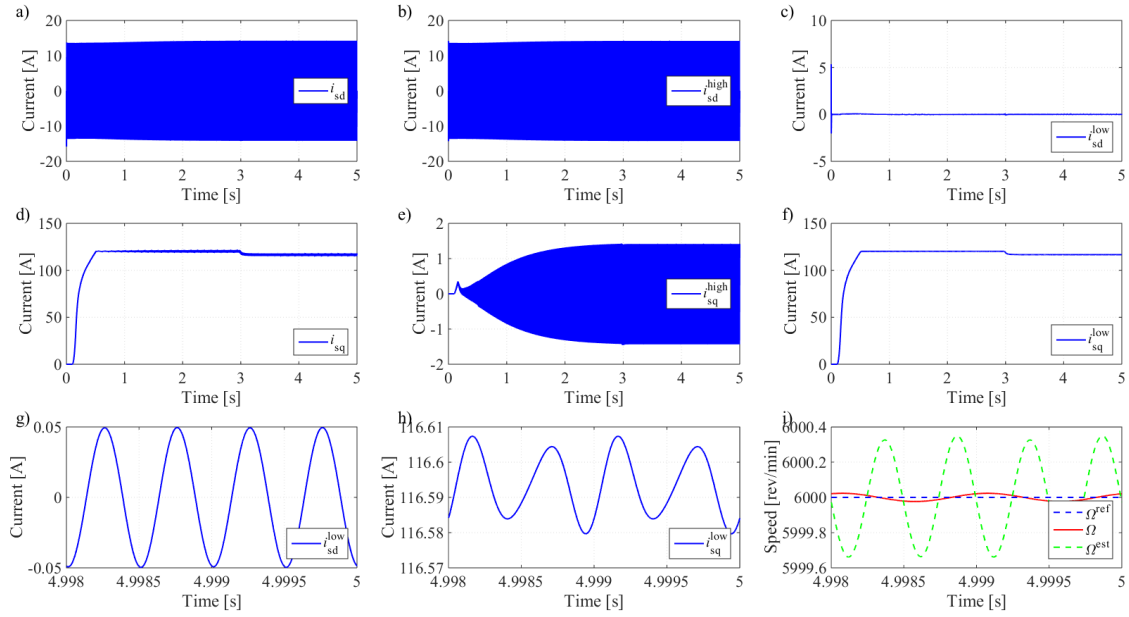
Figure 7-5 HFI performance (Model 2): filters and speed estimation

(a) d-axis current	(b) d-axis HF current	(c) d-axis fundamental current
(d) q-axis current	(e) q-axis HF current	(f) q-axis fundamental current
(g) d-axis fundamental current zoomed-in plot	(h) q-axis fundamental current zoomed-in plot	(i) rotor speed

The 1000 Hz component should be introduced from the HF injection. The explanation for such 2000 Hz may be addressed as follows. The demodulation process shown in Figure 4-3 generates a 2000 Hz signal which cannot be totally removed by the LPF before the PI regulator. Therefore, such a 2000 Hz component still remains in the speed estimation which is proved by (i). Then such a speed estimation oscillating at 2000 Hz generates a current reference in the speed controller and the feedforward terms in the current controller which are also oscillating at 2000 Hz. Therefore, a 2000 Hz voltage component is sent out and a 2000 Hz current is input to the current controller.

In addition, FFT analysis is carried out and the results are plotted in Figure 7-6, which shows that the HF components of the d- and q-axis currents shown in (b) and (e) are successfully extracted from the corresponding input currents shown in (a) and (d) while the remaining parts shown in (c) and (f) are sent to the current controller. The performance of the LPF in the estimator is shown in (g) and (h) which damps the 2000 Hz component. The 2000 Hz component is from the doubling of the injected 1000 Hz component by the demodulation process. Although still a high amount of the 2000 Hz component remains in the output, the angle error information contained in the low frequency component is significant enough for the PI regulator to detect the angle and speed.
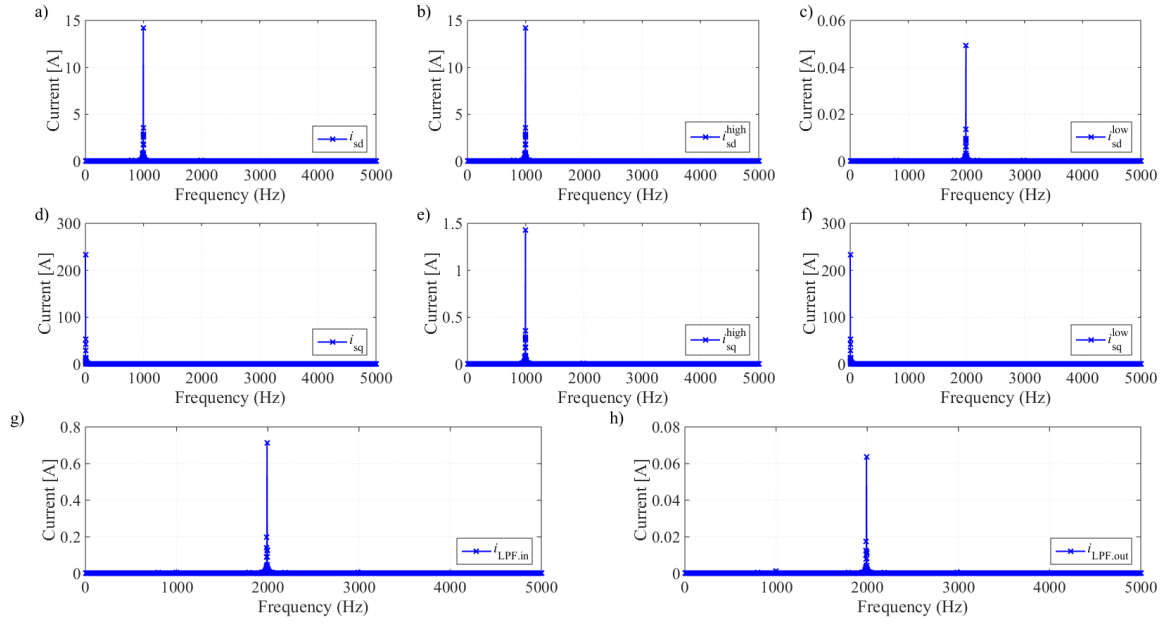
Figure 7-6 HFI performance (Model 2): FFT of dq currents

(a) d-axis current FFT   (b) d-axis HF current FFT   (c) d-axis fundamental current FFT

(d) q-axis current FFT   (e) q-axis HF current FFT   (f) q-axis fundamental current FFT

(g) LPF input FFT   (h) LPF output FFT
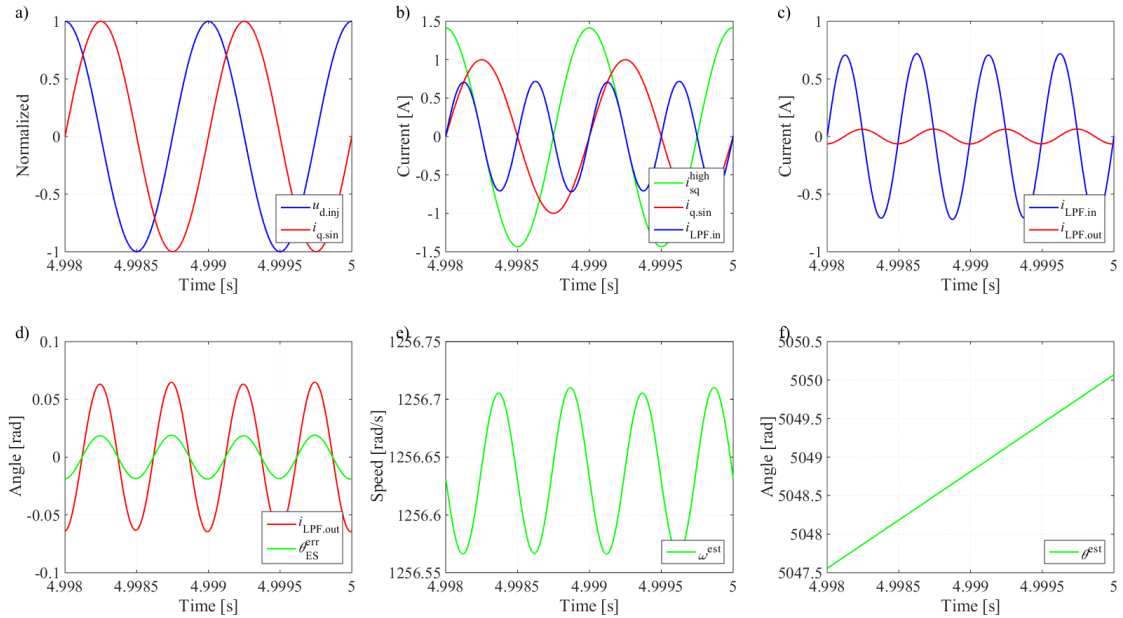
Figure 7-7 HFI performance (Model 2): estimator signals

a) HF voltage and sin current   b) filtered HF current   c) input and output of the LPF

d) error angle into the PLL   e) estimated speed   f) estimated angle

Figure 7-7 shows the signals at each stage of the estimator as illustrated in Figure 4-3. Subplot (a) shows the relative phase difference between the injected HF cos voltage signal and the HF demodulation sin signal. By comparing (a) and (b), the steady state q-axis HF current is in phase with the injected d-axis HF voltage, but due to the derivation of the HFI method in Section 4.3.1, the extracted q-axis HF current should be 90° lagging the d-axis HF voltage.

It should also be pointed out that in the beginning of the start-up, the q-axis HF current is out of phase with the injected d-axis HF voltage. Then, as the speed goes up, the q-axis HF current starts to shift its phase closer to the d-axis HF voltage gradually. When the speed goes up above 3000 rev/min, the q-axis HF current starts to be in phase with the d-axis HF voltage.

The explanation of such q-axis HF current phase shift can be addressed as follows. The HFI method is derived by neglecting the cross-coupling terms, the back-EMF term and the resistive voltage drop in (4-22) since they can be regarded as low frequency terms. However, both of the d- and q-axis currents contain HF components when HFI is working. Therefore, (4-22) can be reformulated in the HF region by only neglecting the back-EMF term due to its low frequency. Then, (4-22) becomes

$$u_{\text{sd·HF}} = R_s i_{\text{sd·HF}} + s L_{\text{sd}} i_{\text{sd·HF}} - \omega_r L_{\text{sq}} i_{\text{sq·HF}} \tag{7-6}$$

$$u_{\text{sq·HF}} = R_s i_{\text{sq·HF}} + s L_{\text{sq}} i_{\text{sq·HF}} + \omega_r L_{\text{sd}} i_{\text{sd·HF}} \tag{7-7}$$

The d- and q-axis HF currents can be solved as

$$i_{\text{sd·HF}} = \frac{u_{\text{sd·HF}} + \omega_r L_{\text{sq}} i_{\text{sq·HF}}}{s L_{\text{sd}} + R_s} \tag{7-8}$$

$$i_{\text{sq·HF}} = \frac{u_{\text{sq·HF}} - \omega_r L_{\text{sd}} i_{\text{sd·HF}}}{s L_{\text{sq}} + R_s} \tag{7-9}$$

The d- and q-axis HF currents can be further completely solved by substituting (7-8) and (7-9) into each other

$$i_{\text{sd·HF}} = \frac{\left(s L_{\text{sq}} + R_s\right) u_{\text{sd·HF}} + \omega_r L_{\text{sq}} u_{\text{sq·HF}}}{s^2 L_{\text{sd}} L_{\text{sq}} + s R_s \left(L_{\text{sd}} + L_{\text{sq}}\right) + R_s{}^2 + \omega_r{}^2 L_{\text{sd}} L_{\text{sq}}} \tag{7-10}$$

$$i_{\text{sq·HF}} = \frac{\left(s L_{\text{sd}} + R_s\right) u_{\text{sq·HF}} - \omega_r L_{\text{sd}} u_{\text{sd·HF}}}{s^2 L_{\text{sd}} L_{\text{sq}} + s R_s \left(L_{\text{sd}} + L_{\text{sq}}\right) + R_s{}^2 + \omega_r{}^2 L_{\text{sd}} L_{\text{sq}}} \tag{7-11}$$

Equations (7-10) and (7-11) are the expressions under perfect flux orientation. If an angle estimation error $\tilde{\theta}$ is introduced, then the injected HF voltage in the real dq frame r is phase shifted from the estimated dq frame r̂ by $\tilde{\theta}$

$$u_{\text{sd·HF}}^{\text{r}} = u_{\text{sd·HF}}^{\hat{\text{r}}} \cdot \cos \tilde{\theta} \tag{7-12}$$

$$u_{\text{sq·HF}}^{\text{r}} = -u_{\text{sd·HF}}^{\hat{\text{r}}} \cdot \sin \tilde{\theta} \tag{7-13}$$

Then the HF current in the real dq frame r can be obtained by substituting (7-12) and (7-13) into (7-10) and (7-11)

$$i_{\text{sd·HF}}^{\text{r}} = \frac{(sL_{\text{sq}} + R_{\text{s}}) \cos \tilde{\theta} - \omega_{\text{r}} L_{\text{sq}} \sin \tilde{\theta}}{s^2 L_{\text{sd}} L_{\text{sq}} + sR_{\text{s}}(L_{\text{sd}} + L_{\text{sq}}) + R_{\text{s}}^2 + \omega_{\text{r}}^2 L_{\text{sd}} L_{\text{sq}}} u_{\text{sd·HF}}^{\hat{\text{r}}} \tag{7-14}$$

$$i_{\text{sq·HF}}^{\text{r}} = \frac{-(sL_{\text{sd}} + R_{\text{s}}) \sin \tilde{\theta} - \omega_{\text{r}} L_{\text{sd}} \cos \tilde{\theta}}{s^2 L_{\text{sd}} L_{\text{sq}} + sR_{\text{s}}(L_{\text{sd}} + L_{\text{sq}}) + R_{\text{s}}^2 + \omega_{\text{r}}^2 L_{\text{sd}} L_{\text{sq}}} u_{\text{sd·HF}}^{\hat{\text{r}}} \tag{7-15}$$

The current vector in the estimated dq frame $\hat{\text{r}}$ is phase shifted from the real dq frame r by $-\tilde{\theta}$. Hence the q-axis HF current in the estimated dq frame $\hat{\text{r}}$ will be

$$i_{\text{sq·HF}}^{\hat{\text{r}}} = i_{\text{sd·HF}}^{\text{r}} \sin \tilde{\theta} + i_{\text{sq·HF}}^{\text{r}} \cos \tilde{\theta}$$

$$= \frac{s(L_{\text{sq}} - L_{\text{sd}}) \sin \tilde{\theta} \cos \tilde{\theta} - \omega_{\text{r}} L_{\text{sq}} \sin^2 \tilde{\theta} - \omega_{\text{r}} L_{\text{sd}} \cos^2 \tilde{\theta}}{s^2 L_{\text{sd}} L_{\text{sq}} + sR_{\text{s}}(L_{\text{sd}} + L_{\text{sq}}) + R_{\text{s}}^2 + \omega_{\text{r}}^2 L_{\text{sq}} L_{\text{sd}}} u_{\text{sd·HF}}^{\hat{\text{r}}} \tag{7-16}$$

The transfer function of the HFI can be expressed by taking $i_{\text{sq·HF}}^{\hat{\text{r}}}$ as the output and $u_{\text{sd·HF}}^{\hat{\text{r}}}$ as the input since it is the estimated dq frame that the HFI is working in, which means

$$G(s) = \frac{i_{\text{sq·HF}}^{\hat{\text{r}}}}{u_{\text{sd·HF}}^{\hat{\text{r}}}} = \frac{(L_{\text{sq}} - L_{\text{sd}}) \sin \tilde{\theta} \cos \tilde{\theta} - \omega_{\text{r}} L_{\text{sq}} \sin^2 \tilde{\theta} - \omega_{\text{r}} L_{\text{sd}} \cos^2 \tilde{\theta}}{s^2 L_{\text{sd}} L_{\text{sq}} + sR_{\text{s}}(L_{\text{sd}} + L_{\text{sq}}) + R_{\text{s}}^2 + \omega_{\text{r}}^2 L_{\text{sd}} L_{\text{sq}}} \tag{7-17}$$

If $\omega_{\text{r}} = 0$ and $R_{\text{s}} = 0$ are assumed, then (7-17) will become

$$G(s) = \frac{i_{\text{sq·HF}}^{\hat{\text{r}}}}{u_{\text{sd·HF}}^{\hat{\text{r}}}} = \frac{i_{\text{sq·HF}}^{\hat{\text{r}}}}{U_{\text{HF}} \cos \omega_{\text{HF}} t} = \frac{L_{\text{sq}} - L_{\text{sd}}}{sL_{\text{sd}} L_{\text{sq}}} \frac{\sin 2\tilde{\theta}}{2} \tag{7-18}$$

which is consistent with the HFI derivation result in (4-29). Therefore, (4-29) is only a special case of (7-17).

Taking the steady state performance $\omega_{\text{r}} = 400\pi$ rad/s into consideration, the Bode diagram of the realistic case (7-17) can be obtained as shown in Figure 7-8 with several different angle estimation errors between ±30°. In addition, the perfect case (7-18) is also plotted as dashed lines with ±20°. As can be seen from Figure 7-8, a resonance frequency at 200 Hz can be detected for the realistic cases. However, it should be pointed out that such a resonance frequency is equal to ω_{r} in each realistic Bode diagram when ω_{r} varies, while the shape of the Bode diagram is still the same, i.e. independent from ω_{r}.
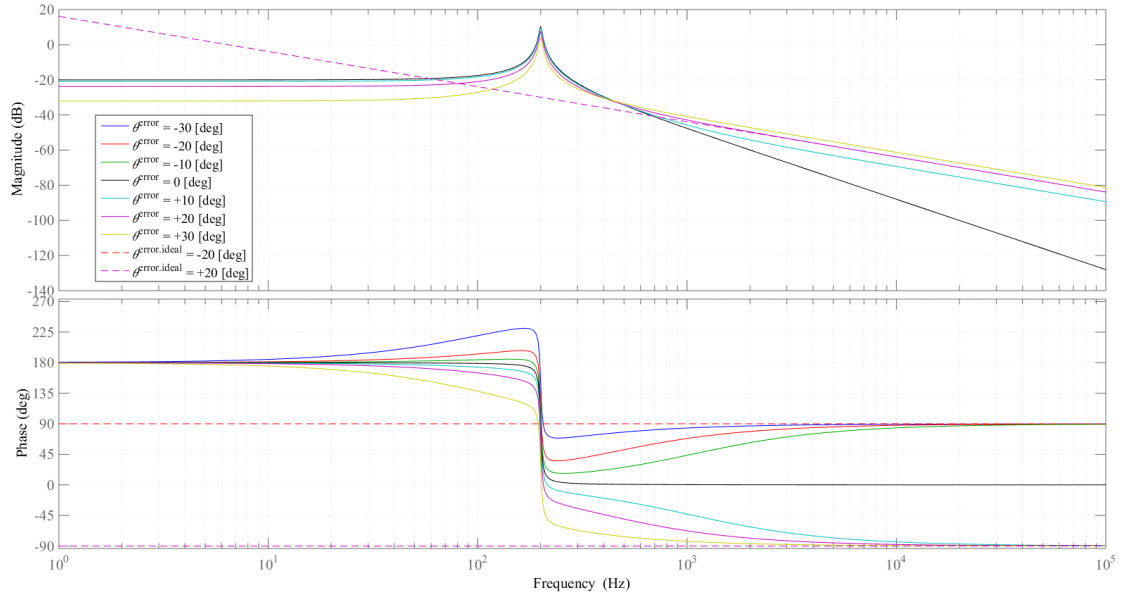
Figure 7-8 HFI performance (Model 2): Bode diagram of the estimator ($\omega_r = 400\pi$ rad/s)

For the ideal cases in Figure 7-8 shown as dashed lines, HFI gives +90° and -90° phase shifts when the angle estimation error is negative and positive respectively, which is expected as illustrated in Section 4.3.1. For the realistic cases in Figure 7-8 shown as solid lines, at the injected frequency of 1000 Hz, HFI gives zero phase shift when the angle estimation error is zero, while HFI gives positive phase shift when the angle estimation error is negative and vice versa. In addition, two important tendencies can be summarized as follows.

- For a specific angle estimation error, when the injected frequency increases, the phase shift in a realistic case gradually converges to the corresponding ideal case, i.e. the solid lines converge to the corresponding dashed lines as the injected frequency goes higher.

- At a specific frequency in the HF region (higher than the resonance frequency), in the realistic cases, a higher angle estimation error gives a higher phase shift while a lower angle estimation error gives a lower phase shift and a zero angle estimation error gives a zero phase shift. This indicates that a higher angle estimation error can be corrected more efficiently compared with a lower angle estimation error.

Therefore, an injected d-axis HF voltage $U_{HF}\cos(\omega_{HF}t)$ will evoke a q-axis HF current with a phase shift $I_{HF}\cos(\omega_{HF}t + \varphi_{HF})$. Then as has been illustrated in Figure 4-3, such a q-axis HF current is demodulated by getting multiplied with a HF sin signal $\sin(\omega_{HF}t)$

$$I_{HF} \cos(\omega_{HF}t + \varphi_{HF}) \sin(\omega_{HF}t)$$
$$= I_{HF}[\cos(\omega_{HF}t)\cos(\varphi_{HF}) - \sin(\omega_{HF}t)\sin(\varphi_{HF})]\sin(\omega_{HF}t)$$
$$= \frac{I_{HF}}{2}\sin(2\omega_{HF}t)\cos(\varphi_{HF}) - I_{HF}\sin^2(\omega_{HF}t)\sin(\varphi_{HF}) \qquad (7\text{-}19)$$
$$= \frac{I_{HF}}{2}\sin(\varphi_{HF}) + \frac{I_{HF}}{2}\sin(2\omega_{HF}t - \varphi_{HF})$$

where I_{HF} is the amplitude of the HF current signal that contains the angle estimation error $\tilde{\theta}$. Then the low frequency term $\frac{I_{HF}}{2}\sin(\varphi_{HF})$ will pass the LPF and be sent to the PLL. It should be noticed that the coefficient $\sin(\varphi_{HF})$ can be regarded as a scaling factor of I_{HF} that decides the intensity of the PLL input, i.e. feedback for correction. Thereafter, the angle estimation error $\tilde{\theta}$ contained in I_{HF} can be further extracted by PLL. Thus it can be concluded that it is the phase shift φ_{HF} between the HF current and voltage that decides the efficiency of the angle estimation error $\tilde{\theta}$ correction by HFI. The mechanism can be illustrated as

$$high~\tilde{\theta} \rightarrow high~\varphi_{HF} \rightarrow high~PLL~input \rightarrow high~\tilde{\theta}~correction~efficiency \qquad (7\text{-}20)$$

Then, the angle estimation error is efficiently corrected and becomes lower which decreases the phase shift according to Figure 7-8

$$\tilde{\theta} \downarrow \quad \rightarrow \quad \varphi_{HF} \downarrow \quad \rightarrow \quad PLL~input \downarrow \quad \rightarrow \quad \tilde{\theta}~correction~efficiency \downarrow \qquad (7\text{-}21)$$

If any disturbance to the HFI estimator occurs, Figure 7-8 and (7-19) will form a feedback mechanism to eliminate the angle estimation error which can be illustrated as

$$\tilde{\theta} \uparrow \quad \rightarrow \quad \varphi_{HF} \uparrow \quad \rightarrow \quad PLL~input \uparrow \quad \rightarrow \quad \tilde{\theta} \downarrow \qquad (7\text{-}22)$$

Therefore, in steady state, there must be almost no phase shift between $i_{sq\cdot HF}^{\hat{r}}$ and $u_{sd\cdot HF}^{\hat{r}}$ as shown in Figure 7-7 since any phase shift angle φ_{HF} will reveal the angle estimation error $\tilde{\theta}$ which will further be corrected until almost no phase shift exists. In addition, if a voltage signal at an even higher frequency is injected, then the performance of the HFI realistic case will be closer to the ideal case as shown in Figure 7-8, which means that for the same $\tilde{\theta}$, a larger φ_{HF} will appear which will make the same angle estimation error $\tilde{\theta}$ be corrected more efficiently by the PLL.

7.2.2 SCVM Method

Figure 7-9 shows the performance of the SCVM method. Since SCVM cannot work in the low speed region for a long time, a step reference is applied at 0.1 s instead of a ramp reference in order to accelerate the PMSM as fast as possible as shown in (a). The large speed error gives a large torque requirement and then the q-axis current along with the electromagnetic torque jumps immediately in (c) and (d).

It should be considered that during the derivation of the SCVM method, the stator current derivative is assumed to be zero and therefore is neglected in the configuration. However, here

occurs a large current derivative in the beginning of the start-up which leads to an error in the speed and angle estimations consequently as shown in (g) and (h). Therefore, the estimated dq frame deviates from the true dq frame in the beginning. Then after the estimated speed goes up, the damping factor λ is activated and damps the estimation error to zero swiftly. (i) shows that the current waveform is perfectly sinusoidal in the steady state performance and therefore, SCVM can be concluded to be more suitable to be applied in steady state compared to HFI for a lower harmonic content.
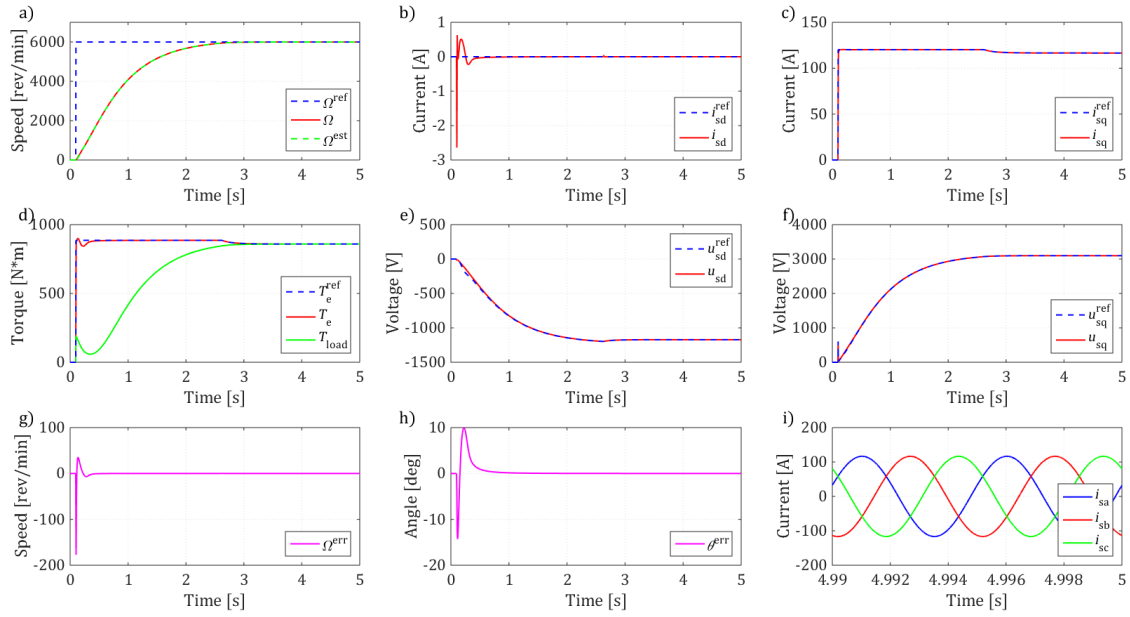
Figure 7-9 SCVM performance (Model 2): speed, torque, estimation, dq and abc quantities

a) rotor speed	b) d-axis current	c) q-axis current
d) torque	e) d-axis voltage	f) q-axis voltage
g) speed estimation error	h) angle estimation error	i) abc currents

7.2.3   Sensorless Control Combination

The merged sensorless control algorithm is introduced in Section 4.4. The frequency spectrum is presented in Figure 7-10. The bandwidth of SCVM is shown as a vague point since the value is roughly estimated and changing with speed. The shut-down point of the HFI is selected to be at the speed of 0.2 p.u., which means the HFI only contributes to the estimation below 1200 rev/min.
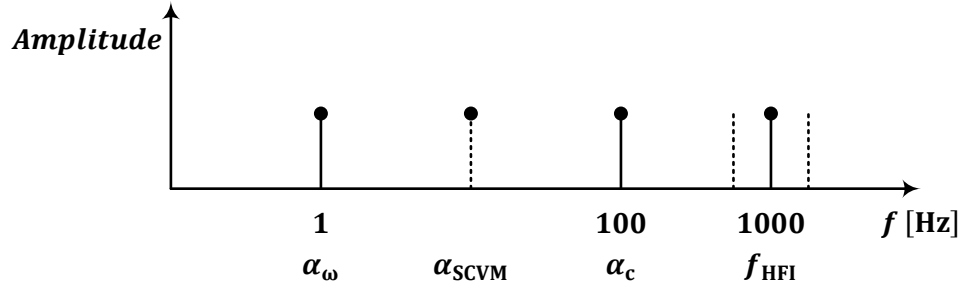
Figure 7-10 Sensorless control combination: frequency spectrum

Figure 7-11 shows the smooth speed rise with the smooth sensorless control algorithm transmission. The HFI algorithm only operates during the beginning from 0 s up to about 0.5 s as can be seen from subplot (b) and (e), where the HF d-axis voltage and current signals are faded out and the waveform becomes smooth gradually.
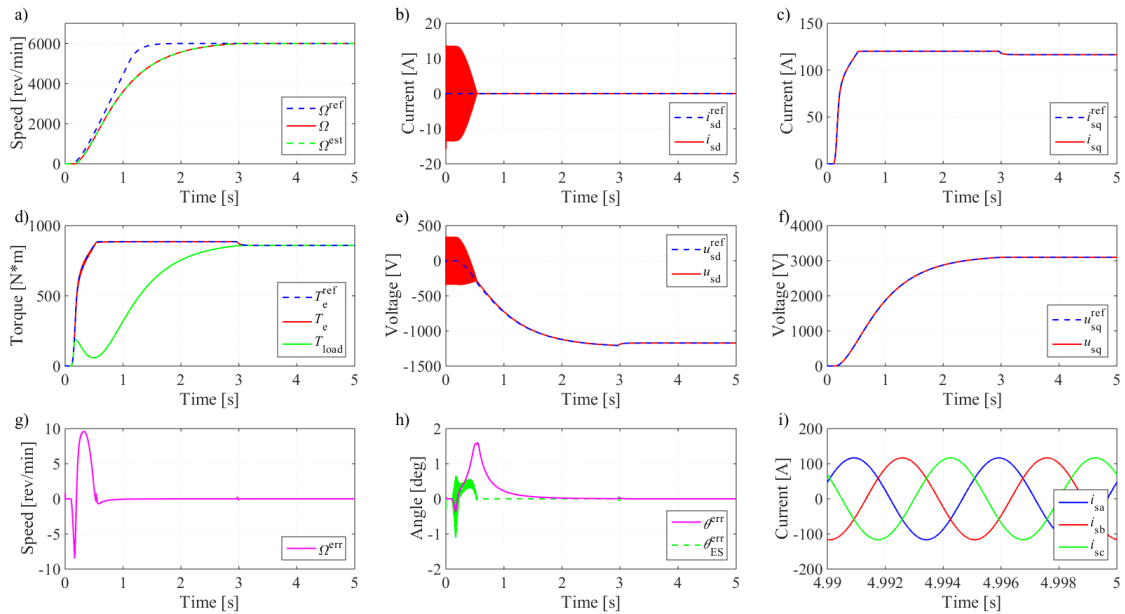
Figure 7-11 Sensorless control combination (Model 2): speed, torque, estimation, abc and dq quantities

a) rotor speed	b) d-axis current	c) q-axis current
d) torque	e) d-axis voltage	f) q-axis voltage
g) speed estimation error	h) angle estimation error	i) abc currents

The speed estimation error in Figure 7-12 shows that the positive speed estimation error from the HFI cancels part of the negative speed estimation error from the SCVM in the beginning of the start-up compared with the previous case with SCVM alone. In other words, the positive and negative speed estimation errors in Figure 7-11 are much smaller than in Figure 7-9. Similar improvement can also be detected if the angle estimation errors are compared. Therefore, it can be concluded that the combined algorithm provides a more accurate estimation compared with each of them independently in the beginning of the start-up.
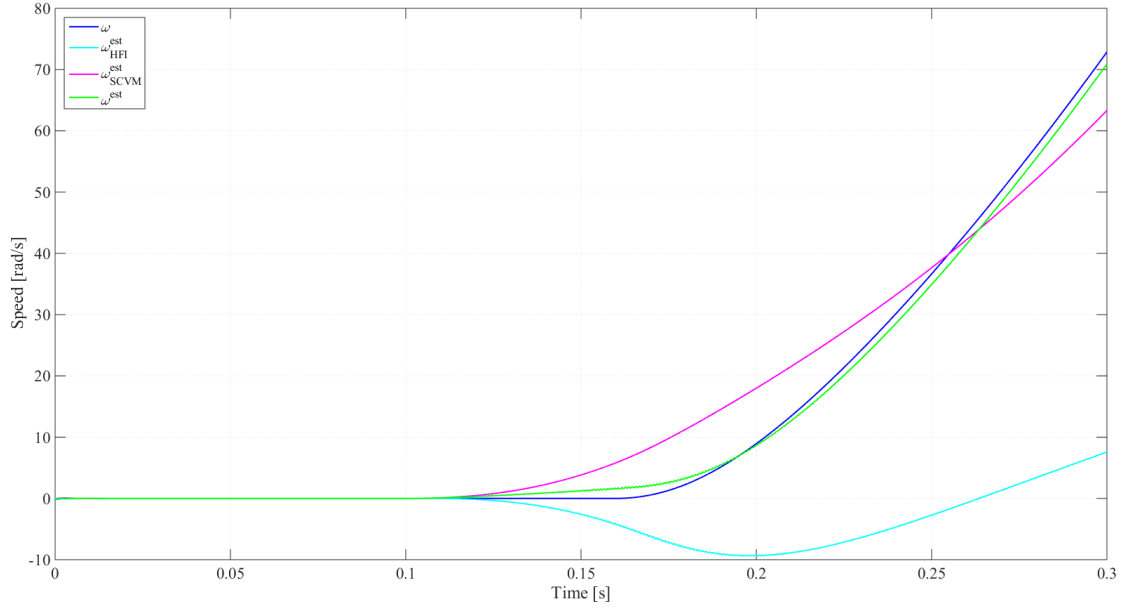
Figure 7-12 Sensorless control combination (Model 2): merged speed estimator

7.3 SVPWM

In order to test the performance of the SVPWM algorithm independently, the inverter input is directly connected to a dc voltage source while the inverter output is directly connected to a Y-connected neutral-point-floating three-phase RL load. Both two-level and five-level SVPWM are implemented and compared in this section. The configuration of this SVPWM test is listed in Table 7-5.

Table 7-5 SVPWM test configuration

Two-level SVPWM dc voltage	$u_{\mathrm{dc}\cdot 2}$	1000	[V]
Five-level SVPWM dc voltage	$u_{\mathrm{dc}\cdot 5}$	500	[V]
Voltage reference	$\left|u^{\mathrm{ref}}\right|$	500	[V]
Amplitude modulation index	m_{a}	0.866	
Switching frequency	f_{sw}	4200	[Hz]
Fundamental frequency	f_{sin}	200	[Hz]
Frequency modulation index	m_{f}	21	
Resistance of the load	R	1	[Ω]
Inductance of the load	L	10	[mH]

The inverter output voltages are shown in Figure 7-13 and the load voltages and currents are shown in Figure 7-14 respectively. The inverter phase voltage $u_{\mathrm{ao}\cdot 2}$ in Figure 7-13 means the voltage across the Phase A output terminal (subscript "a") and the mid-point of the dc-link (subscript "o") in the two-level (subscript "2") SVPWM case. The similar notation is applied for $u_{\mathrm{ao}\cdot 5}$ and so forth. Figure 7-13 clearly shows that the two-level SVPWM gives two phase voltage levels: ± 500 V, while the five-level SVPWM gives five phase voltage levels: ± 500 V,

± 250 V and 0 V. In both the phase voltage subplots and the line voltage subplots, the five-level SVPWM gives more sinusoidal voltage waveforms than the two-level SVPWM does.
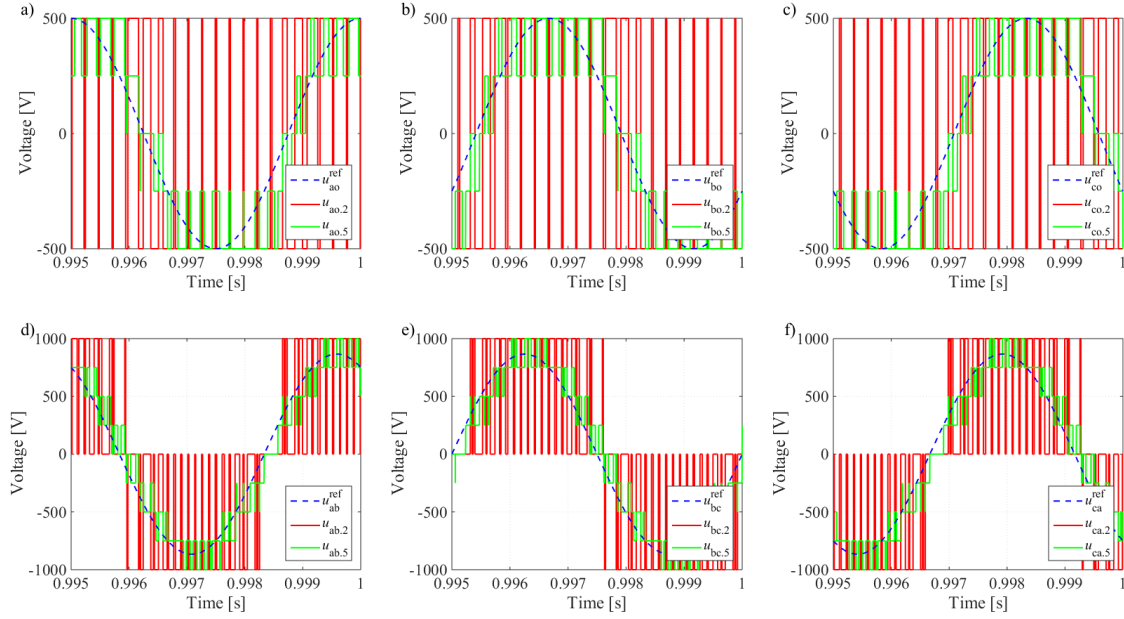
Figure 7-13 SVPWM inverter output voltages

a) inverter phase voltage u_{ao} b) inverter phase voltage u_{bo} c) inverter phase voltage u_{co}

d) inverter line voltage u_{ab} e) inverter line voltage u_{bc} f) inverter line voltage u_{ca}
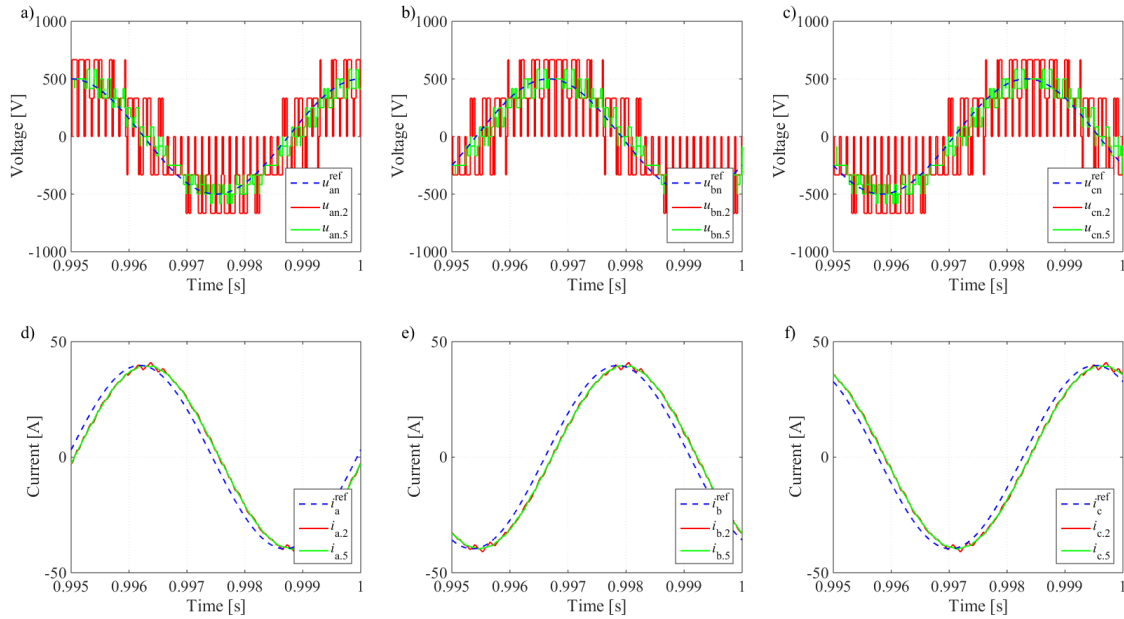
Figure 7-14 SVPWM load voltages and currents (without angle compensation)

a) load phase voltage u_{an} b) load phase voltage u_{bn} c) load phase voltage u_{cn}

d) load phase current i_a e) load phase current i_b f) load phase current i_c

The frequency modulation index of 21 is relative low and therefore harmonics are at a relatively low frequency. As can be detected in Figure 7-14 (d), (e) and (f), the two-level SVPWM current

contains some ripples, but for the five-level SVPWM, a much smoother performance is given due to its ability of shifting harmonics to a higher frequency region.

However, a current phase angle delay can be found in Figure 7-14. The reason for such an angle delay together with the solution of angle compensation are introduced in Section 5.3.2. The angle compensation is implemented and the result is shown in Figure 7-15. Instead of the sampled angle in the beginning of the SVPWM cycle, the predicted average angle over the entire SVPWM cycle is provided for the SVPWM modulator. As can be seen from Figure 7-15, the compensation successfully make the output currents catch the current references.
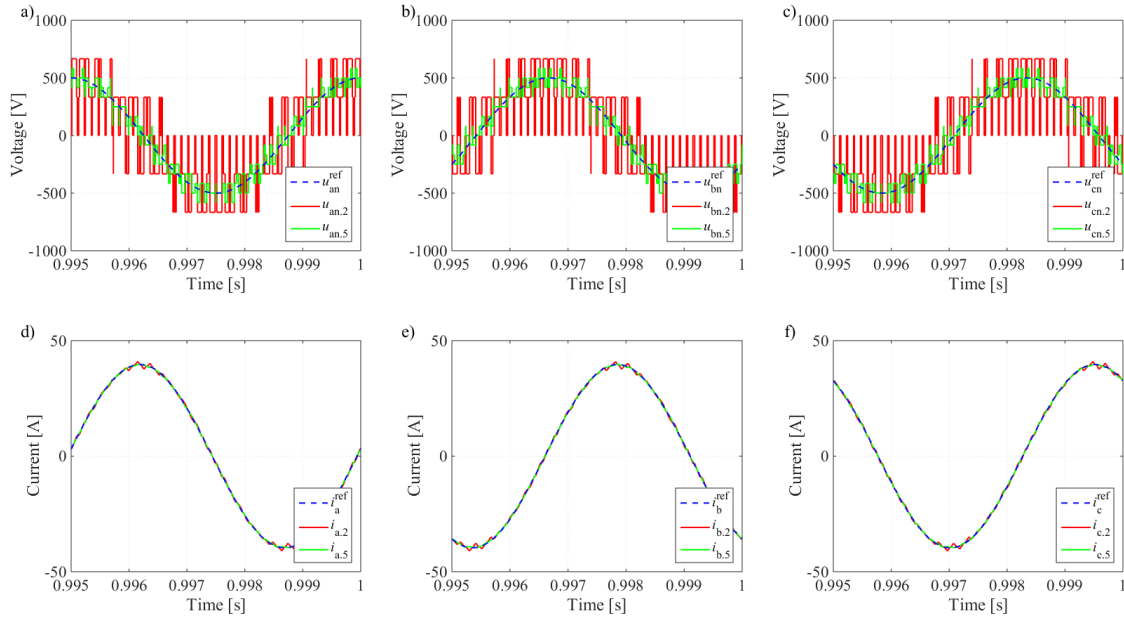
Figure 7-15 SVPWM load voltages and currents (with angle compensation)

a) load phase voltage u_{an} b) load phase voltage u_{bn} c) load phase voltage u_{cn}

d) load phase current i_a e) load phase current i_b f) load phase current i_c

The FFT analyses of both the two-level and five-level SVPWM output line voltages and currents are illustrated in Figure 7-16 and Figure 7-17. It can be clearly seen that for both the two-level and the five-level SVPWM cases, the fundamental component at 200 Hz is the most significant one over the entire spectrum. The harmonic components at the switching frequency of 4200 Hz and its multiples, e.g. 8400 Hz, are cancelled in the line voltage and current due to the center-located switching pattern of the SVPWM technique [49], but the sideband harmonics still remain.
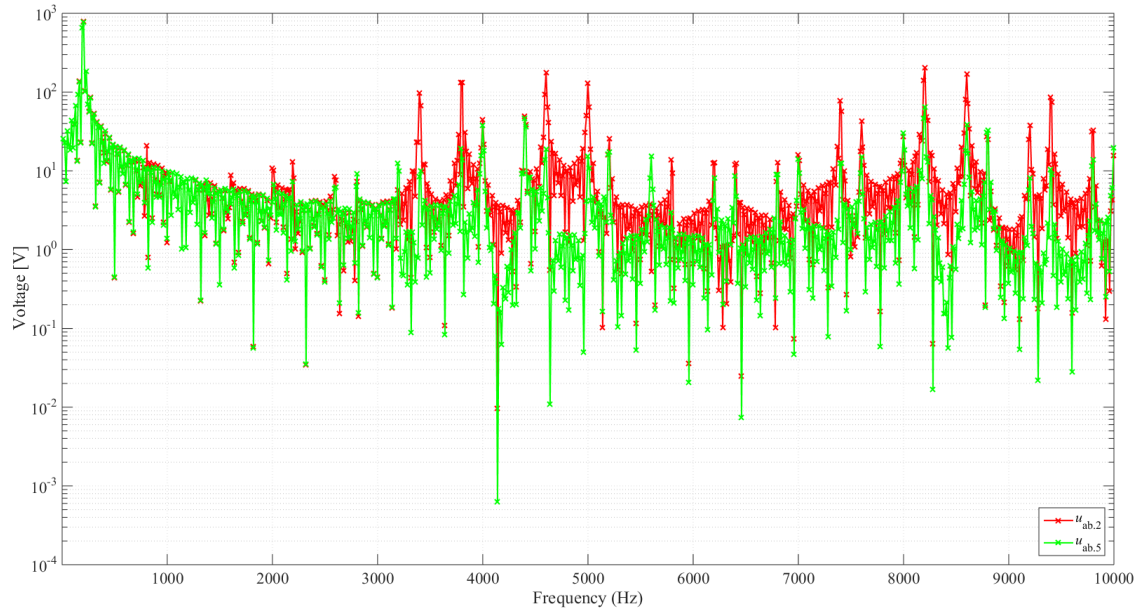
Figure 7-16 SVPWM output line voltage FFT
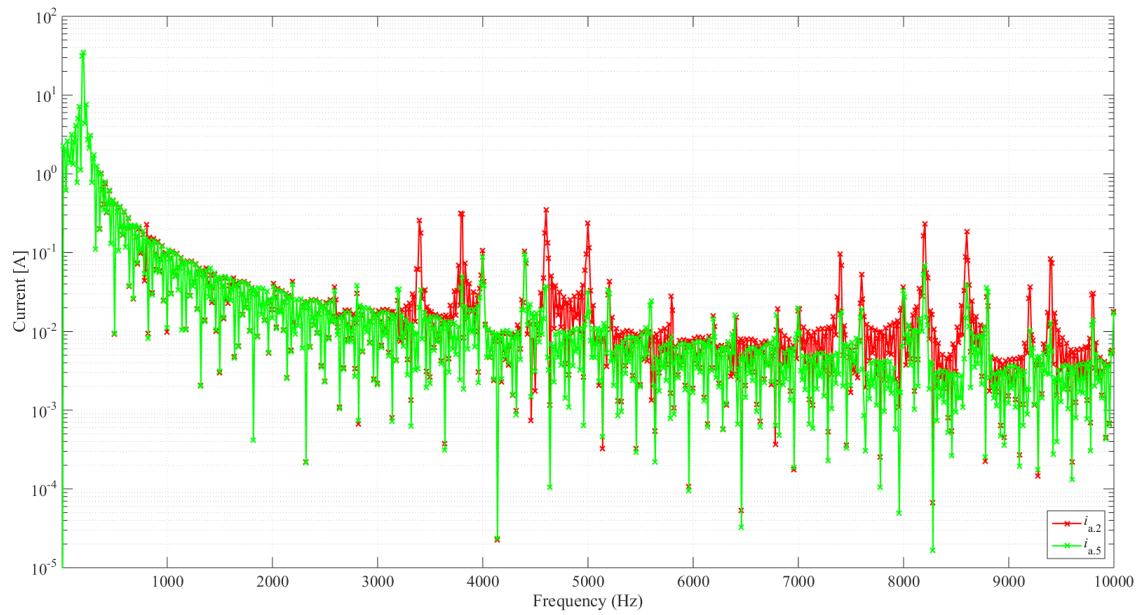
Figure 7-17 SVPWM output current FFT

In addition, the five-level SVPWM gives much lower harmonic contents than the two-level SVPWM over the spectrum as can also be detected from the total voltage and current harmonic distortions listed in Table 7-6. The values of THD in Table 7-6 takes 101 harmonics into consideration. Another observation can be made is that, the higher the frequency is, the larger the difference exists between the two-level and the five-level SVPWM harmonic contents.

Table 7-6 Total voltage and current harmonic distortions of SVPWM

	Two-level SVPWM		Five-level SVPWM	
Voltage THD	$THD_{u \cdot ab \cdot 2}$	58.5422%	$THD_{u \cdot ab \cdot 5}$	16.7221%
Current THD	$THD_{i \cdot a \cdot 2}$	1.9204%	$THD_{i \cdot a \cdot 5}$	0.5354%

7.4 Realistic Converter with Digital Control (Model 3)

The two-level inverter is enough to start the PMSM up to 6000 rev/min and therefore, there is currently no need to apply the five-level inverter in this section. The PWM will generate voltage harmonics in both d- and q-axis and cause current harmonics in both d- and q-axis consequently. Therefore, instead of guaranteeing

$$i_{sd} = 0 \tag{7-23}$$

the controller only tries to make

$$i_{sd \cdot ctrl} = \frac{1}{T_{sw}} \int_0^{T_{sw}} i_{sd} \cdot dt = 0 \tag{7-24}$$

where T_{sw} is the switching period and $i_{sd \cdot ctrl}$ equals the average value of the d-axis current for one switching period. From the equation of the electromagnetic torque in (2-13), an oscillating electromagnetic torque will appear. In the beginning of the start-up, such oscillating electromagnetic torque will give an oscillating PMSM speed around zero, and then the simulation will get halt by *consecutive zero-crossings*.

The solution is to push the q-axis current fast enough which produces a high electromagnetic toque and overwhelms the effects of the current harmonics. Therefore, if such a *consecutive zero-crossings* problem appears, either the speed PI regulator bandwidth or the slop of speed reference is recommended be increased, so that the speed controller can increase the q-axis current reference fast enough.

7.4.1 Control with Sensor

As is aforementioned in Section 5.3.1 , sampling at the end or the middle of the switching period is recommended to avoid the effect from switching harmonics. Therefore, the controller sampling frequency can be selected as equal to or half of the switching frequency.

The single sampling case ($f_{sample} = f_{sw}$) is applied at first in which samplings are only conducted at the terminals of each switching period. Figure 7-18 shows the successful speed rise of the PMSM along with the dq current and voltage performance. Instead of the smooth curves that appear before, switching ripples in the stator voltage and current occur from the beginning until the end. The dq voltages oscillate at almost constant amplitudes due to the switching between the VSC voltage levels while the current ripple amplitudes increase as the speed, i.e. the back-EMF, increases.

92

Figure 7-18 Control with sensor (Model 3): speed, torque and dq quantities

a) rotor speed   b) d-axis current   c) q-axis current

d) torque   e) d-axis voltage   f) q-axis voltage
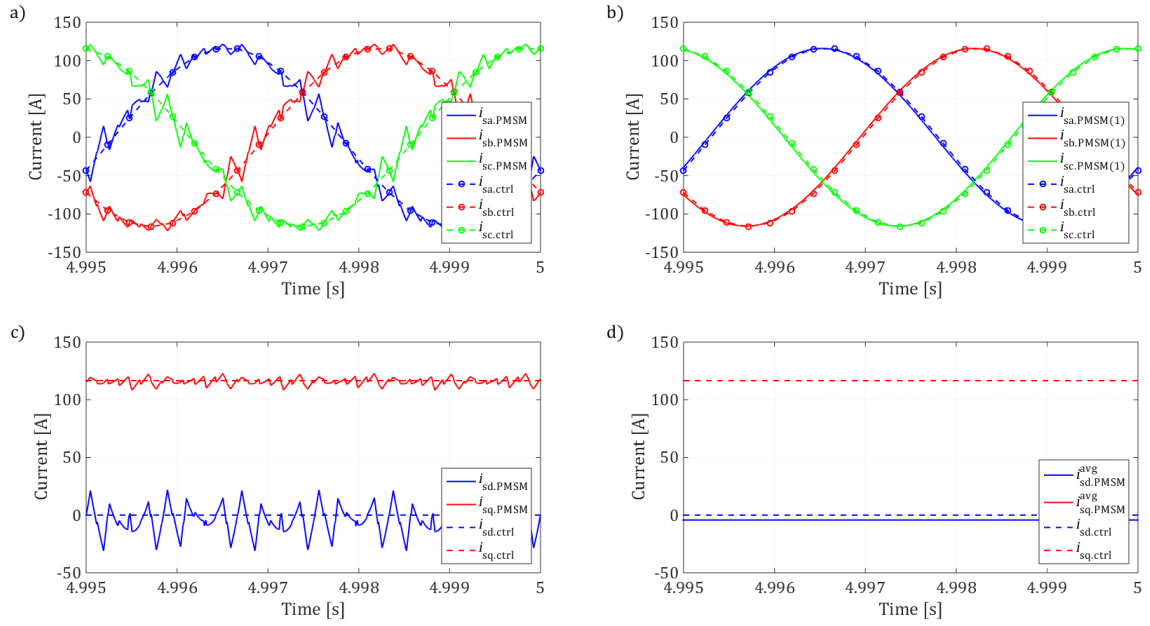
Figure 7-19 Control with sensor (Model 3): current single sampling

a) abc frame current sampling   b) abc frame fundamental current

c) dq frame current sampling   d) dq frame average current

In Figure 7-19 (a) and (b), a small angle delay appears between the sampled currents and real current fundamental components in the three-phase current subplot. The sampled current values

93

are located at almost the average value of the real PMSM current in the dq frame in subplot (c) and (d). $i_{\text{sq·ctrl}}^{\text{avg}}$ cannot be seen in (d) because it is overlapped by $i_{\text{sq·ctrl}}$.

Then the double sampling case ($f_{\text{sample}} = 2f_{\text{sw}}$) follows where samplings are conducted at both the terminals and the midpoints of each switching period, which means the sampling frequency is twice of the switching frequency in this case. In Figure 7-20 (b), the sampling current is jumping forward and backward relative to the current fundamental component which is different from the single sampling case in Figure 7-19 (b). In Figure 7-20 (d), it can be clearly seen that the sampled values jump up and down around the average value which is consistent with the (b). Again, $i_{\text{sq·ctrl}}^{\text{avg}}$ cannot be seen in (d) because it is overlapped by $i_{\text{sq·ctrl}}$.
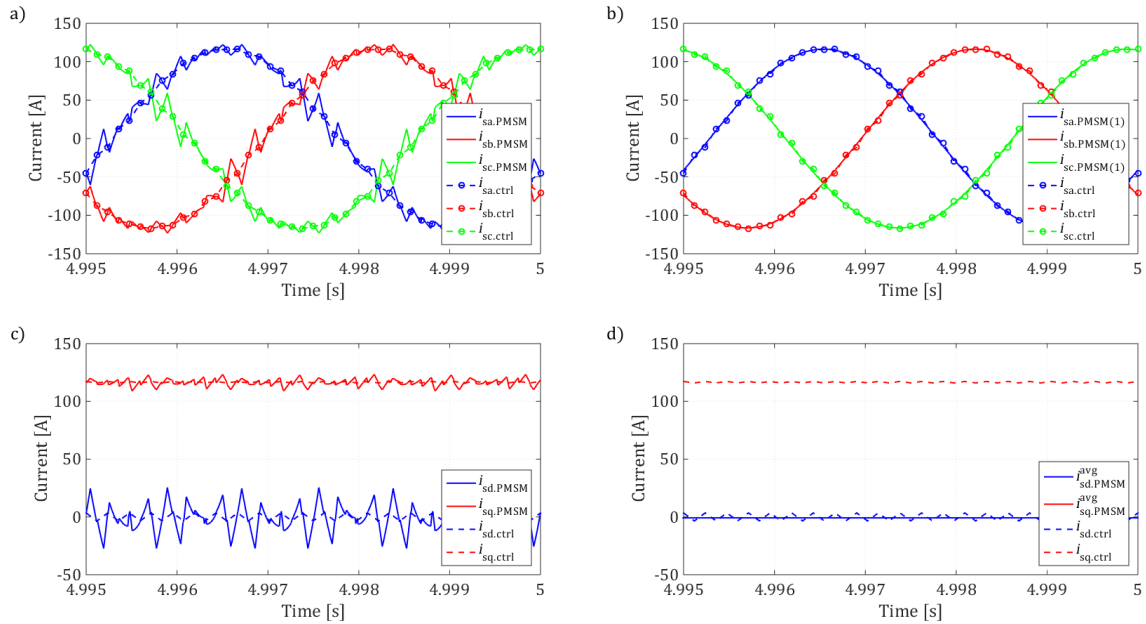
Figure 7-20 Control with sensor (Model 3): current double samplings

a) abc frame current sampling   b) abc frame fundamental current

c) dq frame current sampling   d) dq frame average current

The current controller cannot correct the sampling angle error since the bandwidth of the current controller is much lower than the switching frequency. A comparison between single and double samplings is done in Table 7-7.

Table 7-7 Comparison between single and double sampling

Quantities		Unit	Single Sampling	Double Sampling
Average current	$i_{\text{sd·PMSM·avg}}$	[A]	-4.2249	-0.8294
	$i_{\text{sd·ctrl·avg}}$	[A]	-5.2249e-05	4.6300e-04
	$i_{\text{sq·PMSM·avg}}$	[A]	115.7612	116.4141
	$i_{\text{sq·ctrl·avg}}$	[A]	116.6036	116.6009
Current vector amplitude	$\left\|i_{\text{s·PMSM·avg}}\right\|$	[A]	115.8383	116.4171
	$\left\|i_{\text{s·ctrl·avg}}\right\|$	[A]	116.6036	116.6009
Current vector angle	$\theta_{\text{i·PMSM}}$	[degree]	92.0902	90.4082
	$\theta_{\text{i·ctrl}}$	[degree]	90.0000	89.9998

As can be found out from Table 7-7, the amplitudes of both the sampled and the real current vectors are almost the same, but the dq current ratios are different, which means

$$\left|i_{\text{s·ctrl}}\right| \approx \left|i_{\text{s·PMSM}}^{\text{avg}}\right| \quad \text{but} \quad \frac{i_{\text{sd·ctrl}}}{i_{\text{sq·ctrl}}} \neq \frac{i_{\text{sd·PMSM}}}{i_{\text{sq·PMSM}}} \tag{7-25}$$

Therefore, take the single sampling case as an example, the amplitudes are sampled correctly while an angle error of about 2° is introduced when the αβ-dq transformation is done. The relative position of the real and sampled dq frames are illustrated in Figure 7-21. The current vector in the real system is ahead of the vector in the controller, which means the dq frame in the controller is ahead of the dq frame in the real system. An angle delay of about 30 μs can also be detected from the time-domain plot in Figure 7-19 (d), which is 0.006 times of the fundamental frequency i.e. 2°. Similar calculation can be done for the double sampling case.

(a)   (b)
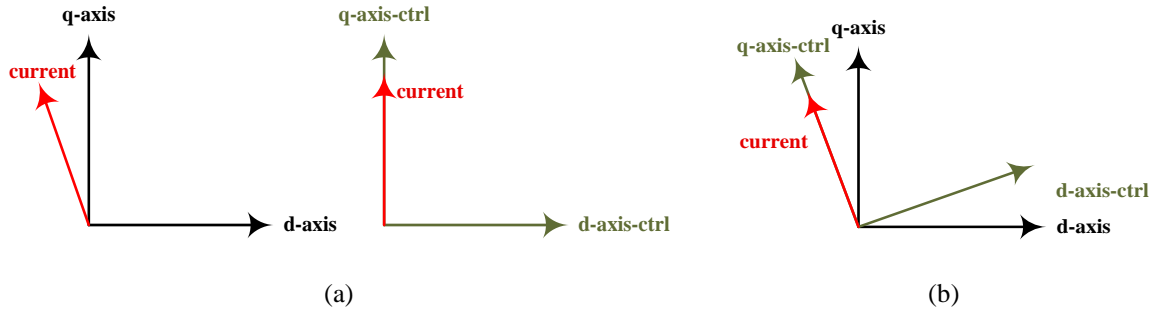
Figure 7-21 Control with sensor (Model 3): sampled current vector in real and estimated dq frames

(a) real and controller dq frame currents   (b) relative position of the dq frames

In addition, the double sampling case gives a much smaller current vector angle error from the real PMSM angle than the single sampling case as can be concluded from Table 7-7. This may be because an additional calculation step is performed during the switching cycle which generates a more accurate voltage vector.

7.4.2 Sensorless Control

As has been concluded that the double sampling can give a better performance than the single sampling, the sensorless control part will only present the case with double sampling. The successful performance is presented in Figure 7-22. As can be seen in (b), during the first 0.8 s, the sampled d-axis current oscillation is mainly caused by the HF injection since the sampling frequency of 8400 Hz is much higher than the injected signal at the frequency of 1000 Hz ~ 1200 Hz, while later on, the oscillation is caused by the sampling jumping back and forth around the fundamental component. In (g) and (h), the estimator performance gives the speed and angle estimation errors at almost the same range as the ones in the analogue control case in Figure 7-11, but the shapes look quite difference. Instead of eliminating the angle estimation error eventually, an angle error of -1.352° still exists in steady state.
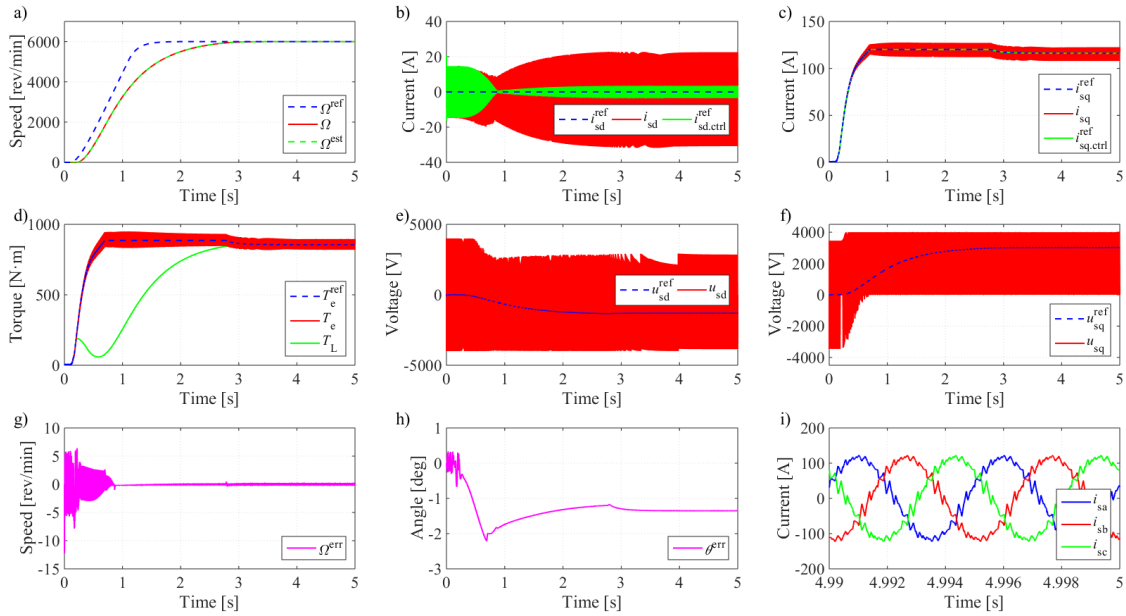
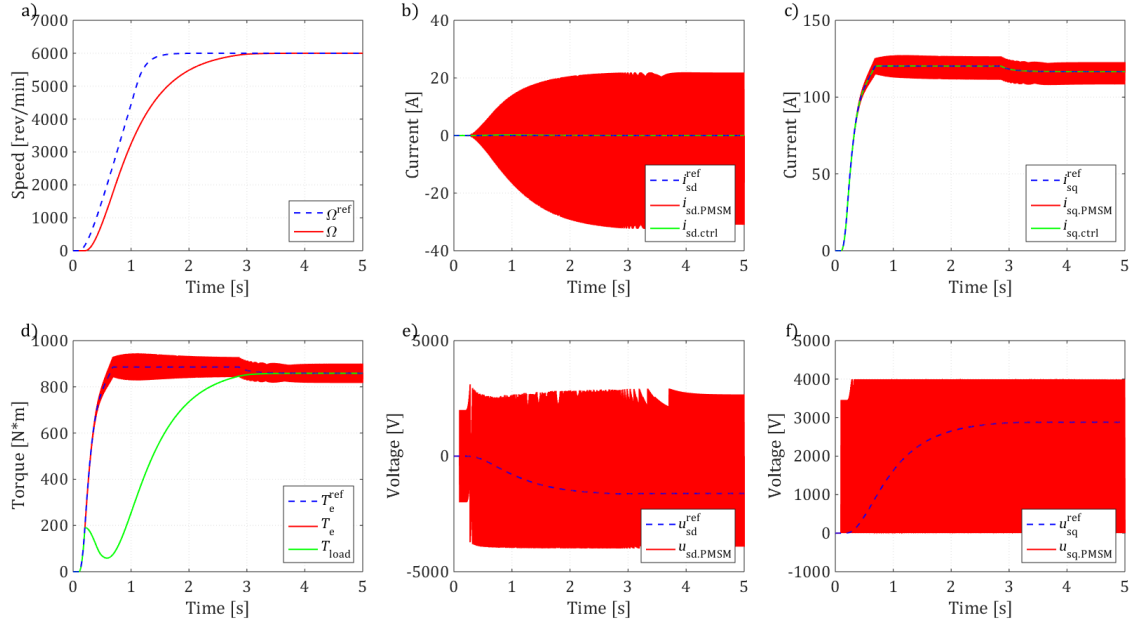Figure 7-22 Sensorless control (Model 3): speed, torque and dq quantities

| a) rotor speed | b) d-axis current | c) q-axis current |
| d) torque | e) d-axis voltage | f) q-axis voltage |
| g) speed estimation error | h) angle estimation error | i) abc currents |
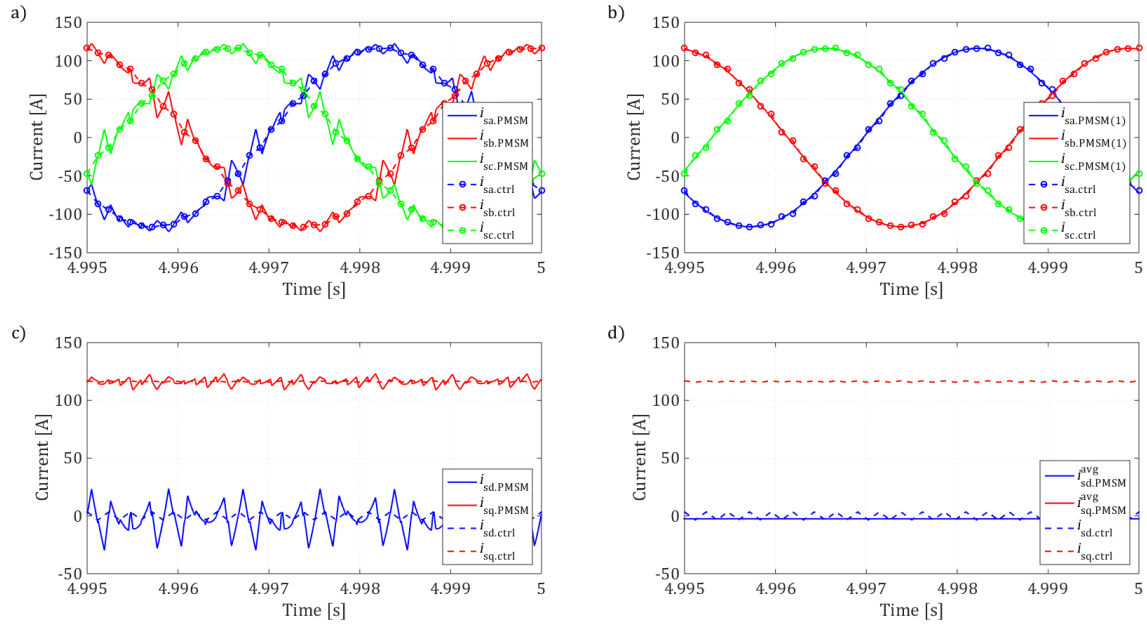
Figure 7-23 Sensorless control (Model 3): current sampling

a) abc frame current sampling

b) abc frame fundamental current

c) dq frame current sampling

d) dq frame average current

The real and sampled quantities are plotted in Figure 7-23 and compared in Table 7-8. The angle error in the real system is larger than the case with sensor in doubling sampling due to the error introduced by the sensorless control algorithm, but still lower than the case with sensor in single sampling.

Table 7-8 Real and sampled quantities comparison

Real quantities			Sampled quantities		
Quantities	Unit	Value	Quantities	Unit	Value
$i_{\text{sd·PMSM·avg}}$	[A]	-2.4970	$i_{\text{sd·ctrl·avg}}$	[A]	3.3189e-04
$i_{\text{sq·PMSM·avg}}$	[A]	116.0892	$i_{\text{sq·ctrl·avg}}$	[A]	116.3004
$\left\|i_{\text{s·PMSM·avg}}\right\|$	[A]	116.1161	$\left\|i_{\text{s·ctrl·avg}}\right\|$	[A]	116.3004
$\theta_{\text{i·PMSM}}$	[degree]	91.2322	$\theta_{\text{i·ctrl}}$	[degree]	89.9998

7.5   Transmission System Compensation

The transmission system including the transformer and the cable is added in this section. In the beginning, a voltage profile simulation is performed to investigate the effects from the length of the cable to the voltage distribution. Then follows the electric drive system simulation.

7.5.1   Voltage Profile

This voltage profile simulation is carried out in order to verify if the selected cable is suitable for the power transmission in the drive system and also to find out the voltage drop across the

transmission system under different load conditions. The parameters of the grid for the voltage profile study is decided as listed in Table 7-9.

Table 7-9 The parameters of the grid

Grid Voltage Source	$E_{line}^{nom \cdot rms}$	690 [V]
Short Circuit Current	$I_{SC}^{nom \cdot rms}$	4 [kA]

The grid short circuit capacity (SCC) is required by Simulink and can be calculated as

$$SCC = \sqrt{3}|E_{line}^{nom \cdot rms}||I_{SC}^{nom \cdot rms}| \qquad (7\text{-}26)$$

which is 4.78 MVA in the thesis work. Cases with different cable lengths are investigated in MATLAB / Simulink and the simulation circuit is presented in Figure 7-24. The parameters of the rectifier, the dc-link and the inverter are selected and presented in Appendix C. The base voltages are selected from the grid voltage source side (grid EMF) and transferred towards right by applying the voltage ratios of the rectifier, the inverter and the transformer. The base voltages are listed in

Table 7-10 and the simulation results in per unit are plotted as a voltage profile in Figure 7-25.
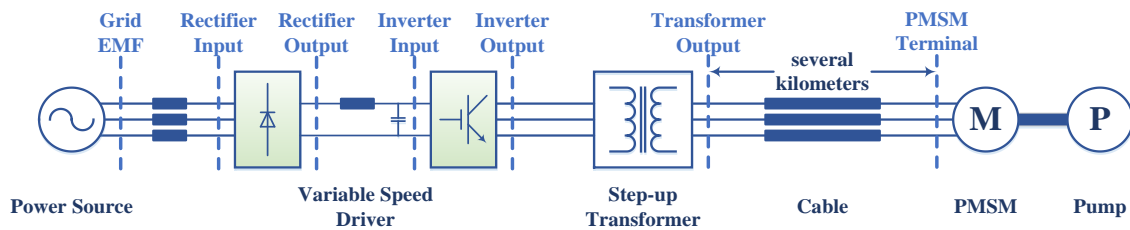
Figure 7-24 Voltage profile simulation circuit

Table 7-10 Voltage profile simulation base voltage [V]

	Grid EMF	Rectifier input	Rectifier output	Inverter input	Inverter output	Transformer output	PMSM terminal
Base	690.00	690.00	931.83	931.83	658.90	5020.20	5020.20
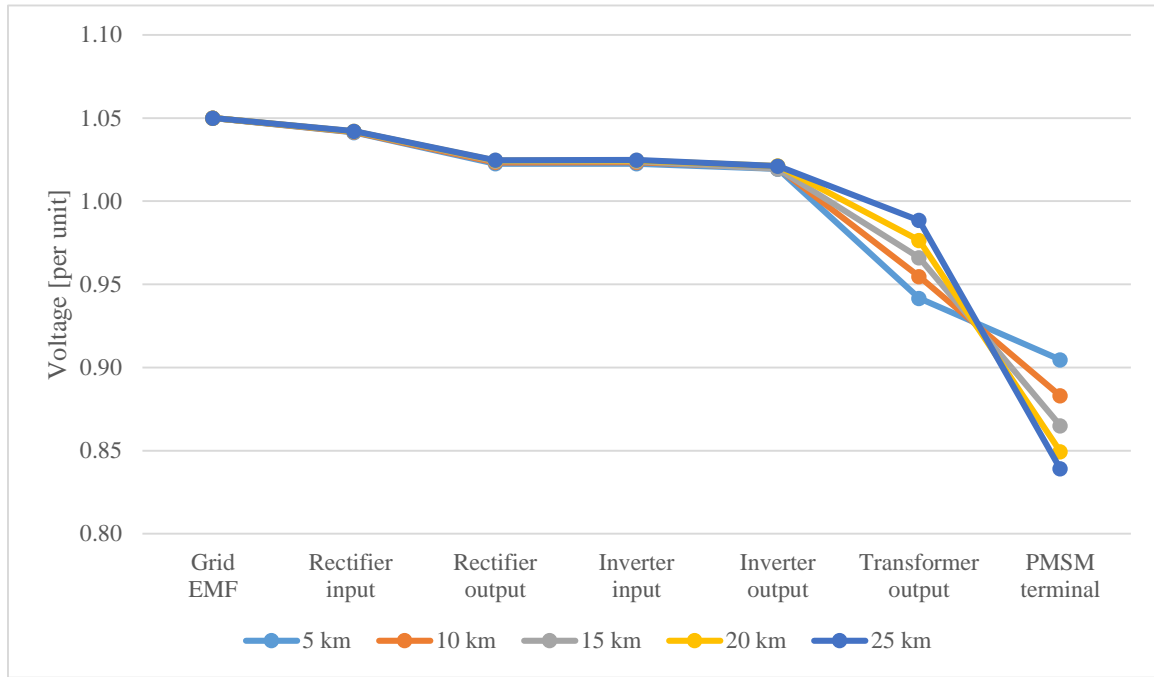
Figure 7-25 Voltage profile

As can be seen from Table 7-10 and Figure 7-25, the selection of the cable is suitable since the voltage drop over the cable is around 10% in the 15 km case. By comparing different cases, it can be concluded that a longer cable gives a larger voltage drop due to the increasing impedance and leads to a lower voltage at the receiving end. However, a longer cable also causes a higher voltage at the sending end due to the higher reactive power compensation by the larger equivalent capacitance of the cable. In addition, such a higher voltage at the sending end causes a lower current in the dc-link and further leads to higher voltages from the rectifier input until the inverter output. Although five cases are studied for the investigation of the effects from the cable length, the thesis work will only continue with the 15 km case which is required by the project.

7.5.2   Per Unit System

After the transformer is added, it becomes inconvenient to compare the voltages and currents on both sides of the transformer in volts and amps. Hence it is preferred to present the results in a per unit system. The base values used for the following simulations are selected and listed in Table 7-11.

Table 7-11 The per unit system base values

Variables	Primary Side Base Values	Secondary Side Base Values
$S_{3\phi}$	600 [kVA]	
Ω_{r}	6000 [rev/min]	6000 [rev/min]
T	796 [N·m]	796 [N·m]
$U_{\mathrm{line·rms}}$	551.25 [V]	4200 [V]
$U_{\mathrm{ph·amp}}$	450.0937 [V]	3429.2856 [V]
$I_{\mathrm{ph·rms}}$	628.4085 [A]	82.4786 [A]
$I_{\mathrm{ph·amp}}$	888.7038 [A]	116.6424 [A]

The controller parameters are accordingly adjusted. In addition, the step-up transformer is YNd11 connected which means the electric quantities on the low voltage side (primary side) lead the ones on the high voltage side (secondary side) by 30°. Hence the PMSM rotor angle needs to be shifted forward by 30° for the abc ↔ dq transformation in the controller so that the controller can work on the same dq frame as the secondary side.

7.5.3   Effects of the Transmission System

The transmission system is added as shown in Figure 6-1 (b), but the controller used in Section 7.1 (Model 1) is still applied here, which is kept unmodified in order to investigate the effects of the adding the transmission system into the control loop. The sensorless control algorithm is temporarily deactivated which means the position-sensor is used in this case so that the effects from the sensorless control algorithm will not appear. The successful start-up is shown in Figure 7-26. As can be noticed, it is the inverter current instead of the PMSM stator current that follows the reference. The speed still follows the reference in steady state, which indicates the right performance of the speed controller.

Since a positive d-axis current appears, a negative value of the reluctance torque term shows up and the total electromagnetic torque further decreases as has been illustrated in (2-13) and (2-15). Therefore, more q-axis current is required to produce enough electromagnetic torque and more q-axis voltage is needed consequently which can be noticed in Figure 7-26. In this way, an over-voltage of the inverter (over 120%) and an over-current of the PMSM (over 110%) occur to support the PMSM running at the target speed. In other words, the existence of a positive d-axis current requires a higher q-axis current which further increases the losses and therefore decreases the efficiency of the electric drive system.

The torque does not follow the reference in steady state since the torque reference corresponds to the inverter current reference, while the real torque corresponds to the PMSM stator current. Instead of controlling the real torque directly, the controller monitors and takes care of the q-axis inverter current. And since the real q-axis PMSM current is larger than the reference, the real electromagnetic torque is larger than the reference as well.
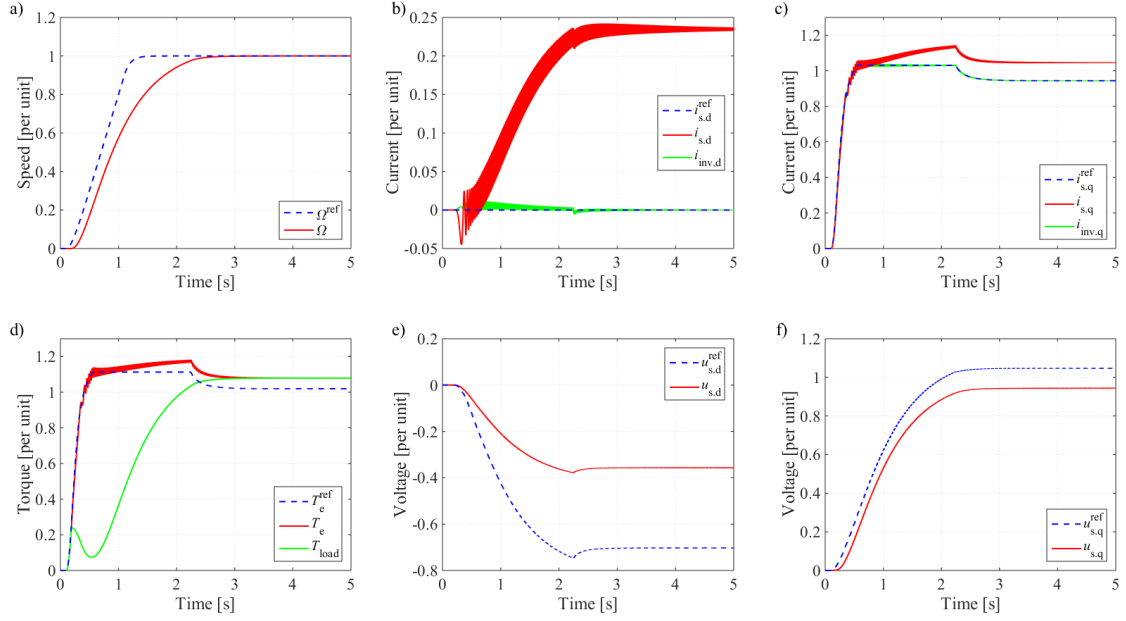
Figure 7-26 Effects of the transmission system: speed, torque and dq quantities

| a) rotor speed | b) d-axis current | c) q-axis current |
| d) torque | e) d-axis voltage | f) q-axis voltage |

The appearance of the d-axis current can also be understood by reactive power balance. Previously, since the d-axis stator current is kept as zero, the active and reactive power can be simplified as

$$p_s = \frac{3}{2}\text{Re}\{\underline{u}_s\underline{i}_s{}^*\} = \frac{3}{2}u_{sq}i_{sq} \tag{7-27}$$

$$q_s = \frac{3}{2}\text{Im}\{\underline{u}_s\underline{i}_s{}^*\} = -\frac{3}{2}u_{sd}i_{sq} \tag{7-28}$$

However, due to the voltage drop across the transmission system, the PMSM q-axis voltage becomes lower. And in order to bring the PMSM to the same operation point, the same amount of active power p_s and reactive power q_s are supposed to be delivered to the PMSM. Thus in order to satisfy the same p_s with a lower u_{sq} in (7-27), the q-axis current i_{sq} needs to be higher. However, the d- and q-axis voltages do not drop by the same ratio across the transmission system, which means when the active power equation (7-27) is satisfied by a larger q-axis current, the reactive power equation (7-28) is not satisfied. Therefore, a d-axis current must be introduced to keep the reactive power equation (7-28) in balance, which means

$$p_s = \frac{3}{2}\text{Re}\{\underline{u}_s\underline{i}_s{}^*\} = \frac{3}{2}\left(u_{sd}i_{sd} + u_{sq}i_{sq}\right)$$
$$q_s = \frac{3}{2}\text{Im}\{\underline{u}_s\underline{i}_s{}^*\} = \frac{3}{2}\left(u_{sq}i_{sd} - u_{sd}i_{sq}\right) \tag{7-29}$$

Table 7-12 lists the active power and the reactive power sent from the inverter output, received by the PMSM stator and the consumption by the transmission system which is the gap between the previous two.

Table 7-12 Average and reactive power in steady state ($4 \text{ s} < t < 5 \text{ s}$)

	Active power [kW]	Reactive power [kVar]
Inverter output	592.8022	398.0314
PMSM stator	541.9698	356.8842
Transmission system consumption	50.8325	41.1472

Table 7-12 indicates that quite a lot active power and reactive power are consumed by the transmission system. Nevertheless, as has been illustrated before, the inverter d-axis current i_{invd} is kept at zero in this unmodified controller case which means

$$
\begin{aligned}
p_{\text{inv}} &= \frac{3}{2} \text{Re}\{\underline{u}_{\text{inv}} \underline{i}_{\text{inv}}{}^*\} = \frac{3}{2}\left(u_{\text{invd}} i_{\text{invd}} + u_{\text{invq}} i_{\text{invq}}\right) = \frac{3}{2} u_{\text{invq}} i_{\text{invq}} \\
q_{\text{inv}} &= \frac{3}{2} \text{Im}\{\underline{u}_{\text{inv}} \underline{i}_{\text{inv}}{}^*\} = \frac{3}{2}\left(u_{\text{invq}} i_{\text{invd}} - u_{\text{invd}} i_{\text{invq}}\right) = -\frac{3}{2} u_{\text{invd}} i_{\text{invq}}
\end{aligned}
\tag{7-30}
$$

This is not an efficient way to generate reactive power q_{inv} since a high u_{invq} is needed to deliver the active power p_{inv} anyway, and if a non-zero i_{invd} exists, then a large term $u_{\text{invq}} i_{\text{invd}}$ will appear and contribute to q_{inv}. Therefore, further compensation is going to be made in order to inject some i_{invd} to contribute to a more efficient reactive power delivery.

Current and torque oscillations can be detected as shown in Figure 7-26 (b), (c) and (d). The oscillation frequency is found to be synchronous with the rotor speed. Therefore, such oscillation should be caused by a DC component in the circuit. In the beginning of the PMSM start-up, current is injected into the system from the inverter while the PMSM stands still since the generated electromagnetic torque is still lower than the static friction torque. Hence the dq frame stands still and the applied voltage vector points at the same direction in the αβ frame before the PMSM starts to rotate. Therefore, a DC voltage is applied and a DC current is injected into the system. Then after the PMSM starts to rotate, the dq frame also starts to rotate and the applied voltage is changed from DC to AC. However, since the transmission system performs as a low pass filter, the DC voltage and current components will remain in the system for quite some time, mainly in the magnetization shunt branch of the transformer.

Since the current controller is implemented in the dq frame, from the controller's point of view, the DC component in the αβ frame is an AC component rotating backwards at the frequency of ω_{r} in the dq frame. In order to eliminate the effect of the DC component, a DC current controller can be implemented so that an additional voltage reference can be added to the output of the inverter to force the DC current to zero quickly. An alternative is to neglect the DC component since it will be damped by the resistance in the system automatically. In this thesis, since the DC component is not large enough to affect the stability of the system, the second option to just neglect the oscillations is taken.

In addition, it can be found out that the inverter voltage also contains some small oscillations. The reason is that the current controller can be regarded as a low pass filter, and since the current oscillation frequency (0 - 200 Hz) is not too high compared with the bandwidth of the current PI regulator (100 Hz), the oscillations from the input of the current controller still remains as part of the output and therefore, an oscillating voltage is output from the inverter. As can be seen from Figure 7-26 (b), (c) and (d), the current oscillations are damped out gradually by the resistance of the circuit throughout the start-up.

7.5.4   Equivalent Induction Machine Current Controller (Model 7)

As has been introduced in Section 6.2, an equivalent IM model is built which regards the entire electric drive system as an equivalent induction machine.

Current Step Tests

Small current step tests are firstly applied to verify the performance of the equivalent IM model as shown in Figure 7-27. The applied d- and q-axis current steps are small enough so that the PMSM speed is kept at zero throughout the test.
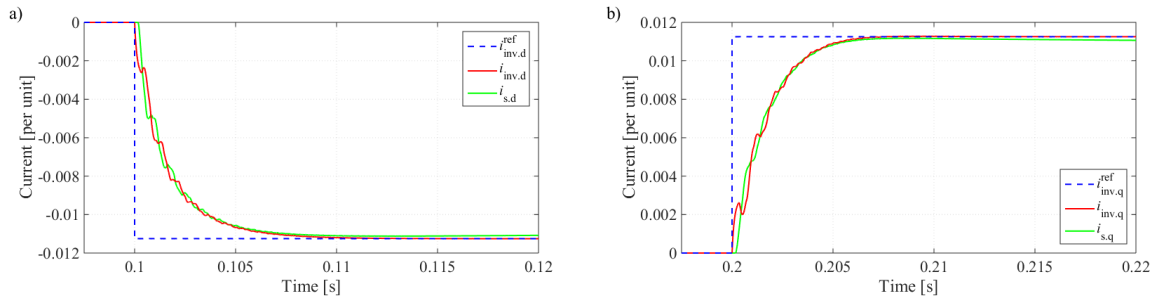
Figure 7-27 Equivalent induction machine model current controller

a) d-axis inverter current   b) q-axis inverter current

The current curves in Figure 7-27 are a little disturbed by the shunt currents in the transmission system but the general shape reveals as an exponential function which indicates that the current controller responds as a first-order system. The d-axis current rise time is 3.8 ms and the q-axis current rise time is 3.5 ms. The main reason of the 3.8 ms d-axis current rise time may be that

$b_\mathrm{d} = b_\mathrm{q}$ is applied as presented in Section 6.2.2 which leads to an approximate model and further an inaccurate rise time.

Speed Control

The equivalent IM model controller is applied with speed control (Model 7) which structure is shown in Figure 6-2 but with the sensorless control estimator block deactivated, which means position and speed feedbacks are applied. The inverter current reference is calculated by adding the PMSM stator current reference with the shunt current estimation from a state space model. The successful start-up of the PMSM and the performance of the dq frame quantities are shown in Figure 7-28. The compensation works quite well as the inverter current is adjusted and the

PMSM stator current follows the reference. Oscillations at the speed frequency occur in the dq frame currents due to the DC component generated in the transformer magnetizing branch before the rotation starts. In order to compensate for the voltage across the transmission system, higher dq frame voltages are applied at the terminal of the inverter compared to the dq frame voltages at the terminal of the PMSM.

The performance of the state space model is shown in Figure 7-29. In the state space model, the cable is represented by 1 π-section, while in the real system, the cable is represented by 15 π-sections. Therefore, such difference leads to some estimation errors. As can be seen, the estimation errors are quite small and it can be concluded that it is possible to use a 1 π-section model for the cable in the controller. However, parameter errors are not introduced here which means the model uses perfect values of the resistance, inductance and capacitance per unit length of the real cable in the controller. The robustness of the state space model is not the focus of this thesis work and therefore, in the following simulations, the state space model will be replaced with a static estimator and another current measuring point will be added after the transformer as has been described in Section 6.1.
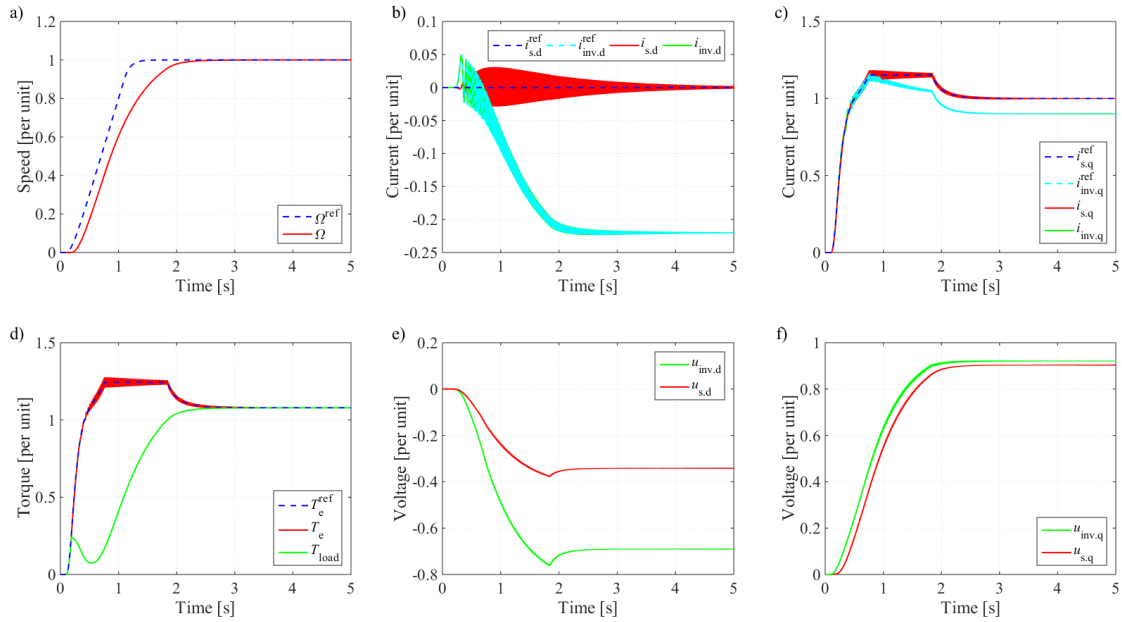
Figure 7-28 Equivalent IM model performance (Model 7): speed, torque and dq quantities

a) rotor speed   b) d-axis current   c) q-axis current

d) torque   e) d-axis voltage   f) q-axis voltage
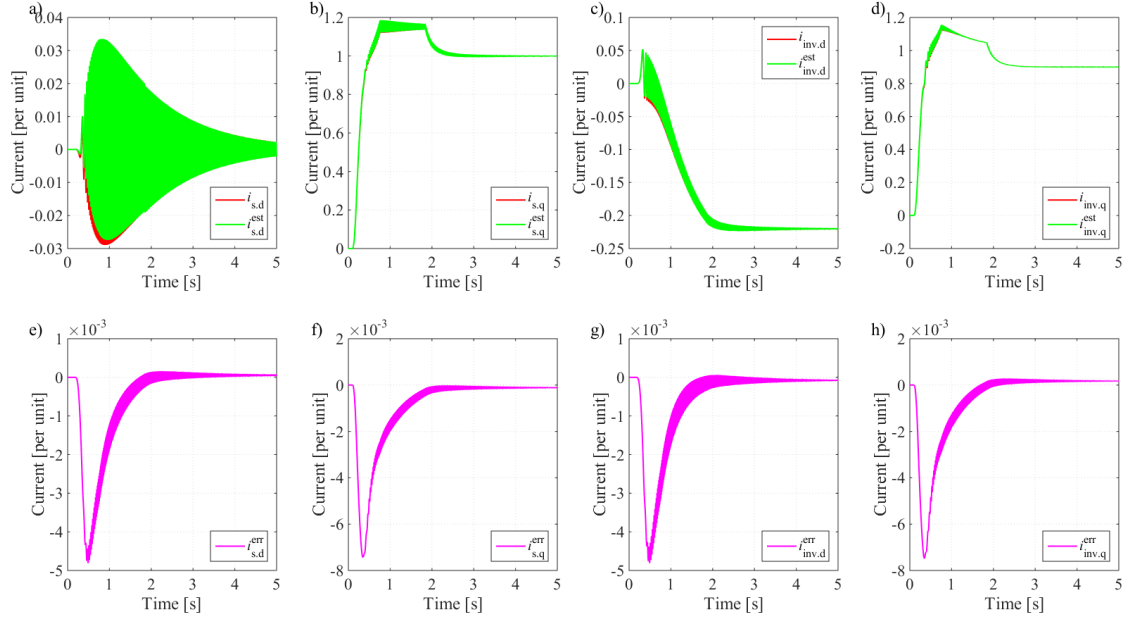
Figure 7-29 Equivalent IM model performance (Model 7): state space model estimations

a) d-axis stator current   b) q-axis stator current   c) d-axis inverter current   d) q-axis inverter current

e) d-axis stator current   f) q-axis stator current   g) d-axis inverter current   h) q-axis inverter current
   estimation error   estimation error   estimation error   estimation error

The shunt currents are plotted in Figure 7-30. The total shunt current i_{shunt} can be decomposed into a component from the transformer excitation branch i_{exc} and a component from the cable capacitive branch i_{cap}. Furthermore, the transformer excitation branch current i_{exc} can be decomposed into a magnetization branch current i_{mag} going through L_{Tm} and a core loss branch current i_{core} going through R_{Tc}. As can be clearly seen from the figure, the oscillations mainly come from the transformer magnetizing branch while the DC current deviation mainly comes from the cable capacitive branch.
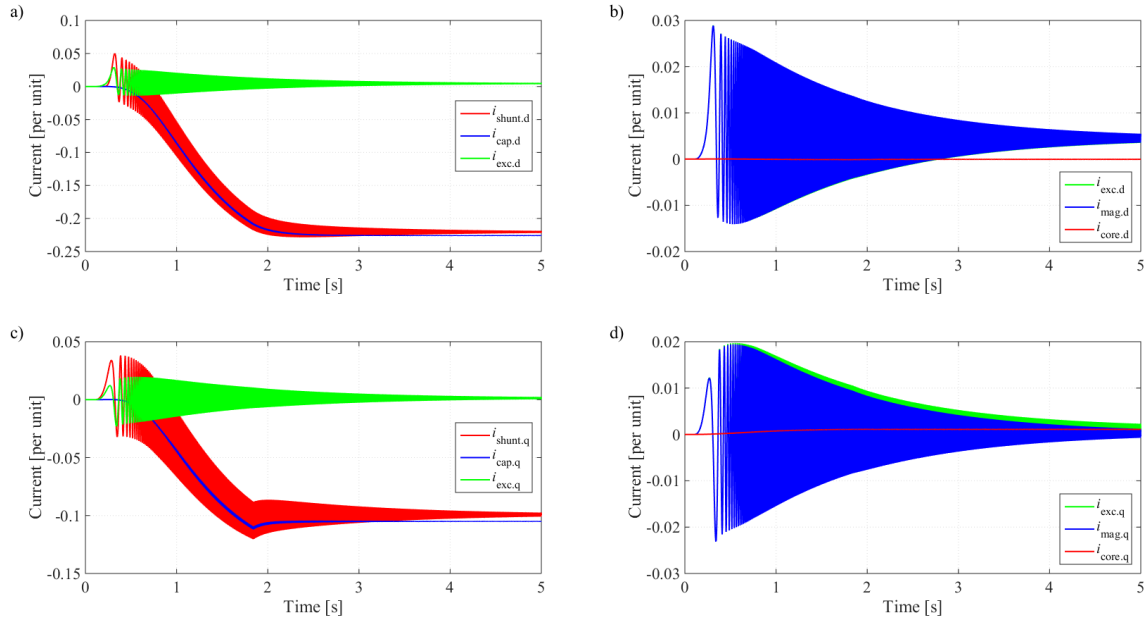
Figure 7-30 Equivalent IM model performance (Model 7): shunt currents

i_{shunt} is the total shunt current, i_{cap} is the cable capacitive shunt current, i_{exc} is the total transformer excitation shunt current, i_{core} is the core loss current going through the R_{Tc} branch and i_{mag} is the magnetization current going through the L_{Tm} branch.

a) d-axis capacitor current and excitation current

b) d-axis magnetizing current and core current

c) q-axis capacitor current and excitation current

d) q-axis magnetizing current and core current

7.5.5   Sensorless Control (Model 8)

Here the configuration in Figure 6-2 is applied with all the blocks activated. The SCVM estimator is applied at first which is followed by the HFI estimator, and in the end the combination of the two algorithms will be applied.

SCVM

SCVM is implemented with the damping factor $\lambda = 0.5$. The performance of the controller is shown in Figure 7-31. A significant oscillation at the PMSM rotation frequency is detected from 0.9 to 1.9 s in the estimator performance subplots (g) and (h), during which time interval, the speed controller hits the limit as the torque and current saturate as shown in (b), (c) and (d). At the same time, the d-axis current oscillation suddenly increases and then reduces to zero at 1.9 s. However, after 1.9 s, the d-axis current oscillation comes back again. The frequency of such oscillation between 0.9 and 1.9 s is at the PMSM rotation frequency, which should be due to the DC component in the circuit. The increase of the oscillation amplitude between 0.9 and 1.9 s is unexpected and the reason is still not clear.
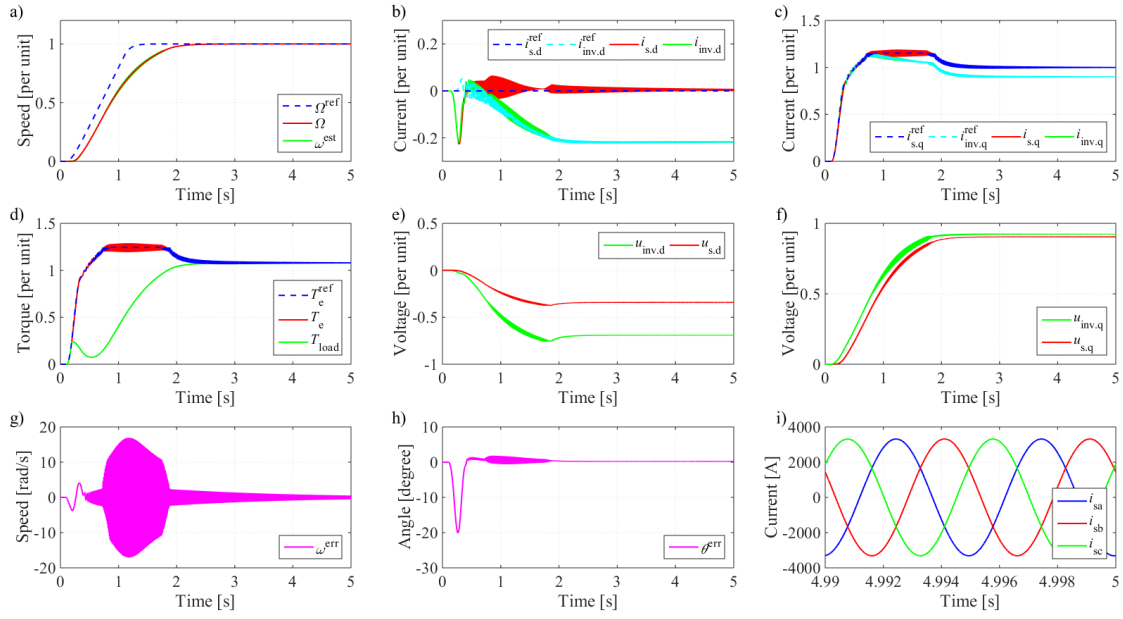
Figure 7-31 SCVM performance (Model 8): speed, torque, estimation, abc and dq quantities

a) rotor speed	b) d-axis current	c) q-axis current
d) torque	e) d-axis voltage	f) q-axis voltage
g) speed estimation error	h) angle estimation error	i) abc currents

HFI

The HFI algorithm has been restructured as illustrated in Section 6.3.2. As has been discussed in Section 6.3.2, the injection frequency is selected at 400 Hz and the scaling factor has also been modified by approximating the transfer function. Figure 7-32 shows the successful start-up of the PMSM under the HFI estimation as the speed catches the reference within 3 s. The d- and q-axis PMSM stator voltages have a lower oscillation level compared with the inverter voltages as can be seen in subplots (e) and (f) due to the damping of the transmission system. The d-axis PMSM current and the average of the electromagnetic torque clearly deviate from the references which indicates a steady state angle estimation error. (g) and (h) clearly shows a speed estimation error of zero but an angle estimation error of about 10 degrees in steady state. As has been illustrated in Section 6.3.2, the error should be caused by the amplitude mismatch and the phase mismatch between the simplified transfer function and the real transfer function. However, since the HFI will be applied only in the beginning of the start-up to help SCVM, such an angle estimation error is not a big problem.

It should be pointed out that, at about 0.6 to 0.7 s, a small estimation oscillation happens which may be due to the sudden change of the current reference. The sudden change of the current reference causes a sudden change of the current which contains large amount of high frequency components. The filter before the HFI estimator cannot clear these components out since they are within the same frequency region as the injected HF signal. Therefore, these signals disturb the HFI. After this sudden change of the current, the HFI estimation curve becomes smooth again. Another observation can be made is that the three-phase current curves in Figure 7-32 (i)

are much smoother than the ones in Figure 7-4 (i) due to the filtering of harmonics by the transmission system.
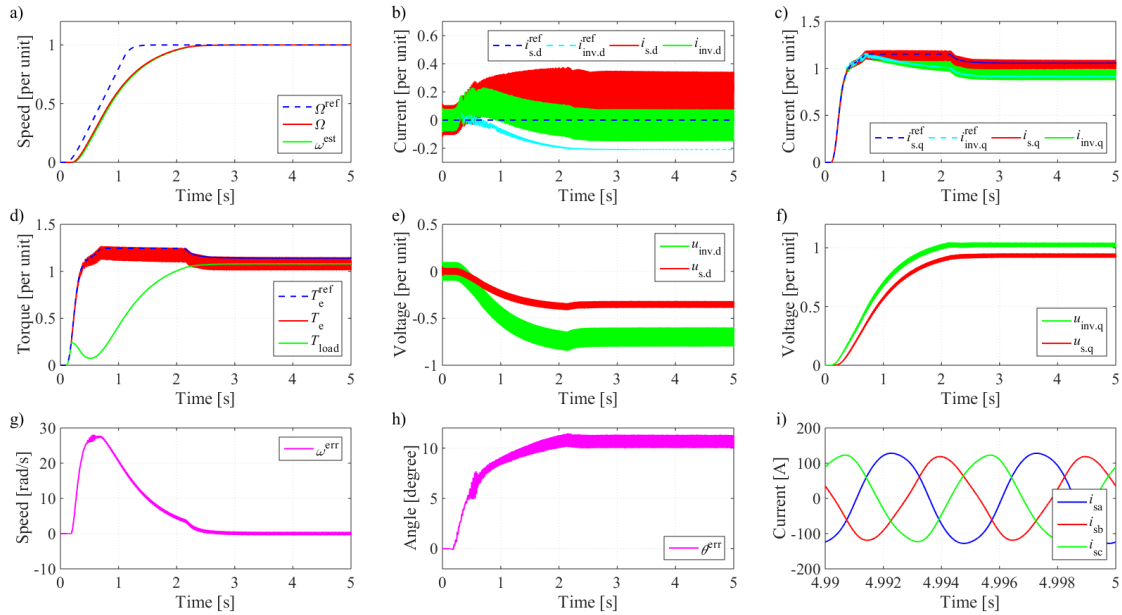
Figure 7-32 HFI performance (Model 8): speed, torque, abc and dq quantities

a) rotor speed	b) d-axis current	c) q-axis current
d) torque	e) d-axis voltage	f) q-axis voltage
g) speed estimation error	h) angle estimation error	i) abc currents

Combination of SCVM and HFI

Figure 7-33 shows the performance of the combination of the SCVM and HFI with the shunt compensation. The HFI is again totally faded out at about 0.7 s as can be noticed in (b) and (e). The speed and angle estimation errors in steady state are eliminated and a smooth three-phase current is obtained in (i) as expected. The maximum angle estimation error here is smaller compared with the cases of pure SCVM and pure HFI. The d- and q-axis current curves are similar to the ones in the SCVM case but the -0.2 p.u. d-axis current deviation at about 0.3 s in the SCVM case in Figure 7-31 (b) disappears here due to the cooperation between SCVM and HFI.

Figure 7-34 shows the speed estimation contributed by the SCVM and HFI respectively. As can be detected, the SCVM gives an over estimation of the speed while HFI gives a negative compensation in the beginning which pulls the total speed estimation back to around the real speed. The conclusion can again be made that, after adding the transmission system, the combination still works better than each of the two algorithms respectively.
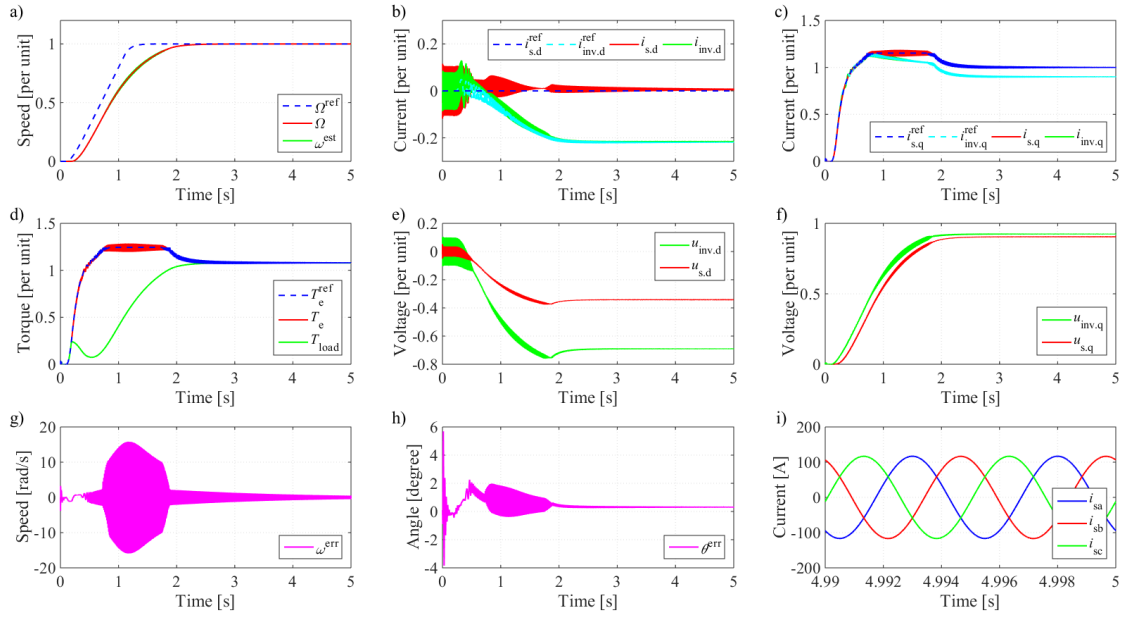
Figure 7-33 Combination of SCVM and HFI performance (Model 8): speed, torque, abc and dq quantities

| a) rotor speed | b) d-axis current | c) q-axis current |
| d) torque | e) d-axis voltage | f) q-axis voltage |
| g) speed estimation error | h) angle estimation error | i) abc currents |
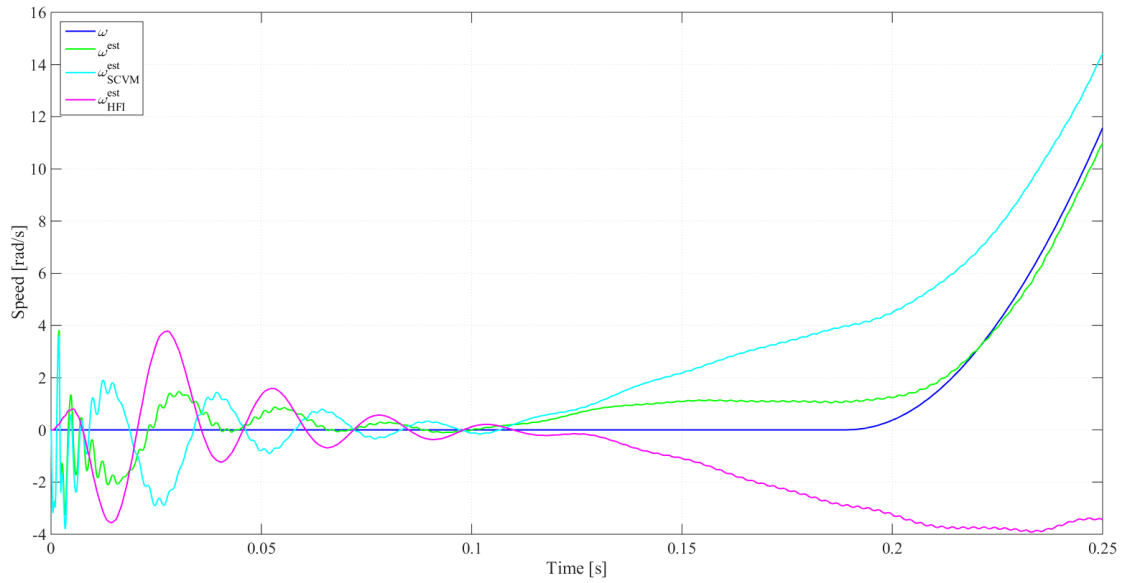
Figure 7-34 Combination of SCVM and HFI performance (Model 8): merged estimation

7.5.6 Realistic Converter with Discrete Controller (Model 9)

Control with sensor is implemented in the beginning which is followed by sensorless control.

Control with Sensor

Direct application of the previous two-level inverter cannot bring the PMSM up to 6000 rev/min maybe due to triggering of the transmission system resonances. Therefore, several improvements have been made. An L filter is added before the transformer to shift the transmission system resonance frequencies to a lower region and the five-level inverter is applied instead of the two-level inverter to shift the switching harmonics to a higher frequency region.

Such two improvements can boost the PMSM up to over 5000 rev/min but still lower than 6000 rev/min. Then another attempt is applied which is to update the SVPWM switching pattern every half of the switching cycle to obtain a faster response of the current controller. However, this configuration breaks the SVPWM symmetry in one switching cycle as indicated in Figure 5-5, and risks a higher amount of harmonics. In addition, the harmonics cause more power loss, and in order to deliver the necessary power, the current limit should be designed a little higher than before.

The performance is given in Figure 7-35, where the speed rises up to 1 p.u. within 3 s which indicates a successful start-up. Voltage and current oscillations are caused by the switching operations. The sampled currents have lower oscillation amplitudes than the real current in the system as can be seen in (b), which is expected by applying the instantaneous sampling technique as illustrated in Section 5.3.1. Both the inverter current and the PMSM stator current follow the references.

Figure 7-35 Control with sensor performance (Model 9): speed, torque and dq quantities

| a) rotor speed | b) d-axis current | c) q-axis current |
| d) torque | e) d-axis voltage | f) q-axis voltage |

The shunt currents are plotted in Figure 7-36, and Figure 7-37 shows the three-phase quantities. The tendency of the estimated shunt currents shown in Figure 7-36 (a) and (d) match the tendency of the real shunt currents with a lower oscillation amplitude, which indicates the

success of the shunt current estimation. The currents though the transformer magnetizing branch shown in Figure 7-36 (c) and (f) almost remain the same compared with the ideal converter case, which indicates that the transformer magnetizing branch cannot conduct the harmonics effectively. As a result, the current curves are kept the same from the inverter output in Figure 7-37 (a) to the transformer output in Figure 7-37 (b). However, instead of the smooth curves in the ideal converter case shown before, the shunt currents through the capacitive branches shown in Figure 7-36 (b) and (e) contain a large amount of harmonics in this realistic converter case. As a result, the current curves become much more sinusoidal from Figure 7-37 (b) to (c).

The phenomenon can be understood with the help from the circuit in Figure 6-3. The transformer magnetizing branch is composed by a high resistance and high inductance, and therefore cannot conduct the switching harmonics efficiently, which means the magnetizing branch can be neglected and the inverter current in Figure 7-37 (a) is equal to the transformer output current in Figure 7-37 (b). The switching harmonic current generates a voltage drop at the harmonic frequency over the transformer series impedance. Hence the remaining transformer output voltage in Figure 7-37 (e) is much more sinusoidal than the inverter PWM voltage in Figure 7-37 (d).

When the current enters the cable, the shunt capacitor provides the harmonic current with a higher admittance ωC than the series inductive admittance $\frac{1}{\omega L}$ in the high frequency region.

Therefore, the PMSM stator current in Figure 7-37 (c) is much smoother than the cable input current in Figure 7-37 (b). In addition, the nearly sinusoidal shape current leads to a nearly sinusoidal shape voltage across the cable series impedance which means the high frequency harmonic voltage components are not consumed by the cable. Hence the input and output voltages of the cable are almost the same as can be seen by comparing Figure 7-37 (e) and (f). Therefore, it can be concluded that, the three-phase current waveforms are smoothened into sinusoids mainly by the cable while the three-phase voltage waveforms are smoothened mainly by the transformer.

In addition, in Figure 7-36 (a) and (d), the static estimation gives much smoother shunt current estimations than the real shunt currents. The static estimations only contain the oscillations caused by the DC component as the oscillation frequency is at the speed frequency, while the real oscillations also contain the switching harmonics. This results in a lower oscillating inverter current reference as shown in Figure 7-35 (b) and (c).
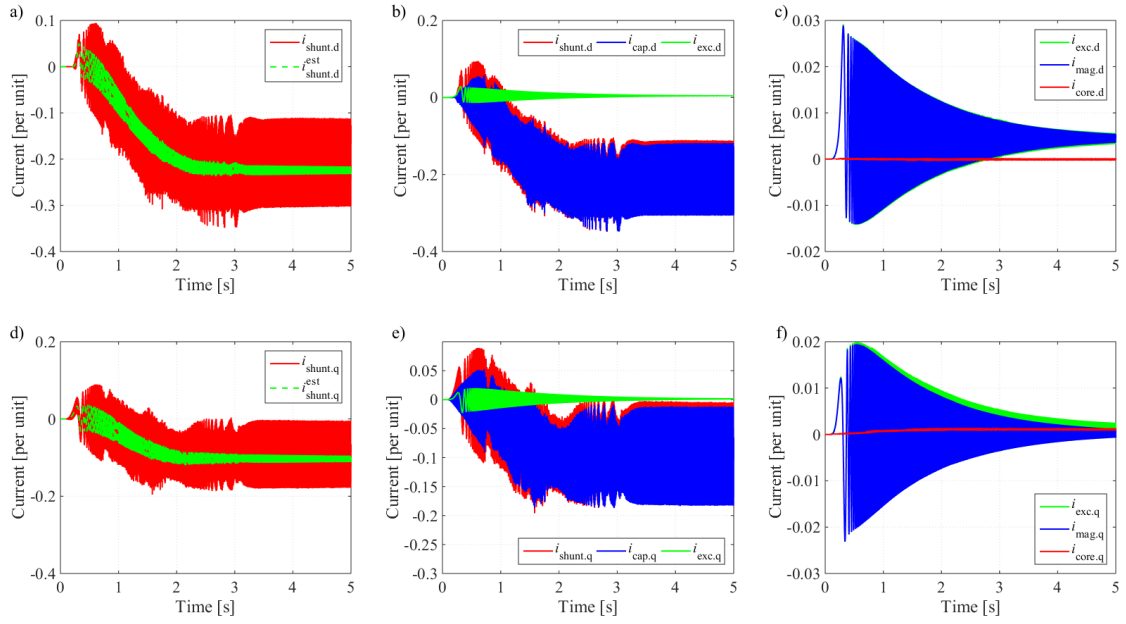
Figure 7-36 Control with sensor performance (Model 9): shunt currents

a) d-axis total shunt current	b) d-axis capacitor current and excitation current	c) d-axis magnetizing current and core current
d) q-axis total shunt current	e) q-axis capacitor current and excitation current	f) q-axis magnetizing current and core current
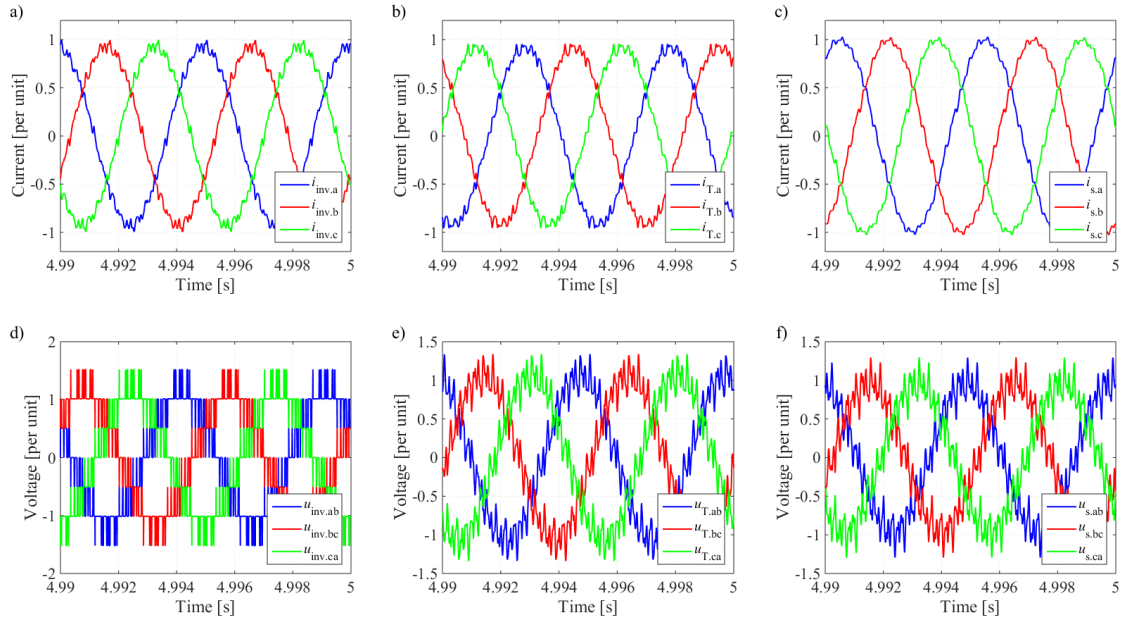
Figure 7-37 Control with sensor performance (Model 9): abc quantities

a) inverter currents	b) transformer currents	c) PMSM stator currents
d) inverter voltages	e) transformer voltages	f) PMSM stator voltages

112
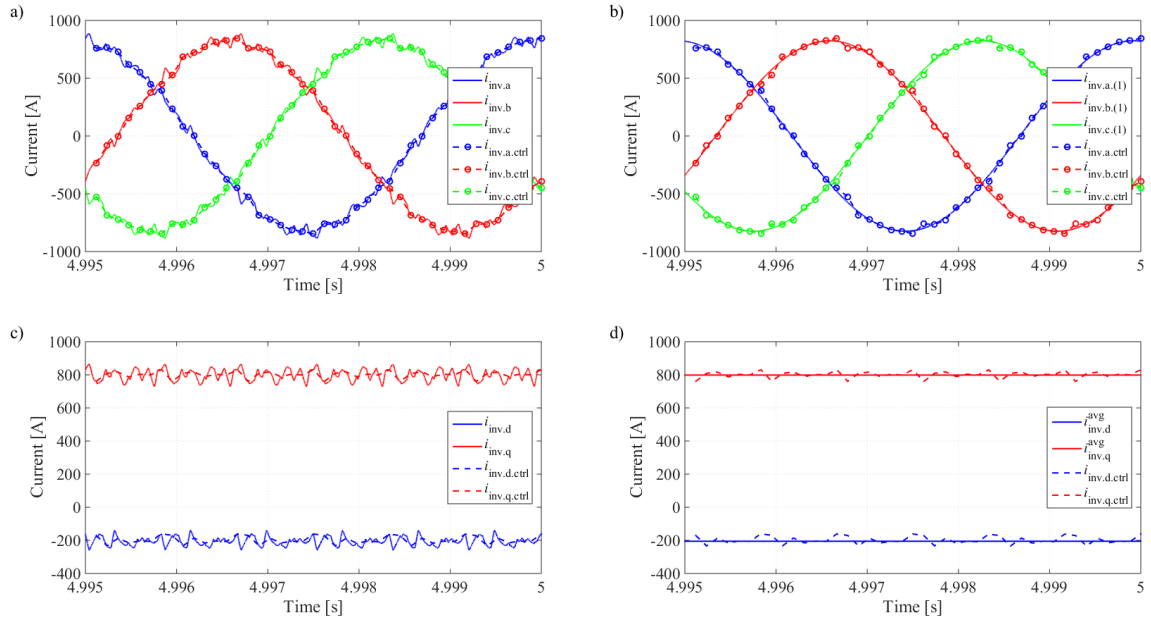
Figure 7-38 Control with sensor performance (Model 9): current sampling

a) abc frame current sampling b) abc frame fundamental current

c) dq frame current sampling d) dq frame average current

The current samplings are illustrated in Figure 7-38. The current sampling jumps between leading and lagging the fundamental component. The corresponding detailed data for steady state performance is listed in Table 7-13 and Table 7-14. As can be seen, $\theta_{i\cdot inv} > \theta_{i\cdot s}$, which indicates the averaged inverter current vector leads the averaged stator current vector. Both the inverter current vector sampled by the controller and the stator current vector estimated by the controller lags the real current vectors since $\theta_{i\cdot inv} > \theta_{i\cdot ctrl}$ in Table 7-13 and $\theta_{i\cdot s} > \theta_{i\cdot s\cdot est}$ in Table 7-14. The angle error of the PMSM flux linkage orientation $\theta_{i\cdot s} - \theta_{i\cdot s\cdot est}$ is as small as 0.7 degree, which proves a successful shunt current estimation and compensation.

Table 7-13 Comparison of the real and sampled inverter current vector

Real quantities			Sampled quantities		
Quantities	Unit	Value	Quantities	Unit	Value
$i_{inv.d\cdot avg}$	[per unit]	-0.2308	$i_{inv.d\cdot ctrl\cdot avg}$	[per unit]	-0.2217
$i_{inv.q\cdot avg}$	[per unit]	0.8982	$i_{inv.q\cdot ctrl\cdot avg}$	[per unit]	0.9016
$\left\|i_{inv\cdot avg}\right\|$	[per unit]	0.9273	$\left\|i_{inv\cdot ctrl\cdot avg}\right\|$	[per unit]	0.9284
$\theta_{i\cdot inv}$	[degree]	104.4125	$\theta_{i\cdot ctrl}$	[degree]	103.8153

Table 7-14 Comparison of the real and estimated PMSM stator current vector

Real quantities			Estimated quantities		
Quantities	Unit	Value	Quantities	Unit	Value
$i_{sd \cdot avg}$	[per unit]	-0.0119	$i_{sd \cdot est \cdot avg}$	[per unit]	6.7021e-06
$i_{sq \cdot avg}$	[per unit]	0.9972	$i_{sq \cdot est \cdot avg}$	[per unit]	1.0032
$\left\| i_{s \cdot avg} \right\|$	[per unit]	0.9973	$\left\| i_{s \cdot est \cdot avg} \right\|$	[per unit]	1.0032
$\theta_{i \cdot s}$	[degree]	90.6863	$\theta_{i \cdot s \cdot est}$	[degree]	89.9996

Sensorless Control

In the end, the combination of SCVM and HFI is applied with the five-level realistic converter which is the final version (Model 9) in this thesis work. Figure 7-39 shows the speed, torque and dq quantities which indicate a successful start-up of the PMSM with this finial structure as the speed goes to 1 per unit before 3 s and the electrical quantities are gradually stabilized after 3 s. Before 0.5 s, the dq voltage and current oscillations are due to both the HF injection and the switching harmonics since the HF injection is modulated by the SVPWM. This part before 0.5 s is the major difference between the sensorless control case in Figure 7-35 and the control with sensor case in Figure 7-39. After 0.5 s, the HFI is faded out quickly and therefore the voltage and current oscillations are only caused by the switching harmonics. This part after 0.5 s is almost the same for the sensorless control case in Figure 7-35 and the control with sensor case in Figure 7-39.
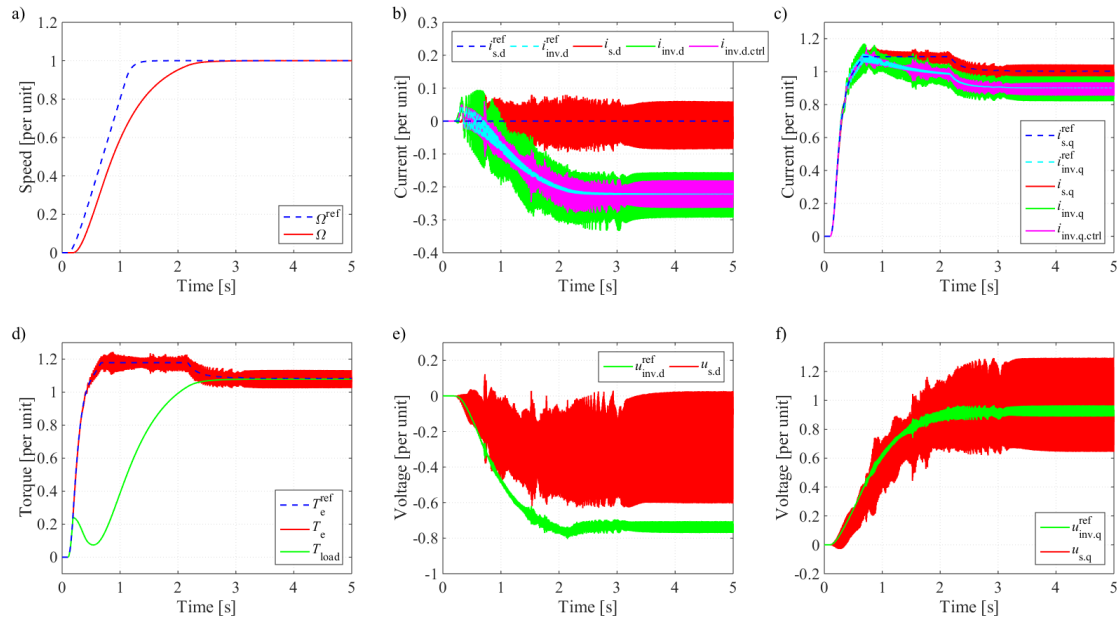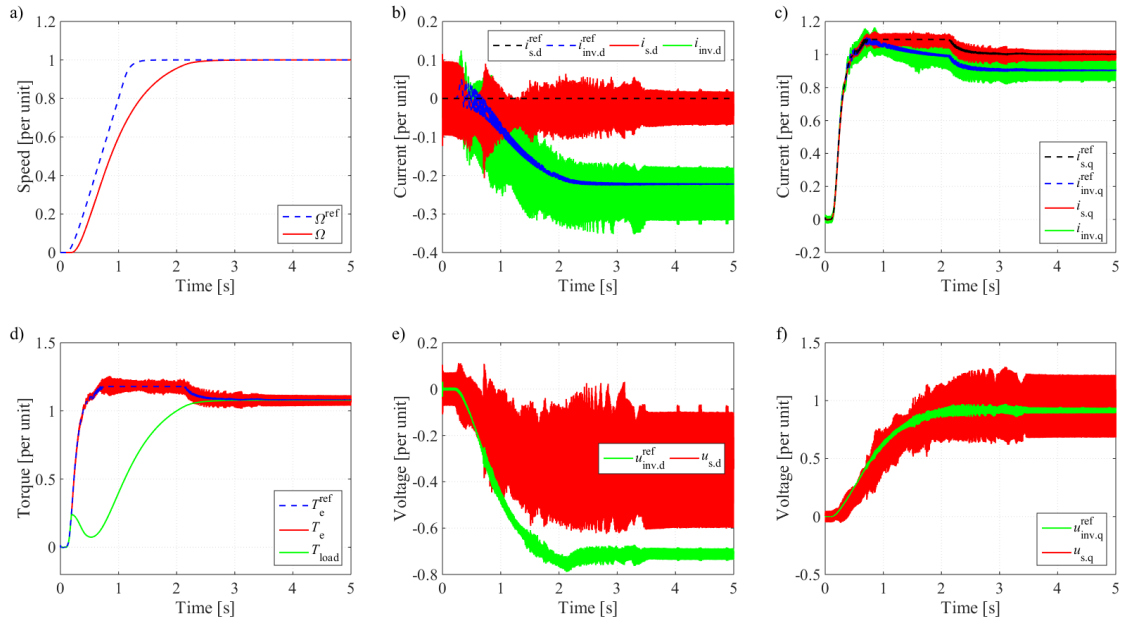

Figure 7-39 Sensorless control performance (Model 9): speed, torque and dq quantities

a) rotor speed   b) d-axis current   c) q-axis current

d) torque   e) d-axis voltage   f) q-axis voltage

The corresponding steady state performance is shown in Figure 7-40. The fluctuations of electrical quantities can be detected from the time domain plot between 4.99 s and 5 s. The periodical oscillations indicate that the PMSM has entered steady state. In order to figure out the harmonic contents of the dq frame currents, an FFT is performed on the steady state dq currents and the results are shown in Figure 7-41. Some major current harmonics are detected from the frequency domain and they are listed in Table 7-15.
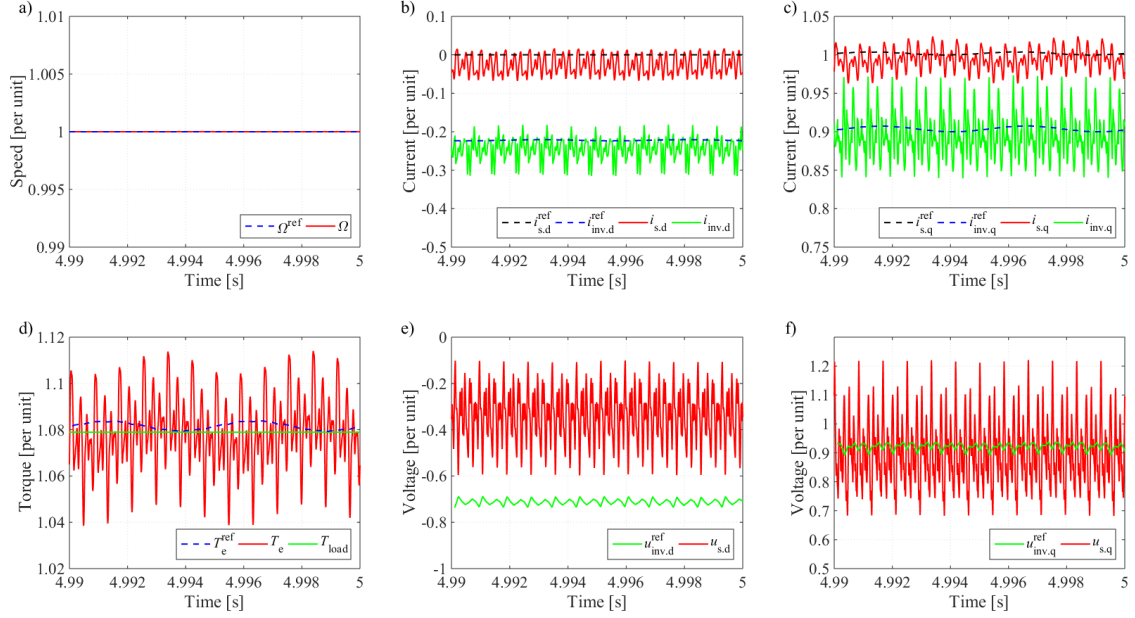
Figure 7-40 Sensorless control performance (Model 9): speed, torque and dq quantities in steady state

a) rotor speed   b) d-axis current   c) q-axis current

d) torque   e) d-axis voltage   f) q-axis voltage
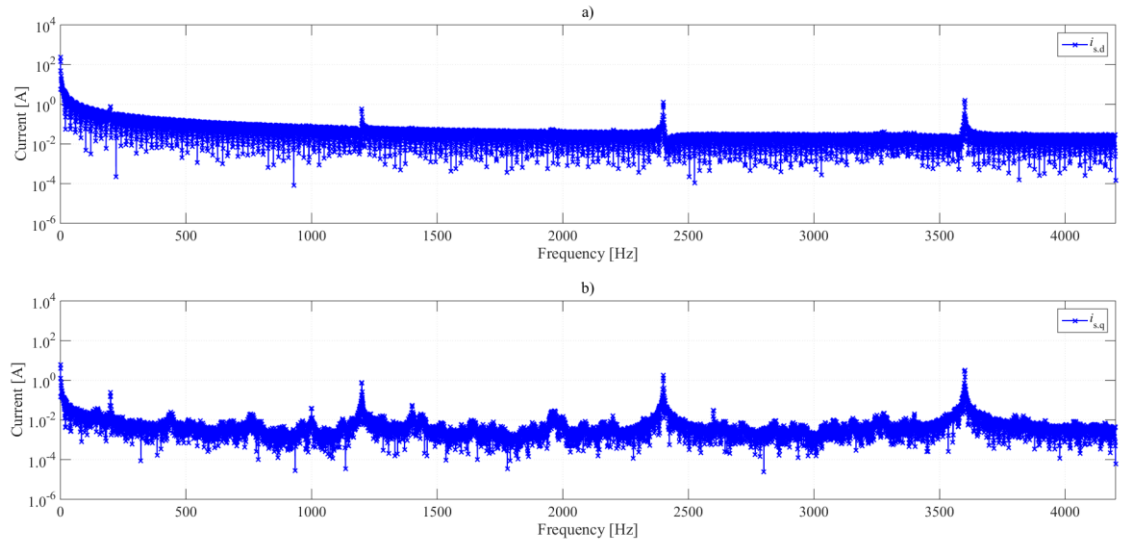
Figure 7-41 Sensorless control performance (Model 9): FFT of dq currents

(a) FFT of d-axis stator current

(b) FFT of q-axis stator current

115

Table 7-15 Major current harmonic contents

		Category 1	Category 2		
f	[Hz]	200	1200	2400	3600
$|i_{\text{sd}}|$	[A]	0.7764	0.5583	1.291	1.566
$|i_{\text{sq}}|$	[A]	0.2466	0.7464	1.803	3.31

The current harmonics can be classified into two categories: one is at 200 Hz which should be caused by the residual DC component remaining in the circuit, while the other group of components may be because of the transmission system resonance shown in Figure 2-8 triggered by the harmonics in the system and the switching harmonics shown in Figure 7-17. In addition, it can be observed that the d-axis current spectrum is quite smooth compared with the q-axis current spectrum which reason is not obvious to find out.

Figure 7-42 (a) and (d) shows the performance of the sensorless control estimator. The speed estimation error goes to zero while the angle estimation error is stabilized within -0.85 degree which is due to the error from the static estimator. However, a relative large estimation oscillation occurs at about 0.76 s. The HFI is deactivated totally at about 0.5 s and therefore, such oscillation should attribute to the SCVM estimator. The curve is zoomed in during the periods of the oscillation and the steady state as shown in Figure 7-42 (b) (c) (e) and (f).
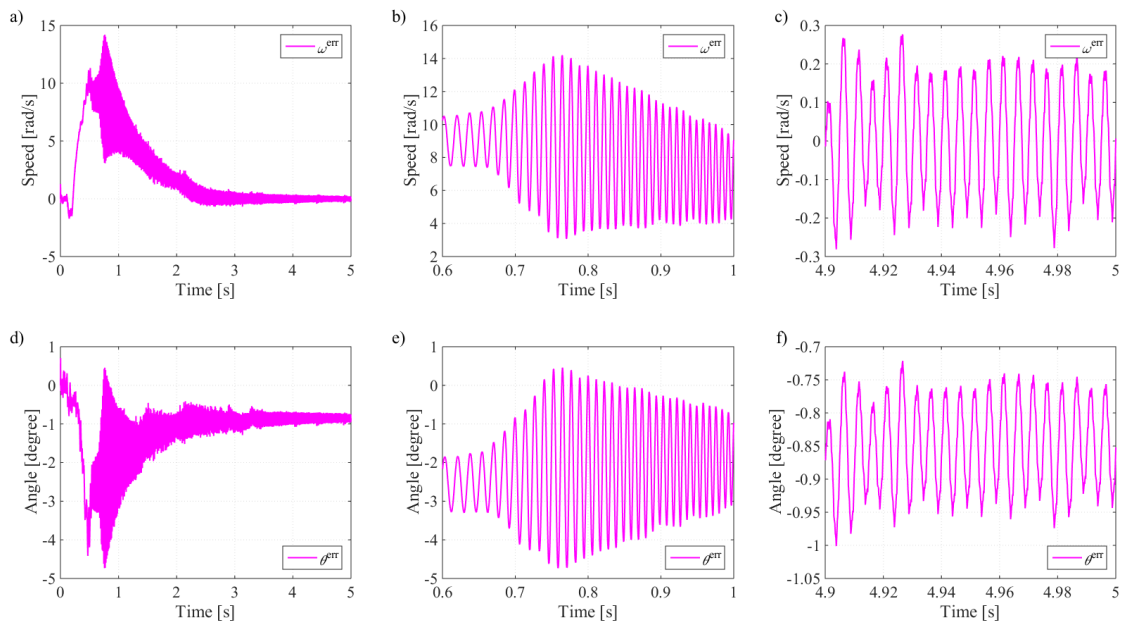
Figure 7-42 Sensorless control performance (Model 9): sensorless control estimator

a) speed estimation error ω^{err} b) ω^{err} (0.6 s < t < 1.0 s)   c) ω^{err} (4.9 s < t < 5.0 s)

d) angle estimation error θ^{err} e) θ^{err} (0.6 s < t < 1.0 s)   f) θ^{err} (4.9 s < t < 5.0 s)

The frequency of the oscillation is at the PMSM rotating speed which should be caused by the DC component. An observation can be made that such a relatively big oscillation starts at the same time as the HFI is totally faded out. Therefore, this oscillation may be caused by the DC component injected into the SCVM estimator: the HFI estimator only works with the high frequency signals, while the SCVM estimator works with low frequency signals. When the HFI

estimator is in operation in the beginning, the DC component cannot affect the HFI estimation and therefore, in the total estimation which is the combination of SCVM and HFI estimations, the effects from the DC component is attenuated. However, when HFI is faded out, such attenuation by the HFI is not valid anymore, so that the estimation oscillation at about 0.76 s occurs. In addition, as the DC component decreases, the oscillation also decreases as shown in Figure 7-42 (a) and (d).

The shunt currents, the three-phase voltage and current quantities and the current sampling in this sensorless control case are similar to the control with sensor case as shown in Figure 7-36, Figure 7-37 and Figure 7-38 respectively and therefore are not shown here again.

Last but not least, the efficiency of the electric system can be calculated. The efficiency can be defined as

$$\eta = \frac{p_{\text{mec}}}{p_{\text{inv}}} \times 100\% \tag{7-31}$$

where $p_{\text{mec}} = T_e \Omega_r$ is the power delivered from the electric part to the mechanical part of the system and $p_{\text{inv}} = u_{\text{inv·a}} i_{\text{inv·a}} + u_{\text{inv·b}} i_{\text{inv·b}} + u_{\text{inv·c}} i_{\text{inv·c}}$ is the power sent out from the inverter. The no load loss of the PMSM is not considered. Then, the steady state operation efficiency of the AC side electric system can be calculated by taking the time interval between 4 s ~ 5 s into consideration which achieves 91.65%.

7.6   Parameter Error Study

Parameter uncertainty is introduced to investigate the robustness of the controller with varying component parameters. Since this is not the focus of the thesis work, only some significant parameters are analyzed and detailed studies may be left for the future work.

7.6.1   Per Unit System

In order to predict the influence from the parameters to the performance, per unit values can be calculated and compared. The bases of the per unit system are listed in Table 7-16 and the corresponding per unit values are calculated and illustrated in Figure 7-43.

Table 7-16 Per unit bases

Variable		Value	Unit
Power	$S_{3\phi \cdot base}$	600	[kVA]
Primary Voltage	$U_{1 \cdot base}$	630	[V]
Secondary Voltage	$U_{2 \cdot base}$	4800	[V]
Primary Impedance	$Z_{1 \cdot base}$	0.6615	[Ω]
Secondary Impedance	$Z_{2 \cdot base}$	38.4000	[Ω]
Primary Admittance	$Y_{1 \cdot base}$	1.5117	[S]
Secondary Admittance	$Y_{2 \cdot base}$	0.0260	[S]
Electrical Frequency	f_{base}	200	[Hz]
Electrical Rotational Speed	ω_{base}	1256.6371	[rad/s]

Figure 7-43 indicates that the series reactances of the transformer, the cable and the PMSM contribute more to the series impedance of the system than the series resistances do. In addition, the cable susceptance shows an overwhelming value than the transformer susceptance. Therefore, it can be predicted that the measurement errors in the series reactances of all the three devices together with the susceptance of the cable capacitive branches will probably lead to more significant effects to the system than the errors in other parameters. Parameter errors are therefore introduced to the controller blocks and the simulation results are presented afterwards.
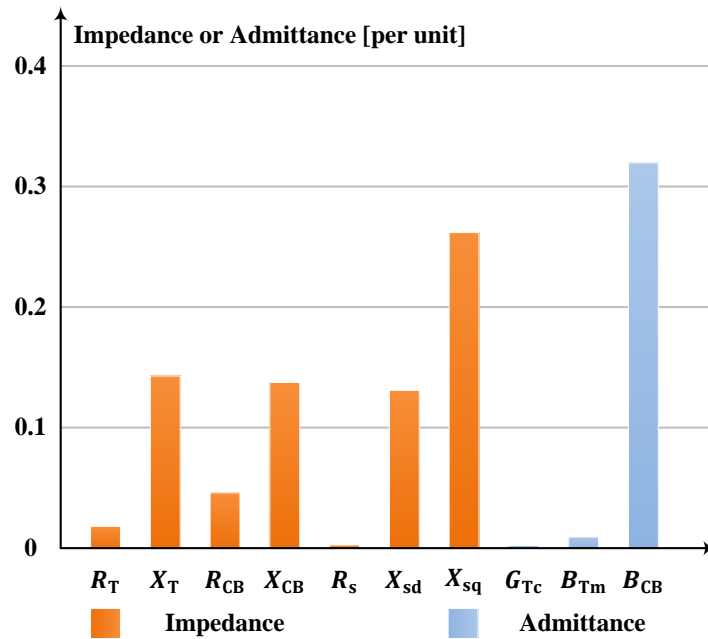
Figure 7-43 Series impedance and shunt admittance [per unit]

7.6.2 Theoretical Parameter Error Analysis

The steady state performance affected by the parameter errors is analyzed in this section. In steady state, the PMSM rotates at the speed of 1 per unit. Thus the estimated PMSM speed equals the real PMSM speed

$$\omega_r^{\text{est}} = \omega_r \tag{7-32}$$

In addition, the estimated d-axis stator current is adjusted to zero since the controller applies perfect flux linkage orientation from its own point of view

$$\hat{\imath}_{sd} = 0 \tag{7-33}$$

Therefore, from the equations of the real PMSM quantities

$$0 = e_d = u_{sd} - R_s i_{sd} + \omega_r L_{sq} i_{sq} \tag{7-34}$$

$$\omega_r \psi_{pm} = e_q = u_{sq} - R_s i_{sq} - \omega_r L_{sd} i_{sd} \tag{7-35}$$

the equations of the estimated PMSM quantities can be derived

$$0 = \hat{e}_d = \hat{u}_{sd} + \omega_r \hat{L}_{sq} \hat{\imath}_{sq} \tag{7-36}$$

$$\omega_r \hat{\psi}_{pm} = \hat{e}_q = \hat{u}_{sq} - \hat{R}_s \hat{\imath}_{sq} \tag{7-37}$$

When only the PMSM parameter errors are introduced, the relationships between the real and estimated equations become

$$\frac{u_{sd} - R_s i_{sd}}{L_{sq} i_{sq}} = \omega_r = \frac{\hat{u}_{sd}}{\hat{L}_{sq} \hat{\imath}_{sq}} \tag{7-38}$$

$$\frac{u_{sq} - R_s i_{sq} - \omega_r L_{sd} i_{sd}}{\psi_{pm}} = \omega_r = \frac{\hat{u}_{sq} - \hat{R}_s \hat{\imath}_{sq}}{\hat{\psi}_{pm}} \tag{7-39}$$

As can be seen, the terms containing the d-axis stator current, i.e. $R_s i_{sd}$ and $\omega_r L_{sd} i_{sd}$, appear on the left hand side to keep the equations in balance. An overestimation of $\hat{L}_{sq}$ or $\hat{\psi}_{pm}$ makes the right hand side smaller, and therefore needs a positive i_{sd} on the left hand side to keep the balance, which leads to a lagging estimated dq frame i.e. a positive angle estimation error and vice versa.

When only the transmission system parameter errors are introduced, the q-axis back-EMF is the same for both the real and the estimated quantities

$$u_{sq} - R_s i_{sq} - \omega_r L_{sd} i_{sd} = \omega_r \psi_{pm} = \hat{u}_{sq} - R_s \hat{\imath}_{sq} \tag{7-40}$$

Then, the d-axis PMSM stator current can be solved

$$i_{sd} = \frac{(u_{sq} - \hat{u}_{sq}) - R_s(i_{sq} - \hat{\imath}_{sq})}{\omega_r L_{sd}} \tag{7-41}$$

where the resistive voltage drop $R_s(i_{sq} - \hat{\imath}_{sq})$ can be neglected for a low PMSM stator resistance. Therefore, an underestimation of the stator voltage, e.g. an overestimation of L_{CB}, L_T or C_{CB}, will give a positive i_{sd} which leads to a lagging estimated dq frame, i.e. a positive angle estimation error and vice versa.

7.6.3 PMSM Parameter Error

A measurement error of 10% for ψ_{pm}, L_{sd}, L_{sq} and R_s is introduced in the beginning. All the cases are successful for the start-up, except for the 90% ψ_{pm} case which gives a start-up failure where the angle estimation error is too large to generate enough electromagnetic torque. An underestimation of 7.5% ψ_{pm} is acceptable for the start-up and therefore, the boundary between the stable and unstable cases for an underestimated ψ_{pm} should be somewhere between 7.5% and 10%. In additional, the differences of the performance given by an error in R_s is negligible for its too low voltage drop and therefore the curves are not presented in the report.

ψ_{pm} Error

The parameter ψ_{pm} decides the feedforward of the back-EMF term in the current controller and the sensorless estimation in SCVM. An over estimation of ψ_{pm} will lead to an over compensation of q-axis inverter voltage reference as well as a temporary underestimation of the PMSM speed by the SCVM estimator and vice versa. However, the inaccurate feedforward of the back-EMF can be adjusted by the PI current regulator while the inaccurate angle estimation will affect the system in steady state. The performance of a 10% overestimation of ψ_{pm} is shown in Figure 7-44.
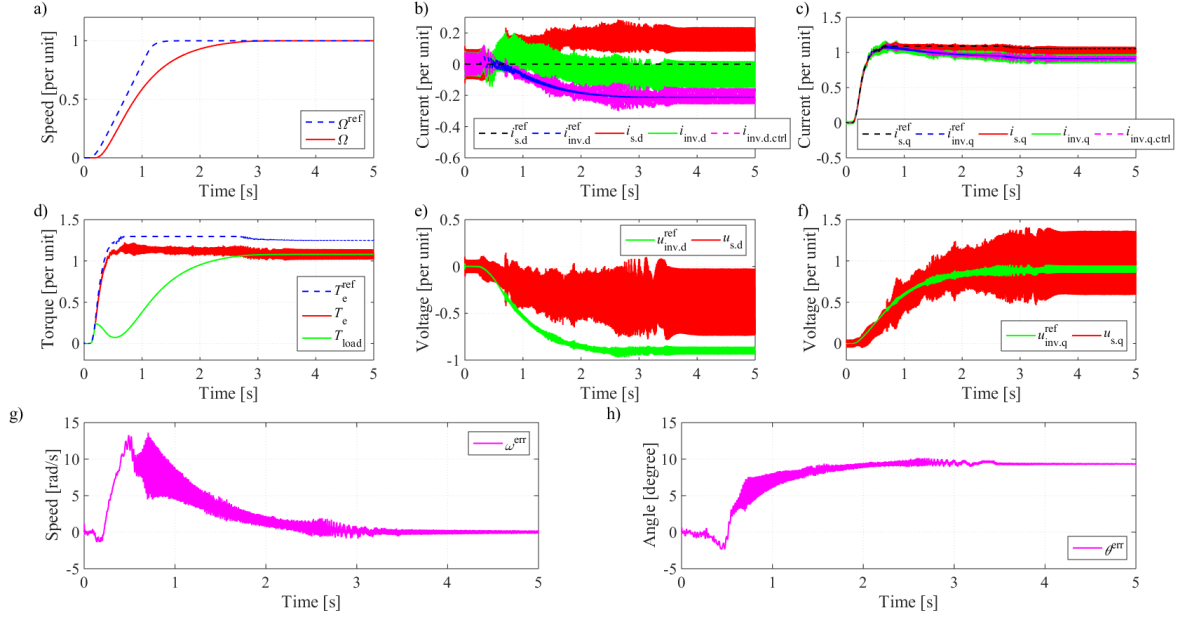
Figure 7-44 Parameter error study: ψ_{pm} 110% performance

a) rotor speed	b) d-axis current	c) q-axis current
d) torque	e) d-axis voltage	f) q-axis voltage
g) rotor speed estimation error		h) rotor angle estimation error

In Figure 7-44, the overestimated ψ_{pm} gives temporarily underestimated speed and statically underestimated angle. The results are consistent with the theoretical expectation based on (7-39) in Section 7.6.2. The speed controller pushes more current to force the underestimated PMSM speed to catch up with the speed reference as close as possible. At the same time, the underestimated angle shifts some q-axis current to d-axis, and therefore, the PMSM generates less electromagnetic torque per ampere which further leads to a deteriorated real PMSM speed. In the end, the deteriorated real PMSM speed and the underestimated PMSM speed meet each other. The whole process can be expressed as

$$\omega_r^{est} < \omega_r \quad \rightarrow \quad \theta_r^{est} < \theta_r \quad \rightarrow \quad \begin{matrix} i_{sd} \uparrow \\ i_{sq} \downarrow \end{matrix} \quad \rightarrow \quad T_e \downarrow \quad \rightarrow \quad \omega_r \downarrow \quad \rightarrow \quad \omega_r^{est} = \omega_r \qquad (7\text{-}42)$$

Therefore, the steady state speed estimation error goes to zero in Figure 7-44 (g) but a non-zero steady state angle estimation error still exists in Figure 7-44 (h).

In addition, although a non-zero d-axis stator current exists, the speed controller still believes that only q-axis current is injected. The blindness to the d-axis current makes T_e^{ref} higher than T_e. Since the speed error decreases to zero gradually, the torque reference is not adjusted any more, and therefore as can be seen in Figure 7-44 (d), the real torque does not follow the torque reference in steady state.

121

As has been illustrated before, the 10% underestimated case is a failure and therefore the 7.5% underestimated case is studied, which shows an opposite performance compared with an overestimation case. The explanations are similar and therefore are not repeated here.

L_{sd} and L_{sq} Error

The d- and q-axis PMSM stator inductance error affects the current controller and the SCVM configuration. Again, the current controller configuration error will not be a big problem due to the robustness of the IMC design so it is the effect to the SCVM that needs to be investigated. The case with an overestimation of both of the d- and q-axis PMSM inductances by 10% is presented in Figure 7-45. As can be seen in the figure, the start-up is still successful which means the system can be tolerant with a 10% PMSM stator inductance estimation error. The

performance of the estimator is similar with the one in the previous case with an error in ψ_{pm}.

As has been derived in Section 7.6.2, an overestimated stator inductance will cause a positive d-axis current. This theoretical analysis is realized as shown in Figure 7-45 (b). The positive d-axis current indicates a positive angle estimation error which is consistent with Figure 7-45 (h) where about +1.8071° appears as the angle estimation error in steady state. The SCVM estimator gives zero speed estimation error in steady state due to the same mechanism as illustrated in (7-42): the inaccurate speed estimation leads to an inaccurate angle estimation which further causes a deviated torque from the reference. Then the PMSM speed deviates and meets the inaccurate speed estimation. The underestimated d- and q-axis PMSM stator inductance error gives opposite performance and the explanation is similar, and therefore is not repeated here.

One observation that can be made by comparing Figure 7-45 with Figure 7-44 is that the d- and q-axis PMSM stator inductance error only gives 1.8071° steady state angle estimation error while the flux linkage error gives as much as 9.3266° steady state angle estimation error. Therefore it can be concluded that for the same level of parameter error, the stator inductance error gives a much smaller effect on the performance than the flux linkage error does. The reason may be that, as is shown in (6-21) and (6-22), the PMSM stator inductance error only affects the accuracy of the back-EMF estimation which is also dependent on other parameters than the PMSM stator inductance only, while the PMSM flux linkage error is the only term in the denominator of (6-22) which affects the speed estimation directly.
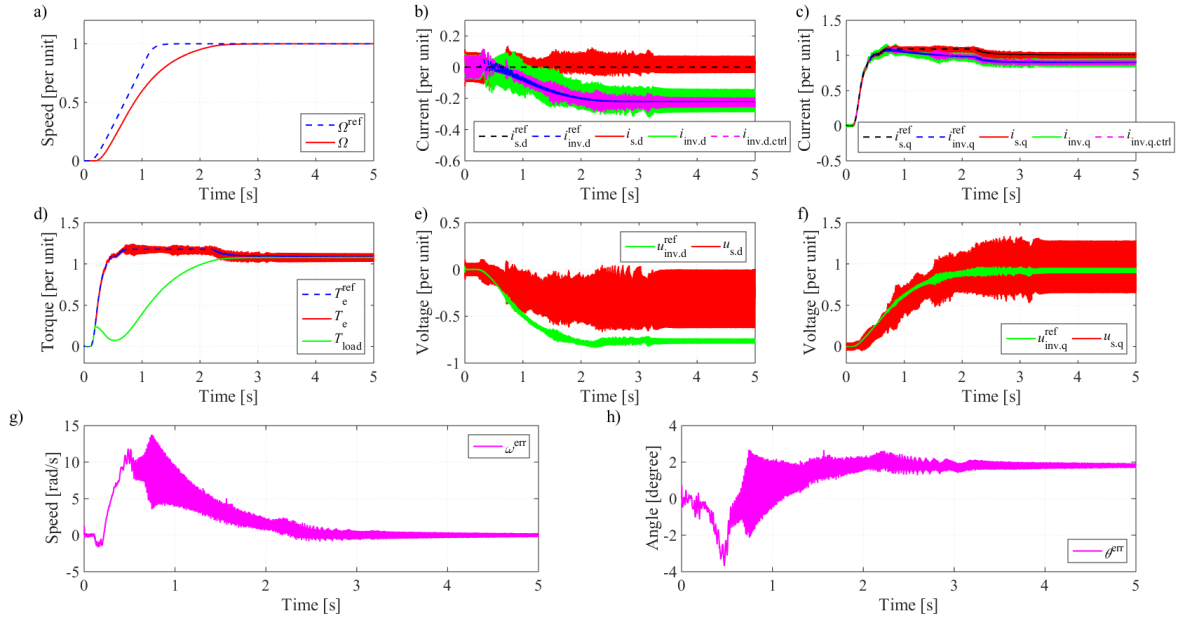
Figure 7-45 Parameter error study: L_{sd} and L_{sq} 110% performance

a) rotor speed	b) d-axis current	c) q-axis current
d) torque	e) d-axis voltage	f) q-axis voltage
g) rotor speed estimation error		h) rotor angle estimation error

7.6.4 Transmission System Parameter Error

Series Parameter Error

The series parameter error in the transmission system causes errors in the current controller and the PMSM static estimator which further affects the SCVM estimator. The imperfect configuration of the current controller will only give a limited influence to the dynamics while the error introduced to the PMSM static estimator will give an error to the SCVM estimator in steady state. The case with an overestimation of L_{cable} is shown in Figure 7-46 which seems not different from the perfect parameter case too much. The overestimation and underestimation of the other series component parameters in the transmission system give similar performances and are therefore are not presented here individually. It can be concluded that the series parameter errors in the transmission system give minor effects to the performance.

As can be seen from Figure 7-46, the d-axis stator current in the overestimation case is slightly shifted to the positive side compared with the perfect parameter case in Figure 7-39. The steady state angle estimation error for such overestimation case is 0.1843° while for an underestimation case is -1.9765° which is not shown here. The explanation for such steady state angle estimation errors is that, an overestimated series impedance yields an underestimation for the stator voltage and therefore an underestimated back-EMF and speed. However, in steady state, the collaboration of the speed controller and the SCVM estimator forces the speed estimation error

123

to zero. As has been derived in (7-41), a smaller $\hat{u}_{sdq}$ gives a positive i_{sd}, which means a lagging estimated dq frame or a positive angle estimation error in steady state and vice versa.
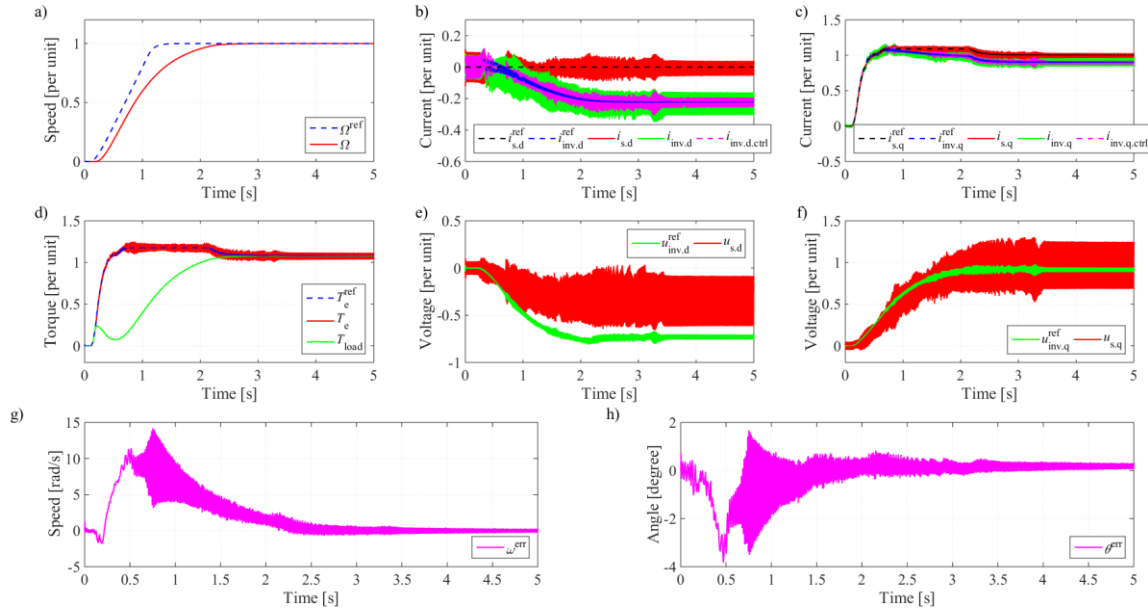
Figure 7-46 Parameter error study: L_{CB} 110% performance

a) rotor speed   b) d-axis current   c) q-axis current

d) torque   e) d-axis voltage   f) q-axis voltage

g) rotor speed estimation error   h) rotor angle estimation error

Shunt Parameter Error

Two shunt parameters are of interest in the transmission system: the energization capacitance of the cable C_{cable} and the magnetizing inductance of the transformer L_{Tm}. The core loss resistance of the transformer R_{Tc} is large enough and since it has been neglected in the controller design, there is no need to discuss the effects of the parameter error in R_{Tc}.

An introduced C_{cable} error will only affect the shunt current estimation and therefore the static estimation of the stator electrical quantities, while the PI controller is untouched. The overestimation and underestimation by 10% are introduced which give +0.0389° and -1.8095° steady state estimation errors respectively. The overestimation of C_{cable} introduces more current leakage at the cable terminals from the controller's point of view and therefore, a lower stator voltage and a lower back-EMF. Again, the steady state speed estimation error will be adjusted to zero due to the collaboration between the speed controller and the SCVM estimator.

As has been derived in (7-41), a lower $\hat{u}_{sdq}$ gives a positive i_{sd}, which means a positive angle estimation error. The opposite case happens in the underestimated case.

In terms of the error introduced in L_{Tm}, only the equivalent IM model will be affected which influences the dynamics of the current controller, while the performance of the SCVM and

shunt current compensation will be untouched. From the simulation results, the overestimation and underestimation of 10% give steady state angle estimation errors of less than 1°, which are negligible.

7.6.5   Comparison and Conclusion

As the PMSM performances with parameter errors presented in Section 7.6.3 and 7.6.4 are similar to each other, the key characteristics of the different cases in the parameter error study can be summarized and discussed in this section so that the results can be clearly compared. Due to the short period of the PMSM start-up, the steady state angle estimation becomes much more important compared with the start-up dynamics. The steady state angle estimation errors can be obtained by taking the average of the instantaneous angle estimation errors between 4 to 5 s when the PMSM has already gone to steady state. The steady state angle estimation errors are calculated and illustrated in Figure 7-47. In the figure, for the parameters other than ψ_{pm} and L_{sdq}, only the performances of ±10% parameter errors are shown, due to the reason that these parameters give limited effects to the system as was expected in Section 7.6.1.
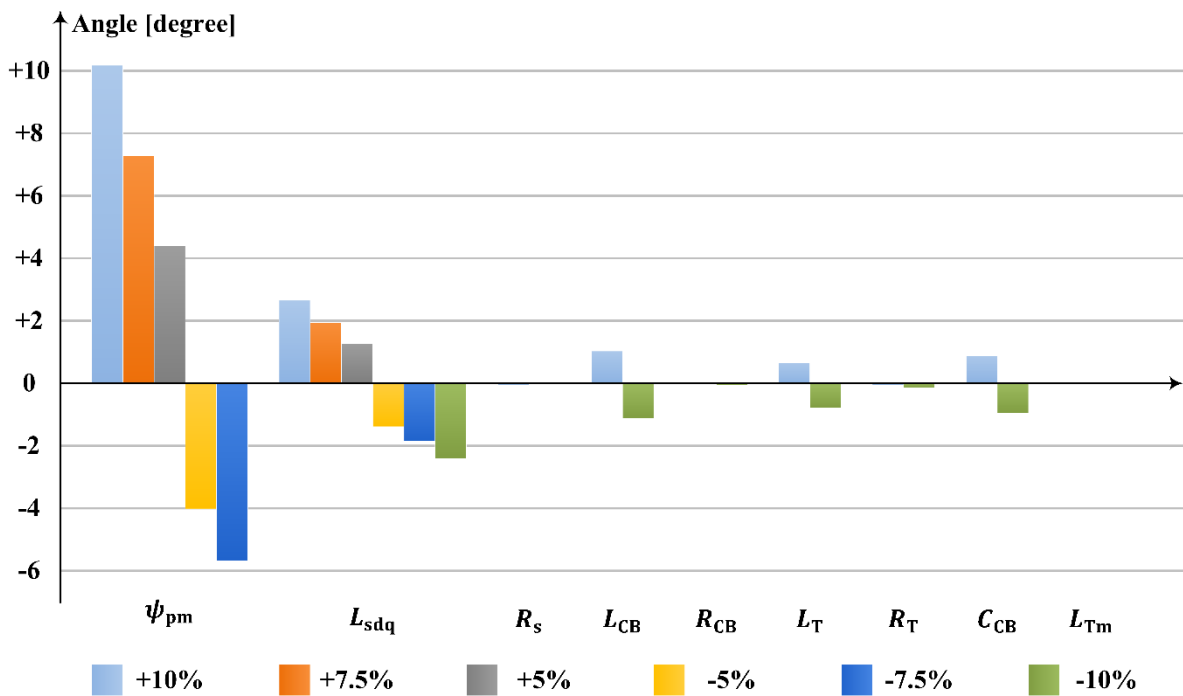
Figure 7-47 Angle estimation error differences in steady state

The -10% ψ_{pm} case is failing due to a too large angle estimation error during the start-up and therefore is not shown in Figure 7-47. The +10% ψ_{pm} case gives more than 10° steady state angle estimation error, and ±10% L_{sd} and L_{sq} cases give more than 2.4° while the other ±10%

125

parameter error cases give less than 1.2° angle error. Therefore, generally speaking, the parameter errors in ψ_{pm}, L_{sd} and L_{sq} give much more significant effects to the steady state angle estimation error compared with the other parameters. The reason is that ψ_{pm}, L_{sd} and L_{sq} are the key parameters in the SCVM estimator and therefore affect the angle estimation directly according to (6-21) and (6-22) while others do not. An overestimation of ψ_{pm}, L_{sd} and L_{sq}, L_{CB}, L_T or C_{CB} gives a positive deviation to the steady state angle estimation and vice versa. These deviations are consistent with the analysis in Section 7.6.2 and further explanations have been given in Section 7.6.3 and 7.6.4 which are based on the theoretical derivation in (7-38), (7-39) and (7-41).

In addition, the key characteristics from the parameter error study cases are collected and presented in Table 7-17. In the table, the maximum and minimum speed estimation errors are given both in rad/s as absolute values and in % as percentages of the perfect case. For instance, in the +10% ψ_{pm} case, the maximum and minimum speed estimation errors pick the positive and negative peak values in Figure 7-44 (g), both of which show the dynamic performance of the case. Similarly, the maximum and minimum angle estimation errors are given both in degree as absolute values and in % as percentages of the perfect case. The steady state angle estimation errors are given in degree both as absolute values and as relative values (marked as "Δ", which indicates "comparison") compared with the perfect case. Even in the perfect case, there is a small steady state angle estimation error and now the comparison is made with this error as a reference.

Table 7-17 Parameter error study comparison

The maximum and minimum speed estimation errors are given both in rad/s as absolute values and in % as percentages of the perfect case; Similarly, the maximum and minimum angle estimation errors are given both in degree as absolute values and in % as percentages of the perfect case. The steady state angle estimation errors are given in degree both as absolute values and as relative values (marked as "Δ", which indicates "comparison") compared with the perfect case.

| | | Speed Estimation Error | | | | Angle Estimation Error | | | | | |
| | | Max | | Min | | Max | | Min | | Steady State | |
		[rad/s]	[%]	[rad/s]	[%]	[deg]	[%]	[deg]	[%]	[deg]	Δ [deg]
Perfect Case		14.1995		-1.7308		0.7063		-4.7335		-0.8506	
ψ_{pm}	10%	13.624	95.95	-1.3771	79.56	10.1612	1438.65	-2.378	50.24	9.3266	10.1772
	7.5%	13.3155	93.77	-1.5686	90.63	6.9524	984.34	-2.822	59.62	6.4303	7.2809
	5%	13.8598	97.61	-1.5797	91.27	4.267	604.13	-3.3421	70.61	3.5546	4.4052
	-5%	14.7522	103.89	-1.9839	114.62	0.7695	108.95	-8.3784	177.00	-4.8706	-4.0200
	-7.5%	15.2095	107.11	-2.4199	139.81	0.7938	112.39	-10.1775	215.01	-6.5322	-5.6816
	-10%	Failure									
L_{sdq}	10%	13.7461	96.81	-1.6532	95.52	2.6748	378.71	-3.6852	77.85	1.8071	2.6577
	7.5%	13.8398	97.47	-1.8922	109.33	2.0488	290.08	-3.9579	83.61	1.0991	1.9497
	5%	13.8553	97.58	-1.881	108.68	1.4574	206.34	-4.0715	86.01	0.4162	1.2668
	-5%	14.5796	102.68	-1.6254	93.91	1.1284	159.76	-6.0357	127.51	-2.2394	-1.3888
	-7.5%	14.4853	102.01	-1.7296	99.93	1.1135	157.65	-6.6409	140.30	-2.7048	-1.8542
	-10%	14.7718	104.03	-2.4976	144.30	1.0875	153.97	-7.281	153.82	-3.2554	-2.4048
R_s	10%	14.1378	99.57	-1.8158	104.91	0.7063	100.00	-4.738	100.10	-0.9113	-0.0607
	-10%	14.2829	100.59	-1.8949	109.48	0.7063	100.00	-4.7647	100.66	-0.8783	-0.0277
L_{CB}	10%	14.202	100.02	-1.832	105.85	1.6726	236.81	-3.8284	80.88	0.1843	1.0349
	-10%	14.5023	102.13	-1.7689	102.20	0.7029	99.52	-6.03	127.39	-1.9765	-1.1259
R_{CB}	10%	14.316	100.82	-1.5096	87.22	0.8232	116.55	-4.5411	95.94	-0.8594	-0.0088
	-10%	14.0694	99.08	-2.154	124.45	1.2185	172.52	-4.9031	103.58	-0.9206	-0.0700
L_T	10%	13.886	97.79	-1.8046	104.26	1.4034	198.70	-4.1583	87.85	-0.1947	0.6559
	-10%	14.4169	101.53	-1.7307	99.99	0.6747	95.53	-5.9269	125.21	-1.6332	-0.7826
R_T	10%	14.3505	101.06	-1.6113	93.10	0.7019	99.38	-4.7063	99.43	-0.9007	-0.0501
	-10%	14.1795	99.86	-1.9346	111.77	0.7078	100.21	-4.8264	101.96	-1.0032	-0.1526
C_{CB}	10%	14.1774	99.84	-1.6756	96.81	0.7063	100.00	-4.5966	97.11	0.0389	0.8895
	-10%	14.1007	99.30	-1.7306	99.99	0.7063	100.00	-4.886	103.22	-1.8095	-0.9589
L_{Tm}	10%	14.1748	99.83	-1.8229	105.32	0.7064	100.01	-4.7994	101.39	-0.8605	-0.0099
	-10%	14.2023	100.02	-1.6631	96.09	0.7063	100.00	-4.7644	100.65	-0.8679	-0.0173

As can be noticed from Table 7-17, the errors introduced to L_{CB} and L_T give limited effects to the steady state angle estimation error which are less than 1°, but huge effects to the dynamic angle estimation error which are +236.81% for +10% L_{CB} and +198.70% for +10% L_T. It can be observed that such huge dynamic angle estimation errors appear when the HFI is faded out.

Therefore, the explanation can be addressed as follows. The static estimator gives inaccurate voltage and current estimation of the PMSM according to the parameter errors of the transmission system. Since the SCVM is based on the output of the static estimator while the HFI is not, from the beginning, the angle estimation does not totally rely on the static estimator, until when the HFI is faded out. The fading out of the HFI is a fast process as can be seen clearly in Figure 7-11 (b), which means the assistance of the HFI is almost turned off all of a sudden. Then the sensorless control estimator suddenly has to trust the inaccurate estimations from the static estimator entirely. However, it takes the sensorless control estimator some time to shift the almost perfect-oriented d-axis current, i.e. introduce some angle estimation error, to cope with such PMSM voltage and current estimation errors from the static estimator. Therefore, during such adaption between the sensorless control estimator and the static estimator, some fluctuations occur in the angle estimation which give such relatively large dynamic angle estimation error.

From Figure 7-47 and Table 7-17, another observation that can be made is that a steady state angle estimation error of less than 0.2° is given by ±10% parameter errors of R_s, R_CB, R_T or L_Tm, which indicates their limited effects to the controller. The reason may be due to the limited values of R_s, R_CB, R_T and B_Tm as shown in Figure 7-43. It can also be noticed that the parameter errors of the series resistances and the shunt inductance always give negative steady state angle estimation errors which are almost negligible and maybe due to the simulation accuracy.

In addition, the parameter errors in ψ_pm, L_sd and L_sq introduce not only large steady state angle estimation errors, but also large dynamic angle estimation errors. For example, the +10% ψ_pm error gives more than 10 times dynamic angle estimation error compared with the perfect case. Therefore, from the observations and discussions illustrated above, it can be concluded that the parameter values of ψ_pm, L_sd and L_sq are essential while the parameter values of R_s, R_CB, R_T and L_Tm are of less importance.

8 Discussion

8.1 Summaries of the Nine Models

Nine models are implemented in the thesis work as listed in Table 1-1, among which, six are presented in details. The summaries of the important investigations are discussed and listed in this chapter.

8.1.1 Model 1 ~ 3

In the simulations of Model 1~3, the inverter is directly connected to the PMSM, i.e. the transmission system is excluded. In Model 1, the current and speed controllers are implemented by applying the IMC design and the rotor position and speed are measured and fed back into the controller to realize vector control. The feedforward terms of the current controller have been verified and a first-order system response with a rise time of 3.5 ms has been achieved. The overall start-up performance is as expected and the speed reaches 6000 rev/min within 3 s.

In Model 2, the sensorless control structure is implemented, firstly the SCVM and the HFI are tested separately, and finally the combination of the two are implemented. Every one of the three can support a successful start-up. Under sensorless control, the perfect-orientation of the flux linkage in Model 1 is not available any more. Both dynamic and steady state angle estimation errors appear, while only dynamic speed estimation error appears and the steady state speed estimation error is eliminated by the PI regulator in the speed estimator. One observation can be made is that the HFI eliminates the angle estimation error after the PMSM reaches steady state, while the SCVM eliminates the angle estimation error within 1 s after the PMSM starts to rotate. However, the maximum angle estimation error of SCVM is over 10° while the maximum angle estimation error of the HFI is less than 1.5°. During the activation of the HFI, the three-phase currents are distorted by the injected HF signal and therefore the HFI is not preferred in steady state performance due to the increased harmonic loss. Therefore, a better performance is expected to be achieved by combining HFI and SCVM. Finally, the combination case achieves a lower estimation error in transients and no current distortion in steady state. The speed reaches 6000 rev/min within 3 s again and a preferred start-up performance is realized.

In Model 3, a two-level inverter is used to drive the system which is enough for a successful start-up. The three-phase currents are distorted by the switching harmonics. The single sampling and double sampling techniques are compared in the configuration with a position-sensor. As is shown in Table 7-7, the double current sampling case, which angle estimation error is less than 0.5°, gives a better steady state performance than the single sampling case does, which angle estimation error is more than 2°. After applying sensorless control, the steady state angle estimation error achieves 1.2324° with the double sampling technique as shown in Table 7-8. The speed rise from standing still to 6000 rev/min is implemented without problem and an expected performance is achieved.

8.1.2   Model 4 ~ 6

In the simulations of Model 4~6, the series impedance of the transmission system is taken into consideration while the shunt branches are excluded. The structure of the system can be simplified by integrating the series impedance of the transmission system into the stator of the PMSM so that the parameters of an equivalent PMSM can be obtained. The controller is modified with such equivalent parameters and a two-level inverter is enough for a successful start-up. The current controller rise time is still 3.5 ms, the same as the previous models. The steady state angle estimation errors are negligible, similar with Model 2 and 3.

8.1.3   Model 7 ~ 9

The entire transmission system is taken into consideration in Mode 7~9, i.e. both the series impedance and the shunt admittance of the system are included. In Model 7, an equivalent IM current controller, a static estimator and a state space model are implemented and a smooth start-up is achieved. A DC component caused by the transformer magnetization before the rotation of the PMSM is detected which gives an oscillation of the dq frame electrical quantities at the PMSM rotating speed during the start-up. The d- and q-axis current rise times are 3.8 and 3.5 ms respectively, which are within the range of the design. A dynamic estimator based on a state space model with perfect parameters is applied to estimate the states of the drive system. The estimation errors are at the level of 10^{-3} per unit and therefore the estimations can be regarded as almost perfect.

In Model 8, an additional current measuring point is added at the output of the transformer and the dynamic estimator based on the state space model is therefore removed. The sensorless control is implemented and the PMSM can be started up with no problem by only using the static estimation.

In Model 9, the switching harmonics from the two-level inverter encounter the resonances of the system. A five-level inverter is applied to achieve a lower amount of harmonics. An L filter is also added to the output of the inverter to reduce the harmonics. The SVPWM switching pattern is updated every half of the switching cycle to obtain a faster response from the current controller. Finally a successful start-up is achieved. The steady state angle estimation error is below 1° which is even better compared with the case without transmission system in Model 3.

8.2   PMSM Parameters

In [2], it is indicated that in subsea applications, non-salient PMSMs are usually applied due to the high speed requirement. In this work, a salient two-pole-pair PMSM is applied which is based on the expectations from the previous work [4] and the aim to provide the reader with different control algorithms. From this thesis work, it can be concluded that a one-pole-pair PMSM has two advantages. Firstly, given a fixed mechanical speed Ω_r, a one-pole-pair PMSM needs a lower fundamental electrical speed or frequency ω_r in steady state performance since

$$\omega_r = n_p \Omega_r \qquad (8\text{-}1)$$

and therefore, it gives a higher PWM frequency modulation index which is defined in (5-18). This indicates that the PWM applied to drive a one-pole-pair PMSM will distort the electrical quantities less than to drive a two-pole-pair PMSM. Secondly, the lower fundamental electrical frequency of the PMSM may set the system operation point farther from the transmission system resonance frequencies which are shown in Table 2-6. Therefore, based on the study in this thesis work, it is suggested to use one-pole-pair PMSMs in realistic subsea applications.

8.3   Sensorless Control

The SCVM can be applied if the PMSM back-EMF can be accurately estimated and the HFI can also work if the injected HF signal can be inserted into a frequency region free from resonance. However, the initial angle insensibility or detectability have not be checked in the work which should be realized in the future.

The operation of the SCVM is not only affected by the PMSM parameters, but also influenced by the static estimation for the transmission system, which provides the SCVM estimator with the PMSM current and voltage. An under-compensation for the transmission system in the controller, i.e. an overestimation of the stator voltage, will lead the estimated dq frame ahead of the real dq frame and vice versa. A 10% parameter error of the transmission system components gives relatively small influences to the start-up of the PMSM, while a 10% parameter error of the PMSM permanent magnet flux linkage or the dq frame inductances brings a much larger angle estimation error. Therefore, an accurate estimation of the PMSM parameters is an essential part for a successful PMSM start-up.

The thesis work considers a 15 km long cable which can be regarded as long enough in reality. However, if a longer cable is used, then the resonance frequencies in the Bode diagram will be shifted towards a lower frequency region and the HFI should only be applied with an even lower frequency. When the frequency of the injected signal is decreased too much, then such HFI cannot work since it will become impossible to separate the injected HF component from the fundamental components.

8.4   Shunt Compensation

The transformer magnetization branch is charged by a DC current in the beginning of the start-up. Such DC component is maintained in the windings for several seconds and therefore it introduces oscillations in the electric quantities at the rotation frequency in the dq frame during the meantime. In addition, the inductance and capacitance in the π-sections of the cable form series-connected low pass filters which introduce phase shift accordingly. As for the solutions, either a low pass filter can be added before the current controller to filter the oscillations in the dq frame out, or the oscillations can be neglected in the controller design since they will be

naturally damped out by the resistance of the transmission system. Static calculation can be applied to compensate for the phase shift caused by the π-sections of the cable.

The currents going through the shunt branches disturb the current controller and therefore the shunt branch currents need to be estimated and compensated. The estimation of the shunt currents in the magnetization branch of the transformer can be tricky. Hence either a state space model with proper self-correction feedback can be implemented, or both sides of the transformer currents can be measured to get around this estimation problem.

The speed controller for the new system is kept the same since the mechanical part is untouched, while the current controller is to be modified since the electrical part is changed. The current controller can be designed as an equivalent IM current controller by restructuring the entire system to an equivalent IM inverse-Γ model as illustrated in Section 6.2.2. However, if two transformers are added in the transmission system, i.e. one step-up and one step-down, the inverse-Γ model may not be applied. The shunt compensation and controller restructure could be redesigned in that case.

9 Conclusions and Future Work

9.1 Conclusions

The aim of the thesis work is to start the two-pole-pair salient PMSM up to 6000 rev/min within 10 s under sensorless control through a transmission system including a step-up transformer and a long feeding cable. The simulation result fulfills the aim of the thesis work, in which the PMSM is started up within 5 s. The electric system efficiency of the steady state operation under sensorless control with a realistic five-level cascade converter achieves 91.65% as calculated in (7-31), which includes the losses in the transmission system and the copper loss of the PMSM, but excludes the iron-core loss of the PMSM.

During the thesis work, the IMC design for the speed and current controllers shows its disturbance rejection ability. The current control loop bandwidth is selected to be 100 Hz and the rise times for both of the d- and q-axis current controls have been verified to be 3.5 ms which fits the design. Although affected by the oscillations introduced by the transmission system, the speed and current references can still be followed and the current rise times are verified to be 3.8 ms and 3.5 ms for d- and q-axis currents respectively. Therefore, the IMC design for the PMSM speed and current controllers can be suggested for the practical implementation.

The effects from the shunt branches of transmission system have been analyzed. The magnetization branch of the transformer generates a DC component of less than 0.05 per unit in the inverter current while the capacitive shunt branches of the cable introduce a phase shift between the inverter current and the PMSM stator current as has been explained in Section 7.5.3. These effects disturb the controller and are therefore compensated by restructuring the current controller from a PMSM controller to an equivalent IM controller and by adding a static estimator, which gives the static estimation of the electrical quantities of the PMSM stator as has been illustrated in Section 6.2. In the equivalent IM current controller, a simplification is performed by neglecting the difference between L_{sd} and L_{sq} to establish an IM inverse-Γ model. In the static estimator, the simplified model with only one π-section is built to describe the long feeding cable of 15 km. Such compensation performed by the static estimator takes care of the phase shift while the DC component is damped gradually by the series resistance in the circuit.

Both the SCVM and the HFI can be applied for the electric drive system, including the transformer and the long feeding cable, to realize sensorless control. As has been illustrated in Section 6.3.2, the application of the HFI with the transmission system needs to locate the injected HF signal at a suitable frequency in the Bode diagram to guarantee both the amplitude and phase requirements of the HFI method. The parameters of the HFI with the transmission system can be calculated by simplifying the transfer function of the transmission system. A five-level inverter modulated by SVPWM is applied and an L filter is added after the inverter

to reduce the switching harmonics. The performance is shown in Section 7.5.6 and the combined sensorless control achieves a steady state angle estimation of -0.8506° which is shown as the perfect case in Table 7-17. The positive and negative peak angle estimation errors during the start-up are 0.7063° and -4.7335° respectively. Overall, the cooperation between the equivalent IM current controller, the static estimator and the sensorless control gives a satisfactory performance.

Parameter errors are introduced for the most significant impedances and admittances individually. The performance of the system is affected much more by the PMSM parameter errors than by the transmission system parameter errors. 10% parameter errors of the transmission system give steady state angle estimation errors of less than 2° while a +10% error of the PMSM permanent magnet flux linkage gives a +9.3266° steady state angle estimation error and a -10% error of the PMSM permanent magnet flux linkage makes the PMSM unable to start up. ±10% d- and q-axis inductance errors give 2.6577° and -2.4048° steady state angle estimation errors respectively. Therefore, the accuracy of the PMSM parameters is much more essential than the accuracy of the transmission system parameters.

9.2   Future Work

Several tasks are suggested for the future work and are summarized as follows. A one-pole-pair PMSM should be considered instead of a multi-pole-pair PMSM which gives two advantages as has been discussed in Section 8.2: a lower fundamental frequency needs to be applied which leads to a higher modulation index and a farther distance from the resonance frequencies of the transmission system. In addition, the transmission system with two transformers can be considered which includes a step-up transformer, a long feeding cable and a step-down transformer. This is a more complicated but also a more general case for the subsea application as was introduced in the previous work [4].

In terms of the control system, sensorless control algorithms are still expected to be applied in order to make the system work reliably as has been illustrated in Section 1.1. Furthermore, the initial angle insensibility or detectability of the sensorless control algorithms should be checked which is out of the scope of this thesis work since the focus of this thesis work is to analyze and solve the effects from the shunt branches of the transmission system. Moreover, since a large amount of current harmonic content have been detected in Figure 7-40, passive or active filters can be designed to better remove the switching harmonics after the inverter in order to deliver a smoother torque from the PMSM to the pump. Last but not least, laboratory tests can be performed if equipment and time permit.

References

[1] M. Horn, F. Coudeville, E. Bespalov and H. Butcher, "Otter: A 21-Kilometer Subsea Tieback With Dual Electric Submersible Pumps," in *SPE Drilling & Completion*, 2004.

[2] M. J. Melfi, S. Evon and R. McElveen, "Induction versus permanent magnet motors," *Industry Applications Magazine, IEEE,* vol. 15, no. 6, pp. 28 - 35, 2009.

[3] G. Heggum, C. Girard, W. Harden, S. McNair and S. McAllister, "Development of Advanced Electric Submersible Pumps to Meet Today's Challenges," in *Society of Petroleum Engineers - Gulf Coast Section Electric Submersible Pump Workshop*, Woodlands, 2013.

[4] D. Stellas, "Master of Science Thesis - Sensorless Scalar and Vector Control of a Subsea PMSM," Chalmers University of Technology, Gothenburg, 2013.

[5] L. Harnefors and H.-P. Nee, "Model-based current control of AC machines using the internal model control method," *IEEE TRANSACTIONS ON INDUSTRY APPLICATIONS,* vol. 34, no. 1, pp. 133 - 141, 1998.

[6] L. Harnefors, "Design of Synchronous-Frame Current Controllers," in *Control of Variable-Speed Drives*, Västerås, Applied Signal Processing and Control, Department of Electronics, Mälardalen University, 2002, pp. 115 - 116.

[7] H. Akagi, E. H. Watanabe and M. Aredes, "THE INSTANTANEOUS POWER THEORY," in *Instantaneous Power Theory and Applications to Power Conditioning*, Tokyo, Wiley-IEEE Press, 2007, pp. 41 - 107.

[8] P. D. C. Perera, "Sensorless Control of Permanent-Magnet Synchronous Motor Drives," Aalborg University, Aalborg, 2002.

[9] P. Roshanfekr, T. Thiringer, M. Alatalo and S. Lundmark, "Performance of two 5 MW permanent magnet wind turbine generators using surface mounted and interior mounted magnets," in *Electrical Machines (ICEM), 2012 XXth International Conference on*, Marseille, 2012.

[10] R. Bojoi, M. Pastorelli, J. Bottomley, P. Giangrande and C. Gerada, "Sensorless control of PM motor drives — A technology status review," in *Electrical Machines Design Control and Diagnosis (WEMDCD), 2013 IEEE Workshop on*, Paris, 2013.

[11] F. Meier, "Permanent-Magnet Synchronous Machines with Non-Overlapping Concentrated Windings for Low-Speed Direct-Drive Applications," Royal Institute of Technology, Stockholm, 2008.

[12] L. Harnefors, "Torque Production and Control Principle," in *Control of Variable-Speed Drives*, Västerås, Applied Singnal Processing and Control, Department of Electronics, Mälardalen University, 2002, pp. 86 - 87.

[13] K. Baricuatro, "Sensorless Start-up and Control of Permanent Magnet Synchronous Motor with Long Tieback," Department of Electric Power Engineering, Norwegian University of Science and Technology, Trondheim, 2014.

[14] J. Zou , W. Qi, Y. Xu, F. Xu, Y. Li and J. Li, "Design of Deep Sea Oil-Filled Brushless DC Motors Considering the High Pressure Effect," *IEEE Transactions on Magnetics,* vol. 48, no. 11, pp. 4220 - 4223, 2012.

[15] W. Qi, J. Zou and J. Li, "Numerical Calculation of Viscous Drag Loss of Oil-filled BLDC Motor for Underwater Applications," in *2010 International Conference on Electrical Machines and Systems (ICEMS)*, Incheon, 2010.

[16] MØRE TRAFO AS, *150515-Tekniske Data Ao PORS-11000-420VOLT.123,* SYKKYLVEN: MØRE TRAFO AS, 2015.

[17] Helmerverken AB, *ATT VÄLJA RÄTT TRANSFORMATOR,* Helmerverken AB, 2015.

[18] ABB, *XLPE Cable Systems User's Guide,* Västerås: ABB, 2015.

[19] H. Saadat, Power System Analysis, PSA Publishing, 2010.

[20] MATLAB Documentation, *PI Section Line - Implement single-phase transmission line with lumped parameters,* The MathWorks, Inc., 2014.

[21] H. Olsson, K. Åström, C. C. d. Wit and M. Gäfv, "Friction Models and Friction Compensation," *European Journal of Control,* vol. 4, no. 3, pp. 176-195, 1998.

[22] D. Stellas, M. T. Hansen, T. Thiringer, T. Strømsvik and H. B. Ulvestad, "Position-sensorless control of a submersible PMSM fed over a long cable and two transformers," in *Power Electronics and Applications (EPE'14-ECCE Europe), 2014 16th European Conference on*, Lappeenranta, 2014.

[23] L. Harnefors, "Current Control," in *Control of Variable-Speed Drives*, Applied Signal Processing and Control, Department of Electronics, Mälardalen University, 2002, pp. 19 - 29.

[24] M. Documentation, *c2d - Convert model from continuous to discrete time,* MathWork.

[25] S. Cheng and C. Ifrim, "Long step sensorless control of permanent magnet synchronous machines with extended Kalman filter," in *2012 IEEE Symposium on Sensorless Control for Electrical Drives (SLED)*, Milwaukee, WI, 2012.

[26] P. Snary, B. Bhangu, C. Bingham, D. Stone and N. Schofield, "Matrix converters for sensorless control of PMSMs and other auxiliaries on deep-sea ROVs," in *IEE Proceedings - Electric Power Applications*, 2005.

[27] N. LI, L. DONG, Y. YOU, Y. GAO and X. LIAO, "Initial Rotor Position Estimation of IPMSM Based on Improved Rotating High Frequency Signal Injection," in *2014 IEEE Conference and Expo Transportation Electrification Asia-Pacific (ITEC Asia-Pacific)*, Beijing, 2014.

[28] Q. Tang, A. Shen and X. Luo, "Pulsating signal injection-based sensorless initial rotor position detection of PMSM using three symmetrical injection axes," in *2014 IEEE 23rd International Symposium on Industrial Electronics (ISIE)*, Istanbul, 2014.

[29] N.-C. Park and S.-H. Kim, "Simple sensorless algorithm for interior permanent magnet synchronous motors based on high-frequency voltage injection method," *IET Electric Power Applications,* vol. 8, no. 2, pp. 68 - 75, 2014.

[30] L. Harnefors, "The "Voltage Model"," in *Control of Variable-Speed Drives*, Västerås, Applied Signal Processing and Control, Department of Electronics, Mälardalen University, 2002, pp. 131 - 150.

[31] P. P. Acarnley and J. F. Watson, "Review of Position-Sensorless Operation of Brushless Permanent-Magnet Machines," in *IEEE Transactions on Industrial Electronics (Volume:53 , Issue: 2)*, 2006.

[32] S.-K. Sul, Control of Electric Machine Drive Systems, Piscataway: Wiley-IEEE Press , 2011.

[33] M. J. Corley and R. D. Lorenz, "Rotor Position and Velocity Estimation for a Permanent Magnet Synchronous Machine at Standstill and High Speeds," *IEEE Transactions on Industry Applications,* vol. 34, no. 4, pp. 784 - 789, 1998.

[34] S. Kim , J.-I. Ha and S.-K. Sul, "PWM Switching Frequency Signal Injection Sensorless Method in IPMSM," *IEEE Transactions on Industry Applications,* vol. 48, no. 5, pp. 1576 - 1587, 2012.

[35] J. M. Liu and Z. Q. Zhu, "Sensorless Control Strategy by Square-Waveform High-Frequency Pulsating Signal Injection Into Stationary Reference Frame," *IEEE Journal of Emerging and Selected Topics in Power Electronics,* vol. 2, no. 2, pp. 171 - 180, 2013.

[36] X. e. Chen, S. m. Gu, S. w. Ye and L. Wang, "Study on initial rotor position identification of permanent magnet synchronous motor based on high frequency signal injection," in *Informatics in Control, Automation and Robotics (CAR), 2010 2nd International Asia Conference on*, Wuhan, 2010.

[37] M. Jansson, L. Harnefors, O. Wallmark and M. Leksell, "Synchronization at Startup and Stable Rotation Reversal of Sensorless Nonsalient PMSM Drives," *Industrial Electronics,* vol. 53, no. 2, pp. 379 - 387, 2006.

[38] A. Piippo, M. Hinkkanen and J. Luomi, "Sensorless control of PMSM drives using a combination of voltage model and HF signal injection," in *Industry Applications Conference, 2004. 39th IAS Annual Meeting. Conference Record of the 2004 IEEE*, 2004.

[39] L. Harnefors, "Vector Control Using Speed and Position tracking," in *Control of Variable-Speed Drives*, Västerås, Applied Signal Processing and Control, Department of Electronics, Mälardalen University, 2002, pp. 163 - 173.

[40] P. T. Finlayson, "Output filters for PWM drives with induction motors," *IEEE Industry Applications Magazine,* vol. 4, no. 1, pp. 46 - 52, 1998.

[41] A. I. Systems, *Effects of AC drives on motor insulation. Technical guide No. 102,* New Berlin: ABB Industrial Systems Inc., 1998.

[42] K. V. Kumar, P. A. Michael, J. P. John and S. S. Kumar, "SIMULATION AND COMPARISON OF SPWM AND SVPWM CONTROL FOR THREE PHASE

INVERTER," *Asian Research Publishing Network (ARPN),* vol. 5, no. 7, pp. 61 - 74, 2010.

[43] S. P. Singh and R. K. Tripathi, "Performance Comparison of SPWM and SVPWM Technique in NPC Bidirectional Converter," in *2013 Students Conference on Engineering and Systems (SCES)*, Allahabad, 2013.

[44] K. H. Ahmed , S. J. Finney and B. W. Williams, "Passive Filter Design for Three-Phase Inverter Interfacing in Distributed Generation," in *Compatibility in Power Electronics*, Gdansk, 2007.

[45] E. C. D. S. JR. and E. R. C. D. SILVA, "CASCADE CONFIGURATION," in *Advanced Power Electronics Converters: PWM Converters Processing AC Voltages*, Wiley-IEEE Press, 2014, pp. 125 - 171.

[46] L. C. G. Vasquez, "Control of a Variable Speed Drive with a Multilevel Inverter for Subsea Applications," Department of Electric Power Engineering, Norwegian University of Science and Technology, Trondheim, 2010.

[47] L. C. G. Vasquez, "Control of a Variable Speed Drive with a Multilevel Inverter for subsea applications," Norwegian University of Science and Technology, ELKRAFT, 2010.

[48] J. P. John, D. S. S. Kumar and J. B., "Space Vector Modulation based Field Oriented Control scheme for Brushless DC motors," in *2011 International Conference on Emerging Trends in Electrical and Computer Technology (ICETECT)*, Tamil Nadu, 2011.

[49] D. G. Holmes and T. A. Lipo, "Zero Space Vector Placement Modulation Strategies," in *Pulse Width Modulation for Power Converters: Principles and Practice*, Wiley-IEEE Press, 2003, pp. 259 - 336.

[50] E. C. D. S. JR. and E. R. C. D. SILVA, "SPACE VECTOR MODULATION (SVPWM)," in *Advanced Power Electronics Converters: PWM Converters Processing AC Voltages*, Wiley-IEEE Press, 2014, pp. 243 - 247.

[51] A. Matsa, I. Ahmed and M. A. Chaudhari, "Optimized Space Vector Pulse-width Modulation Technique for a Five-level Cascaded H-Bridge Inverter," *Journal of Power Electronics,* vol. 14, no. 5, pp. 937 - 945, 2014.

[52] E. dos Santos and E. da Silva, "Cascade Configuration," in *Advanced Power Electronics Converters: PWM Converters Processing AC Voltages*, Wiley-IEEE Press, 2014, pp. 125 - 171.

[53] S. Wei, B. Wu, F. Li and C. Liu, "A General Space Vector PWM Control Algorithm for Multilevel Inverters," in *Applied Power Electronics Conference and Exposition, 2003. APEC '03. Eighteenth Annual IEEE*, Miami Beach, FL, USA, 2003.

[54] V. Blasko, V. Kaura and W. Niewiadomski, "Sampling of Discontinuous Voltage and Current Signals in Electrical Drives: A System Approach," *Industry Applications, IEEE Transactions on,* vol. 34, no. 5, pp. 1123 - 1130, 1998.

[55] M. Bongiorno, "On Control of Grid-connected Voltage Source Converters - Mitigation of Voltage Dips and Subsynchronous Resonances," Department of Energy and Environment, Chalmers University of Technology, Gothenburg, 2007.

[56] N. Mohan, T. M. Undeland and W. P. Robbins, "Switch-Mode dc-ac Inverters: dc-sinusoidal ac," in *Power Electronics: Converters, Applications, and Design*, John Wiley & Sons, inc., 2003, pp. 200 - 248.

[57] D. G. Holmes and T. A. Lipo, "Modulation of One Inverter Phase Leg," in *Pulse Width Modulation for Power Converters: Principles and Practice*, Wiley-IEEE Press, 2003, pp. 95 - 153.

[58] L. Harnefors, "Dynamic Model for the Induction Machine," in *Control of Variable-Speed Drives*, Västerås, Applied Signal Processing and Control, Department of Electronics, Mälardalen University, 2002, pp. 66 - 85.

[59] Open Electrical, "Cable Impedance Calculations," Open Electrical, 9 May 2015. [Online]. Available: http://www.openelectrical.org/wiki/index.php?title=Cable_Impedance_Calculations.

[60] Siemens, *SINAMICS S120 Drive System 0.12 kW to 1200 kW Catalog D 21.1,* Siemens, 2006.

[61] I. The MathWorks, "Solver Pane," in *MATLAB Documentation*, The MathWorks, Inc., 2014.

[62] I. The MathWorks, "Powergui," in *MATLAB Documentation*, The MathWorks, Inc., 2014.

[63] I. The MathWorks, "ashow," in *MATLAB Documentation*, The MathWorks, Inc., 2014.

[64] D. Saban and H. Artinian, "PERMANENT-MAGNET MOTORS FOR SUB-SEA APPLICATIONS," FMC Technologies, Cerritos.

[65] X. Liang and E. Fleming, "Electrical Submersible Pump Systems: Evaluating Their Power Consumption," *Industry Applications Magazine,* vol. 19, no. 6, pp. 46 - 55, 2013.

[66] A. Sayee Krishna and S. Kumar, "Position-Sensorless Operation of Brushless Permanent-Magnet Machines- A Review," in *Green Computing Communication and Electrical Engineering (ICGCCEE), 2014 International Conference on*, Coimbatore, 2014.

Appendix A   Salient PMSM S-Function

An m-file s-function defines a routine composed by several m-code functions. The s-function makes a sequence of calls to this routine to perform the task. An m-file s-function can be built in three parts:

- Initialization
  - Define the number of inputs, continuous states, discrete states and outputs;
  - Define the initial condition of the states;
  - Define the sample times.
- Algorithms
  - For continuous-time model, define the derivatives;
  - For discrete-time model, define the updates.
- Outputs

The inputs, states and outputs of the PMSM s-function are shown in Figure A-1.
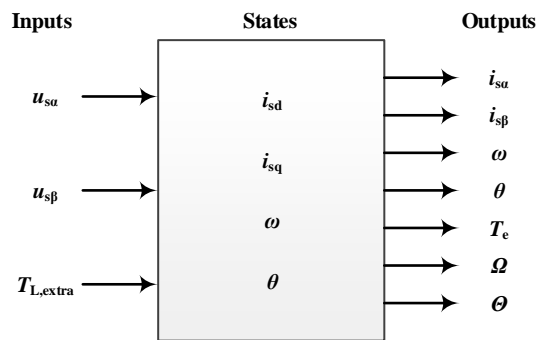
Figure A-1 PMSM s-function in MATLAB

```
%%%%%%%%%%%%%%%%%%%%%%%%%%%%%%%%%%%%%%%%%%%%%%%%%%%%%
%   The States:
%   x(1) = i_s_d     d-axis Current [A]
%   x(2) = i_s_q     q-axis Current [A]
%   x(3) = omega     Electrical Angular Speed [rad/s]
%   x(4) = theta     Electrical Angle [rad]
%
%   The Inputs:
%   u(1) = u_s_alpha Alpha-axis Voltage [V]
%   u(2) = u_s_beta  Beta-axis Voltage [V]
%   u(3) = T_extra   Extra Load Torque [N*m]
%
%   The Outputs:
%   y(1) = i_s_alpha Alpha-axis Current [A]
```

142

```matlab
%   y(2) = i_s_beta   Beta-axis Current [A]
%   y(3) = omega      Electrical Angular Speed [rad/s]
%   y(4) = theta      Electrical Angle [rad]
%   y(5) = T_e        PMSM Electromagnetic Torque [N*m]
%   y(6) = OMEGA      Mechanical Angular Speed [rad/s]
%   y(7) = THETA      Mechanical Angle [rad]
%%%%%%%%%%%%%%%%%%%%%%%%%%%%%%%%%%%%%%%%%%%%%%%%%%%%%%

function [sys,x0,str,ts] =
PMSM_Model(t,x,u,flag,J,B,n_p,R_s,L_s_d,L_s_q,PSI_m,xi)
%   CSFUNC An example M-file S-function for defining a continuous system.
%   Example M-file S-function implementing continuous equations:
%      x' = Ax + Bu
%      y  = Cx + Du
%   See sfuntmpl.m for a general S-function template.
switch flag,

  %%%%%%%%%%%%%%%%%%
  % Initialization %
  %%%%%%%%%%%%%%%%%%
  % flag = 0: Return the number of inputs, outputs, continuous and
discontinuous state variables, etc.
  case 0,
    [sys,x0,str,ts] =
mdlInitializeSizes(t,x,u,flag,J,B,n_p,R_s,L_s_d,L_s_q,PSI_m,xi);

  %%%%%%%%%%%%%%%
  % Derivatives %
  %%%%%%%%%%%%%%%
  % flag = 1: Return the continuous state derivatives
  case 1,
    sys = mdlDerivatives(t,x,u,flag,J,B,n_p,R_s,L_s_d,L_s_q,PSI_m,xi);

  %%%%%%%%%%%
  % Outputs %
  %%%%%%%%%%%
  % flag = 3: Commands the function to provide the block with the outputs
  case 3,
    sys = mdlOutputs(t,x,u,flag,J,B,n_p,R_s,L_s_d,L_s_q,PSI_m,xi);

  %%%%%%%%%%%%%%%%%%%
  % Unhandled flags %
  %%%%%%%%%%%%%%%%%%%
```

```matlab
  % flag = 2: The discrete updates
  case { 2, 4, 9 },
    sys = [];


  %%%%%%%%%%%%%%%%%%%%
  % Unexpected flags %
  %%%%%%%%%%%%%%%%%%%%
  otherwise
    error(['Unhandled flag = ',num2str(flag)]);
end
% end csfunc
%
%================================================================
===
% mdlInitializeSizes
% Return the sizes, initial conditions, and sample times for the S-
function.
%================================================================
===
%
function [sys,x0,str,ts] =
mdlInitializeSizes(t,x,u,flag,J,B,n_p,R_s,L_s_d,L_s_q,PSI_m,xi)

sizes = simsizes;
sizes.NumContStates  = 4;   % Number of continuous states
sizes.NumDiscStates  = 0;   % Number of discrete states
sizes.NumOutputs     = 7;   % Number of outputs
sizes.NumInputs      = 3;   % Number of inputs
sizes.DirFeedthrough = 0;   % Flag for direct feedthrough
sizes.NumSampleTimes = 1;   % Number of sample times

sys = simsizes(sizes);
x0  = xi;                   % initial states
str = [];
ts  = [0 0];
% end mdlInitializeSizes
%
%================================================================
===
% mdlDerivatives
% Solving State-Space Equations
% Return the derivatives for the continuous states.
```

```matlab
%===============================================================================
===
%
function sys = mdlDerivatives(t,x,u,flag,J,B,n_p,R_s,L_s_d,L_s_q,PSI_m,xi)

% States:
i_s_d  = x(1);    % d-axis Current [A]
i_s_q  = x(2);    % q-axis Current [A]
omega  = x(3);    % Electrical Angular Speed [rad/s]
theta  = x(4);    % Electrical Angle [rad]

% Input Signals:
u_s_alpha = u(1);    % Alpha-axis Voltage [V]
u_s_beta  = u(2);    % Beta-axis Voltage [V]
T_extra   = u(3);    % Extra Load Torque [N*m]

% From alphabeta to dq
u_s_d  = u_s_alpha * cos(theta) + u_s_beta * sin(theta);
u_s_q  = -u_s_alpha * sin(theta) + u_s_beta * cos(theta);

% Torques
T_e = 3 * n_p / 2 * ((L_s_d - L_s_q) * i_s_d * i_s_q + PSI_m * i_s_q);
T_L = B / n_p * omega + T_extra;

% Derivatives of the States
% Derivative of i_s_d
sys(1) = (u_s_d - R_s * i_s_d + omega * L_s_q * i_s_q) / L_s_d;
% Derivative of i_s_q
sys(2) = (u_s_q - R_s * i_s_q - omega * L_s_d * i_s_d - omega * PSI_m) /
L_s_q;
% Derivative of omega
sys(3) = n_p * (T_e - T_L) / J;
% Derivative of theta
sys(4) = omega;
% end mdlDerivatives
%
%===============================================================================
===
% mdlOutputs
% Return the block outputs.
%===============================================================================
===
%
```

```matlab
function sys = mdlOutputs(t,x,u,flag,J,B,n_p,R_s,L_s_d,L_s_q,PSI_m,xi)


i_s_d  = x(1); % [A]
i_s_q  = x(2); % [A]


omega  = x(3); % [rad/s]
theta  = x(4); % [rad]


T_e = 3 * n_p / 2 * ((L_s_d - L_s_q) * i_s_d * i_s_q + PSI_m * i_s_q); %
[N*m]


OMEGA  = omega / n_p;   % [rad/s]
THETA  = theta / n_p;   % [rad]


i_s_alpha = i_s_d * cos(theta) - i_s_q * sin(theta); % [A]
i_s_beta  = i_s_d * sin(theta) + i_s_q * cos(theta); % [A]


y(1) = i_s_alpha; % Alpha-axis Current [A]
y(2) = i_s_beta;  % Beta-axis Current [A]
y(3) = omega;     % Electrical Angular Speed [rad/s]
y(4) = theta;     % Electrical Angle [rad]
y(5) = T_e;       % PMSM Electromagnetic Torque [N*m]
y(6) = OMEGA;     % Mechanical Angular Speed [rad/s]
y(7) = THETA;     % Mechanical Angle [rad]


sys = [y(1),y(2),y(3),y(4),y(5),y(6),y(7)];
% end mdlOutputs
```

Appendix B   Cable Calculation

The conversion from Cable DC resistance to AC resistance is based on [59]. The DC resistance at temperature T can be calculated as

$$R_{\mathrm{DC \cdot T}} = R_{\mathrm{DC \cdot 20}}[1 + \alpha_{20}(T - 20)] \tag{B-1}$$

where $R_{\mathrm{DC \cdot 20}}$ is the DC resistance at $20\,°C$ $[\Omega/m]$; α_{20} is the temperature coefficient of the conductor material per K at $20\,°C$ $[K^{-1}]$, and for copper conductors, $\alpha_{20} = 3.93 \times 10^{-3}$ $[K^{-1}]$; T is the conductor operating temperature $[°C]$.

In addition, the corresponding AC resistances should be calculated. In steady state, the four-pole 6000 rpm PMSM requires an AC power at the frequency of

$$f_{\mathrm{C}} = \Omega_{\mathrm{r}}^{\mathrm{rated}} n_{\mathrm{p}} \frac{1}{60} = 6000 \times 2 \times \frac{1}{60}\ [\mathrm{Hz}] = 200\ [\mathrm{Hz}] \tag{B-2}$$

The AC resistance can be corrected from the DC resistance as

$$R_{\mathrm{AC}} = R_{\mathrm{DC}}(1 + y_{\mathrm{s}} + y_{\mathrm{p}}) \tag{B-3}$$

where R_{AC} is the AC resistance at the operating temperature $[\Omega/m]$; R_{DC} is the DC resistance at the operation temperature $[\Omega/m]$; y_{s} is the skin effect factor; y_{p} is the proximity effect factor. The skin effect factor y_{s} is calculated as

$$y_{\mathrm{s}} = \frac{x_{\mathrm{s}}^{4}}{192 + 0.8 x_{\mathrm{s}}^{4}} \tag{B-4}$$

where the factor x_{s}^{4} can be calculated as

$$x_{\mathrm{s}}^{4} = \left(\frac{8\pi f_{\mathrm{C}}}{R_{\mathrm{DC}}} k_{\mathrm{s}} \times 10^{-7}\right)^{2} \tag{B-5}$$

For a equilateral triangular placed cable, $k_{\mathrm{s}} = 1$. The proximity effect factor y_{p} is calculated as

$$y_{\mathrm{p}} = \frac{x_{\mathrm{p}}^{4}}{192 + 0.8 x_{\mathrm{p}}^{4}} \left(\frac{d_{\mathrm{c}}}{s}\right)^{2} \left[0.312\left(\frac{d_{\mathrm{c}}}{s}\right)^{2} + \frac{1.18}{\dfrac{x_{\mathrm{p}}^{4}}{192 + 0.8 x_{\mathrm{p}}^{4}} + 0.27}\right] \tag{B-6}$$

where d_{c} is the diameter of the conductor $[\mathrm{mm}]$; s is the center-to-center distance between conductor axes $[\mathrm{mm}]$ and the factor x_{p}^{4} can be calculated as

$$x_p{}^4 = \left(\frac{8\pi f_C}{R_{DC}} k_p \times 10^{-7}\right)^2 \tag{B-7}$$

For a round, stranded and non-impregnated cable, $k_p = 1$.

Appendix C Power Electronic Device Parameters

A 800 kW Power Electronic Converter including a three-phase diode rectifier, an energy storage capacitor bank and a three-phase inverter should be designed and implemented in Simulink for the simulation of the voltage profile of the entire system in Section 7.5.1. Since the voltage profile is presented in steady state, the calculation here focuses on the steady state performance.
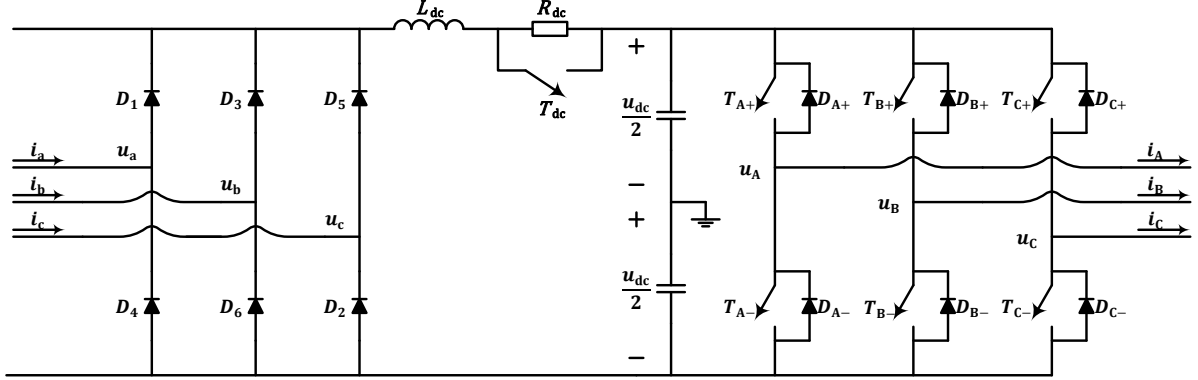
Figure C-1 The power electronic converter

The structure of the power electronic converter is shown in Figure C-1. In the beginning, the dc-link capacitors are charged through the dc-link resistance R_{dc}. After the charging process of the capacitors is finished, the switch T_{dc} is turned on and short-circuits R_{dc}. Then the PMSM speed reference is given and the PMSM starts to rotate. From the safety point of view, the midpoint of the inverter dc-link should be grounded. However, this will not influence the performance since the delta connection of the transformer will be connected to the inverter which will block the zero sequence component.

The power electronic converter takes power from a three-phase grid

$$U_{\text{in·line}}^{\text{rms}} = 690 \text{ [V]} \quad f = 50 \text{ [Hz]} \tag{C-1}$$

The diode rectifier converts the AC power into DC power and stores the energy in a dc-link capacitor bank. Under steady-state operation, the dc-link together with the load can be regarded as a DC current source, which means the rectified DC voltage can be calculated as

$$U_{\text{dc}} = \frac{3\sqrt{2}}{\pi} U_{\text{in·line}}^{\text{rms}} = 932 \text{ [V]} \tag{C-2}$$

However, the peak of the DC voltage appears after the capacitors are charged but before the load is connected. In this condition, the DC voltage reaches the peak of the input line voltage

$$U_{\text{dc}}^{\text{peak}} = \sqrt{2} U_{\text{in·line}}^{\text{rms}} = 976 \text{ [V]} \tag{C-3}$$

Considering an 800 kVA inverter, the DC current can be calculated as

149

$$I_{dc} = \frac{P_{3\phi}}{U_{dc}} = \frac{800}{932} \text{ [kA]} = 858 \text{ [A]} \tag{C-4}$$

The three-phase inverter converts the DC power into AC power again at the switching frequency of f_{sw}

$$f_{sw} = 4.2 \text{ [kHz]} \tag{C-5}$$

The maximum output phase voltage is $\frac{u_{dc}}{\sqrt{3}}$, and considering a power factor of 0.9, the output line voltage and current can be calculated as

$$U_{out \cdot line}^{max \cdot rms} = \frac{\sqrt{3}}{\sqrt{2}} \frac{U_{dc}}{\sqrt{3}} = U_{in \cdot line}^{rms} = 690 \text{ [V]} \tag{C-6}$$

$$I_{out}^{max \cdot rms} = \frac{P_{3\phi}}{\sqrt{3} u_{out}^{max \cdot rms} \cos \varphi} = \frac{800}{\sqrt{3} \times 690 \times 0.9} \text{ [kA]} = 744 \text{ [A]} \tag{C-7}$$

Three-Phase Diode Rectifier

Since the dc-link blocks the reactive power from the drive system, the rectifier only takes active power from the grid. The maximum voltage the diodes need to withstand is

$$U_{D}^{peak} = U_{dc}^{peak} = \sqrt{2} \times 690 \text{ [V]} = 976 \text{ [V]} \tag{C-8}$$

The average current and rms current going through each diode are

$$I_{D}^{avg} = \frac{I_{dc}}{3} = \frac{820}{3} \text{ [A]} = 273 \text{ [A]} \tag{C-9}$$

Based on the calculation result, the rectifier diode DD600N from Infineon Technologies can be selected which parameters are listed in Table C-1.

Table C-1 Rectifier diode parameters

Parameters	Symbols	Values	Units
Repetitive Peak Reverse Voltage	V_{RRM}	1800	[V]
Average On-State Current	I_{FAVM}	600	[A]
Threshold Voltage	$V_{F(T0)}$	0.75	[V]
On-State Resistance	R_{on}	0.215	[mΩ]

In practice, snubber circuits should be added due to over-voltages caused by stray or leakage inductance in series with the diodes. However, in this thesis work, stray or leakage inductance is not included in the consideration. Therefore, no snubber circuit is included in the simulation.

DC-Link Capacitance and Inductance

In steady state, the dc-link resistance is short-circuited. Therefore, it is the dc-link capacitance that should be focused on. The dc-link capacitance is selected based on two criteria

- The current ripple passing through the capacitor should be below the capacitor rating.

- The voltage ripple across the capacitor should be below the system requirements.

In this thesis work, since no real capacitor is selected, only the second criterion is considered, which is set to 5%.

The direct calculation of the minimum capacitance can be tricky. The selection can be started by taking a dc-link capacitance of an inverter at an equivalent power level from a datasheet and then verify the value of capacitance in the simulation. In the thesis work, 11.1 [mF] is selected based on an 800 kVA inverter configuration in [60].

The dc-link inductance is selected based on two criteria

- The LC filter should filter out the ripple voltage caused by the rectifier.

- The Total Harmonic Distortion (THD) that coursed by the rectifier.

As the grid THD is not within the scope of this thesis work, the first criterion is the one that should be focused on here. Since the rectifier uses six diodes, the voltage ripple should be at 300 [Hz]. The DC-link capacitance and inductance build up a LC low pass filter

$$H_{dc}(j\omega) = \frac{\frac{1}{j\omega C_{dc}}}{j\omega L_{dc} + \frac{1}{j\omega C_{dc}}} = \frac{1}{1 - \omega^2 L_{dc} C_{dc}} \tag{C-10}$$

The corresponding cut-off frequency can be calculated as

$$\left| H_{dc}(j\omega) \right| \Big|_{\omega = \omega_{cutoff}} = \frac{\sqrt{2}}{2} \Rightarrow \omega_{cutoff}^2 = \frac{\sqrt{2} - 1}{L_{dc} C_{dc}} \tag{C-11}$$

The voltage fundamental component from the rectifier

$$f_{h1} = 6f = 6 \times 50 \, [\text{Hz}] = 300 \, [\text{Hz}] \tag{C-12}$$

should be filtered out. It would be safe to make the cut-off frequency 100 times lower than the frequency component that should be filtered out, which yields

$$\omega_{cutoff}^{max} = 0.01 \cdot 2\pi f_{h1} = 0.01 \times 2\pi \times 300 \, [\text{rad/s}] = 18.85 \, [\text{rad/s}] \tag{C-13}$$

And therefore, the inductance L_{dc} can be calculated as

$$L_{dc}^{min} = \frac{\sqrt{2} - 1}{\omega_{cutoff}^{max}{}^2 C_{dc}} = \frac{\sqrt{2} - 1}{18.85^2 \times 11.1 \times 10^{-3}} \, [\text{H}] = 105.02 \, [\text{mH}] \tag{C-14}$$

The dc-link resistance R_{dc} is needed in order to damp the over-voltage out during the charging process, which means

$$\frac{1}{LCs^2 + RCs + 1} = \frac{\frac{1}{LC}}{s^2 + \frac{R}{L}s + \frac{1}{LC}} = \frac{\omega_n{}^2}{s^2 + 2\zeta\omega_n s + \omega_n{}^2} \tag{C-15}$$

$$\omega_n = \frac{1}{\sqrt{LC}} \quad \zeta = \frac{R}{2}\sqrt{\frac{C}{L}} \tag{C-16}$$

Apply $\zeta = 1$

$$R = 2\sqrt{\frac{L}{C}} = 2 \times \sqrt{\frac{105.02}{11.1}} = 6.1518 \ [\Omega] \tag{C-17}$$

Three-Phase Two-Level Inverter

The maximum voltage that one IGBT needs to withstand is

$$u_{IGBT}^{max} = U_{dc}^{peak} = 976 \ [V] \tag{C-18}$$

The peak current of the IGBT module is

$$I_{IGBT}^{peak} = \sqrt{2}I_{out}^{max \cdot rms} = \sqrt{2} \times 744 \ [A] = 1102 \ [A] \tag{C-19}$$

Based on the calculation result, the IGBT module FF650R17IE4 from Infineon Technologies can be selected which parameters are listed in Table C-2.

Table C-2 IGBT module parameters

IGBT Parameters			
Collector-Emitter Voltage	V_{CES}	1700	[V]
Repetitive Peak Collector Current	I_{CRM}	1300	[A]
On-State Forward Voltage Drop	$V_{CE(sat)}$	2.35	[V]
Fall Time	t_f	0.49	[µs]
Diode Parameters			
Repetitive Peak Reverse Voltage	V_{RRM}	1700	[V]
Repetitive Peak Forward Current	I_{FRM}	1300	[A]
On-State Forward Voltage Drop	V_F	1.95	[V]

It should be pointed out that since the repetitive peak collector current level of the selected IGBT module is only 18% higher than the needed maximum phase current, snubber circuits should be implemented in this case to protect the IGBT module.

Appendix D   State Space Model

Connecting the inverter, the transformer, the cable and the PMSM in series, the complex differential equations can be derived and the state space model can be further implemented. The models of resistance, inductance and capacitance in the dq frame together with the entire circuit in the dq frame are presented in Section 6.1. The transmission cable is represented by 1 π-section in the controller. However, in order to provide the reader with a more general case, a set of equations representing n π-sections is presented here, which includes totally n inductor currents and $(n+1)$ capacitor voltages.

Complex Differential Equations

(1) The transformer contains 3 inductor currents

$$\underline{u}_{inv} - \underline{u}_m = L_{T1}\frac{d\underline{i}_{inv}}{dt} + (R_{T1} + j\omega_r L_{T1})\underline{i}_{inv}$$

$$\underline{u}_m = L_{Tm}\frac{d\underline{i}_m}{dt} + j\omega_r L_{Tm}\underline{i}_m$$

$$\underline{u}_m - \underline{u}_{C(1)} = L_{T2}\frac{d\underline{i}_t}{dt} + (R_{T2} + j\omega_r L_{T2})\underline{i}_t$$

where $\underline{u}_m$ represents the voltage at the mid-point of the transformer and KCL can be applied at this point

$$\underline{i}_{inv} - \underline{i}_t = \underline{i}_c + \underline{i}_m = \frac{\underline{u}_m}{R_{Tc}} + \underline{i}_m$$

(2) The transmission cable totally contains n π-sections, which means totally n inductor currents and $(n+1)$ capacitor voltages. The n inductor current equations are

$$\underline{u}_{C(1)} - \underline{u}_{C(2)} = L_c\frac{d\underline{i}_{L(1)}}{dt} + (R_c + j\omega_r L_c)\underline{i}_{L(1)}$$

$$\underline{u}_{C(2)} - \underline{u}_{C(3)} = L_c\frac{d\underline{i}_{L(2)}}{dt} + (R_c + j\omega_r L_c)\underline{i}_{L(2)}$$

$$\cdots = \cdots$$

$$\underline{u}_{C(n-1)} - \underline{u}_{C(n)} = L_c\frac{d\underline{i}_{L(n-1)}}{dt} + (R_c + j\omega_r L_c)\underline{i}_{L(n-1)}$$

$$\underline{u}_{C(n)} - \underline{u}_s = L_c\frac{d\underline{i}_{L(n)}}{dt} + (R_c + j\omega_r L_c)\underline{i}_{L(n)}$$

and the $(n+1)$ capacitor voltage equations are

$$\underline{i}_t - \underline{i}_{L(1)} = \frac{C_c}{2}\frac{d\underline{u}_{C(1)}}{dt} + j\omega_r \frac{C_c}{2}\underline{u}_{C(1)}$$

$$\underline{i}_{L(1)} - \underline{i}_{L(2)} = C_c \frac{\mathrm{d}\underline{u}_{C(2)}}{\mathrm{d}t} + \mathrm{j}\omega_r C_c \underline{u}_{C(2)}$$

$$\underline{i}_{L(2)} - \underline{i}_{L(3)} = C_c \frac{\mathrm{d}\underline{u}_{C(3)}}{\mathrm{d}t} + \mathrm{j}\omega_r C_c \underline{u}_{C(3)}$$

$$\cdots = \cdots$$

$$\underline{i}_{L(n-1)} - \underline{i}_{L(n)} = C_c \frac{\mathrm{d}\underline{u}_{C(n)}}{\mathrm{d}t} + \mathrm{j}\omega_r C_c \underline{u}_{C(n)}$$

$$\underline{i}_{L(n)} - \underline{i}_s = \frac{C_c}{2}\frac{\mathrm{d}\underline{u}_s}{\mathrm{d}t} + \mathrm{j}\omega_r \frac{C_c}{2}\underline{u}_s$$

(3) The PMSM contains 1 complex inductor current equation which should be decomposed into two real equations

$$u_{sd} = R_s i_{sd} + L_{sd}\frac{\mathrm{d}i_{sd}}{\mathrm{d}t} - \omega_r L_{sq} i_{sq}$$

$$u_{sq} = R_s i_{sq} + L_{sq}\frac{\mathrm{d}i_{sq}}{\mathrm{d}t} + \omega_r L_{sd} i_{sd} + \omega_r \psi_m$$

State Space Model Equations

The transmission system equations can be reformulated into the state space form.

(1) The transformer contains 3 differential equations with one arithmetic equation:

$$\underline{u}_m = R_{Tc}\left(\underline{i}_{inv} - \underline{i}_t - \underline{i}_m\right) = R_{Tc}\underline{i}_{inv} - R_{Tc}\underline{i}_t - R_{Tc}\underline{i}_m$$

$$\frac{\mathrm{d}\underline{i}_{inv}}{\mathrm{d}t} = -\left(\frac{R_{T1}}{L_{T1}} + \mathrm{j}\omega_r\right)\underline{i}_{inv} + \frac{1}{L_{T1}}\left(\underline{u}_{inv} - \underline{u}_m\right)$$

$$\frac{\mathrm{d}\underline{i}_m}{\mathrm{d}t} = -\mathrm{j}\omega_r\underline{i}_m + \frac{1}{L_{Tm}}\underline{u}_m$$

$$\frac{\mathrm{d}\underline{i}_t}{\mathrm{d}t} = -\left(\frac{R_{T2}}{L_{T2}} + \mathrm{j}\omega_r\right)\underline{i}_t + \frac{1}{L_{T2}}\left(\underline{u}_m - \underline{u}_{C(1)}\right)$$

or

$$\frac{\mathrm{d}\underline{i}_{inv}}{\mathrm{d}t} = -\left(\frac{R_{T1} + R_{Tc}}{L_{T1}} + \mathrm{j}\omega_r\right)\underline{i}_{inv} + \frac{R_{Tc}}{L_{T1}}\underline{i}_m + \frac{R_{Tc}}{L_{T1}}\underline{i}_t + \frac{1}{L_{T1}}\underline{u}_{inv}$$

$$\frac{\mathrm{d}\underline{i}_m}{\mathrm{d}t} = \frac{R_{Tc}}{L_{Tm}}\underline{i}_{inv} - \left(\frac{R_{Tc}}{L_{Tm}} + \mathrm{j}\omega_r\right)\underline{i}_m - \frac{R_{Tc}}{L_{Tm}}\underline{i}_t$$

$$\frac{\mathrm{d}\underline{i}_t}{\mathrm{d}t} = \frac{R_{Tc}}{L_{T2}}\underline{i}_{inv} - \frac{R_{Tc}}{L_{T2}}\underline{i}_m - \left(\frac{R_{Tc} + R_{T2}}{L_{T2}} + \mathrm{j}\omega_r\right)\underline{i}_t - \frac{1}{L_{T2}}\underline{u}_{C(1)}$$

(2) The transmission cable contains n inductor current equations

$$\frac{\mathrm{d}\underline{i}_{L(1)}}{\mathrm{d}t} = -\left(\frac{R_c}{L_c} + \mathrm{j}\omega_r\right)\underline{i}_{L(1)} + \frac{1}{L_c}\left(\underline{u}_{C(1)} - \underline{u}_{C(2)}\right)$$

$$\frac{d\underline{i}_{L(2)}}{dt} = -\left(\frac{R_c}{L_c} + j\omega_r\right)\underline{i}_{L(2)} + \frac{1}{L_c}\left(\underline{u}_{C(2)} - \underline{u}_{C(3)}\right)$$

$$\cdots = \cdots$$

$$\frac{d\underline{i}_{L(n-1)}}{dt} = -\left(\frac{R_c}{L_c} + j\omega_r\right)\underline{i}_{L(n-1)} + \frac{1}{L_c}\left(\underline{u}_{C(n-1)} - \underline{u}_{C(n)}\right)$$

$$\frac{d\underline{i}_{L(n)}}{dt} = -\left(\frac{R_c}{L_c} + j\omega_r\right)\underline{i}_{L(n)} + \frac{1}{L_c}\left(\underline{u}_{C(n)} - \underline{u}_s\right)$$

and $(n + 1)$ capacitor voltage equations

$$\frac{d\underline{u}_{C(1)}}{dt} = -j\omega_r\underline{u}_{C(1)} + \frac{2}{C_c}\left(\underline{i}_t - \underline{i}_{L(1)}\right)$$

$$\frac{d\underline{u}_{C(2)}}{dt} = -j\omega_r\underline{u}_{C(2)} + \frac{1}{C_c}\left(\underline{i}_{L(1)} - \underline{i}_{L(2)}\right)$$

$$\frac{d\underline{u}_{C(3)}}{dt} = -j\omega_r\underline{u}_{C(3)} + \frac{1}{C_c}\left(\underline{i}_{L(2)} - \underline{i}_{L(3)}\right)$$

$$\cdots = \cdots$$

$$\frac{d\underline{u}_{C(n)}}{dt} = -j\omega_r\underline{u}_{C(n)} + \frac{1}{C_c}\left(\underline{i}_{L(n-1)} - \underline{i}_{L(n)}\right)$$

$$\frac{d\underline{u}_s}{dt} = -j\omega_r\underline{u}_s + \frac{2}{C_c}\left(\underline{i}_{L(n)} - \underline{i}_s\right)$$

(3) The PMSM contains 1 complex equation

$$\frac{di_{sd}}{dt} = \frac{-R_s i_{sd} + \omega_r L_{sq} i_{sq} + u_{sd}}{L_{sd}}$$

$$\frac{di_{sq}}{dt} = \frac{-R_s i_{sq} - \omega_r L_{sd} i_{sd} + u_{sq} - \omega_r \psi_m}{L_{sq}}$$

State Space Model Matrix

A state space model can be represented as

$$\frac{dx}{dt} = Ax + Bu + N$$

$$y = Cx$$

where x is the state variable vector which includes all the inductor currents and capacitor voltages, y is the output variable vector which includes the d- and q-axis PMSM currents, A is the dynamic matrix, B is the input matrix, C is the output matrix and N is the surplus matrix which appears because of the back-EMF term $\omega_r\psi_m$.

The states in the state variable vector x are placed as

$$x^T = [\underline{i}_{inv} \quad \underline{i}_m \quad \underline{i}_t \quad \underline{i}_{L(1)} \quad \cdots \quad \underline{i}_{L(n)} \quad \underline{u}_{C(1)} \quad \cdots \quad \underline{u}_{C(n)} \quad \underline{u}_s \quad i_{sd} \quad i_{sq}]$$

155

from which the matrices A, B, C and N in the state space model can therefore be formed as follows. Complex matrix A is

$$A = \begin{bmatrix} A_{11} & A_{12} & A_{13} \\ A_{21} & A_{22} & A_{23} \\ A_{31} & A_{32} & A_{33} \end{bmatrix}$$

In Row One

$$A_{11} = \begin{bmatrix}
-\dfrac{R_{T1}+R_{Tc}}{L_{T1}} & \omega_r & \dfrac{R_{Tc}}{L_{T1}} & 0 & \dfrac{R_{Tc}}{L_{T1}} & 0 \\[2.5ex]
-\omega_r & -\dfrac{R_{T1}+R_{Tc}}{L_{T1}} & 0 & \dfrac{R_{Tc}}{L_{T1}} & 0 & \dfrac{R_{Tc}}{L_{T1}} \\[2.5ex]
\dfrac{R_{Tc}}{L_{Tm}} & 0 & -\dfrac{R_{Tc}}{L_{Tm}} & \omega_r & -\dfrac{R_{Tc}}{L_{Tm}} & 0 \\[2.5ex]
0 & \dfrac{R_{Tc}}{L_{Tm}} & -\omega_r & -\dfrac{R_{Tc}}{L_{Tm}} & 0 & -\dfrac{R_{Tc}}{L_{Tm}} \\[2.5ex]
\dfrac{R_{Tc}}{L_{T2}} & 0 & -\dfrac{R_{Tc}}{L_{T2}} & 0 & -\dfrac{R_{Tc}+R_{T2}}{L_{T2}} & \omega_r \\[2.5ex]
0 & \dfrac{R_{Tc}}{L_{T2}} & 0 & -\dfrac{R_{Tc}}{L_{T2}} & -\omega_r & -\dfrac{R_{Tc}+R_{T2}}{L_{T2}}
\end{bmatrix}_{6\times6}$$

$$A_{12} = \begin{bmatrix} 0 & \cdots & 0 \\ \vdots & \ddots & \vdots \\ 0 & \cdots & 0 \end{bmatrix}_{6\times(2n+2)}$$

$$A_{13} = \begin{bmatrix} 0 & 0 & 0 & \cdots & 0 \\ \vdots & \vdots & \vdots & \ddots & \vdots \\ 0 & 0 & 0 & \cdots & 0 \\ -\dfrac{1}{L_{T2}} & 0 & 0 & \cdots & 0 \\ 0 & -\dfrac{1}{L_{T2}} & 0 & \cdots & 0 \end{bmatrix}_{6\times(2n+2)}$$

In Row Two

$$A_{21} = \begin{bmatrix} 0 & \cdots & 0 \\ \vdots & \ddots & \vdots \\ 0 & \cdots & 0 \end{bmatrix}_{(2n+2)\times6}$$

$$A_{22} = \begin{bmatrix} -\dfrac{R_{\mathrm{C}}}{L_{\mathrm{C}}} & \omega_{\mathrm{r}} & 0 & 0 & & & & & \\[2mm] -\omega_{\mathrm{r}} & -\dfrac{R_{\mathrm{C}}}{L_{\mathrm{C}}} & 0 & 0 & & & & & \\[2mm] 0 & 0 & -\dfrac{R_{\mathrm{C}}}{L_{\mathrm{C}}} & \omega_{\mathrm{r}} & & & & & \\[2mm] 0 & 0 & -\omega_{\mathrm{r}} & -\dfrac{R_{\mathrm{C}}}{L_{\mathrm{C}}} & & & & & \\[2mm] & & & & \ddots & & & & \\[2mm] & & & & & -\dfrac{R_{\mathrm{C}}}{L_{\mathrm{C}}} & \omega_{\mathrm{r}} & 0 & 0 \\[2mm] & & & & & -\omega_{\mathrm{r}} & -\dfrac{R_{\mathrm{C}}}{L_{\mathrm{C}}} & 0 & 0 \\[2mm] & & & & & 0 & 0 & -\dfrac{R_{\mathrm{s}}}{L_{\mathrm{sd}}} & \dfrac{\omega_{\mathrm{r}}L_{\mathrm{sq}}}{L_{\mathrm{sd}}} \\[2mm] & & & & & 0 & 0 & -\dfrac{\omega_{\mathrm{r}}L_{\mathrm{sd}}}{L_{\mathrm{sq}}} & -\dfrac{R_{\mathrm{s}}}{L_{\mathrm{sq}}} \end{bmatrix}_{(2n+2)\times(2n+2)}$$

$$A_{23} = \begin{bmatrix} \dfrac{1}{L_{\mathrm{C}}} & 0 & -\dfrac{1}{L_{\mathrm{C}}} & 0 & & & & & \\[2mm] 0 & \dfrac{1}{L_{\mathrm{C}}} & 0 & -\dfrac{1}{L_{\mathrm{C}}} & & & & & \\[2mm] & \dfrac{1}{L_{\mathrm{C}}} & 0 & -\dfrac{1}{L_{\mathrm{C}}} & 0 & & & & \\[2mm] & 0 & \dfrac{1}{L_{\mathrm{C}}} & 0 & -\dfrac{1}{L_{\mathrm{C}}} & & & & \\[2mm] & & & \ddots & & \ddots & & & \\[2mm] & & & & \dfrac{1}{L_{\mathrm{C}}} & 0 & -\dfrac{1}{L_{\mathrm{C}}} & 0 & \\[2mm] & & & & 0 & \dfrac{1}{L_{\mathrm{C}}} & 0 & -\dfrac{1}{L_{\mathrm{C}}} \\[2mm] & & & & & \dfrac{1}{L_{\mathrm{sd}}} & 0 & \\[2mm] & & & & & 0 & \dfrac{1}{L_{\mathrm{sq}}} \end{bmatrix}_{(2n+2)\times(2n+2)}$$

In Row Three

$$A_{31} = \begin{bmatrix} 0 & \cdots & \dfrac{2}{C_\mathrm{C}} & 0 \\[2mm] 0 & \cdots & 0 & \dfrac{2}{C_\mathrm{C}} \\[2mm] \vdots & \ddots & \vdots & \vdots \\[2mm] 0 & \cdots & 0 & 0 \end{bmatrix}_{(2n+2)\times 6}$$

$$A_{32} = \begin{bmatrix} -\dfrac{2}{C_\mathrm{C}} & 0 & & & & & & \\[2mm] 0 & -\dfrac{2}{C_\mathrm{C}} & & & & & & \\[2mm] \dfrac{1}{C_\mathrm{C}} & 0 & -\dfrac{1}{C_\mathrm{C}} & 0 & & & & \\[2mm] 0 & \dfrac{1}{C_\mathrm{C}} & 0 & -\dfrac{1}{C_\mathrm{C}} & & & & \\[2mm] & \ddots & \ddots & \ddots & \ddots & & & \\[2mm] & & \dfrac{1}{C_\mathrm{C}} & 0 & -\dfrac{1}{C_\mathrm{C}} & 0 & & \\[2mm] & & 0 & \dfrac{1}{C_\mathrm{C}} & 0 & -\dfrac{1}{C_\mathrm{C}} & & \\[2mm] & & & & \dfrac{2}{C_\mathrm{C}} & 0 & -\dfrac{2}{C_\mathrm{C}} & 0 \\[2mm] & & & & 0 & \dfrac{2}{C_\mathrm{C}} & 0 & -\dfrac{2}{C_\mathrm{C}} \end{bmatrix}_{(2n+2)\times(2n+2)}$$

$$A_{33} = \begin{bmatrix} 0 & \omega_\mathrm{r} & & & & & \\ -\omega_\mathrm{r} & 0 & & & & & \\ & & 0 & \omega_\mathrm{r} & & & \\ & & -\omega_\mathrm{r} & 0 & & & \\ & & & & \ddots & & \\ & & & & & 0 & \omega_\mathrm{r} \\ & & & & & -\omega_\mathrm{r} & 0 \end{bmatrix}_{(2n+2)\times(2n+2)}$$

As can be seen matric A contains a variable ω_r which means the state space model is not a LTI (Linear Time-Invariant) system but a Linear Time-Variant system. Matrix B is

$$B = \begin{bmatrix} \dfrac{1}{L_{\mathrm{T}1}} & 0 \\[2mm] 0 & \dfrac{1}{L_{\mathrm{T}1}} \\[2mm] 0 & 0 \\[2mm] \vdots & \vdots \\[2mm] 0 & 0 \end{bmatrix}_{(4n+10)\times 2}$$

158

An additional Matrix N is needed to represent the back-EMF of the PMSM

$$N = \begin{bmatrix} 0 \\ \vdots \\ 0 \\ -\dfrac{\omega_r \psi_m}{L_{sq}} \\ 0 \\ \vdots \\ 0 \end{bmatrix}_{(4n+10)\times 1}$$

where $-\dfrac{\omega_r \psi_m}{L_{sq}}$ appears at the $(2n+8)^{\text{th}}$ row, in the $\underline{i}_{sq}$ equation

$$C = \begin{bmatrix} 1 & 0 & 0 & \cdots & 0 \\ 0 & 1 & 0 & \cdots & 0 \end{bmatrix}_{2\times(4n+10)}$$

Appendix E   T Model to Inverse-Γ Model Transformation

This T model to inverse-Γ model transformation is performed in order to build the circuit presented in Section 6.2.2. In the αβ frame, the equations of the T model are

$$\underline{u}_1^s = R_1 \underline{i}_1^s + \frac{d\underline{\psi}_1^s}{dt}$$

$$\underline{u}_2^s = R_2 \underline{i}_2^s + \frac{d\underline{\psi}_2^s}{dt} - j\omega\psi_{pm}e^{j\theta} = 0$$

In the dq frame

$$\underline{u}_1 = R_1 \underline{i}_1 + \frac{d\underline{\psi}_1}{dt} + j\omega\underline{\psi}_1$$

$$\underline{u}_2 = R_2 \underline{i}_2 + \frac{d\underline{\psi}_2}{dt} + j\omega\underline{\psi}_2 - j\omega\psi_{pm} = 0$$

Define the inductance and the flux linkage

$$L_1 = L_{1\lambda} + L_m$$
$$L_2 = L_{2\lambda} + L_m$$

$$\underline{\psi}_1 = \underline{\psi}_{1\lambda} + \underline{\psi}_m = L_{1\lambda}\underline{i}_1 + L_m(\underline{i}_1 + \underline{i}_2)$$

$$= (L_{1\lambda} + L_m)\underline{i}_1 + L_m\underline{i}_2 = L_1\underline{i}_1 + L_m\underline{i}_2$$

$$\underline{\psi}_2 = \underline{\psi}_{2\lambda} + \underline{\psi}_m = L_{2\lambda}\underline{i}_2 + L_m(\underline{i}_1 + \underline{i}_2)$$

$$= (L_{2\lambda} + L_m)\underline{i}_2 + L_m\underline{i}_1 = L_2\underline{i}_2 + L_m\underline{i}_1$$

For a salient PMSM

$$u_{1d} = R_1 i_{1d} + L_1 \frac{di_{1d}}{dt} + L_m \frac{di_{2d}}{dt} - \omega L_1 i_{1q} - \omega L_m i_{2q}$$

$$u_{1q} = R_1 i_{1q} + L_1 \frac{di_{1q}}{dt} + L_m \frac{di_{2q}}{dt} + \omega L_1 i_{1d} + \omega L_m i_{2d}$$

$$u_{2d} = R_2 i_{2d} + L_2 \frac{di_{2d}}{dt} + L_m \frac{di_{1d}}{dt} - \omega L_2 i_{2q} - \omega L_m i_{1q} = 0$$

$$u_{2q} = R_2 i_{2q} + L_2 \frac{di_{2q}}{dt} + L_m \frac{di_{1q}}{dt} + \omega L_2 i_{2d} + \omega L_m i_{1d} - \omega\psi_{pm} = 0$$

The transfer from T model to inverse Γ model keeps the power unchanged. Therefore, the voltage and flux linkage are magnified by a factor b while the current is down scaled by the same factor b. The primary side variables are unchanged

$$\underline{u}_I = \underline{u}_1 \quad \underline{i}_I = \underline{i}_1 \quad \underline{\psi}_I = \underline{\psi}_1$$

The secondary side variables are scaled

$$\underline{u}_{II} = b\underline{u}_2 \quad \underline{i}_{II} = \frac{\underline{i}_2}{b} \quad \underline{\psi}_{II} = b\underline{\psi}_2 \quad \underline{\psi}_{PM} = b\underline{\psi}_{pm}$$

The corresponding parameters in the inverse Γ model can be calculated. From the T model, the secondary side flux linkage is

$$\underline{\psi}_{II} = b\underline{\psi}_2 = b\left(L_2\underline{i}_2 + L_m\underline{i}_1\right) = b^2L_2\underline{i}_{II} + bL_m\underline{i}_I$$

From the inverse Γ model, the secondary side flux linkage is

$$\underline{\psi}_{II} = L_M\underline{i}_{II} + L_M\underline{i}_I \quad \Rightarrow \quad \underline{i}_I + \underline{i}_{II} = \frac{\underline{\psi}_{II}}{L_M}$$

The comparison gives

$$b^2L_2 = bL_m = L_M \quad \Rightarrow \quad b = \frac{L_m}{L_2} \quad L_M = bL_m = \frac{L_m^2}{L_2}$$

From the T model, the primary side flux linkage is

$$\underline{\psi}_I = L_1\underline{i}_1 + L_m\underline{i}_2 = L_1\underline{i}_I + L_m\frac{L_m}{L_2}\underline{i}_{II} = L_1\underline{i}_I + L_M\underline{i}_{II}$$

From the inverse Γ model, the primary side flux linkage is

$$\underline{\psi}_I = (L_\sigma + L_M)\underline{i}_I + L_M\underline{i}_{II}$$

The comparison gives

$$L_\sigma = L_1 - L_M$$

Besides, the relationship between $\underline{\psi}_I$ and $\underline{\psi}_{II}$ is

$$\underline{\psi}_I = \underline{\psi}_{II} + L_\sigma\underline{i}_I$$

The primary equation can be presented as

- The T model

$$\underline{u}_1 = R_1\underline{i}_1 + \frac{d\underline{\psi}_1}{dt} + j\omega\underline{\psi}_1$$

161

- The inverse Γ model

$$\underline{u}_{\mathrm{I}} = R_{\mathrm{I}}\underline{i}_{\mathrm{I}} + \frac{\mathrm{d}\underline{\psi}_{\mathrm{I}}}{\mathrm{d}t} + \mathrm{j}\omega\underline{\psi}_{\mathrm{I}}$$

Therefore,

$$R_{\mathrm{I}} = R_1$$

and

$$\underline{u}_{\mathrm{I}} = R_{\mathrm{I}}\underline{i}_{\mathrm{I}} + L_\sigma\frac{\mathrm{d}\underline{i}_{\mathrm{I}}}{\mathrm{d}t} + \frac{\mathrm{d}\underline{\psi}_{\mathrm{II}}}{\mathrm{d}t} + \mathrm{j}\omega L_\sigma\underline{i}_{\mathrm{I}} + \mathrm{j}\omega\underline{\psi}_{\mathrm{II}}$$

The secondary equation can be presented as

- The T model

$$R_2\underline{i}_2 + \frac{\mathrm{d}\underline{\psi}_2}{\mathrm{d}t} + \mathrm{j}\omega\underline{\psi}_2 - \mathrm{j}\omega\psi_{\mathrm{pm}} = 0$$

$$R_2 b\underline{i}_{\mathrm{II}} + \frac{1}{b}\frac{\mathrm{d}\underline{\psi}_{\mathrm{II}}}{\mathrm{d}t} + \mathrm{j}\frac{\omega}{b}\underline{\psi}_{\mathrm{II}} - \mathrm{j}\frac{\omega}{b}\psi_{\mathrm{PM}} = 0$$

$$R_2 b^2\underline{i}_{\mathrm{II}} + \frac{\mathrm{d}\underline{\psi}_{\mathrm{II}}}{\mathrm{d}t} + \mathrm{j}\omega\underline{\psi}_{\mathrm{II}} - \mathrm{j}\omega\psi_{\mathrm{PM}} = 0$$

- The inverse Γ model

$$R_{\mathrm{II}}\underline{i}_{\mathrm{II}} + \frac{\mathrm{d}\underline{\psi}_{\mathrm{II}}}{\mathrm{d}t} + \mathrm{j}\omega\underline{\psi}_{\mathrm{II}} - \mathrm{j}\omega\psi_{\mathrm{PM}} = 0$$

Therefore,

$$R_{\mathrm{II}} = b^2 R_2$$

Quantities and parameters concluded as

Table E-1 T to inverse Γ transformation

Scaling factor	$b = \dfrac{L_{\mathrm{m}}}{L_2}$			
Primary side quantities	$\underline{u}_{\mathrm{I}} = \underline{u}_1 \quad \underline{i}_{\mathrm{I}} = \underline{i}_1 \quad \underline{\psi}_{\mathrm{I}} = \underline{\psi}_1$			
Secondary side quantities	$\underline{u}_{\mathrm{II}} = b\underline{u}_2 \quad \underline{i}_{\mathrm{II}} = \dfrac{\underline{i}_2}{b} \quad \underline{\psi}_{\mathrm{II}} = b\underline{\psi}_2 \quad \underline{\psi}_{\mathrm{PM}} = b\underline{\psi}_{\mathrm{pm}}$			
Parameters	$R_{\mathrm{I}} = R_1 \quad L_{\mathrm{M}} = bL_{\mathrm{m}} \quad L_\sigma = L_1 - L_{\mathrm{M}} \quad R_{\mathrm{II}} = b^2 R_2$			

Substituting the secondary side relationship

$$-R_{\mathrm{II}}\underline{i}_{\mathrm{II}} + \mathrm{j}\omega\psi_{\mathrm{PM}} = \frac{\mathrm{d}\underline{\psi}_{\mathrm{II}}}{\mathrm{d}t} + \mathrm{j}\omega\underline{\psi}_{\mathrm{II}}$$

into the primary side

$$\underline{u}_\mathrm{I} = R_\mathrm{I}\underline{i}_\mathrm{I} + L_\sigma \frac{\mathrm{d}\underline{i}_\mathrm{I}}{\mathrm{d}t} + \frac{\mathrm{d}\underline{\psi}_\mathrm{II}}{\mathrm{d}t} + \mathrm{j}\omega L_\sigma \underline{i}_\mathrm{I} + \mathrm{j}\omega\underline{\psi}_\mathrm{II}$$

yields

$$\underline{u}_\mathrm{I} = (R_\mathrm{I} + R_\mathrm{II} + \mathrm{j}\omega L_\sigma)\underline{i}_\mathrm{I} + L_\sigma \frac{\mathrm{d}\underline{i}_\mathrm{I}}{\mathrm{d}t} + \mathrm{j}\omega\psi_\mathrm{PM} - \frac{R_\mathrm{II}}{L_\mathrm{M}}\underline{\psi}_\mathrm{II}$$

$$0 = R_\mathrm{II}\underline{i}_\mathrm{II} + \frac{\mathrm{d}\underline{\psi}_\mathrm{II}}{\mathrm{d}t} + \mathrm{j}\omega\underline{\psi}_\mathrm{II} - \mathrm{j}\omega\psi_\mathrm{PM}$$

where the flux linkages are

$$\underline{\psi}_\mathrm{I} = L_\sigma\underline{i}_\mathrm{I} + L_\mathrm{M}\underline{i}_\mathrm{I} + L_\mathrm{M}\underline{i}_\mathrm{II}$$

$$\underline{\psi}_\mathrm{II} = L_\mathrm{M}\underline{i}_\mathrm{I} + L_\mathrm{M}\underline{i}_\mathrm{II}$$

The transfer function for designing the current controller is

$$\underline{i}_\mathrm{I} = \frac{\underline{u}_\mathrm{I} - \mathrm{j}\omega\psi_\mathrm{PM} + \frac{R_\mathrm{II}}{L_\mathrm{M}}\underline{\psi}_\mathrm{II}}{sL_\sigma + R_\mathrm{I} + R_\mathrm{II} + \mathrm{j}\omega L_\sigma}$$

$$\underline{\psi}_\mathrm{II} = \frac{-R_\mathrm{II}\underline{i}_\mathrm{II} - \mathrm{j}\omega\underline{\psi}_\mathrm{II} + \mathrm{j}\omega\psi_\mathrm{PM}}{s}$$

Since the term $\frac{R_\mathrm{II}}{L_\mathrm{M}}\underline{\psi}_\mathrm{II}$ is quite small, it can be neglected.

The decoupling for a salient PMSM cannot be done easily and since the transmission system inductance is integrated with the PMSM stator inductance, the small salience is neglected and the scaling factor is assumed to be the same for both d- and q-axis.

Appendix F   Solver Configuration

Before the simulation, the simulation configuration must be clarified and properly selected. The global Simulink solver sets the configuration for all standard blocks provided by Simulink, while powergui solver only sets the configuration for *SimPowerSystems* blocks. The information provided in this appendix mainly comes from the help files of MATLAB [61] [62] [63]

Global Simulink Solver

Two solvers are provided in Simulink: the global solver for standard Simulink blocks and the powergui solver for *SimPowerSystem* blocks [61]. The details are provided in the help file and here only lists some important issues. The global solver is shown in Figure F-1.
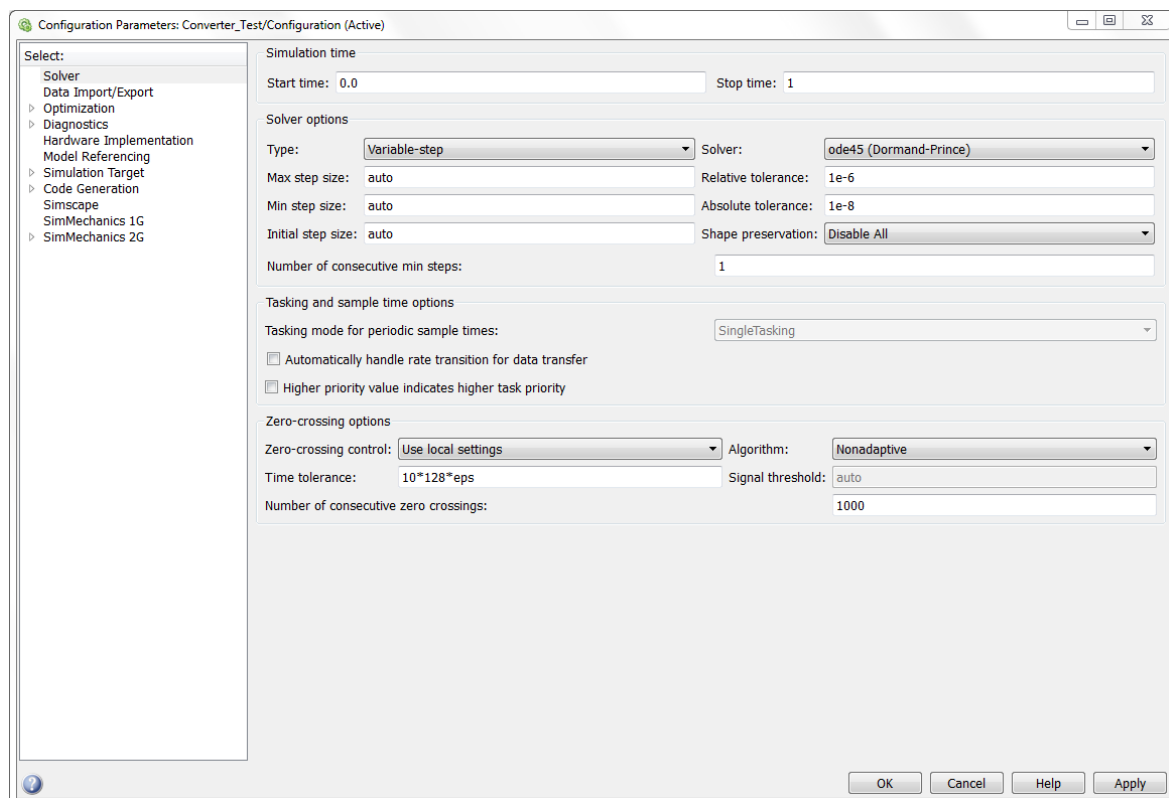

Figure F-1 Global Simulink Solver

Fixed-Step or Variable-Step Solver

The solver *type* can be selected as *fixed-step* or *variable-step*. The *fixed-step solver* keeps the step size as a constant throughout the simulation, while the *variable-step solver* decides the step size at each step based on the system dynamics, and the step size is reduced or increased to satisfy the specified error tolerances. In addition, a technique called *Zero-Crossing Detection* can be activated to improve the accuracy of the switching simulation only if the *variable-step* type is selected which is the case in this thesis work.

164

Discrete or Continuous Solver

A *discrete* or a *continuous* solver can be further selected for either the *fixed-step* or the *variable-step* type. The *discrete* solver can only be applied when the system only has discrete states, while a *continuous* solver can be applied when the system has both discrete and continuous states. When a *continuous* solver is applied, the discrete states in the system will update in the discrete way and the continuous states in the system will be integrated numerically in the continuous way respectively. In terms of a system with only discrete states, even if a *continuous* solver is specified, Simulink will use the *discrete* solver automatically. The ode45 continuous solver is suggested by Simulink which gives both excellent accuracy and fast simulation speed, and therefore, it is applied in this thesis work.

Step Sizes and Tolerances

The step sizes and tolerances decide the accuracy and the time cost of the simulation. The meanings of *max step size*, *min step size* and *initial step size* are obvious. In terms of the tolerances, at each simulation step i^{th}, the local error e_i of the state vector y is estimated by the solver. The simulation converges at step i^{th} if e_i satisfies:

$$|e_i| \leq \max(RelativeTolerance \cdot |y_i|, AbsoluteTolerance) \qquad \text{(I-F-1)}$$

Hence, *relative tolerance* decides the convergence at high state values while *relative tolerance* decides the convergence in the zero vicinity. The *relative tolerance* and *relative tolerance* determine the accuracy and the time cost of the simulation, and therefore, tradeoff can be cautiously made.

Zero-Crossing Detection

In the generation of PWM signals, several comparisons must be made in order to determine the instant for switching actions. The result will be inaccurate if the simulation solver steps over the zero-crossing point. Therefore, a technique called *Zero-Crossing Detection* should be applied in this case . If the solver steps over the zero-crossing point, then the solver will come back and estimate the zero-crossing instant, so the exact zero-crossing point can be located and the simulation becomes more accurate consequently. This *Zero-Crossing Detection* technique is only activated when the *Zero-Crossing Detection* option of the comparison block is ticked and the global solver is set at the type of "Variable-Step".

Another issue should be taken into consideration is that, if the powergui solver is set to be a *Discrete Solver*, then even if the *Zero-Crossing Detection* is activated in standard blocks and the zero-crossing signal is sent to the *SimPowerSystems* blocks, *SimPowerSystems* blocks will not react in time since they only wait for their discrete step defined by powergui and neglect the accurate zero-crossing point between the steps provided by the standard blocks. Therefore, in order to make the *SimPowerSystems* blocks act at the exact point, powergui solver should be defined as "Continuous".

165

Powergui Solver

Three options are provided the powergui solver: *continuous*, *discrete* and *phasors* [62]. The powergui solver will inherit the configuration from the global solver only if *continuous* is selected. If *discrete* is selected, then a sampling time T_s should be indicated, and in this case, the blocks from *SimPowerSystems* are simulated under the configuration of the powergui solver, while other blocks are still simulated under the configuration of the global solver.

In addition, when the *continuous* solver is applied, the use of *ideal switching devices* can be activated and the snubbers, the on-state resistance R_{on} and the forward voltage V_f can be selected to be disabled separately. When snubbers are disabled, the fall time t_f, tail time t_t and the on-state inductance L_{on} of the power electronic devices will also be disabled. The current waveform goes straight up and down and the switching losses are therefore neglected.

In this thesis work, *continuous* solver is applied and since the snubbers are not used, *ideal switching devices* are activated and snubbers are disabled.

Common Simulation Problems

- Algebraic Loop

An algebraic loop occurs when the output of the loop depends on its input, and therefore, the solver does not know where it should start to solve the loop. The algebra loop can be shown in Simulink by

```
ashow s#n
```

where `s` is the number of the system and `n` is the algebraic loop numbered [63].

The solution of an algebraic loop is to add a memory into the loop, so that the solver can start from the memory value to solve the loop. Insert a "memory" block into the loop in a continuous-time system, while insert a "unit delay" block into the loop in a discrete-time system. In this case, the signal will be delayed by an integration step time and the output of the "memory" or "unit delay" block is the previous input. Another choice can be to add a low pass filter. In this case, the bandwidth of the low pass filter α_{LPF} should be high enough so that the added phase shift can be negligible.

It should also be noticed that if a "memory" or "unit delay" block is added, then the corresponding measurement is delayed. In order to make the controller operate normally, it is essential to provide the controller with the measurement at the same time instant. Therefore, all the inputs to the controller should be delayed by the same time length. In addition, the abc-αβ transformation angle should be compensated in the same way as is described in Section 5.3.2.

- Consecutive Zero Crossing Detection

A *consecutive zero crossing* happens mostly because of the fluctuating angle estimation. The oscillating estimated frame will give a fluctuating q current. The controller then reacts to such

an estimated q current and results in an even fiercer q current which generates fierce electromagnetic force. Consequently, this will cause speed oscillation around zero and lead to a *consecutive zero crossing*. The solution is to adjust the estimator configuration and stabilize the angle estimation.